Copy No. 7

DEFENCE DÉFENSE

Improved Nonlinear Solution Techniques in the VAST Finite Element Program

L. Jiang

M.W. Chernuka

MARTEC Ltd.,
Suite 400, 1888 Brunswick Street,
Halifax, NS B3J 3J8

DEFENCE RESEARCH ESTABLISHMENT ATLANTIC

Contractor Report

DREA CR 2000-101

February 2000

National Defence Défense nationale

Canad

THIS IS AN UNEDITED REPORT ON SCIENTIFIC OR TECHNICAL WORK CONTRACTED BY THE DEFENCE RESEARCH ESTABLISHMENT ATLANTIC OF THE RESEARCH AND DEVELOPMENT BRANCH OF THE DEPARTMENT OF NATIONAL DEFENCE, CANADA.

THE CONTENTS OF THE REPORT ARE THE RESPONSIBILITY OF THE CONTRACTOR, AND DO NOT NECESSARILY REFLECT THE OFFICIAL POLICIES OF THE DEPARTMENT OF NATIONAL DEFENCE.

PLEASE DIRECT ENQUIRIES TO:

THE DIRECTOR GENERAL
DEFENCE RESEARCH ESTABLISHMENT ATLANTIC
P.O. BOX 1012
DARTMOUTH, NOVA SCOTIA, CANADA
B2Y 3Z7

REPRODUCTION QUALITY NOTICE

This document is the best quality available. The copy furnished to DRDCIM contained pages that may have the following quality problems:

: Pages smaller or Larger than normal

: Pages with background colour or light coloured printing

: Pages with small type or poor printing; and or

: Pages with continuous tone material or colour photographs

Due to various output media available these conditions may or may not cause poor legibility in the hardcopy output you receive.

☒ If this block is checked, the copy furnished to DRDCIM contained pages with colour printing, that when reproduced in Black and White, may change detail of the original copy.

Improved Nonlinear Solution Techniques in the VAST Finite Element Program

L. Jiang

M.W. Chernuka

MARTEC Ltd.,
Suite 400, 1888 Brunswick Street,
Halifax, NS B3J 3J8

Defence Research Establishment Atlantic

Contractor Report

DREA CR 2000-101

February 2000

Author

L. Jiang and M. W. Chernuka

Approved by

Malcolm Smith

Malcolm Smith

Contract Scientific Authority

Approved for release by

Walter E Ellis

Walter E Ellis

Chair, DREA Document Review Panel

© Her Majesty the Queen as represented by the Minister of National Defence, 2000

© Sa majesté la reine, représentée par le ministre de la Défense nationale, 2000

102-02516/

IMPROVED NONLINEAR SOLUTION TECHNIQUES IN THE VAST FINITE ELEMENT PROGRAM

Martec Report No.: TR-99-32

By:

L. Jiang
M.W. Chernuka

Prepared for:

Defence Research Establishment Atlantic
9 Grove Street
Dartmouth, NS B2Y 3Z7

Contract No.:	W7707-8-5876/001/HAL
SSC File No.:	HAL-8-40207

Martec Limited
Advanced Engineering and Research Consultants

400-1888 Brunswick Street
Halifax, NS B3J 3J8
Tel: (902) 425-5101
Fax: (902) 421-1923

101-717 boul St. Joseph
Hull, PQ J8Y 4B6
Tel: (819) 595-3526
Fax: (819) 595-1739

February 2000

ABSTRACT

This report presents theoretical and implementation details related to recent improvements in various linear and nonlinear solution techniques in the VAST finite element program. In order to improve the efficiency of the VAST solver, the preconditioned conjugate gradient method was implemented to provide an alternative means for solving systems of linear algebraic equations. Seven pre-conditioners, derived from the stationary iterative methods and incomplete factorization algorithms, were implemented and benchmarked. Numerical results suggest that for well conditioned problems, iterative solvers can be considerably more efficient than the direct solver. However, for poorly-conditioned problems, such as those resulted from structural analysis of thin shell structures, the performance of the preconditioned conjugate gradient method was not satisfactory. In order to further improve the efficiency of the iterative solver, pre-conditioners based on the multi-level or multi-grid methods have been recommended.

In order to provide an accurate and reliable method for generating residual stresses for load-shortening curve computations of stiffened panels, a linear thermal stress capability was developed in the VAST program. A stress scaling factor was employed to ensure that the maximum residual stress along the plate-web junction equals the yield stress. This capability has now been provided in the seven most commonly used elements in VAST and the extension to other elements is straightforward. The capability has been verified by extensive numerical studies and its efficiency in load-shortening curve generation was demonstrated.

The efficiency of the STRESS module for treating multiple load cases has also been improved. This was achieved by minimizing I/O operations. The driver subroutine of the module was completely restructured and each element subroutine was divided into two subroutines, one for I/O operations and the other for arithmetic calculations. Numerical results demonstrated that the improved STRESS module could be more efficient than the original one by many times if a large number of load cases are considered.

A capability of performing multiple analyses within a single execution of the VAST program has been developed. This feature is useful in all types of analyses. For example, for dynamic analyses, it allows the entire time period to be divided into multiple solution blocks with different time step sizes. With this feature, the process of calculating load-shortening curves, which includes four different analyses, can be fully automated. The possibility of using higher-order harmonic functions to replace the buckling mode shape as the additional imperfection has also been investigated. This study indicated that it was feasible to use higher order harmonic modes to obtain stable nonlinear solutions, however, the use of buckling mode shapes had significant advantages and was still recommended.

Finally, the adequacy of the previously generated generic load-shortening curve database for the ultimate strength analyses of the CPF was assessed. The effects of various parameters on the load-shortening behavior of stiffened panels were also studied in detail. This study suggests extensions of both the existing database and the interpolation algorithm in the ultimate strength analysis programs.

RÉSUMÉ

Le présent rapport explique les aspects détaillés de la théorie et de la mise en œuvre des améliorations apportées récemment à différentes techniques de solutions linéaires et non linéaires dans le programme à éléments finis VAST. Pour améliorer l'efficacité du solutionneur VAST, la méthode du gradient du conjugué préconditionné a été d'abord intégrée à titre de méthode de rechange pour résoudre des systèmes d'équations algébriques linéaires. Sept préconditionneurs, dérivés de méthodes itératives stationnaires et d'algorithmes de factorisation incomplets, ont été mis en œuvre et mis au banc d'essai. Les résultats numériques laissent supposer que pour les problèmes bien conditionnés, des solutionneurs itératifs pourraient être considérablement plus efficaces que le solutionneur direct; cependant, dans le cas des problèmes mal conditionnés, comme ceux qui résultent de l'analyse structurale des structures de voiles minces, la performance de la méthode du gradient du conjugué n'est pas satisfaisante. Pour améliorer davantage l'efficacité du solutionneur itératif, des préconditionneurs fondés sur les méthodes à plusieurs niveaux ou à plusieurs grilles sont recommandés.

Dans le but d'obtenir une méthode précise et fiable pour générer des contraintes résiduelles dans les calculs des courbes de réduction des charges de panneaux rigides, une capacité de contrainte thermique linéaire a été mise au point dans le programme VAST. On a employé un facteur d'échelle des contraintes pour s'assurer que la contrainte résiduelle maximale le long de la jonction plaque-âme est égale à la limite d'élasticité apparente. La capacité est maintenant intégrée dans les sept éléments du VAST les plus couramment utilisés et l'application aux autres éléments est directe. La capacité a été vérifiée par de nombreuses études numériques et son efficacité de réduction des charges a été démontrée.

L'efficacité du module STRESS pour traiter les cas de charges multiples a également été améliorée. Pour ce faire, on a réduit au minimum les opérations d'entrée et de sortie. Le sous-programme du schéma de commande du module a été complètement restructuré et chaque sous-programme d'éléments a été divisé en deux sous-programmes, l'un pour les opérations d'entrée et de sortie et l'autre pour les calculs arithmétiques. Les résultats numériques démontrent que le module STRESS amélioré pourrait être plus efficace que le module original, et ce, de plusieurs ordres de grandeur, si l'on considère un grand nombre de cas de charges.

On a mis au point une caractéristique qui consiste à effectuer des analyses multiples à l'aide d'une seule exécution du programme VAST. Cette caractéristique a été utile dans tous les types d'analyse. Par exemple, dans le cas des analyses dynamiques, elle permet que la période de temps totale soit divisée en blocs de solutions multiples, avec différents pas de calculs. Grâce à cette caractéristique, le processus de calcul des courbes de réduction des charges, qui comportait quatre analyses différentes, pourrait également être entièrement automatisé. La possibilité d'utiliser des fonctions harmoniques d'ordre élevé pour remplacer les formes de flambage comme imperfection additionnelle a également été étudiée. L'étude a démontré qu'il était effectivement possible de recourir à des modes harmoniques d'ordre élevé pour obtenir des solutions non linéaires stables, mais que

l'utilisation de formes de flambage présentait des avantages considérables et qu'elle était encore recommandée.

Enfin, on a évalué la pertinence de la base de données des courbes de réduction des charges génériques créées antérieurement pour les analyses de résistance à la rupture du CPF. Les effets des divers paramètres sur le comportement des panneaux rigides en réduction de charge ont également fait l'objet d'une étude détaillée. L'étude propose d'accroître les bases de données existantes et de formuler un algorithme d'interpolation dans les programmes d'analyse de la résistance à la rupture.

IMPROVED NONLINEAR SOLUTION TECHNIQUES IN THE VAST FINITE ELEMENT PROGRAM

DREA CR 2000-101

L. Jiang and M.W. Chernuka
Martec Limited

EXECUTIVE SUMMARY

Introduction

The finite element programme VAST (Vibration And STrength) has been under development at Martec Limited, under contract to DREA, since the late 1970s. It is a general-purpose finite element code for structural analysis with a number of specialised elements for ship structure applications. In the early 1990s, work began on a nonlinear version of the programme for general purpose use, and which in recent years has been successfully used to evaluate the longitudinal strength of stiffened panels of the Halifax class frigate. The VAST programme is to play a major role in the DRDB major project ISSMM (Improved Ship Structures Maintenance Management), which will provide rapid assessments of structural damage and design modifications. To meet the requirements of the ISSMM project, it was perceived that greater computational speed and more automated analysis procedures will be required of VAST. The work described in this report addresses both of these areas.

Principal Results

A major effort was undertaken to improve the computational speed of VAST by implementing an iterative equation solver for use with static analysis. The solver implemented uses a pre-conditioned conjugate gradient (PCG) method, which has been used successfully in commercial finite element codes. Further improvements in speed were achieved through streamlining the algorithm used in VAST's stress computation module.

The procedure for calculating load-shortening curves of stiffened panels, which are used in evaluating both component and the overall hull girder strength of ships, has been further automated in several areas. An automatic procedure for generating weld-induced residual stress patterns in stiffened panels was implemented using temperature distributions and thermal expansion coefficients. Also, VAST was modified to allow a series of analyses to be performed from a single input file. It is now also possible to perform a nonlinear static analysis with multiple solution step sizes.

Significance of Results

With the new PCG solver, significant improvement was observed in the computational speed of VAST, but this was only for three-dimensional elasticity and two-dimensional membrane structures. For plate and shell structures with combined membrane and bending action, which make up the majority of ship structure applications, no significant improvement was obtained. This is attributed to an inadequate preconditioner and further work is recommended in this area.

The level of automation now in the load-shortening curve procedure should enable it to be used in the ISSMM project. Previously, the calculation had to be carried out in three separate steps (pre-load, linear buckling, and nonlinear analysis steps), but these can now be carried out in a single run. Using initial temperature distributions (and their associated stress field) to prescribed residual stresses allows this aspect of the analysis to be carried out automatically.

Future Plans

Further enhancements to the VAST code may be required for integration with the ISSMM software. These changes will be made within the current ISSMM contract. No additional contracts are anticipated for further VAST enhancements in the areas described in this report.

TECHNIQUES DE SOLUTIONS NON LINÉAIRES AMÉLIORÉES DANS LE PROGRAMME À ÉLÉMENTS FINIS VAST

L. Jiang et M. W. Chernuka
Martec Limited

RÉSUMÉ

Introduction
Le programme à éléments finis VAST (Vibration and Strength) est en cours d'élaboration chez Martec Limited dans le cadre d'un contrat octroyé par le CRDA à la fin des années 70. Il s'agit d'un programme à éléments finis tout usage pour l'analyse structurale accompagnée d'un certain nombre d'éléments spécialisés pour les structures de navire. Au début des années 90, on a commencé des travaux relatifs à une version non linéaire du programme à des fins d'usage général, qui au cours des dernières années ont été utilisés avec succès pour évaluer la résistance longitudinale des panneaux rigides de la classe frégates de Halifax. Le programme VAST doit jouer un rôle important dans le projet GAMSN (Gestion améliorée de la maintenance de la structure des navires) de la DRDD, et permettra d'obtenir des évaluations rapides des dommages structuraux et de la modification de conception. Pour satisfaire aux exigences du projet GAMSN, on estime qu'il faudra accroître la vitesse de calcul et la vitesse des procédures d'analyse automatisées du VAST. Les travaux décrits dans le présent rapport traitent de ces deux questions.

Principaux résultats
Un effort considérable a été déployé pour améliorer la vitesse de calcul du VAST en mettant en œuvre un solutionneur d'équations qui sera utilisé dans l'analyse statique. Le solutionneur mis en œuvre utilise la méthode du gradient du conjugué préconditionné (GPC), qui a été employé avec succès dans des programmes à éléments finis commerciaux. D'autres améliorations de la vitesse ont été obtenues par la rationalisation de l'algorithme utilisé dans le module de calcul des contraintes du VAST.

De nombreux aspects de la procédure de calcul des courbes de réduction des charges pour les panneaux rigides, qui servent à évaluer la résistance des composantes et de la poutre longitudinale des coques de navires, ont été automatisés. Une procédure automatique qui tient compte des distributions de température et des coefficients de dilatation thermique et qui a pour but de générer des modèles de contraintes résiduelles induites par les soudures dans les panneaux rigides a été mise en œuvre. En outre, le programme VAST a été modifié pour permettre d'effectuer une série d'analyses à partir d'un fichier d'entrées unique. Il est maintenant possible de réaliser une analyse statique non linéaire pour des pas de solution multiple.

Importance des résultats
Avec le nouveau solutionneur GPC, on a observé une amélioration considérable de la vitesse de calcul du VAST, mais seulement pour les structures à élasticité

tridimensionnelle et à membrane bidimensionnelle. Pour les structures de plaques et de coques avec action combinée de membrane et de pliage, qui constituent la majorité des structures de navires, aucune amélioration n'a été réalisée, à cause d'un préconditionneur inadéquat, et d'autres travaux sont recommandés dans ce domaine.

Le niveau d'automatisation qui caractérise maintenant la procédure relative aux courbes de réduction des charges devrait permettre de l'utiliser dans le projet GAMSN. Antérieurement, les calculs devaient être effectués lors de trois étapes distinctes (précharge, flambage linéaire, et étapes d'analyses non linéaires), mais on peut maintenant les réaliser lors d'un seul essai. Ainsi, on peut réaliser automatiquement cet aspect de l'analyse en utilisant des distributions de la température initiales (accompagnées de leurs champs de contraintes associés) dans les contraintes résiduelles.

Plans à venir

D'autres améliorations devront peut-être être apportées au programme VAST avec le logiciel GAMSN. Ces changements seront apportés dans le cadre du contrat GAMSN en vigueur. Aucun autre contrat n'est prévu en ce qui concerne les améliorations à venir du VAST pour les domaines précisés dans le présent rapport.

TABLE OF CONTENTS

ABSTRACT ii
TABLE OF CONTENTS iii
LIST OF TABLES v
LIST OF FIGURES vii

1. INTRODUCTION 1.1

2. DEVELOPMENT OF AN ITERATIVE LINEAR ALGEBRAIC EQUATION SOLVER IN THE VAST PROGRAM 2.1
   2.1 Conjugate Gradient Method 2.1
   2.2 Preconditioned Conjugate Gradient Method 2.5
   2.3 Formulation of the Pre-conditioners 2.7
   2.4 Implementation of the Pre-conditioned Conjugate Gradient Method in VAST 2.13
   2.5 Verification of the Pre-conditioned Conjugate Gradient Method in VAST 2.17
   2.6 Multi-Level Iterative Methods and Hierarchical Pre-conditioners 2.23

3. DEVELOPMENT OF A THERMAL STRESS ANALYSIS CAPABILITY IN VAST FOR AUTOMATIC GENERATION OF RESIDUAL STRESS FOR NONLINEAR ANALYSIS OF STIFFENED PANELS 3.1
   3.1 Development of a Thermal Stress Analysis Capability in VAST 3.1
   3.2 Automatic Generation of Residual Stresses for Load-Shortening Curve Calculation of Stiffened Panel Structures 3.10

4. IMPROVEMENT OF THE EFFICIENCY OF STRESS MODULE FOR MULTIPLE DISPLACEMENT VECTORS 4.1

5. IMPLEMENTATION OF MULTIPLE SOLUTION STEP SIZES FOR NONLINEAR AND DYNAMIC ANALYSES 5.1

6. USE OF FOURIER SERIES TO DEFINE ADDITIONAL GEOMETRIC IMPERFECTIONS FOR STIFFENED PANELS 6.1

7. ADEQUACY ASSESSMENT OF THE NORMALIZED EFFECTIVE STRESS-STRAIN CURVE DATABASE FOR ULTIMATE STRENGTH ANALYSES OF THE CPF MODEL 7.1
   7.1 Determination of Ranges of the β and λ Parameters for a Typical CPF Model 7.2
   7.2 Parametric Study on Nonlinear Behavior of Stiffened Panels with Extreme Values of Geometric Parameters β and λ 7.4
   7.3 Parametric Study on Effects of Other Parameters on the Nonlinear Behavior of Stiffened Panels 7.5

8. CONCLUSIONS AND RECOMMENDATIONS FOR FURTHER WORK 8.1

9. REFERENCES 9.1

LIST OF TABLES

Table 2.1: Comparison of Solution Times Required by Different Linear Matrix Solvers for the Cube Problem Modeled by Uniform Meshes of 20-Noded Solid Elements. 2.28

Table 2.2: Comparison of Solution Times Required by Different Linear Matrix Solvers for the Cube Problem Modeled by Uniform Meshes of 8-Noded Solid Elements. 2.29

Table 2.3: Comparison of Solution Times Required by Various Linear Equation Solvers for the Cube Problem Solved by 8-Noded Solid Elements With Severe Aspect Ratios 2.30

Table 2.4: Comparison of the Solution Times Obtained on a Window-Based PC for the Cube Problem Modeled Using 4x4x30 Mesh of 8-Noded Solid Elements 2.30

Table 2.5: Comparison of Disk Storage Spaces Required by Direct and Iterative Solvers for the Cube Problem modeled Using 20-Noded Solid Elements 2.30

Table 2.6: Comparison of Solution Times for a Cantilevered Square Plate Under Membrane and Bending Loads 2.31

Table 2.7: Comparison of Solution Times Required by Various Linear Equation Solvers for a Lower Spar Cap From Airplane Wing Modeled by 8-Noded Solid Elements 2.31

Table 2.8: Comparison of Solution Times for a Simply Supported Plate Subjected to Uniform Pressure Modeled by 8-Noded Solid Elements 2.32

Table 2.9: Comparison of Solution Times for the Simply Supported Plate Modeled by 3-Noded Triangular Plate Element 2.32

Table 2.10: Comparison of Solution Times for a Typical Stiffened Panel Model 2.32

Table 3.1: Comparison of VAST Results With Analytical and ADINA Solutions for Thermal-Elastic Analysis of a Cantilever Beam 3.15

Table 3.2: Comparison of VAST Results With Analytical and ADINA Solutions for Thermal-Elastic Analysis of a Simply-Supported Circular Plate 3.15

Table 3.3: Comparison of VAST Results With Analytical and ADINA Solutions for Thermal Buckling Analysis of a Hinged Rectangular Plate 3.16

Table 4.1: Comparison of Elapsed Times Required by the Original and Modified STRESS Modules for Different Numbers of Elements and Load Cases. 4.4

Table 4.2: Comparison of Elapsed Times Taken by Each Module of Material-Nonlinear-Only and Combined Geometrically and Materially Nonlinear Analyses of a Typical Stiffened Panel Model. 4.5

Table 5.1: USE File for Geometrically Nonlinear Analysis of a Hinged Shallow Spherical Shell Subjected to a Center Point Load Using Variable Displacement Increments 5.4

Table 5.2: USE File for Linear Dynamic Analysis of a Solid Block Using Variable Time Steps 5.6
Table 5.3: USE File for Automated Load-Shortening Curve Calculation of a Typical Stiffened Panel. 5.7

Table 7.1: Ranges of the Column Slenderness Ratio (λ), the Plate Slenderness Ratio (β) and the Stiffener/Total Area Ratio (A_s/A) Computed by the Ultimate Strength Program for Various Cross-sections of a Typical CPF Model. 7.8

LIST OF FIGURES

Figure 2.1 Uniform Meshes of a Cube Using the 20-Noded Solid Element. 2.33
(a) 2x2x2 Mesh. (b) 4x4x4 Mesh
(c) 6x6x6 Mesh. (d) 8x8x8 Mesh
(e) 10x10x10 Mesh. (f) 12x12x12 Mesh
Figure 2.2: Uniform Meshes of a Cube Using the 8-Noded Solid Element. 2.36
(a) 5x5x5 Mesh. (b) 7x7x7 Mesh
(c) 10x10x10 Mesh. (d) 14x14x14 Mesh
(e) 17x17x17 Mesh. (f) 20x20x20 Mesh
Figure 2.3: 8-Noded Solid Element Meshes of the Cube With Severe Aspect Ratios. 2.39
(a) 4x4x30 Mesh, Aspect Ratio 7.5:7.5:1. (b) 12x12x60 Mesh, Aspect Ratio 5:5:1.
Figure 2.4: Final Deformed Configurations of the Cube Predicted by Various Meshes. 2.40
(a) 12x12x12 Mesh of 20-Noded Solid Element
(b) 20x20x20 Mesh of 8-Noded Solid Element
(c) 12x12x602 Mesh of 8-Noded Solid Element
Figure 2.5: Von Mises Stress Distribution in the Cube Predicted by Various Meshes.. 2.43
(a) 12x12x12 Mesh of 20-Noded Solid Element
(b) 20x20x20 Mesh of 8-Noded Solid Element
(c) 12x12x602 Mesh of 8-Noded Solid Element
Figure 2.6: A Cantilevered Square Plate Modeled by 3-Noded Triangular Plate Elements. 2.46
Figure 2.7: Von Mises Stress Distribution in Mid Surface of the Plate Caused by Uniform In-plane Edge Force.......... 2.47
Figure 2.8: Von Mises Stress Distribution in Upper Surface of the Plate Caused by Uniform Transverse Edge Force 2.48
Figure 2.9: A Lower Spar Cap in Airplane Wing Modeled by 8-Noded Solid Elements. 2.49
Figure 2.10: Final Deformed Configuration of the Lower Spar Cap.......... 2.50
Figure 2.11: Von Mises Stress Distribution in the Lower Spar Cap 2.51
Figure 2.12: Original and Deformed Configuration of a Simply Supported Plate Subjected to Uniform Pressure Modeled by 8-Noded Solid Elements. 2.52
(a) 5x5x2 Mesh
(b) 10x10x4 Mesh
(c) 15x15x6 Mesh
Figure 2.13: Von Mises Stress Distribution in the Simply Supported Plate Predicted by the 15x15x6 Mesh of the 8-Noded Solid Element 2.55
Figure 2.14: 3-Noded Triangular Plate Element Meshes of the Simply Supported Plate .. 2.56
(a) 10x10 Mesh
(b) 20x20 Mesh
(c) 40x40 Mesh
Figure 2.15: Von Mises Stress Distribution in the Simply Supported Plate Predicted by the 40x40 Mesh of the 3-Noded Triangular Plate Element.......... 2.59

Figure 2.16: 4-Noded Quadrilateral Shell Element Meshes of a Typical Stiffened Panel 2.60
(a) Coarse Mesh
(b) Intermediate Mesh
(c) Fine Mesh
Figure 2.17: 3-Noded Triangular Plate/Shell Element Meshes of a Typical Stiffened Panel 2.63
(a) Coarse Mesh
(b) Intermediate Mesh
(c) Fine Mesh
Figure 2.18: Von Mises Stress Distribution in the Stiffened Panel Predicted by the Fine Mesh of the Stiffened Panel 2.66

Figure 3.1: Problem Geometry, Material Properties and Boundary Conditions for Thermal-Elastic Analysis of a Cantilevered Beam. 3.17
Figure 3.2: Initial Finite Element Mesh and Final Deformed Configuration of the Cantilevered Beam Obtained by the ADINA Program. 3.18
Figure 3.3: Initial Finite Element Mesh and Final Deformed Configuration of the Cantilevered Beam Obtained by the VAST Program........ 3.19
(a) 8-Noded Shell Element, (b) 3-Noded Beam Element
(c) 4-Noded Quadrilateral Shell Element, (d) 3-Noded Plate/Shell Element
(e) 20-Noded Solid Element, (f) 8-Noded Solid Element
Figure 3.4: Problem Geometry and Material Properties for Thermal-Elastic Analysis of a Simply-Supported Circular Plate. 3.22
Figure 3.5: Initial Finite Element Mesh and Final Deformed Configuration of the Circular Plate Obtained by the ADINA Program........ 3.23
Figure 3.6: Initial Finite Element Mesh and Final Deformed Configuration of the Circular Plate Obtained by the VAST Program 3.24
(a) Collapsed 4-Noded Shell Element,
(b) Collapsed 8-Noded Solid Element
Figure 3.7: Problem Geometry, Material Properties and Boundary Conditions for Thermal Buckling Analysis of a Hinged Rectangular Plate........ 3.25
Figure 3.8: Finite Element Mesh and the First Thermal Buckling Mode Shape of the Hinged Rectangular Plate Obtained by the ADINA Program........ 3.26
Figure 3.9: The First and Second Thermal Buckling Mode Shapes of the Hinged Rectangular Plate Predicted by the VAST Program. 3.27
(a) 8-Noded Thick/Thin Shell Element
(b) 4-Noded Quadrilateral Shell Element
(c) 3-Noded Plate/Shell Element
(d) 20-Noded Solid Element
(e) 8-Noded Solid Element
Figure 3.10 Four-Noded Quadrilateral Shell Element Mesh for Stiffened Panel with $\beta=4.0$, $\lambda=0.3$, $A_r=0.2$, $\omega_0=0.3\ \beta^2 t$. 3.32
Figure 3.11: Comparison of Load-Shortening Curves Obtained by Using the Four-Noded Element and Various Residual Stress Distributions. 3.33

Figure 3.12: Final Deformed Configuration of the Stiffened Panel Predicted by the Four-Noded Shell Element. ... 3.34

Figure 3.13: Axial Stress Distribution in the Stiffened Panel Predicted by Thermal Stress Analysis. ... 3.35

Figure 3.14: Comparison of Load-Shortening Curves Obtained by Using Thermal Residual Stresses Generated With and Without Temperature Variation at the Web-Flange Junction. ... 3.36

Figure 3.15: Eight-Noded Thick/Thin Shell Element Mesh for Stiffened Panel with β=4.0, λ=0.3, A_r=0.2, ω_0=0.3 β^2 t. ... 3.37

Figure 3.16: Comparison of Load-Shortening Curves Obtained by Using the Eight-Noded Element and Various Residual Stress Distributions. ... 3.38

Figure 3.17: Final Deformed Configuration of the Stiffened Panel Predicted by the Eight-Noded Shell Element. ... 3.39

Figure 3.18: Axial Stress Distribution in the Stiffened Panel Predicted by Thermal Stress Analysis Using the Eight-Noded Shell Element. ... 3.40

Figure 3.19: Refined Eight-Noded Thick/Thin Shell Element Mesh for Stiffened Panel with β=4.0, λ=0.3, A_r=0.2, ω_0=0.3 β^2 t. ... 3.41

Figure 3.20: Final Deformed Configuration of the Stiffened Panel Predicted by the Refined Eight-Noded Shell Element Mesh. ... 3.42

Figure 3.21: Comparison of Load-Shortening Curves Obtained by Using the Refined Eight-Noded Element and Various Residual Stress Distributions. ... 3.43

Figure 3.22: Axial Stress Distribution in the Stiffened Panel Predicted by Thermal Stress Analysis Using the Refined Eight-Noded Element Mesh. ... 3.44

Figure 3.23: Eight-Noded Thick/Thin Shell Element Mesh for Stiffened Panel with β=2.0, λ=0.6, A_r=0.2, ω_0=0.1 β^2 t. ... 3.45

Figure 3.24: Final Deformed Configuration of the Stiffened Panel Predicted by ... 3.46

Figure 3.25: Axial Thermal Stress Distribution in the Stiffened Panel Predicted by Using the Eight-Noded Shell Element. ... 3.47

Figure 3.26: Axial Thermal Stress Distribution Along the Plate Width at the End of the Stiffened Panel. ... 3.48

Figure 3.27: Comparison of Load-Shortening Curves Obtained by Using the Eight-Noded Shell Element and Various Residual Stress Distributions. ... 3.49

Figure 4.1: A Ship Detail Model Used for Benchmarking the STRESS Module. ... 4.6

Figure 4.2: A Typical Stiffened Panel Model Used for Benchmarking Nonlinear Analysis Capabilities. ... 4.7

Figure 5.1: Problem Geometry, Material Property and Finite Element Mesh for Geometrically Nonlinear Analysis of a Shallow Spherical Shell. ... 5.9

Figure 5.2: Load-Center Deflection Curve of the Spherical Shell Predicted Using Four Different Displacement Increments. ... 5.10

Figure 5.3: Finite Element Mesh of a Solid Block Employed for Linear Dynamic Analysis. ... 5.11

Figure 5.4: Comparison of Time Histories of Center Vertical Displacement Obtained Using Constant and Variable Time Steps ... 5.12

Figure 5.5: Comparison of Time Histories of Corner Vertical Displacement Obtained Using Constant and Variable Time Steps 5.13

Figure 5.6: Finite Element Mesh of A Typical Stiffened Panel for Load-Shortening Curve Calculation 5.14

Figure 5.7: Final Deformed Configuration of the Stiffened Panel Predicted Automatically by the VAST Program. 5.15

Figure 5.8: The Normalized Load-Shortening Curve of the Stiffened Panel Predicted Automatically by the VAST Program. 5.16

Figure 6.1: Finite Element Mesh for Stiffened Panel with Geometric Parameters: $\beta=3.0, \lambda=0.9, A_r=0.35, \omega_0=0.1\,\beta^2 t$. 6.5

Figure 6.2: Load-Shortening Curves of the Stiffened Panel Obtained by Using the Original and Additional Geometric Imperfection Based on Buckling Mode. 6.6

Figure 6.3: Final Deformed Configuration of the Stiffened Panel Obtained by Using Only the Original Stiffener and Plate Imperfections. 6.7

Figure 6.4: The Linear Buckling Mode Shape Superimposed Onto the Finite Element Model as Additional Imperfection. 6.8

Figure 6.5: Final Deformed Configuration of the Stiffened Panel Obtained by Using the Buckling Mode Shape as Additional Imperfection. 6.9

Figure 6.6: Higher-Order Imperfection Pattern with Three Half Sine Waves. 6.10

Figure 6.7: Higher-Order Imperfection Pattern with Five Half Sine Waves. 6.11

Figure 6.8: Higher-Order Imperfection Pattern with Seven Half Sine Waves. 6.12

Figure 6.9: Higher-Order Imperfection Pattern with Nine Half Sine Waves. 6.13

Figure 6 10: Load-Shortening Curves of the Stiffened Panel Obtained by Using Different Amounts of the Nice Half-Since Wave Imperfection. 6.14

Figure 6.11: Final Deformed Configuration of the Stiffened Panel Obtained Using the Nine Half Sine Wave Imperfection. 6.15

Figure 6.12: Load-Shortening Curves of the Stiffened Panel Obtained by Using One and Four Higher-Order Sine Wave Imperfections. 6.16

Figure 6.13: Load-Shortening Curves of the Stiffened Panel Obtained by Using Different Amounts of All Four Higher-Order Imperfections. 6.17

Figure 6.14: Linear Buckling Mode Suitable for being Used in Load-Shortening Curve Calculation for Stiffened Panel With $\beta=1.0, \lambda=0.3$. 6.18

Figure 6.15: Linear Buckling Mode Suitable for being Used in Load-Shortening Curve Calculation for Stiffened Panel With $\beta=2.0, \lambda=0.3$. 6.19

Figure 6.16: Linear Buckling Mode Suitable for being Used in Load-Shortening Curve Calculation for Stiffened Panel With $\beta=3.0, \lambda=0.3$. 6.20

Figure 6.17: Linear Buckling Mode Suitable for being Used in Load-Shortening Curve Calculation for Stiffened Panel With $\beta=4.0, \lambda=0.3$. 6.21

Figure 6.18: Linear Buckling Mode Suitable for being Used in Load-Shortening Curve Calculation for Stiffened Panel With $\beta=1.0, \lambda=0.6$. 6.22

Figure 6.19: Linear Buckling Mode Suitable for being Used in Load-Shortening Curve Calculation for Stiffened Panel With $\beta=2.0, \lambda=0.6$. 6.23

Figure 6.20: Linear Buckling Mode Suitable for being Used in Load-Shortening Curve Calculation for Stiffened Panel With $\beta=3.0$, $\lambda=0.6$. 6.24

Figure 6.21: Linear Buckling Mode Suitable for being Used in Load-Shortening Curve Calculation for Stiffened Panel With $\beta=4.0$, $\lambda=0.6$. 6.25

Figure 6.22: Linear Buckling Mode Suitable for being Used in Load-Shortening Curve Calculation for Stiffened Panel With $\beta=1.0$, $\lambda=0.9$. 6.26

Figure 6.23: Linear Buckling Mode Suitable for being Used in Load-Shortening Curve Calculation for Stiffened Panel With $\beta=2.0$, $\lambda=0.9$. 6.27

Figure 6.24: Linear Buckling Mode Suitable for being Used in Load-Shortening Curve Calculation for Stiffened Panel With $\beta=3.0$, $\lambda=0.9$. 6.28

Figure 6.25: Linear Buckling Mode Suitable for being Used in Load-Shortening Curve Calculation for Stiffened Panel With $\beta=4.0$, $\lambda=0.9$. 6.29

Figure 6.26: Linear Buckling Mode Suitable for being Used in Load-Shortening Curve Calculation for Stiffened Panel With $\beta=1.0$, $\lambda=1.2$. 6.30

Figure 6.27: Linear Buckling Mode Suitable for being Used in Load-Shortening Curve Calculation for Stiffened Panel With $\beta=2.0$, $\lambda=1.2$. 6.31

Figure 6.28: Linear Buckling Mode Suitable for being Used in Load-Shortening Curve Calculation for Stiffened Panel With $\beta=3.0$, $\lambda=1.2$. 6.32

Figure 6.29: Linear Buckling Mode Suitable for being Used in Load-Shortening Curve Calculation for Stiffened Panel With $\beta=4.0$, $\lambda=1.2$. 6.33

Figure 7.1: CPF Cross-section at Station 30.5 Which Contains Stiffened Panels with the Maximum Plate Slenderness Ratio β. 7.9

Figure 7.2: Details of CPF Cross-section at Station 30.5 Which Contains Stiffened Panels with the Maximum Plate Slenderness Ratio β. 7.10

Figure 7.3: CPF Cross-section at Station 50.75 Which Contains Stiffened Panels with the Minimum Plate Slenderness Ratio β. 7.11

Figure 7.4: Details of CPF Cross-section at Station 50.75 Which Contains Stiffened Panels with the Minimum Plate Slenderness Ratio β. 7.12

Figure 7.5: Global Finite Element Mesh of a CPF Model After Removal of Superstructures. 7.13

Figure 7.6: CPF Cross-section at Station 3.0 Generated by MGDSA. 7.14

Figure 7.7: CPF Cross-section at Station 39.0 Generated by MGDSA. 7.15

Figure 7.8: CPF Cross-section at Station 60.0 Generated by MGDSA. 7.16

Figure 7.9: Cross-section Information Dialog Box of the Ultimate Strength Analysis Program. 7.17

Figure 7.10: CPF Cross-section at Station 3.0 Generated Using the DIGFEM File. 7.18

Figure 7.11: Comparison of Load-Shortening Curves for Stiffened Panels with Different Column Slenderness Ratio λ. 7.19

Figure 7.12: Comparison of Peak Loads Predicted by the Nonlinear Finite Element Method and the Interpolation (Extrapolation) Scheme for Different λ Values. 7.20

Figure 7.13: Comparison of Load-Shortening Curves for Stiffened Panels with Different Plate Slenderness Ratio β. 7.21

Figure 7.14: Comparison of Peak Loads Predicted by the Nonlinear Finite Element Method and the Interpolation (Extrapolation) Scheme for Different β Values 7.22
Figure 7.15: Comparison of Load-Shortening Curves for Stiffened Panels with Different Stiffener/Plate Area Ratio A_s/A 7.23
Figure 7.16: Peak Loads Predicted by the Nonlinear Finite Element Method for Stiffened Panels with Different A_s/A Values 7.24
Figure 7.17: Comparison of Load-Shortening Curves for Stiffened Panels with Different Magnitudes of Stiffener Imperfection 7.25
Figure 7.18: Peak Loads Predicted by the Nonlinear Finite Element Method for Stiffened Panels with Different Magnitudes of Stiffener Imperfection. 7.26
Figure 7.19: Comparison of Load-Shortening Curves for Stiffened Panels with Different Magnitudes of Residual Stress 7.27
Figure 7.20: Peak Loads Predicted by the Nonlinear Finite Element Method for Stiffened Panels with Different Magnitudes of Residual Stress. 7.28

1. INTRODUCTION

One of the major requirements of the ISSMM project is to develop a highly efficient numerical capability for assessing structural integrity of undamaged and damaged ship hull structures under extreme loading conditions. The assessment requires linear finite element analyses of global ship models and nonlinear analyses of structural details. The linear analyses normally involve a large number of load cases, whereas in the nonlinear analyses, plasticity and instability are often encountered. Because of the large scale of the global finite element model and the highly nonlinear nature of the local detailed analyses, efficiency and robustness of the finite element program utilized in this numerical capability become very important.

The vibration and strength (VAST) finite element program is a general purpose structural analysis program developed by Martec Limited under the sponsorship of DREA. This program is able to handle both linear and nonlinear problems. Recently, the efficiency of the direct linear algebraic equation solver in VAST was significantly enhanced by combining operations for assembly, modification and decomposition of the global stiffness matrix into a single module. On the other hand, the convergence property of the VAST nonlinear capability was improved by incorporating the consistent tangent stiffness formulation. In addition to the above developments, an overlay plasticity model had been implemented to handle multi-linear stress-strain relations, and the prescribed displacement capability, which is required in top-down analyses, had been extended to nonlinear problems. The improved nonlinear VAST program had been successfully utilized to create a normalized generic load-shortening curve database for the Halifax class frigate.

In the present contract, the efficiency and robustness of the VAST program were further improved. These included provision of an efficient iterative linear algebraic equation solver, implementation of a thermal stress analysis feature, enhancement of the stress computation algorithm, and development of a multi-analysis capability. In addition, the adequacy of the previously generated load-shortening curve database for ultimate strength analysis of CPF was assessed. Recommendations were made on future extension of the l-s curve database and the interpolation scheme utilized in the ultimate strength analysis programs.

The use of direct linear equation solution algorithms had been dominant in finite element programs for a long time, mainly due to their robustness. The computational effort required by a direct solver is predictable because it does not depend upon the condition number of the stiffness matrix. In contrast, the solution time required by an iterative solver is normally unpredictable as the convergence rate of the iterative solver is related to the condition number of the coefficient matrix and the quality of the pre-conditioner. However, in recent years, the use of the iterative solution algorithms in finite element analysis became more and more popular and excellent performance from iterative solvers on various structural problems has been reported in many text books and technical papers. Today, almost all the leading commercial finite element packages offer some sort of iterative solver.

In this contract, we concentrated on the preconditioned conjugate gradient method, one of the most popular iterative solvers. Following the implementation of the basic conjugate gradient algorithm, seven pre-conditioners were incorporated. The first two were derived from the Jacobi and the symmetric successive over-relaxation (SSOR) iterative methods, respectively, and the other five were all based on the original and modified incomplete factorisation algorithms. An extensive numerical study was then carried out to compare the performance of the direct and iterative solvers. It has been found that for well-conditioned problems, the iterative solver significantly outperformed the direct one, however, for poorly-condition problems, the direct solver was more efficient. One way to further improve the performance of the iterative solver for poorly-conditioned problems was to utilise better pre-conditioners. At this point, it was discovered that the pre-conditioners developed using the concept of multi-level or multi-grid iterative method have the potential to form a highly efficient iterative solver for very poorly-conditioned problems and have been recommended for future implementation. Detailed theoretical derivations and numerical studies of the iterative solvers are presented in the next chapter.

The development of a thermal stress analysis capability in VAST is addressed in Chapter 3. Both theoretical formulation and computer implementation issues are presented in detail. The thermal load is specified through nodal temperature variations, which can be defined by three methods:

(1) binary files generated from previous heat transfer analysis, (2) ASCII files containing data at displacement nodes, and (3) ASCII files containing data at all corners of solid or structural elements. The third data format provides an option for handling temperature gradient in the thickness direction in shell and beam elements. In the present implementation, the thermal stress capability was provided in seven commonly used VAST elements: 8-noded shell, 20-noded solid, 3-noded plate, 4-noded shell, 13-noded transition, 3-noded beam and 8-noded solid elements. Three numerical examples, including thermal-induced bending and buckling of rectangular and circular plates, were used to verify the newly developed thermal stress capability. For all of them, the VAST results were in excellent agreement with the analytical and published numerical solutions. For load-shortening curve calculations, in order to ensure that the maximum residual stress generated by thermal stress analysis equals the yield stress, a stress scaling factor has been introduced. The efficiency of the thermal stress capability in load-shortening curve generation for stiffened panels with severe initial geometric imperfections has also been demonstrated by numerical examples.

The modification of the STRESS module for efficient handling of multiple load cases is discussed in Chapter 4. Before the present modification, I/O operations on both the stress matrix file .T43 and the displacement file .T52 were handled inefficiently. The former was rewound for each data card defining an element range for stress calculation, whereas the later was rewound for each element of which stresses were calculated. Numerical studies indicated that for large problems with large numbers of load cases, the I/O operations involved in the stress calculation took almost all the elapsed time. In order to improve the efficiency of the STRESS module for multiple load cases, the driver subroutine was completely restructured in this contract. All data cards defining element ranges were read at the beginning, and the stress matrices of all the selected elements were stored on an intermediate file in a compact format. On the other hand, multiple displacement vectors were kept in core based on the available in core memory. Numerical results indicated that the saving on computation time due to the present modification was very significant.

The development and verification of the multiple-analysis capability in VAST is presented in Chapter 5. With this capability, different solution step sizes can be used in different portions of dynamic or nonlinear analyses, and the procedure of calculating load-shortening curves can also be fully automated. Three numerical examples were used to demonstrate the effectiveness of this capability. The last of these examples, which involved generation of load-shortening curve of a typical stiffened panel, required four analyses: (1) a linear static analysis to generate initial stresses for the buckling analysis; (2) a linear buckling analysis to generate buckling mode shapes to be used as additional geometric imperfection; (3) a thermal stress analysis to generate residual stresses; and (4) a nonlinear analysis to compute the load-shortening curve.

In an attempt to simplify this procedure, the possibility of using higher-order harmonic functions to define the additional imperfections were investigated. The results are presented in Chapter 6. By studying the patterns of the buckling mode shapes, the higher-order sine functions, which were contained in these buckling modes, were identified and implemented into the LSPANEL program. Numerical results indicated that only the magnitude of the sine function which was closest to the buckling mode had a significant effect on the predicted overall nonlinear behaviour of the stiffened panel. This finding suggested that a uniform distribution of the sine functions could be used to define additional imperfections in nonlinear analysis of single stiffened panels. However, in order to achieve the same peak load, a bigger amplitude of additional imperfection must be used for the higher-order sine functions than for the linear buckling mode shapes. This enlarged geometric imperfection led to a noticeable reduction on the pre-buckling stiffness. Due to the robustness of the nonlinear analysis using the buckling mode and the automation of the procedure, the use of buckling mode shape is still highly recommended.

The adequacy of the previously generated effective stress-strain curve database for ultimate strength analysis of the CPF is assessed in Chapter 7. For representative ship cross-sections generated using the DIGFEM file and global finite element model, ranges of various geometric parameters, such as the plate slenderness ratio β and the column slenderness ratio λ, were calculated and compared with the available ranges of these parameters in the database. The effects of the stiffener/total area ratio A_S/A, the residual stress level, and the magnitude of the stiffener imperfection on the nonlinear behaviour of stiffened panels were also investigated. The results of the present study suggest that the presently available load-shortening curve database should be expanded and the interpolation algorithm used in the present version of the ultimate strength programs should be extended to include more parameters.

Finally, conclusions and recommendations for further work are presented in Chapter 8.

2. DEVELOPMENT OF AN ITERATIVE LINEAR ALGEBRAIC EQUATION SOLVER IN THE VAST PROGRAM

During the past few years, the use of iterative solvers in finite element analysis has become increasingly popular. A large number of books [2.1-2.7] and research papers [2.8-2.29] have been published on this topic and various iterative solvers have been implemented in almost all of the commercial finite element packages. In the present work, attempts were also made to develop an iterative linear algebraic equation solver in the VAST program based on the preconditioned conjugate gradient method.

2.1 Conjugate Gradient Method

Consider a system of linear algebraic equations, such as those resulting from finite element spatial discretizations, as:

$$Ax = b \tag{2.1}$$

where A denotes the coefficient matrix, b the right hand side vector and x the solution vector. In finite element analysis, A, b, x indicate the stiffness matrix, the load vector and the nodal displacement vector, respectively.

Let $\bar{x}$ be a trial solution vector, the corresponding vector of residuals can be expressed as:

$$r = b - A\bar{x}\,. \tag{2.2}$$

An error function is defined as [2.2]:

$$h = r^T A^{-1} r\,. \tag{2.3}$$

If the coefficient matrix is symmetric and positive definite, its inverse will also be symmetric and positive definite. Hence the above error function must have a positive value for all possible vectors $\bar{x}$ except the correct solution $\bar{x} = x$, where $h=0$. Substituting Equation (2.2) into

(2.3), the error function can be written as a function of the trial solution vector as:

$$h = \bar{x}^T A \bar{x} - 2b^T \bar{x} + c . \tag{2.4}$$

Assume x_k represents a point in the n-dimensional solution space, the equation

$$\bar{x} = x_k + \alpha d_k \tag{2.5}$$

defines a line through the point whose direction is governed by vector d_k. The parameter α is proportional to the distance between $\bar{x}$ and x_k. Substituting Equation (2.5) into (2.4) gives a quadratic function of α as:

$$h = \alpha^2 d_k{}^T A d_k - 2\alpha d_k^T r_k + x_k{}^T A x_k - 2b^T x_k + c \tag{2.6}$$

which has a local minimum at:

$$\frac{\partial h}{\partial \alpha} = 2d_k^T \left(\alpha A d_k - r_k \right) = 0 . \tag{2.7}$$

In the conjugate gradient method, the position of this local minimum is used to define the next trial vector as:

$$x_{k+1} = x_k + \alpha_k d_k \tag{2.8}$$

where

$$\alpha_k = \frac{d_k^T r_k}{d_k^T A d_k} . \tag{2.9}$$

In the meantime, the vector of residuals can be updated as:

$$r_{k+1} = r_k - \alpha_k A d_k \, . \tag{2.10}$$

It should be noticed that the search direction vector, d_k, and the residual vector, r_{k+1}, satisfy the following orthogonality condition:

$$d_k^T r_{k+1} = d_k^T r_k - \alpha_k d_k^T A d_k = 0 . \tag{2.11}$$

We now assume that the search direction vectors are updated by an iteration of the form:

$$d_{k+1} = r_{k+1} + \beta_k d_k \tag{2.12}$$

where the coefficients β_i, $i \in \{0,1,2,....,k\}$ are determined by minimizing the error function *h* over the k-th Krylov subspace given by:

$$K_k = span\left(r_0,\ A r_0,\ A^2 r_0, ...,\ A^k r_0\right). \tag{2.13}$$

It can be proved that the search directions, which minimize the error functions *h*, and the corresponding residual vectors satisfy the following orthogonality relations [2.1]:

$$r_k^T r_l = 0 \qquad for\ k \neq l \tag{2.14}$$

and

$$d_k^T A d_l = 0 \qquad for\ \ k > l . \tag{2.15}$$

Substituting Equation (2.12) into the following orthogonal equation:

$$d_{k+1}^T A d_k = 0 ,$$

a new value for coefficient β is readily obtained as:

$$\beta_k = -\frac{r_{k+1}^T A d_k}{d_k^T A d_k} . \tag{2.16}$$

It is useful to obtain alternative expressions for α_k and β_k in terms of the residual vector, r_k. In order to reach this goal, we first expand d_k as a linear combination of the residual vectors $r_i, i \in \{0, 1, 2, \ldots, k\}$ as:

$$\begin{aligned} d_k &= r_k + \beta_{k-1} d_{k-1} = r_k + \beta_{k-1}\left(r_{k-1} + \beta_{k-2} d_{k-2}\right) = r_k + \beta_{k-1} r_{k-1} + \beta_{k-1}\beta_{k-2} d_{k-2} \\ &= r_k + \beta_{k-1} r_{k-1} + \beta_{k-1}\beta_{k-2} r_{k-2} + \ldots. + \beta_{k-1}\beta_{k-2} \ldots \beta_1 \beta_0 r_0 \end{aligned} \tag{2.17}$$

and then multiply Equation (2.17) by r_k. Using the orthogonality relations given in Equation (2.14), we finally obtain [2.1]:

$$d_k^T r_k = r_k^T r_k \,. \tag{2.18}$$

On the other hand, Equation (2.10), which updates the residual vector, can be rearranged into the following form:

$$A d_k = \frac{1}{\alpha_k}\left(r_k - r_{k+1}\right). \tag{2.19}$$

Multiplying Equation (2.19) by d_k and again using Equation (2.17) and the orthogonality relation, we have:

$$d_k^T A d_k = \frac{1}{\alpha_k} r_k^T r_k \,. \tag{2.20}$$

Similarly,

$$r_{k+1}^T A d_k = -\frac{1}{\alpha_k} r_{k+1}^T r_{k+1} \,. \tag{2.21}$$

Substituting Equations (2.18), (2.20) and (2.21) into (2.9) and (2.16), alternative expressions for parameters α_k and β_k can be readily obtained as:

$$\alpha_k = \frac{r_k^T r_k}{d_k^T A d_k}, \quad \beta_k = \frac{r_{k+1}^T r_{k+1}}{r_k^T r_k} \tag{2.22}$$

In these expressions, several matrix-vector multiplications in the original ones, as defined in Equations (2.9) and (2.16), respectively, are eliminated.

Although all the conjugate gradient methods, which use different formulas to update the residual vector r_k and coefficients α_k and β_k, are mathematically equivalent, their computer implementation is not. After a comparison with respect to computational effort, storage requirement, and accuracy, the following algorithm has been suggested [2.1]:

$$\begin{aligned} u_k &= A d_k \\ \alpha_k &= \frac{r_k^T r_k}{d_k^T u_k} \\ x_{k+1} &= x_k + \alpha_k d_k \\ r_{k+1} &= r_k - \alpha_k u_k \\ \beta_k &= \frac{r_{k+1}^T r_{k+1}}{r_k^T r_k} \\ d_{k+1} &= r_{k+1} + \beta_k d_k \end{aligned} \tag{2.23}$$

where $k = 0, 1, \ldots$. In order to start the iterative algorithm, we have to make an initial guess to the solutions vector as x_0 and calculate:

$$d_0 = r_0 = b - A x_0 . \tag{2.24}$$

2.2 Preconditioned Conjugate Gradient Method

Let C be an approximation to the coefficient matrix, A. Since A is a symmetric and positive definite matrix, we assume that C is also symmetric and positive definite and can be factored in the following form:

$$C = E E^T . \tag{2.25}$$

The quadratic functional defined in Equation (2.4) can be transformed using the transformation $\bar{y} = E^T \bar{x}$ as:

$$h = \bar{y}^T \widetilde{A}\, \bar{y} - 2\widetilde{b}^T \bar{y} + c \tag{2.26}$$

where the transformed coefficient matrix and right hand side vectors are:

$$\widetilde{A} = E^{-1} A E^{-T}, \; \widetilde{b} = E^{-1} b. \tag{2.27}$$

The condition number of the preconditioned coefficient matrix can be defined as:

$$\kappa(\widetilde{A}) = \widetilde{\lambda}_N / \widetilde{\lambda}_1 \tag{2.28}$$

where $\widetilde{\lambda}_1$ and $\widetilde{\lambda}_N$ denote the lowest and highest eigenvalues of matrix $C^{-1}A$ (or equivalently $\widetilde{A}$), respectively. Because the pre-conditioner matrix, C, is an approximation to A, the condition number of the transformed coefficient matrix $\widetilde{A}$ should be much closer to unity than the original coefficient matrix A, resulting in an improved convergence rate of the conjugate gradient method.

The preconditioned conjugate gradient method can be formulated in two versions, which are referred as the "transformed" and "untransformed" methods, respectively. In the transformed method, iterations are performed on the transformed solution vector y as follows:

$$\begin{aligned}
\widetilde{u}_k &= \widetilde{A}\widetilde{d}_k \\
\widetilde{\alpha}_k &= \frac{\widetilde{r}_k^T \widetilde{r}_k}{\widetilde{d}_k^T \widetilde{u}_k} \\
y_{k+1} &= y_k + \widetilde{\alpha}_k \widetilde{d}_k \\
\widetilde{r}_{k+1} &= \widetilde{r}_k - \widetilde{\alpha}_k \widetilde{u}_k \\
\widetilde{\beta}_k &= \frac{\widetilde{r}_{k+1}^T \widetilde{r}_{k+1}}{\widetilde{r}_k^T \widetilde{r}_k} \\
\widetilde{d}_{k+1} &= \widetilde{r}_{k+1} + \widetilde{\beta}_k \widetilde{d}_k
\end{aligned} \tag{2.29}$$

To initiate the iteration process, an initial guess of y must be provided and the initial residual vector and search direction vector must be computed as:

$$\tilde{d}_0 = \tilde{r}_0 = \tilde{b} - \tilde{A} y_0 . \tag{2.30}$$

Upon the convergence of the iteration, the solution vector must be obtained through backward substitution as:

$$x = E^{-T} y . \tag{2.31}$$

On the other hand, in the untransformed method, the solution vector x is calculated directly as:

$$\begin{aligned} u_k &= A d_k \\ \alpha_k &= \frac{r_k^T q_k}{d_k^T u_k} \\ x_{k+1} &= x_k + \alpha_k d_k \\ r_{k+1} &= r_k - \alpha_k u_k \\ q_{k+1} &= C^{-1} r_{k+1} \\ \beta_k &= \frac{r_{k+1}^T q_{k+1}}{r_k^T q_k} \\ d_{k+1} &= q_{k+1} + \beta_k d_k \end{aligned} \tag{2.32}$$

Unlike the transformed version, the untransformed version of the preconditioned conjugate gradient method works with the solution vector x directly. Because of this advantage of the untransformed method, it has been adopted in the present implementation. It is very interesting to note that in the untransformed method, only the pre-conditioner matrix is involved in the solution of a linear algebraic equation in each iteration.

2.3 Formulation of the Pre-conditioners

Generally speaking, a good pre-conditioner must have the following properties:

i. The condition number of the preconditioned coefficient matrix, $\kappa(\tilde{A})$, is significantly less than that of the original coefficient matrix, $\kappa(A)$;
ii. The decomposition of the preconditioning matrix, C, can be performed quickly and does not require excessive storage compared with the coefficient matrix A; and
iii. The system $Cq_{k+1} = r_{k+1}$ can be solved much more efficiently than the original system of equation $Ax = b$.

One of the most important sources of preconditioning matrices is the stationary iterative methods for solving systems of linear algebraic equations. Assume that a stationary iteration can be expressed in general form as:

$$M x_{k+1} = -R x_k + b, \quad k = 0,1,2,..., \tag{2.33}$$

it can be shown that the matrix M is suitable for being used as pre-conditioner [2.1].

Let the symmetric positive definite coefficient matrix A be decomposed into a diagonal matrix, a lower triangular matrix and a upper triangular matrix as:

$$A = D + L + L^T, \tag{2.34}$$

the Jacobi iteration method can be readily expressed in matrix form as:

$$D x_{k+1} = -(L + L^T) x_k + b, \quad k = 0,1,2,... \tag{2.35}$$

As a result, the diagonal matrix D is a good candidate for the pre-conditioner as:

$$C = D \tag{2.36}$$

Intuitively, C is not a very accurate approximation to the coefficient matrix A. This means that the reduction in the number of iterations resulting from the application of this pre-conditioner will be relatively modest compared with those of the original unpreconditioned equations. However, because the Jacobi pre-conditioner is very easy to implement and the system of equations $Cq = r$ can be solved in a highly efficient manner, it is still very useful in practical computations, especially on parallel and vector computers.

Another efficient stationary iterative method-based pre-conditioner can be derived from the symmetric successive overrelaxation method (SSOR), which is a two-step iterative procedure defined as follows [2.1]:

$$\begin{aligned} x_{k+1/2} &= (1-\omega)x_k - \omega D^{-1}\left(L x_{k+1/2} + L^T x_k - b\right) \\ x_{k+1} &= (1-\omega)x_{k+1/2} - \omega D^{-1}\left(L x_{k+1/2} + L^T x_{k+1} - b\right) \end{aligned} \qquad (2.37)$$

where ω is the over-relaxation parameter. Eliminating the intermediate solution vector $x_{k+1/2}$ from the above equations, we come up with an iteration algorithm in the form of Equation (2.33), in which the coefficient matrix is [2.1]:

$$C = \frac{1}{2-\omega}\left(\frac{1}{\omega}D + L\right)\left(\frac{1}{\omega}D\right)^{-1}\left(\frac{1}{\omega}D + L\right)^T. \qquad (2.38)$$

This matrix is already in a factored form and is suitable for being used as a pre-conditioner. In practical implementation, the leading scaling factor, $1/(2-\omega)$, is normally ignored. However, it should be noted that ignoring this scaling factor does not alter the condition number of the preconditioned coefficient matrix, $\kappa(\tilde{A})$.

The convergence rate of the conjugate gradient iteration method with SSOR preconditioning is obviously related to the value of the over-relaxation parameter ω. Fortunately, it has been shown [2.1] that although the value of the optimal over-relaxation parameter, ω^*, is problem dependent, the performance of the preconditioned conjugate gradient iteration is remarkably insensitive to ω.

Another important approach for constructing pre-conditioners for the conjugate gradient method involves computing an incomplete Cholesky factorization of the coefficient matrix A such that

$$C = LDL^T = A - R \tag{2.39}$$

where R indicates the error matrix. Unlike the full (complete) factorization, the incomplete factorization involves ignoring the nonzero entries in the factors if their positions are outside a sparsity structure S, which is a properly selected subset of the set $\{(i,j); 1 \le i \le n, 1 \le j \le n$ where n is the order of matrix A. This sparsity structure can be chosen either before the factorization takes place, or dynamically during the process of factorization, where small entries are neglected if they satisfy

$$\left(a_{ij}^{(r+1)}\right)^2 \le c\left|a_{ii}^{(r+1)}\right|\left|a_{jj}^{(r+1)}\right| \tag{2.40}$$

where $0 < c < 1$ is a user defined scaling factor and $(r+1)$ denotes the step of the Cholesky factorization [2.1-2.7]. The former is normally referred as incomplete factorization by *position*, whereas the latter is often called incomplete factorization by *value*.

It is readily recognized that the most critical step in the factorization by position method is to select a suitable sparsity structure to ensure that the incomplete factors are close to the exact ones. One of the simplest choices is to force the factor L to have the same sparsity pattern as the original coefficient matrix A defined as [2.8]:

$$P = \{(i,j) \mid a_{i,j} \ne 0; 1 \le i \le n, 1 \le j \le n \ . \tag{2.41}$$

In this method, which is often referred as ICCG(0), all the fill-in entries generated during the factorisation are simply neglected.

Various methods using higher levels of fill-in, which are normally referred as ICCG(k), where k denotes the level of fill-in, were also proposed. In these methods, the terms in the positions of the nonzero entries of the original matrix are of order zero, and approximate elimination is performed by retaining terms only through a certain order, called the level of fill-in. Thus an incomplete factorisation with fill-in level zero is such that the factors have exactly the same sparse pattern as the original coefficient matrix as defined in Equation (2.41). In the method, factors become less sparse with the increase of the level of fill-in until the complete factorisation is achieved. It is obvious that by increasing the level of fill-in, the generated pre-conditioner C becomes increasingly closer to the coefficient matrix A, thus fewer iterations are required to reach converged solutions. However, computational work and storage requirements also increase with higher level of fill-in, and each iteration will require more operations. In addition, this method is based on an assumption that the "order" of a term is an approximate measure of its magnitude, which does not necessarily hold for general sparse matrices generated by the finite element method. For the above reasons, the methods with higher level of fill-in were not considered in the present implementation.

The common and most important step of all incomplete factorization by value algorithms is the definition of the rejection criterion or drop-tolerance, which has the general form as given in Equation (2.40). In the algorithm proposed by Ajiz and Jennings [2.9], the following criterion was chosen to reject terms a_{ij}^{*}, namely if

$$\left(a_{ij}^{*}\right)^2 < \psi^2 \, \bar{a}_{ii} \, \bar{a}_{jj} \tag{2.42}$$

where a_{ij}^{*} indicates the current value of a_{ij} at the time the rejection test is carried out, and $\bar{a}_{ii}$, $\bar{a}_{jj}$ the current values of the diagonal terms. ψ is a pre-selected rejection parameter. A choice of $\psi = 0$ will retain all fill-in elements, thus leading to a complete Cholesky factorization. On the other hand, a choice of $\psi = 1$ will cause all off-diagonal terms be rejected, so resulting in a diagonal pre-conditioning matrix. It has been suggested that the use of intermediate ψ values (say $0.01 < \psi < 0.2$) is likely to give the most effective incomplete factorizations [2.9].

In order to develop an incomplete factorization strategy which is suitable for "black-box" implementation in the application software, Jones and Plassmann [2.10, 2.11] proposed an approach by incorporating features of both by *position* and by *value* algorithms. In this method, the numbers of nonzero terms in the factors in each row and column were fixed to the numbers of nonzeros in the original coefficient matrix. However, the sparsity pattern of the original matrix was not preserved in the factors, and only those terms with largest magnitude were retained. In this way, the space required for factorization was fixed, and by keeping the nonzero terms with the largest magnitude, some of the benefits of the drop-tolerance based algorithms were achieved without having to choose a rejection parameter. This method can be implemented in two ways, based on row and column storage of the sparse matrix. In the present study, both variations of the method were implemented and benchmarked.

It has been shown, however, that the stability (or existence) of an incomplete factorization is only guaranteed if the coefficient matrix is a M-matrix [2.8]. A symmetric positive definite matrix $A = (a_{ij})$ is an M-matrix if $a_{ij} \leq 0$ for $i \neq j$. Unfortunately, global stiffness matrices resulting from finite element discretization of general engineering structures do not satisfy this definition. In order to ensure the existence of positive definite factors in an incomplete factorization, Kershaw [2.12] proposed to simply set the diagonal terms of the factor L_{ii} to some pre-defined positive value if L_{ii} was detected equal or less than zero during factorization. Manteuffel [2.13] suggested an alternative procedure in which the diagonal of the sparse coefficient matrix was shifted priori to the incomplete factorization as:

$$a_{ii} \Leftarrow (1+\alpha)a_{ii} \quad 1 < i < n \tag{2.43}$$

where α is a pre-selected scaling factor. Proper selection of the scaling factor ensured that the resulting matrix was diagonally dominant, and then the stability of the incomplete factorization was guaranteed. However, in both methods, pre-selected parameters were required and a trial-and-error process was normally used to determine the optimum values of these parameters for a given linear algebraic system. Although these methods have been utilized by some researchers [2.14], they have been found to result in slow convergence for stiff elasticity problems [2.15].

An alternative method for preserving the positive definiteness of the incomplete factorization was to simply add the off-diagonal terms to be discarded onto the diagonal terms of the corresponding row and column [2.9, 2.16]. In this way, the row sum or column sum of the original sparse matrix could be preserved. Such a factorization scheme is usually called a "modified incomplete factorization". It has been shown that for some problems, the application of pre-conditioners generated by this method could reduce the condition number of the coefficient matrix from $O(h^{-2})$ to $O(h^{-1})$, however, very poor performance of the modified incomplete factorization method had been reported by Brussino and Sonnad [2.17].

2.4 Implementation of the Pre-conditioned Conjugate Gradient Method in VAST

An earlier attempt for providing an iterative linear algebraic equation solver in the VAST finite element program was made by Pegg [2.18] in 1988. At that time, the conjugate gradient method with the SSOR preconditioning was implemented based on the algorithm given in by Axelsson in [2.1]. The assembled global stiffness matrix was read from the .T48 file and stored in two separate one-dimensional arrays. The first contained the diagonal terms, whereas the second array contained the upper triangular portion of the stiffness matrix stored row-wise in a banded matrix format. An integer array was utilized to store the position of the first term in each row. Although the use two additional vectors, which stored the column numbers of the first and last non-zero entries in each row, eliminated many multiplications by zeroes, a large number of zero entries still existed in the middle of each row due to the sparsity of the global stiffness matrix.

Because the product of the global stiffness matrix and solution vector needs to be calculated repeatedly in the conjugate gradient iterative solver, it is very important to take full advantage of the sparsity of the stiffness matrix to make this operation efficient. In the current implementation of the iterative solver, the global stiffness matrix was stored in a sparse matrix format [2.9] in which all zero components in the matrix were eliminated and two integer arrays were used to store the column number of each non-zero stiffness component and the position of the first term in each row. For example, a symmetric matrix

$$A = \begin{bmatrix} 8.3 & -3.2 & 0 & -2.7 \\ & 13.7 & -5.6 & 0 \\ & & 10.5 & -2.2 \\ & & & 9.2 \end{bmatrix}$$

can be stored in three arrays as:

READ ARRAY A $\{8.3 \quad -3.2 \quad -2.7 \quad 13.7 \quad -5.6 \quad 10.5 \quad -2.2 \quad 9.2\}$;
INTEGER ARRAY IC $\{1 \quad 2 \quad 4 \quad 2 \quad 3 \quad 3 \quad 4 \quad 4\}$; and
INTEGER ARRAY IR $\{1 \quad 4 \quad 6 \quad 8 \quad 9\}$.

In the efficient implementation of the incomplete factorization scheme, more arrays are normally required to reduced the overhead involved in the array operations. It is readily recognized that the percentage of non-zero terms below the skyline in the global stiffness matrix is an important indicator of the efficiency of sparse storage format. This value is now calculated automatically by VAST during the iterative solution.

This present implementation of the preconditioned conjugate gradient method in VAST involved development of a new module, DECOM7, which performs assembly and modification of the global stiffness matrix, transforms global stiffness matrix into the sparse matrix storage format, constructs the pre-conditioner matrix and stores all the information used by the iterative solution algorithm on intermediate binary files. The iterations are carried out in the DISP1 module after the global load vector became available. This iterative solution algorithm is operational for static analyses and can be activated by setting solution method control parameter ISOLVE=3 and the master control code IDECOM=7 in the PREFX.USE file.

Seven pre-conditioners were implemented in the present work. They are defined by a parameter IMPC. The first one (IMPC=1) was the Jacobi pre-conditioner, which contained the diagonal terms of the global stiffness matrix. The second one (IMPC=2) was the symmetric successive overrelaxation (SSOR) pre-conditioner defined in Equation (2.38) in this chapter. As mentioned earlier, the convergence rate of the SSOR preconditioned conjugate gradient method is insensitive to the value of the overrelaxation parameter, ω. Based on numerical experiments presented in Reference [2.19], the default value of ω had been set to 1.15. During the literature survey conducted in the present work, it had been noticed that Papadrakakis [2.19] had proposed a modification to the SSOR pre-conditioner, in which the drop tolerance concept from the incomplete factorization method was adopted to reduced the storage requirement of the original SSOR pre-conditioner. However, this modification normally resulted in an increase in the number of iterations, which eventually let to an increase of the execution time. For this reason, this modification was not implemented in VAST.

The remaining five (third–seventh) pre-conditioners were all based on the incomplete factorization method. Among them, the third pre-conditioner (IMPC=3) was developed using the level-zero incomplete factorization, which preserved the sparsity pattern of the original stiffness matrix. In order to avoid failure of the incomplete factorization, in the present implementation, the preconditioning matrix was decomposed into the form:

$$M = LDL^T .$$

For some elasticity problems, such as those involving very thin structural components, negative elements may exist in the diagonal matrix D. In this case, the preconditioned conjugate gradient method no longer led to a minimization problem, but rather a simple least square projection of the solution over the Krylov space [2.15]. As mentioned earlier, various techniques have been proposed to maintain the positive definiteness of the preconditioning matrix by modifying the diagonal matrix during the incomplete factorization, i.e.[2.12, 2.16]. However, experience with stiff elasticity problems indicates that all these modification methods result in a very large number of iterations [2.15]. It has been suggested that the negative terms be left untouched and the algorithm unmodified.

The fourth pre-conditioner (IMPC=4) was developed based on the algorithm proposed by Ajiz and Jennings [2.9]. This method involved a drop criterion given in Equation (2.42) and the discarded off-diagonal terms were added to the diagonal to preserve the row sums. The rejection parameter, ψ, which was used in the drop criterion must be pre-defined by the user. It should be noticed that with this algorithm, the size of the pre-conditioner depends on the value of the rejection parameter and cannot be predicted before the incomplete factorization.

The last two pre-conditioners (IMPC=6,7) were based on the improved incomplete Cholesky factorization method presented by Jones and Plassmann [2.10] using the row and column wise stored stiffness matrices, respectively. The Fortran subroutines developed by Jones and Plassmann [2.11] are available as Algorithm 740 on the web site of NETLIB. In the present work, these Fortran subroutines were downloaded and incorporated into the VAST program. However, it should be noted that because this implementation was based on the LL^T decomposition of the pre-conditioner, they would break down when negative values appeared on the diagonal during the factorization. In addition to those subroutines based on the improved incomplete Cholesky factorization, one subroutine for the original incomplete factorization was also provided at the same web location. This subroutine was implemented as pre-conditioner five (IMPC=5) in VAST and used as an independent check to pre-conditioner IMPC=3, which was written by ourselves. It should be noted that although only seven pre-conditioners were implemented in the present work due to budgetary constraints, a proper program structure has been set up in VAST for the preconditioned conjugate gradient methods so that additional pre-conditioners can be conveniently implemented.

To terminate the iterations, a convergence criterion based on the norms of the load and residual vectors was adopted as:

$$\|r_{k+1}\| < \varepsilon \|b\|$$

where ε is a user prescribed small positive number. In the present work, $\varepsilon = 10^{-5}$ had been used throughout the numerical experimentation to be presented in the next section. With such a small value of ε, major displacement components in the solution vectors obtained using the direct and iterative linear equation solvers normally agreed to the fifth digit.

It has been discovered by a number of researchers that the nodal numbering in a finite element mesh might have significant influence on the performance of the preconditioned conjugate gradient algorithm [2.15]. This is due to the fact that the entries in pre-conditioners generated by incomplete factorization are significantly related to the order in which these entries are computed. However, it appears that the optimum numbering scheme for a general coefficient matrix is not yet available.

2.5 Verification of the Pre-conditioned Conjugate Gradient Method in VAST

Extensive numerical experiments have been conducted to verify and benchmark the newly developed iterative solution algorithm with various pre-conditioners during the course of the present development. Some key numerical results will be summarized in this section. All these results were obtained using a Pentium II 266 MHz with 64 Mb of RAM.

Example 1: A Linear Elastic Cube Subjected to an Uniform Pressure on Top Surface. This test case involved a linear elastic analysis of a 1x1x1 cube subjected to uniform pressure load on its top surface. The bottom surface of the cube was fully constrained. Material properties utilized in these analyses were $E=205{,}000$ and $\nu=0.3$.

This problem was first solved by using a series of uniform meshes of the 20-noded and 8-noded solid elements. In these meshes, the same number of solid elements were utilized in all three dimensions, resulting in an aspect ratio of 1:1:1. These finite element meshes are displayed in Figures 2.1 and 2.2, respectively, and the solution times required by the decomposition and displacement modules in different solvers are compared in Tables 2.1 and 2.2. In these tables, the decomposition module, denoted by DECOM, not only performed decomposition of the global stiffness matrix and calculation of the preconditioning matrix, which were required in the direct and iterative solvers, respectively, but also included assembly and modification of the global stiffness matrix. For the direct solver, forward reductions and backward substitutions were performed in the displacement module, whereas for the iterative solver, iterations were carried out. As indicated by the numerical results, the most computationally intensive operation involved in the direct linear equation solver was the decomposition of the coefficient matrix. However, for the iterative solver, most of the computation time was spent in the displacement module where the iterations took place. Comparing the total computation times, it is readily recognized that for the present problem, the preconditioned conjugate gradient solver was far more efficient than the direct solver, especially for fine finite element models.

The results presented in Tables 2.1 and 2.2 indicated that the pre-conditioner could have a very significant effect on the overall performance of the iterative solver. In order to compare the qualities of the different pre-conditioners implemented in the VAST program, the number of iterations associated with each pre-conditioner are also included in Table 2.1. Use of high quality pre-conditioners, such as those generated using the improved incomplete factorization methods (IMPC=6,7), resulted in lower number of iterations. However, the computational effort required in the generation of these pre-conditioners and the calculation involved in each iteration increased. The pre-conditioners derived from the stationary iterative methods and the original incomplete Cholesky factorization seem to be favorable.

Among these pre-conditioners, both IMPC=3 and IMPC=5 were developed based on original incomplete Cholesky factorization, with different implementations. The former was developed by the authors, whereas the latter was written by Jones and Plassmann [2.11] and downloaded from the Internet. As a result, the latter subroutine was used to verify our implementation. The numerical study showed that the use of these pre-conditioners not only results in the identical number of iterations, but also identical residual vectors. However, due to the difference in implementations, the execution times required by these two pre-conditioner are slightly different.

The pre-conditioner proposed by Ajiz and Jennings [2.9], which had been implemented in VAST as IMPC=4, was also tested on these problems. Extremely poor convergence properties were obtained. As discussed earlier, in this modified incomplete factorization algorithm, a reject criterion was used to ignore small off-diagonal terms and these ignored terms were added to the related diagonal components to preserve row sums of the original coefficient matrix. The poor performance of this algorithm on the present test case was probably related to the modifications to the diagonal terms [2.15].

Also included in these tables are the model dimension parameters and the percentage of the non-zero terms below the skyline of the global stiffness matrix. The latter could be used to measure the sparsity level of a matrix. As indicated in Tables 2.1 and 2.2, with the increase of problem size, the percentage of zeroes below the skyline increases rapidly. This observation suggests that the iterative solvers might outperform the direct one for very large problems. This is due to the fact that the direct solver was based on complete factorization, in which all the zeroes below the skyline in the original matrix may be filled with nonzero terms in the factors. On the other hand, in the iterative solver, because the sparse matrix storage format is adopted to store the highly sparse coefficient matrix, and because a large number of fill-in terms is ignored in the incomplete factorization algorithm, the computation of the pre-conditioner and evaluation of matrix-vector product can be performed more efficiently. The potential of the iterative solver was indeed demonstrated by this example.

It had been reported that the performance of the iterative solvers would degrade when the mesh aspect ratio became more extreme because in this case, the global stiffness matrix would become more poorly-conditioned. In order to study the effect of the mesh aspect ratio, two additional meshes were generated using the 8-noded solid element with different numbers of elements in the in-plane and transverse directions, as summarized in Figure 2.3. The mesh aspect ratios corresponded to these meshes were 7.5:7.5:1 and 5:5:1, respectively. The solution times obtained using different solvers are compared in Table 2.3. As expected, the iterative solver did slow down due to the poorly-conditioned stiffness matrices, but it still outperformed the direct solver. For the fine 12×12×60 mesh, the most efficient pre-conditioner was the one based on the original incomplete factorization algorithm. However, for the coarse mesh, the time results shown in Table 2.3 are not consistent. For confirmation purposes, additional runs were carried out for the coarse mesh using the iterative solver with various pre-conditioners without rebooting the computer. The results are summarized in Table 2.4. It is evident the execution time may vary considerably for a given analysis, especially for relatively small problems. This variation appears to be caused by the internal data management system of the operating system. Once the I/O operations are finished, some data may still be left in the memory. However, the action of the data management system is not quite predictable. As a result, the timing results obtained for small meshes may not be very reliable.

In addition to the computational efficiency, the iterative solvers have another advantage in their low disk storage requirement. Table 2.5 compares the disk spaces required by the direct and iterative solvers for various meshes of the 20-noded solid elements. For the finest mesh, the direct solver required as much as five times of the storage space required by the iterative solver.

The final deformed configuration and stress distributions obtained using various solid element meshes and different linear algebraic equation solvers were in excellent agreement. A set of typical results obtained using the finest meshes and iterative solver are presented in Figures 2.4 and 2.5.

Example 2: Cantilevered Square Plate Under In-Plane and Vertical Loads. In order to study the performance of the direct solver in structural analysis involving thin shell structures, in-plane and bending deformations of a cantilevered plate were investigated in this example problem. The finite element mesh of the plate is displayed in Figure 2.6, which contained 3200 3-noded triangular plate elements. The in-plane dimension and the thickness of the plate were taken as 4.0 and 0.2, respectively and the material properties were $E=2.07\times10^{11}$ and $\nu=0.3$. The 3-noded triangular plate/shell was utilized in this test example because in this element, the membrane and bending stiffnesses were defined independently. To prescribe the cantilever boundary condition, all nodes along edge $X=4.0$ were fully constrained. The in-plane and bending loads were achieved by an uniformly distributed tensile force along edge $X=0$ and an uniform pressure acting on the top surface, respectively.

The solution times taken by direct and iterative solvers for both load cases are presented in Table 2.6. For the direct solver, the times required by the decomposition and displacement modules for different load cases were very close. This is because the number of arithmetic operations required by the direct solver is independent of the nature of the load vector. However, the iterative solver is different. Although the times required for assembly, matrix modification and computation of pre-conditioners are quite similar, considerably more iterations were required to obtain converged solutions for the bending situation. For membrane load, the pre-conditioner based on the original incomplete factorization method resulted in the most efficient solution method. However, convergence was not achieved for the bending case using the same pre-conditioner. Identical results were obtained by including only the membrane and bending stiffness matrices in the in-plane and pressure loading cases, respectively. These numerical results led to a very interesting observation. In most text books on iterative solvers, such as [2.1-2.7], it is mentioned that the convergence property of the preconditioned conjugate gradient method depends on the condition number of the coefficient matrix. However, the present results indicate that this statement is incomplete. It should be modified to state that the convergence property depends on the condition number evaluated using the smallest and biggest eigenvalues corresponding to the eigen modes involved in the present deformation pattern.

Some timing results obtained by using pre-conditioner IMPC=4 are also given in Table 2.6. By setting $\psi=0$ in this algorithm, no fill-in terms were ignored and the incomplete factorization became identical to the complete factorization. As a result, convergence was achieved in one iteration. With the increase of reject parameter ψ, the number of iterations increased very rapidly, causing significant increase of the total solution time. Based on the present test results, this pre-conditioner cannot compete with the other pre-conditioners and should never be used in practical engineering analyses.

Because a small convergence tolerance $\varepsilon=10^{-5}$ was utilized in the present analyses, the displacement vectors and element stresses obtained by all the solution methods were in exact agreement. The contour plots of the von Mises stress in the middle and upper surfaces for the membrane and bending situations are displayed in Figures 2.7 and 2.8, respectively. These plots were generated using the results of the iterative solver with the SSOR pre-conditioner (IMPC=2).

Example 3: Linear Static Analysis of a Lower Spar Cap. In this example problem, linear static analysis of a practical engineering structure, a lower spar cap from an airplane wing, was considered. The finite element mesh of the cap is displayed in Figure 2.9. In order to capture detailed stress variations, a very fine mesh of 8-noded solid elements was utilized, which included a total of 8344 nodes and 6890 elements. The solution times required by various solvers are compared in Table 2.7. For this practical problem, the iterative solver still outperformed the direct one. Among the pre-conditioners, the one based on the symmetric successive overrelaxation (SSOR) method (IMPC=2) resulted in the shortest computation time. Similar to the previous example, the displacements and stresses obtained using different solution techniques were in excellent agreement. The final deformed configuration and von Mises stress distribution predicted by one of the solution method were displayed in Figures 2.10 and 2.11, respectively.

Example 4: Simply Supported Plate Subjected to Uniform Pressure. In this example problem, we focused on the performance of the iterative solver for pure bending problems of thin structural members. A simply-supported square plate subjected to an uniform pressure was considered for this purpose. The in-plane dimensions and thickness of the plate were 8.0 and 0.2, whereas the material properties were $E=2.07\times10^{11}$ and $\nu=0.3$. The intensity of the uniform pressure used in the analysis was 1.125×10^{6}. Due to the symmetry in this problem, only half of the plate needed to be included in the finite element mesh.

The 8-noded solid element was first considered and three meshes with different levels of refinement were created as shown in Figure 2.12. Multiple layers of elements were used through the thickness to achieve a sufficiently accurate representation of the bending strain field. The timing results obtained using different solvers on these meshes are summarized in Table 2.8. For the finest mesh, the iterative solver with the SSOR pre-conditioner (IMPC=2) outperformed all other iterative solvers, but was still significantly slower than the direct one. Once again, these results confirmed that the convergence property of the preconditioned conjugate gradient method depends mainly on the condition number related to the physical problem, but not on the particular finite element formulation. The final deformed configurations of the plate are superimposed on the original finite element meshes in Figure 2.12 and von Mises stress distribution in the plate, predicted by the fine mesh, is presented in Figure 2.13. As indicated by the stress plot, in order to catch the high stress gradient near the boundary, a locally refined mesh may be required.

The same square plate was then modeled using the 3-noded triangular plate element, as shown in Figure 2.14. The timing results are shown in Table 2.9. For the finest mesh of plate element, the simplest pre-conditioner, Jacobi diagonal pre-conditioner (IMPC=1), gave the best performance. The iterations preconditioned by the incomplete factorization (IMPC=3) failed to converge. The pre-conditioner based on the improved incomplete Cholesky factorization method (IMPC=6) was also considered. However, this method broke down due to the negative diagonal terms appeared during the incomplete factorization. Von Mises stress distribution on the top surface of the plate predicted by the fine mesh is displayed in Figure 2.15.

Example 5: Linear Static Analysis of a Typical Stiffened Panel. In this problem, linear static analysis of a typical stiffened panel was considered. This panel, which contained a plate and Tee stiffener, was simply supported at both ends and subjected to a pair of compressive forces in its neutral plane. To ensure that all the end nodes still were coplanar after deformation, multi-point constraint equations were been employed. Since these multi-point constraints were treated using the penalty method, the penalty stiffness terms could have an impact on the condition number of the global stiffness matrix.

Both the 4-noded quadrilateral and the 3-noded triangular plate elements were considered in this example problem. For each element, three meshes were generated as shown in Figure 2.16 and 2.17, respectively. Because the stiffened panel was composed of thin plate structural components, it was not surprising to see that the iterative solver was less efficient than the direct solver, as indicated in Table 2.10. The solutions obtained using different solvers were still identical and the von Mises stress contour plot generated using the fine mesh of the 4-noded shell element is given in Figure 2.18.

2.6 Multi-Level Iterative Methods and Hierarchical Pre-conditioners

The multi-level iteration methods and the pre-conditioners constructed based on the same idea have recently been found very effective in solving poorly-conditioned system of linear algebraic equations [2.20-2.29]. The success of the multi-level methods is due to the fact that many iterative methods are very effective at eliminating the high-frequency or oscillatory components of the residual vector, while leaving the low-frequency and smooth components relatively unchanged. Because in the multi-level methods, the coarse and fine meshes represent the same physical problem, the residual components on the coarse mesh correspond to the same residual components on the fine mesh, and for a given component on both meshes, the one on the coarse mesh is closer to the high-frequency end of the representable spectrum than the one on the fine mesh. This observation suggests that when the convergence rate of an iterative solution becomes slow on the fine mesh, it is helpful to move it to a coarse mesh, on which the smooth residual modes become more oscillatory and can be reduced more effectively by the iterations.

To demonstrate the concept of the multi-level method, we consider a basic two-level multigrid method. Assume that our objective is to solve equilibrium equations on a fine mesh given by:

$$A_f x_f = b_f . \tag{2.44}$$

The *k*-th iteration consists of the following steps [2.20]:

1. Starting with the current fine mesh approximation $x_f^{(k)}$, perform an appropriate iteration to obtain an improved approximate solution $\bar{x}_f^{(k)}$;
2. Compute the residual vector associated with the improved solution as:

$$\bar{r}_f^{(k)} = b_f - A_f \bar{x}_f^{(k)} ; \tag{2.45}$$

3. Restrict the fine mesh residual vector onto the coarse mesh using the fine-to-coarse mesh restriction operator T^T as:

$$\bar{r}_c^{(k)} = T^T \bar{r}_f^{(k)} ; \tag{2.46}$$

4. Solve the coarse mesh residual equation to produce the coarse mesh correction:

$$A_c \Delta \bar{x}_c^{(k)} = \bar{r}_c^{(k)} \tag{2.47}$$

where

$$A_c = T^T A_f T \,. \tag{2.48}$$

If the number of unknowns of the coarse mesh is sufficiently small, Equation (2.47) can be solved using a direct method.

5. Transform the coarse mesh correction back to the fine mesh using the coarse-to-fine elongation operator as:

$$\Delta\bar{x}_f^{(k)} = T\,\Delta\bar{x}_c^{(k)} \tag{2.49}$$

6. Compute the new approximate solution on the fine mesh as:

$$\hat{x}_f^{(k)} = \bar{x}_f^{(k)} + \Delta\bar{x}_f^{(k)} \tag{2.50}$$

7. Finally, perform appropriate relaxation starting with $\hat{x}_k^{(k)}$ to produce the new fine mesh solution $x_f^{(k+1)}$.

The multi-level or hierarchical pre-conditioners are derived using the same concept. Consider a two-level mesh and use the hierarchical base functions, the linear algebraic system for the fine mesh can be expressed as:

$$\begin{bmatrix} A_c & \bar{A}_{cf} \\ \bar{A}_{cf}^T & \bar{A}_f \end{bmatrix} \begin{Bmatrix} x_c \\ \bar{x}_f \end{Bmatrix} = \begin{Bmatrix} b_c \\ \bar{b}_f \end{Bmatrix} \tag{2.51}$$

where A_c, x_c, b_c denote the stiffness matrix, displacement vector and load vector of the coarse mesh such that:

$$A_c\, x_c = b_c \tag{2.52}$$

and the superposed bar indicates relative higher-level degrees-of-freedom and the corresponding load components in the fine mesh.

A number of pre-conditioners have been proposed based on the hierarchical stiffness matrix given in Equation (2.51). The simplest one is to ignore the coupling matrix between the coarse and fine degrees-of-freedom [2.20-2.24], so the preconditioning matrix can be defined as:

$$C = \begin{bmatrix} (LDL^T)_c & 0 \\ 0 & (LDL^T)_f \end{bmatrix} \tag{2.53}$$

or

$$C = \begin{bmatrix} (LDL^T)_c & 0 \\ 0 & D_f \end{bmatrix}. \tag{2.54}$$

Either exact or incomplete factorization algorithms can be utilized to perform the LDL^T decomposition involved in these pre-conditioners. This method of constructing pre-conditioner is called *H reduction* [2.24], and the spectrum equivalence between the pre-conditioner C and the original coefficient matrix A has been proved [2.22]. Numerical results have demonstrated that the use of these pre-conditioners in conjunction with the conjugate gradient method leads to highly efficient iterative solvers for very poorly-conditioned linear systems, such as those resulted from finite element discretization of thin shell structures [2.24]. Several more accurate pre-conditioners, which involve the coupling matrix, have also been proposed [2.22, 2.24]. However, the additional computational efforts involved in these pre-conditioners do not outweigh the savings gained by the reduction of iterations.

It is not a trivial task to transform a given system of finite element equilibrium equations generated using a fine mesh of regular elements into the hierarchical form as shown in Equation (2.51). Dracopoulos and Crisfield proposed a coarse/fine mesh pre-conditioner [2.25], in which the coarse-to-fine transformation operator T was constructed using the shape functions of the elements in the coarse mesh and the hierarchical stiffness matrix was constructed through matrix transformations at either the global or the element level of the fine mesh. Although the nodes in the coarse mesh are normally a subset of the nodes in the fine mesh, the element edges in the coarse mesh do not necessarily coincide with the element edges in the fine one. Details were given in Reference [2.25] on how to handle the fine mesh nodes which were outside the coarse element. As pointed out by the authors, this method is particularly suitable for implementation into existing general purpose finite element programs.

In order to construct a hierarchy of coarser problems without actually doing a sequence of coarser discretizations, aggregation-based multilevel solvers have been developed [2.26, 2.27]. In these methods, the coarse grid was substituted with an aggregation coarse model based on mechanical principles. However, for poorly conditioned problems such as thin shells, the coarse problem constructed by the regular aggregation scheme was unable to adequately capture the lower-frequency response of the original fine problem. In order to achieve the optimum rate of convergence, Fish and Belsky [2.27] proposed a generalization of the basic aggregation method by which the approximation space of each aggregate was adaptively and automatically selected depending on the special characteristics of the aggregate. This generalized aggregation multi-level solver had been tested on a number of large scale problems of thin shell structures, and the numerical results showed that this procedure significantly out-performed the Power Solver of the ANSYS finite element program [2.27].

The hierarchical stiffness matrix can be naturally obtained using the p-version finite elements. Mandel [2.28] has developed a general formulation of pre-conditioner using the abstract additive Schwarz method. In this procedure, the stiffness matrix was viewed as a linear mapping of the matrix onto a series of subspaces of the original finite element space *V*. The nodes of p-version finite elements were divided into different categories, such as vertex nodes, edge nodes, surface nodes and interior nodes, and different strategies were utilized to construct subspaces for each of these node categories. This pre-conditioner has also been benchmarked using large thin shell problems and excellent performance has been demonstrated. Mitchell and Reddy [2.29] also proposed a hierarchical pre-conditioner based on p-version elements. This multi-level pre-conditioner was defined recursively and its potential for treating poorly-conditioned problems has been demonstrated. However, all these methods are based on the p-version elements, which are not currently available in the VAST finite element program.

Table 2.1: Comparison of Solution Times Required by Different Linear Matrix Solvers for the Cube Problem Modeled by Uniform Meshes of 20-Noded Solid Elements.

		Mesh					
	Module	2×2×2	4×4×4	6×6×6	8×8×8	10×10×10	12×12×12
# of Nodes		81	975	1225	2673	4961	8281
# of Elements		8	64	216	512	1000	1728
% of non-zeroes below skyline		60.26	25.81	13.02	8.15	5.27	3.64
Direct solver	DECOM	0.11*	1.65	17.14	134.95	566.45	2141.21
	DISP1	0.01	0.17	0.44	30.81	90.19	232.28
PCG (IMPC=0)	DECOM	0.17	0.17	0.82	2.09	11.86	18.40
	DISP1	0.06	2.37	8.85	18.40	38.83	89.58
	# of Iter.	75	203	418	364	456	625
PCG (IMPC=1)	DECOM	0.05	0.32	1.38	2.14	5.32	15.82
	DISP1	0.05	1.21	3.51	8.57	17.96	44.87
	# of Iter.	29	66	125	134	167	288
PCG (IMPC=2)	DECOM	0.05	0.17	0.82	2.41	6.10	18.89
	DISP1	0.11	1.65	5.49	16.92	31.42	62.35
	# of Iter.	42	54	84	113	135	162
PCG (IMPC=3)	DECOM	0.05	0.44	1.65	11.69	11.09	29.33
	DISP1	0.01	1.21	3.35	9.78	16.75	22.63
	# of Iter.	13	25	38	53	66	51
PCG (IMPC=5)	DECOM	0.22	0.33	1.43	3.52	17.63	28.13
	DISP1	0.11	1.31	3.57	8.85	17.25	23.24
	# of Iter.	13	25	38	53	66	51
PCG (IMPC=6)	DECOM	0.06	0.33	1.37	5.33	16.92	32.79
	DISP1	0.06	1.32	1.49	6.37	15.21	22.14
	# of Iter.	9	17	25	32	42	48
PCG (IMPC=7)	DECOM	0.22	0.27	11.15	47.45	145.39	261.99
	DISP1	0.17	0.39	1.32	6.21	10.54	20.71
	# of Iter.	9	15	22	28	36	43

*Times are in seconds.

Table 2.2: Comparison of Solution Times Required by Different Linear Matrix Solvers for the Cube Problem Modeled by Uniform Meshes of 8-Noded Solid Elements.

	Module	Mesh					
		5×5×5	7×7×7	10×10×10	14×14×14	17×17×17	20×20×20
# of Nodes		216	512	1331	3375	5832	28331
# of Elements		125	343	1000	2744	4913	8000
% of non-zeroes below skyline		25.15	14.61	8.08	4.56	3.23	2.53
Direct solver	DECOM	0.11*	1.97	17.96	111.06	556.61	2095.90
	DISP1	0.06	0.27	0.94	3.30	71.07	208.83
PCG (IMPC=0)	DECOM	0.30	0.24	1.08	5.46	28.56	142.62
	DISP1	0.24	1.92	2.34	8.70	15.48	31.62
PCG (IMPC=1)	DECOM	0.33	0.27	0.83	6.98	27.71	141.76
	DISP1	0.16	2.09	1.87	4.99	7.79	19.44
PCG (IMPC=2)	DECOM	0.11	0.33	0.99	6.97	24.94	163.08
	DISP1	0.11	2.14	2.30	6.15	9.56	44.00
PCG (IMPC=3)	DECOM	0.33	0.38	1.32	6.43	30.76	157.30
	DISP1	0.16	1.71	1.65	5.11	7.97	25.98
PCG (IMPC=5)	DECOM	0.33	0.39	2.36	3.57	27.14	117.10
	DISP1	0.06	1.97	1.81	3.51	7.80	26.36
PCG (IMPC=6)	DECOM	0.11	0.33	2.86	5.71	32.51	117.70
	DISP1	0.11	1.76	0.82	3.07	6.54	18.89
PCG (IMPC=7)	DECOM	0.39	3.57	4.28	15.93	53.11	241.95
	DISP1	0.05	0.22	0.77	4.61	7.86	16.81

*Times are in second.

Table 2.3: Comparison of Solution Times Required by Various Linear Equation Solvers for the Cube Problem Solved by 8-Noded Solid Elements With Severe Aspect Ratios

Linear Equation Solver	4×4×30 Mesh (7.5:7.5:1)			12×12×60 Mesh (5:5:1)		
	DECOM	DISP1	# of Iter.	DECOM	DISP1	# of Iter.
Direct Solver	6.26*	0.33		195.37	38.78	
PCG (IMPC=0)	0.93	2.69	341	36.14	42.73	568
PCG (IMPC=1)	3.63	0.88	121	35.97	20.32	216
PCG (IMPC=2)	1.60	0.60	51	36.86	24.11	124
PCG (IMPC=3)	3.41	0.60	55	38.06	8.73	37
PCG (IMPC=5)	0.60	0.88	55	39.99	8.18	37
PCG (IMPC=6)	3.74	0.60	35	40.65	8.35	31
PCG (IMPC=7)	2.31	0.44	30	62.51	7.47	32

*Times are in seconds.

Table 2.4: Comparison of the Solution Times Obtained on a Window-Based PC for the Cube Problem Modeled Using 4×4×30 Mesh of 8-Noded Solid Elements

Linear Equation Solver	Run1		Run 2		Run 3	
	DECOM	DISP1	DECOM	DISP1	DECOM	DISP1
PCG (IMPC=0)	0.93*	2.69	0.28	3.74		
PCG (IMPC=1)	3.63	0.88	0.33	2.80		
PCG (IMPC=2)	1.60	0.60	0.77	2.85		
PCG (IMPC=3)	3.41	0.60	0.39	3.46	0.98	1.82
PCG (IMPC=5)	0.60	0.80	0.32	2.37	1.21	1.82
PCG (IMPC=6)	3.74	0.60	1.15	0.93	0.55	0.82
PCG (IMPC=7)	2.31	0.44	4.34	0.39		

*Times are in seconds.

Table 2.5: Comparison of Disk Storage Spaces Required by Direct and Iterative Solvers for the Cube Problem Modeled Using 20-Noded Solid Elements

Mesh	No. of Nodes	No. of Elements	Direct Solver	Iterative Solver
2×2×2	81	8	349,020*	559,960
4×4×4	975	64	5,874,832	4,316,668
6×6×6	1225	216	25,382,908	13,836,380
8×8×8	2673	512	80,486,116	32,477,788
10×10×10	4961	1000	218,791,508	62,965,560
12×12×12	8281	1728	501,213,428	108,402,256

*Disk spaces are in bytes.

Table 2.6: Comparison of Solution Times for a Cantilevered Square Plate Under Membrane and Bending Loads

Linear Equation Solver	Membrane Load			Bending Load		
	DECOM	DISP1	# of Iter.	DECOM	DISP1	# of Iter.
Direct Solver	11.04*	0.99		9.88	0.88	
PCG (IMPC=0)	2.19	14.78	1301	1.98	164.39	15022
PCG (IMPC=1)	1.81	5.17	394	2.20	30.48	2604
PCG (IMPC=2)	2.74	3.79	122	1.87	26.36	1085
PCG (IMPC=3)	1.87	3.19	103	1.98	Diverged	
PCG (IMPC=4,$\psi=0$)	7.63	4.29	1	8.07	1.26	1
PCG (IMPC=4,$\psi=10^{-6}$)	8.46	28.01	256	7.14	67.50	692
PCG (IMPC=4,$\psi=10^{-5}$)	6.15	69.65	779		Diverged	

* Times are in seconds.

Table 2.7: Comparison of Solution Times Required by Various Linear Equation Solvers for a Lower Spar Cap From Airplane Wing Modeled by 8-Noded Solid Elements

Linear Equation Solver	Module		Total Time
	DECOM	DISP1	
Direct Solver	7.963*	1.264	9.227
PCG (IMPC=1)	0.840	7.883	8.723
PCG (IMPC=2,$\omega=1.0$)	0.840	4.517	5.357
PCG (IMPC=2,$\omega=1.15$)	0.843	4.380	5.223
PCG (IMPC=3)	0.887	6.448	7.335

* Times are in minutes.

Table 2.8: Comparison of Solution Times for a Simply Supported Plate Subjected to Uniform Pressure Modeled by 8-Noded Solid Elements

Linear Equation Solver	5×5×2		10×10×4		15×15×6	
	DECOM	DISP1	DECOM	DISP1	DECOM	DISP1
Direct Solver	0.17*	0.11	1.10	0.16	14.17	1.54
PCG (IMPC=0)	0.11	0.27	0.33	13.40	1.15	84.14
PCG (IMPC=1)	0.22	0.17	2.08	4.61	3.13	38.83
PCG (IMPC=2)	0.06	0.11	1.59	4.34	2.09	28.89
PCG (IMPC=3)	0.11	0.17	2.91	2.97	2.08	32.29

*Times are in seconds.

Table 2.9: Comparison of Solution Times for the Simply Supported Plate Modeled by 3-Noded Triangular Plate Element

Linear Equation Solver	10×10		20×20		40×40	
	DECOM	DISP1	DECOM	DISP1	DECOM	DISP1
Direct Solver	0.16*	0.05	1.04	0.11	11.10	0.94
PCG (IMPC=0)	0.11	0.16	1.49	3.79	1.92	94.58
PCG (IMPC=1)	0.28	0.16	0.50	0.77	2.53	16.58
PCG (IMPC=2)	0.11	0.11	2.31	1.05	3.13	22.80
PCG (IMPC=3)	0.11	0.06	2.58	1.70	6.04	Diverged
PCG (IMPC=6)	Failed		Failed		Failed	

*Times are in seconds.

Table 2.10: Comparison of Solution Times for a Typical Stiffened Panel Model

IEC	Mesh	No. of Nodes	No. of Elements	Direct Solver		PCG (IMPC=2)	
				DECOM	DISP1	DECOM	DISP1
5	Coarse	401	360	3.57*	0.27	3.90	10.99
5	Intermediate	1273	1200	8.62	1.10	5.65	68.16
5	Fine	4619	4480	97.33	16.70	14.23	366.46
4	Coarse	401	720	4.50	0.11	3.95	11.37
4	Intermediate	1273	2400	12.58	0.39	4.95	136.99
4	Fine	4619	8960	143.19	50.37	98.49	587.38

*Times are in seconds.

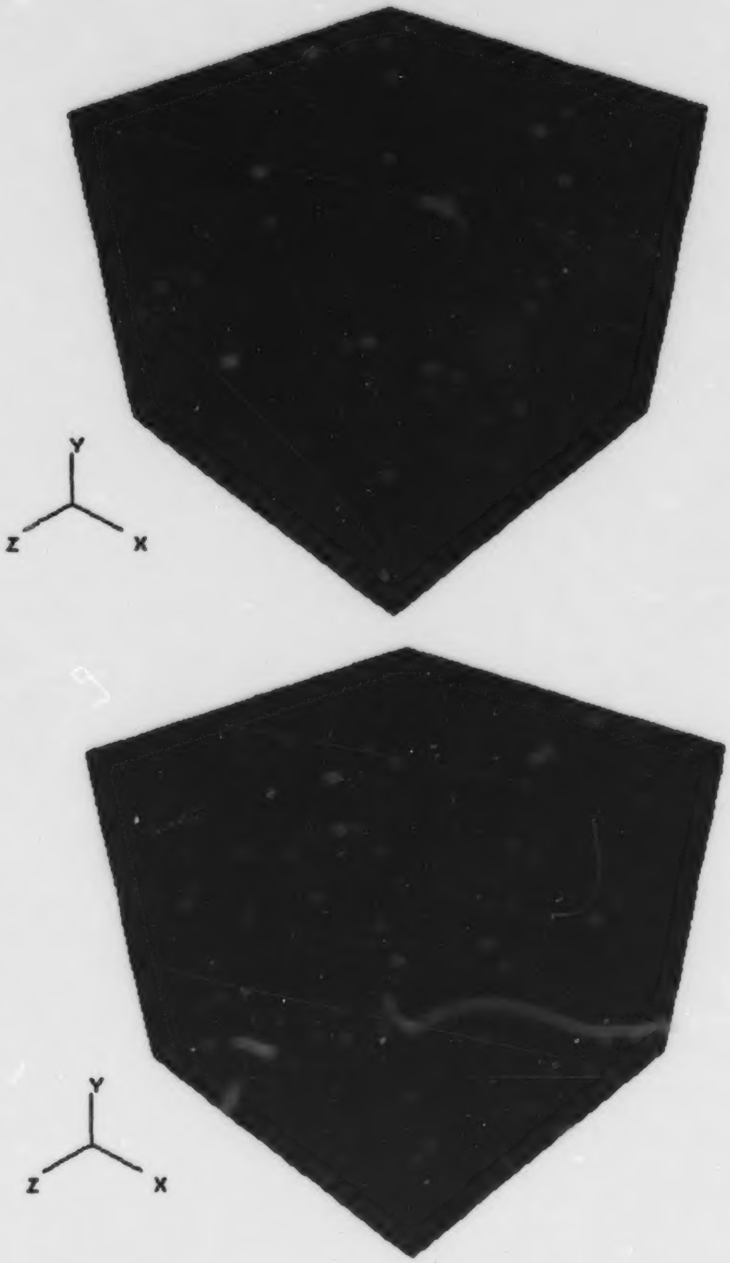

Figure 2.1: Uniform Meshes of a Cube Using the 20-Noded Solid Element.
(a) 2×2×2 Mesh. (b) 4×4×4 Mesh.

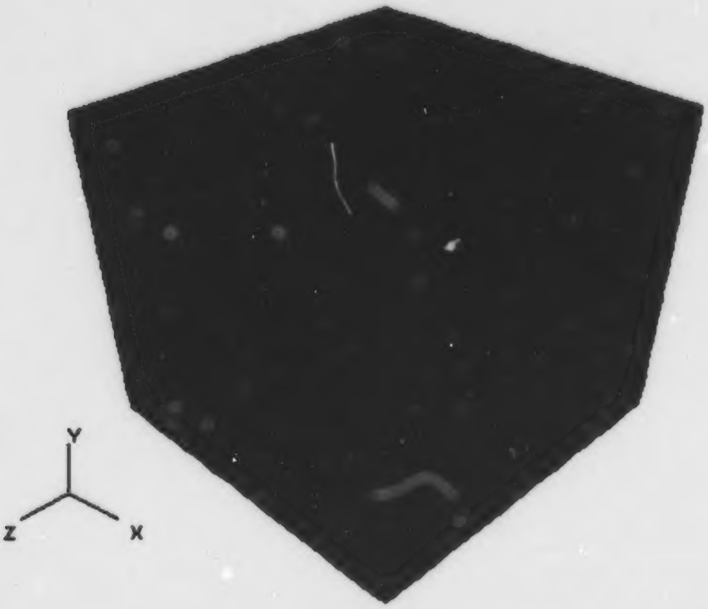

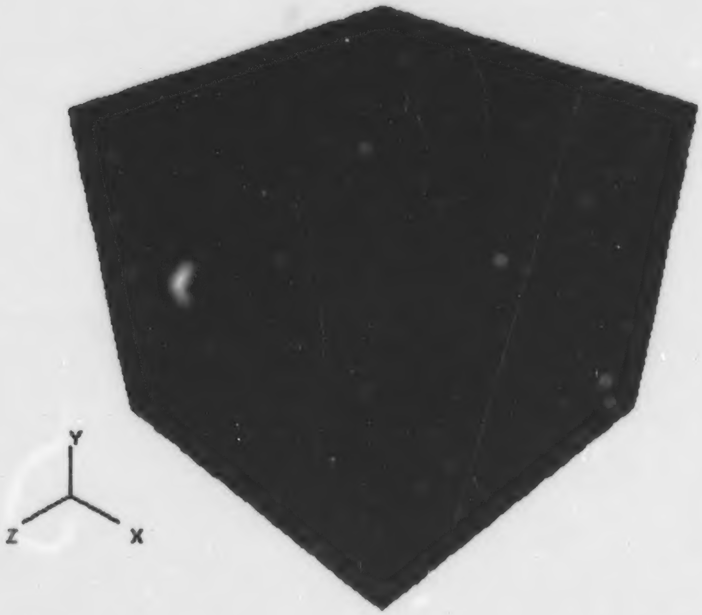

Figure 2.1(Continued): Uniform Meshes of a Cube Using the 20-Noded Solid Element. (c) 6×6×6 Mesh. (d) 8×8×8 Mesh.

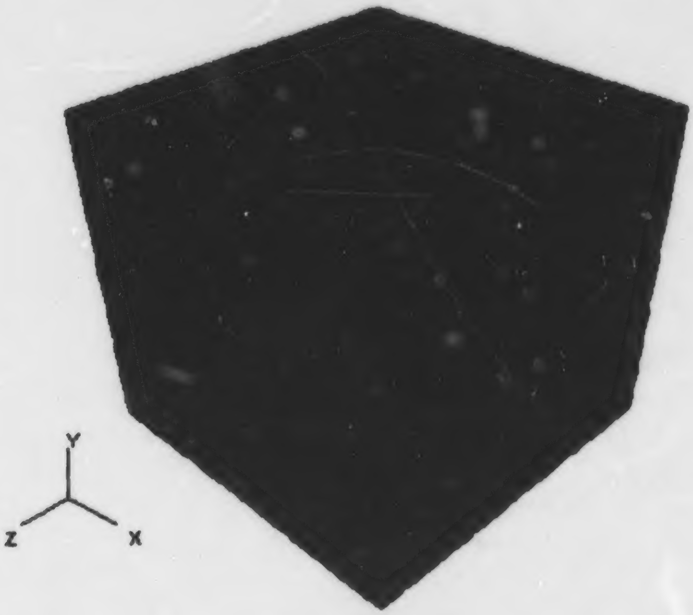

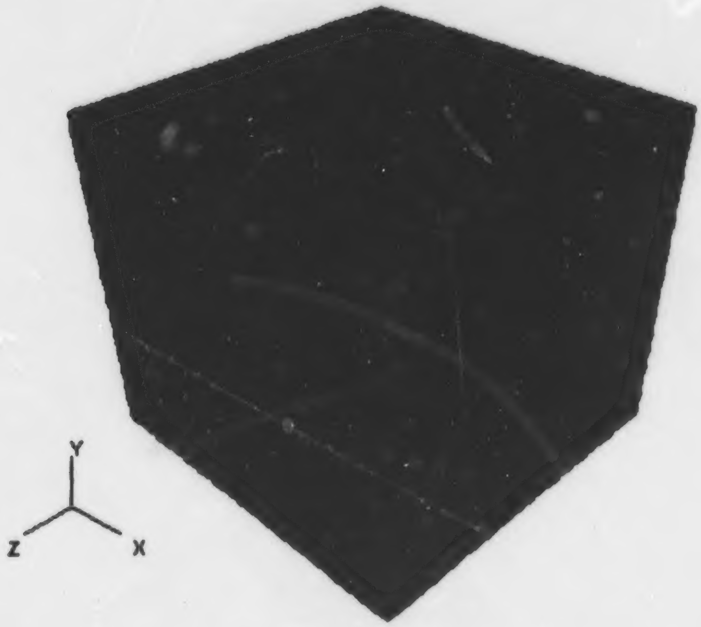

Figure 2.1(Continued): Uniform Meshes of a Cube Using the 20-Noded Solid Element.
(e) 10×10×10 Mesh. (f) 12×12×12 Mesh.

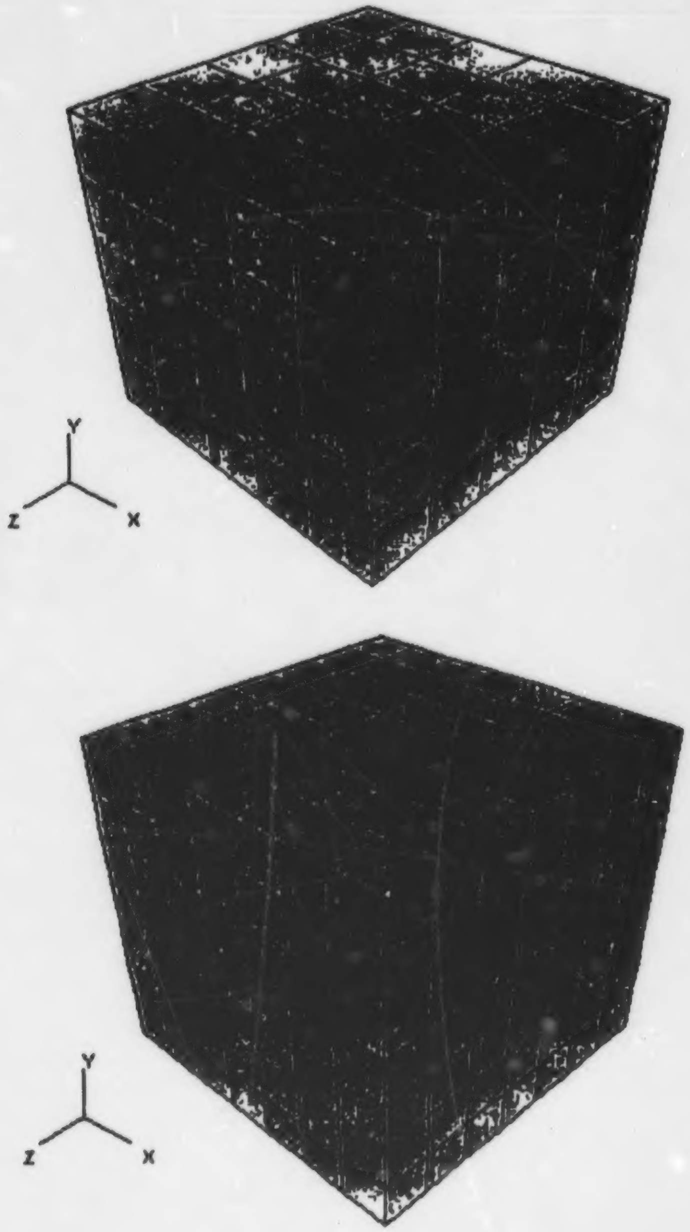

Figure 2.2: Uniform Meshes of a Cube Using the 8-Noded Solid Element.
(a) 5×5×5 Mesh. (b) 7×7×7 Mesh.

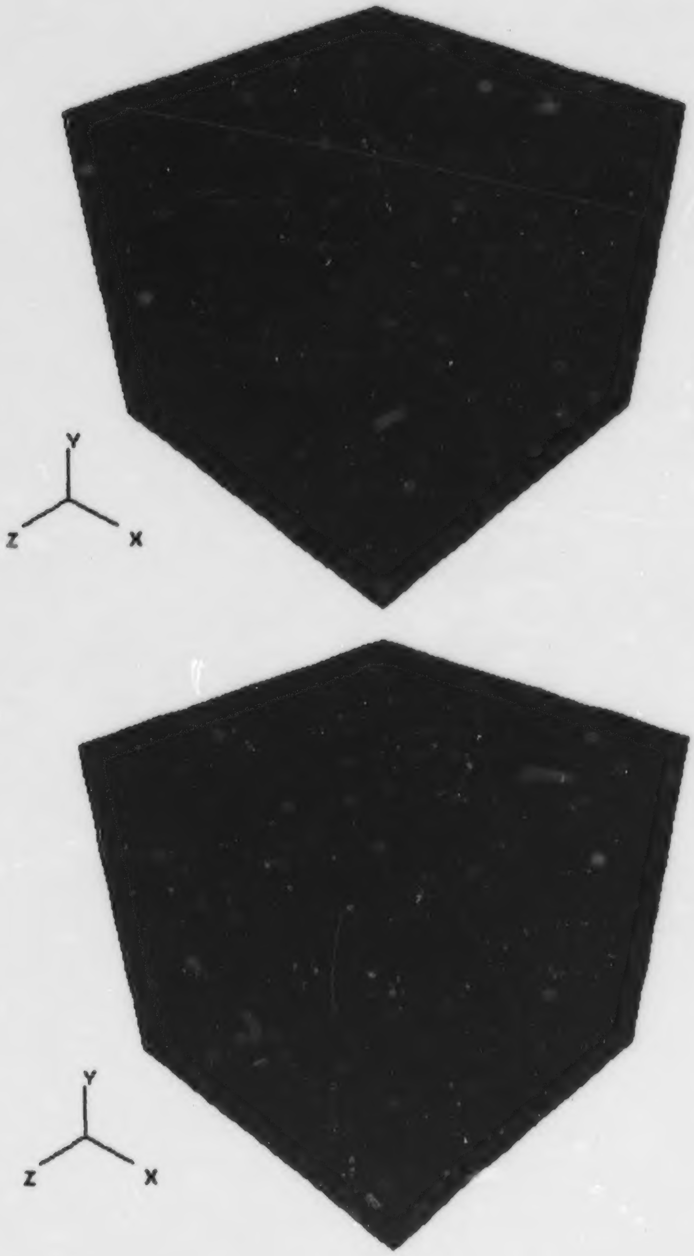

Figure 2.2(Continued): Uniform Meshes of a Cube Using the 8-Noded Solid Element. (c) 10×10×10 Mesh. (d) 14×14×14 Mesh.

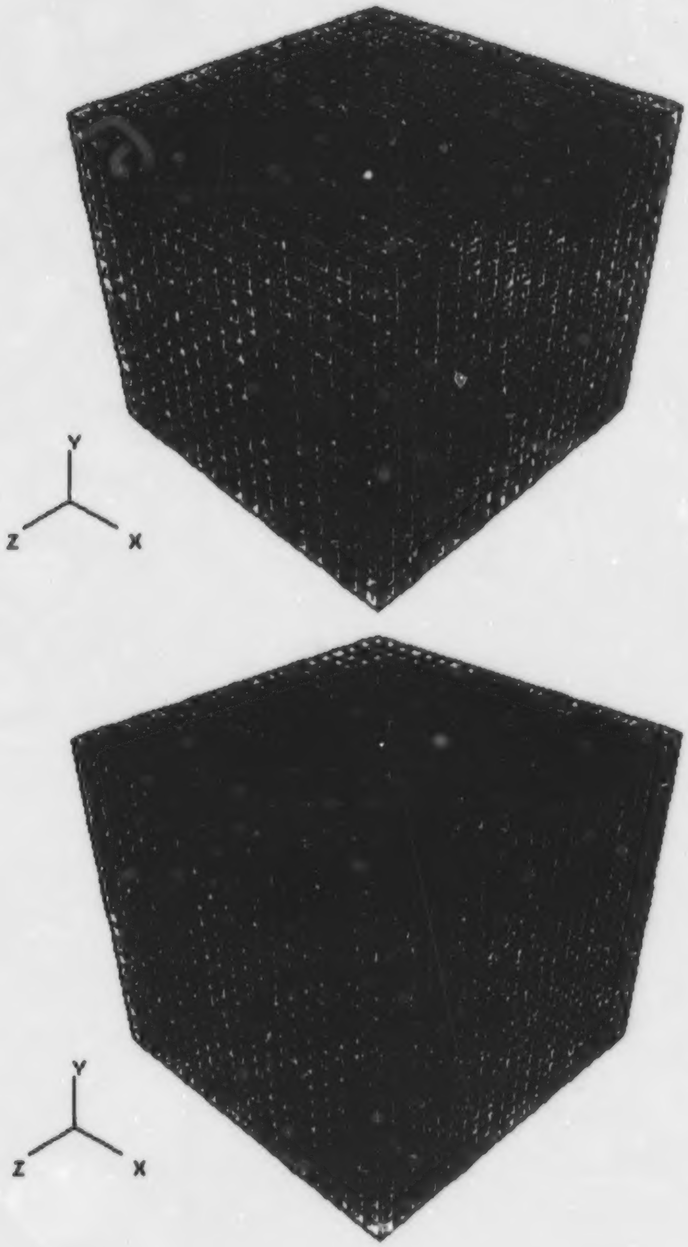

Figure 2.2(Continued): Uniform Meshes of a Cube Using the 8-Noded Solid Element. (e) 17×17×17 Mesh. (f) 20×20×20 Mesh.

Figure 2.3: 8-Noded Solid Element Meshes of the Cube With Severe Aspect Ratios. (a) 4×4×30 Mesh, Aspect Ratio 7.5:7.5:1. (b) 12×12×60 Mesh, Aspect Ratio 5:5:1.

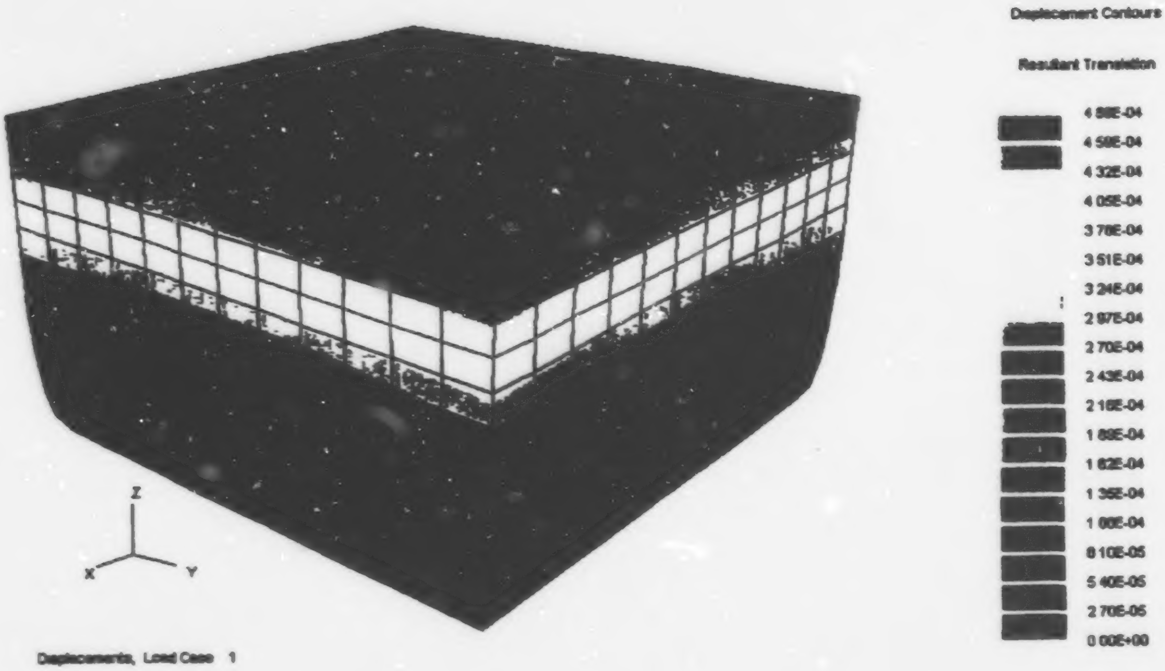
Displacement Contours
Resultant Translation
4.86E-04
4.59E-04
4.32E-04
4.05E-04
3.78E-04
3.51E-04
3.24E-04
2.97E-04
2.70E-04
2.43E-04
2.16E-04
1.89E-04
1.62E-04
1.35E-04
1.08E-04
8.10E-05
5.40E-05
2.70E-05
0.00E+00
Z
X
Y
Displacements, Load Case 1

Figure 2.4: Final Deformed Configurations of the Cube Predicted by Various Meshes.
(a) 12×12×12 Mesh of 20-Noded Solid Element.

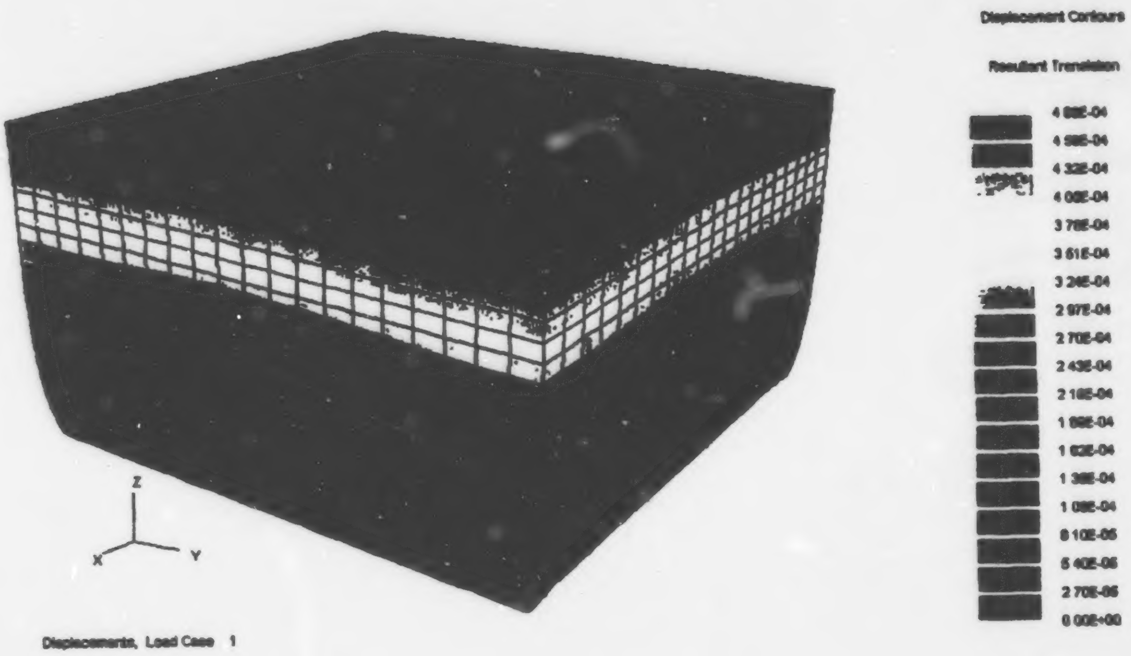
Displacement Contours
Resultant Translation
4.86E-04
4.59E-04
4.32E-04
4.05E-04
3.78E-04
3.51E-04
3.24E-04
2.97E-04
2.70E-04
2.43E-04
2.16E-04
1.89E-04
1.62E-04
1.35E-04
1.08E-04
8.10E-05
5.40E-05
2.70E-05
0.00E+00
Z
X
Y
Displacements, Load Case 1

Figure 2.4(Continued): Final Deformed Configurations of the Cube Predicted by Various Meshes. (b) 20×20×20 Mesh of 8-Noded Solid Element.

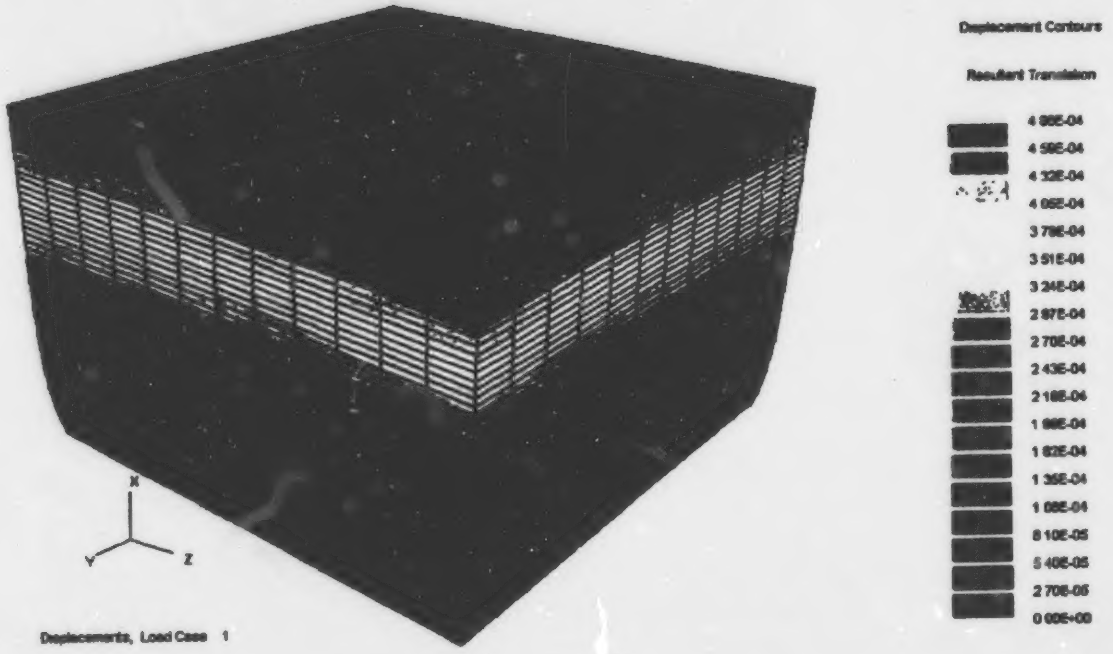
Displacement Contours
Resultant Translation
4 86E-04
4 59E-04
4 32E-04
4 05E-04
3 78E-04
3 51E-04
3 24E-04
2 97E-04
2 70E-04
2 43E-04
2 16E-04
1 89E-04
1 62E-04
1 35E-04
1 08E-04
8 10E-05
5 40E-05
2 70E-05
0 00E+00
X
Y
Z
Displacements, Load Case 1

Figure 2.4(Continued): Final Deformed Configurations of the Cube Predicted by Various Meshes. (c) 12×12×60 Mesh of 8-Noded Solid Element.

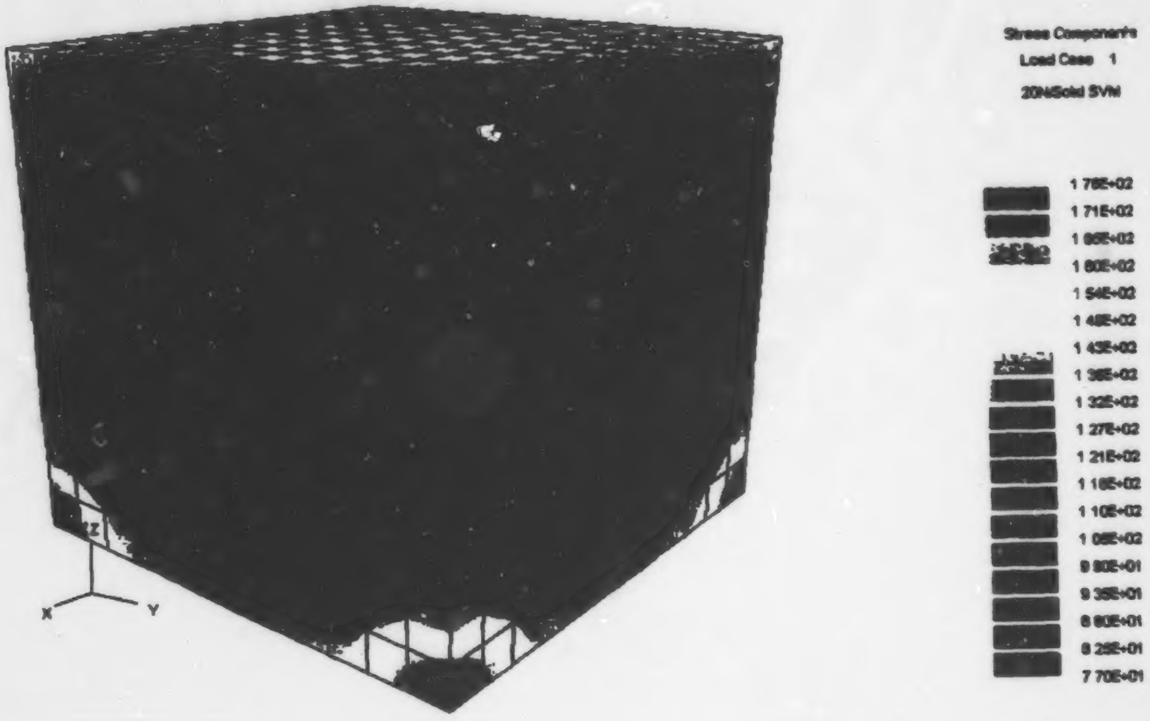

Figure 2.5: Von Mises Stress Distribution in the Cube Predicted by Various Meshes.
(a) 12×12×12 Mesh of 20-Noded Solid Element.

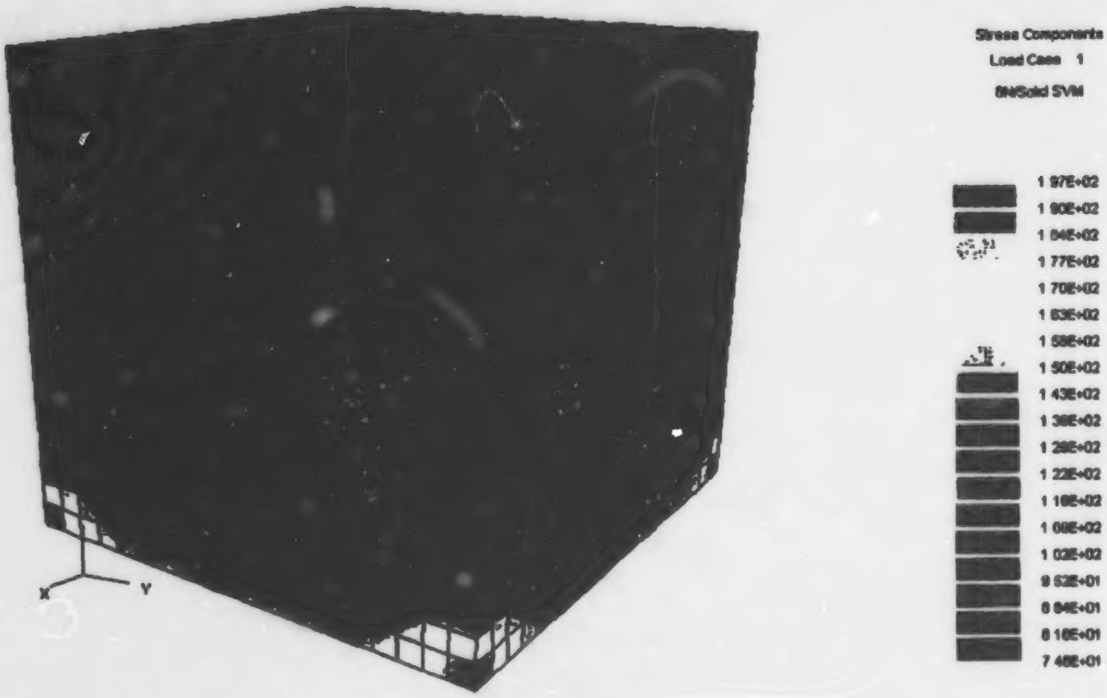
X
Y
Stress Components
Load Case 1
8N/Solid SVM
1.97E+02
1.90E+02
1.84E+02
1.77E+02
1.70E+02
1.63E+02
1.56E+02
1.50E+02
1.43E+02
1.36E+02
1.29E+02
1.22E+02
1.16E+02
1.09E+02
1.02E+02
9.52E+01
8.84E+01
8.16E+01
7.48E+01

Figure 2.5(Continued): Von Mises Stress Distribution in the Cube Predicted by Various Meshes. (b) 20×20×20 Mesh of 8-Noded Solid Element.

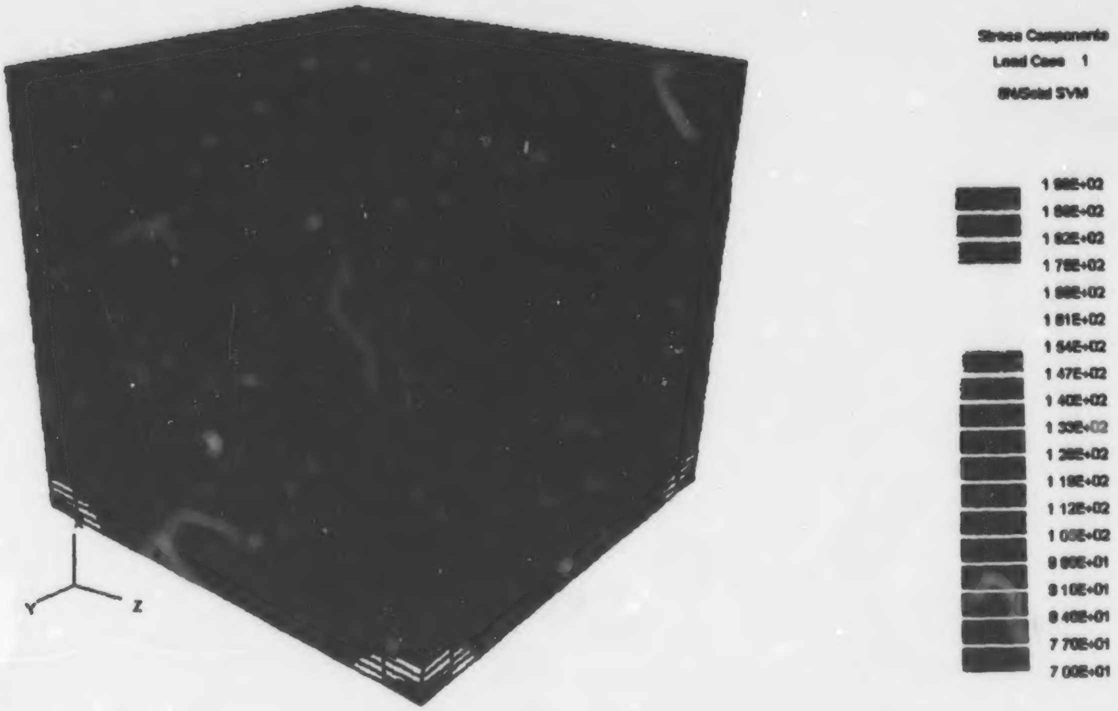
Y
Z
Stress Components
Load Case 1
8N/Solid SVM
1 96E+02
1 89E+02
1 82E+02
1 75E+02
1 68E+02
1 61E+02
1 54E+02
1 47E+02
1 40E+02
1 33E+02
1 26E+02
1 19E+02
1 12E+02
1 05E+02
9 80E+01
9 10E+01
8 40E+01
7 70E+01
7 00E+01

Figure 2.5(Continued): Von Mises Stress Distribution in the Cube Predicted by Various Meshes. (c) 12×12×60 Mesh of 8-Noded Solid Element.

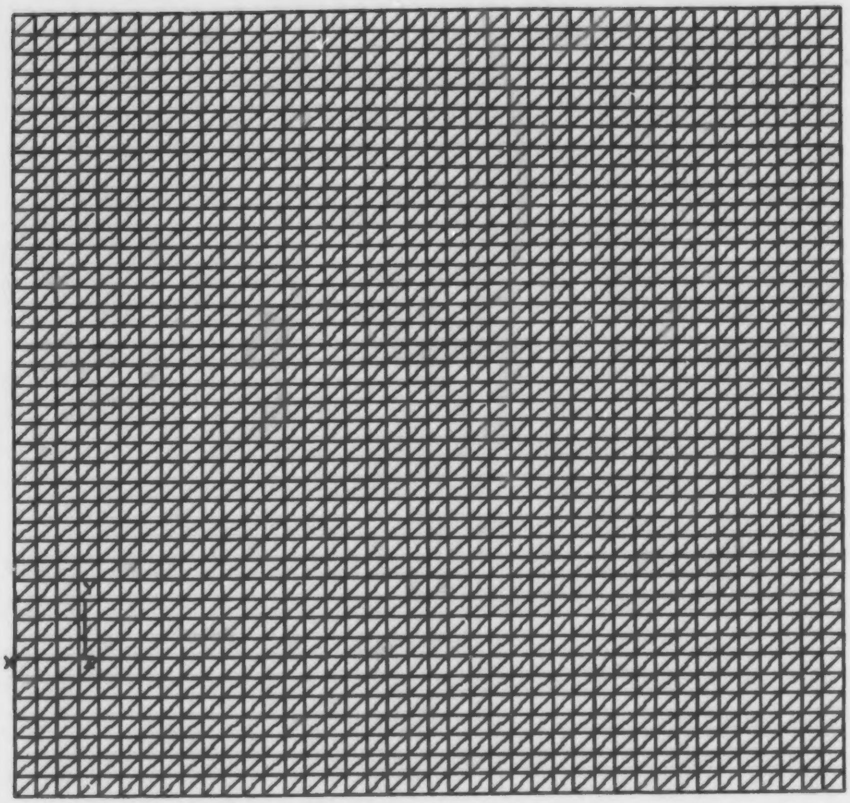

Figure 2.6: A Cantilevered Square Plate Modeled by 3-Noded Triangular Plate Elements.

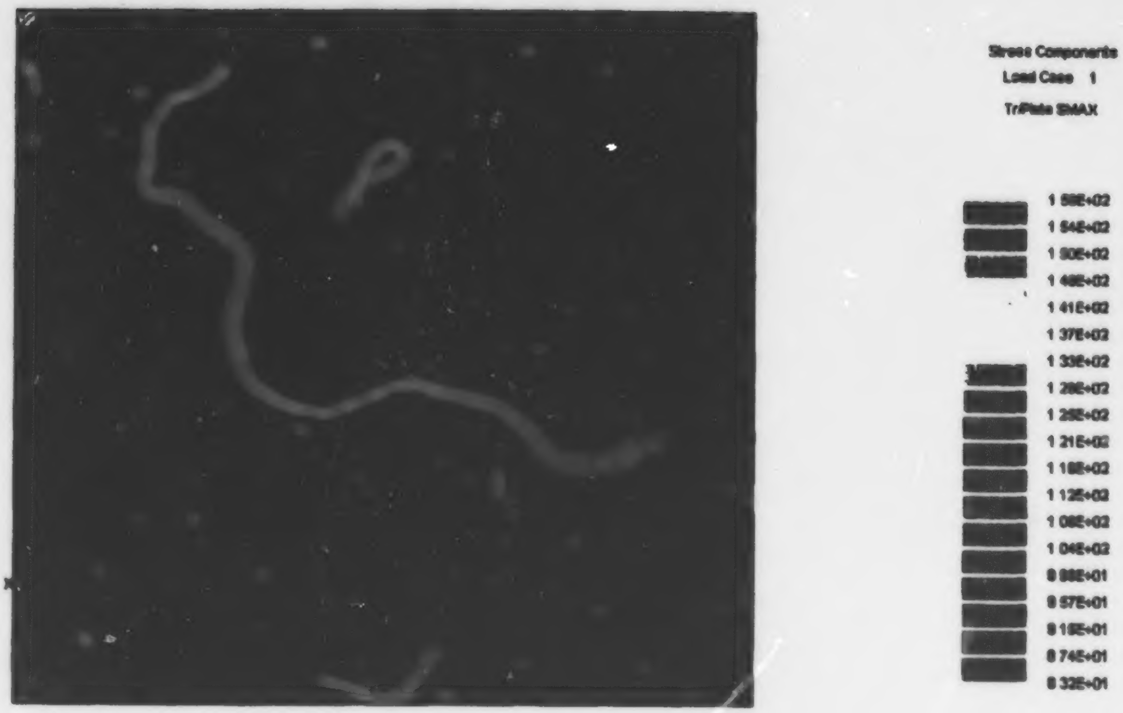
Stress Components
Load Case 1
TriPlate SMAX
1.58E+02
1.54E+02
1.50E+02
1.46E+02
1.41E+02
1.37E+02
1.33E+02
1.29E+02
1.25E+02
1.21E+02
1.16E+02
1.12E+02
1.08E+02
1.04E+02
9.98E+01
9.57E+01
9.15E+01
8.74E+01
8.32E+01

Figure 2.7: Von Mises Stress Distribution in Mid Surface of the Plate Caused by Uniform In-plane Edge Force.

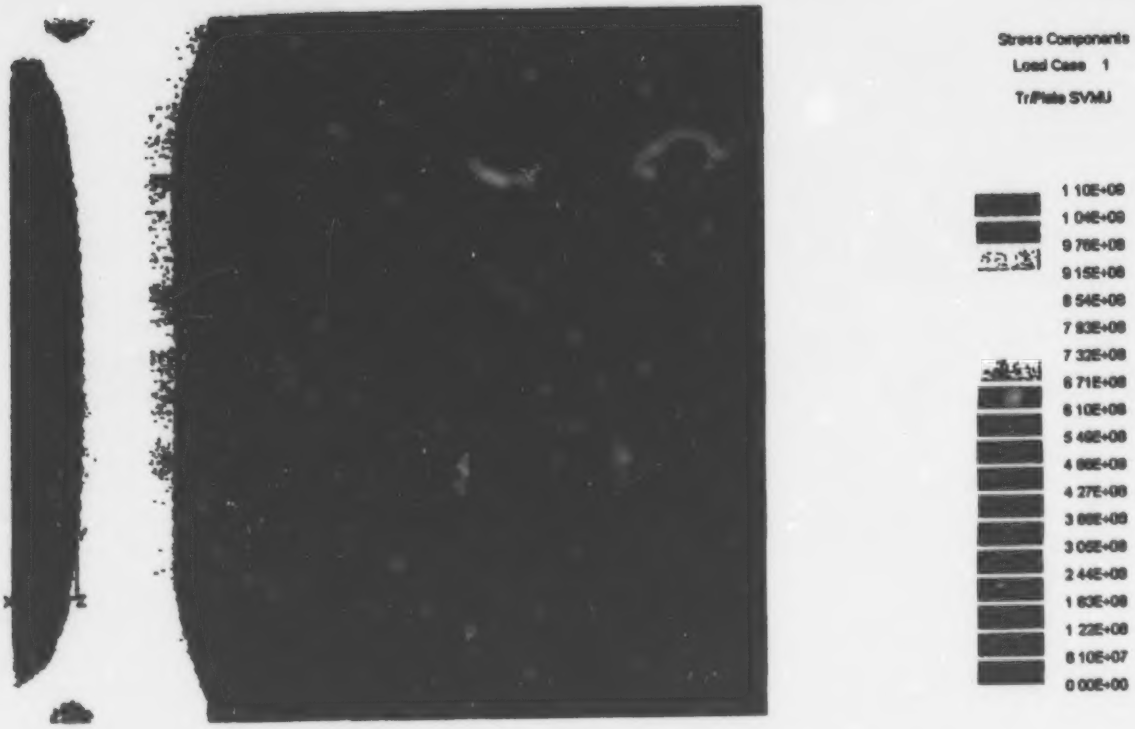

Figure 2.8: Von Mises Stress Distribution in Upper Surface of the Plate Caused by Uniform Transverse Edge Force.

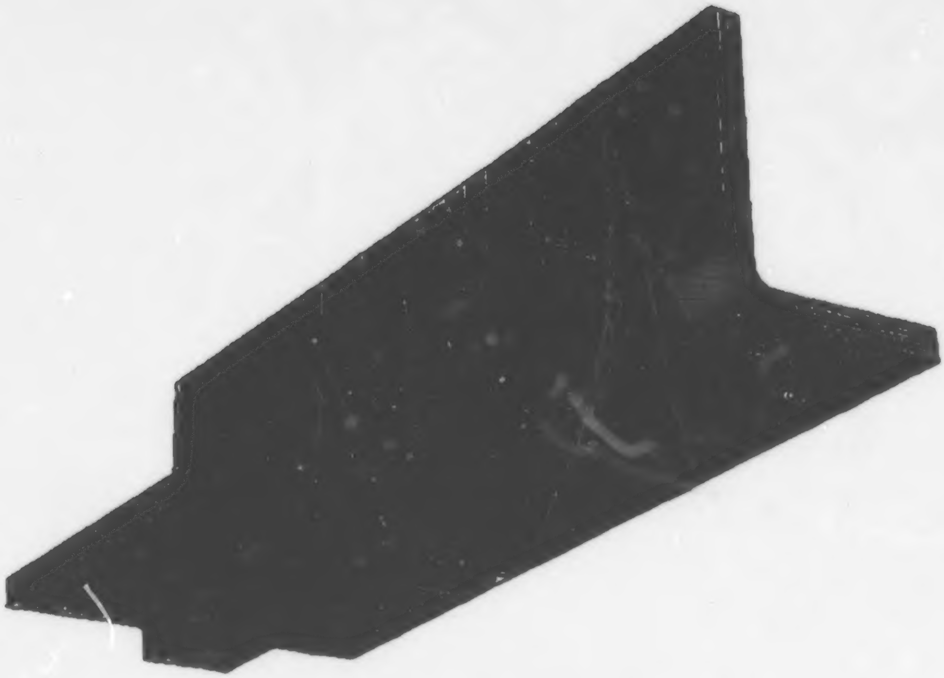

Figure 2.9: A Lower Spar Cap in Airplane Wing Modeled by 8-Noded Solid Elements.

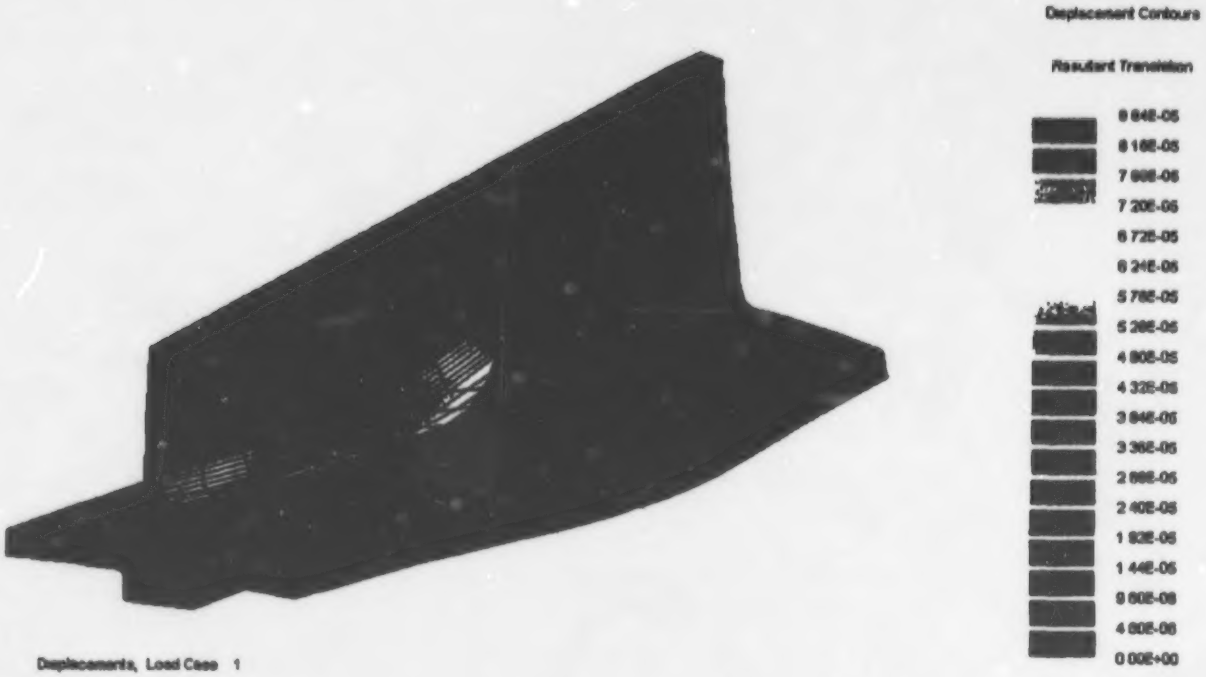
Displacement Contours
Resultant Translation
8 64E-05
8 16E-05
7 68E-05
7 20E-05
6 72E-05
6 24E-05
5 76E-05
5 28E-05
4 80E-05
4 32E-05
3 84E-05
3 36E-05
2 88E-05
2 40E-05
1 92E-05
1 44E-05
9 60E-06
4 80E-06
0 00E+00
Displacements, Load Case 1

Figure 2.10: Final Deformed Configuration of the Lower Spar Cap.

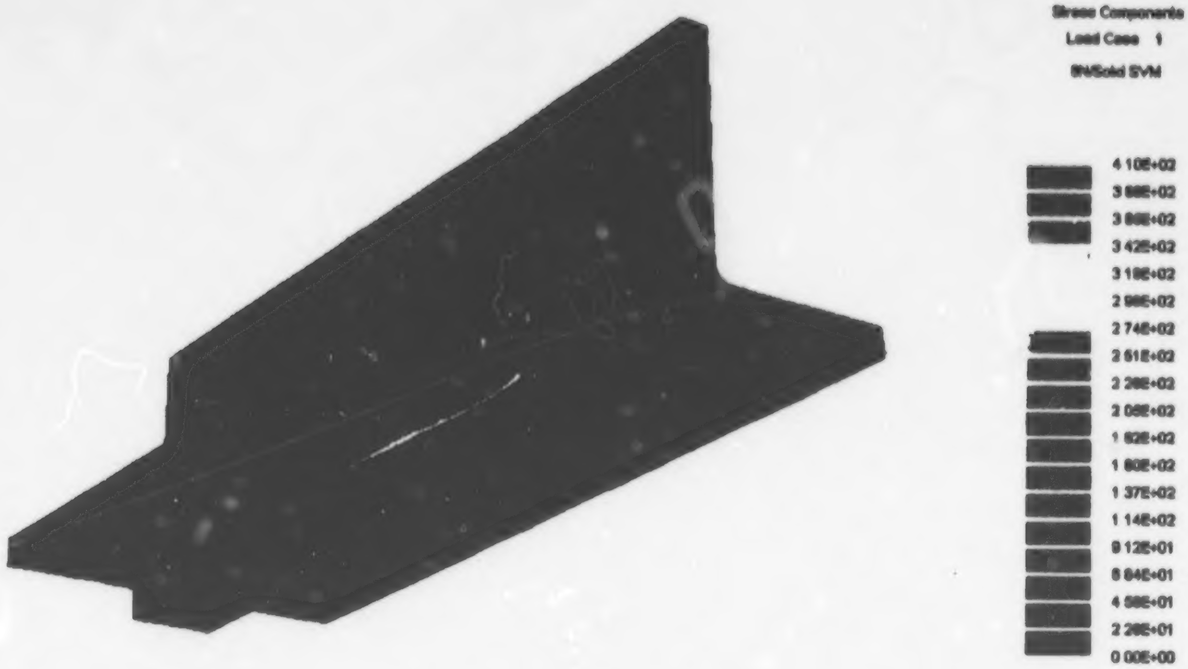
Stress Components
Load Case 1
8N/Solid SVM
4 10E+02
3 87E+02
3 65E+02
3 42E+02
3 19E+02
2 96E+02
2 74E+02
2 51E+02
2 28E+02
2 05E+02
1 82E+02
1 60E+02
1 37E+02
1 14E+02
9 12E+01
6 84E+01
4 56E+01
2 28E+01
0 00E+00

Figure 2.11: Von Mises Stress Distribution in the Lower Spar Cap.

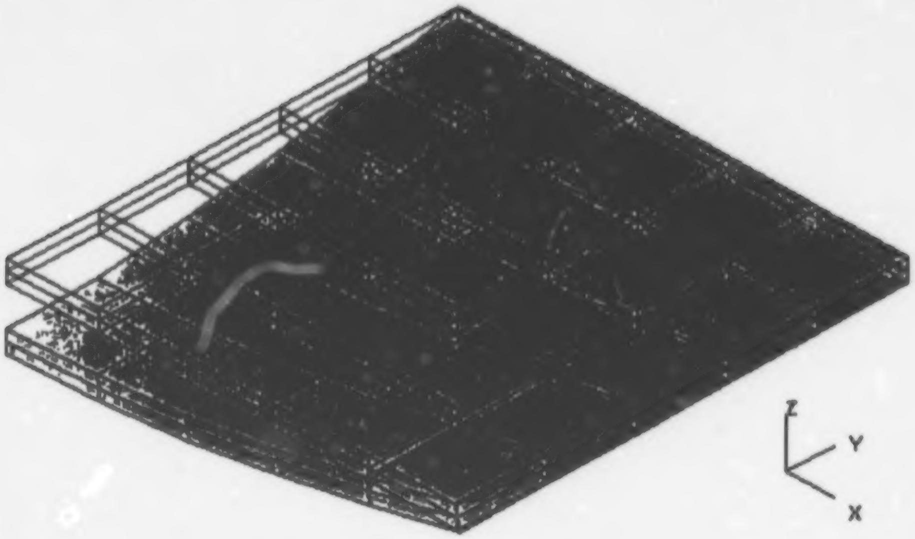
Z
Y
X

Displacements, Load Case 1

Figure 2.12: Original and Deformed Configuration of a Simply Supported Plate Subjected to Uniform Pressure Modeled by 8-Noded Solid Elements.
(a) 5×5×2 Mesh.

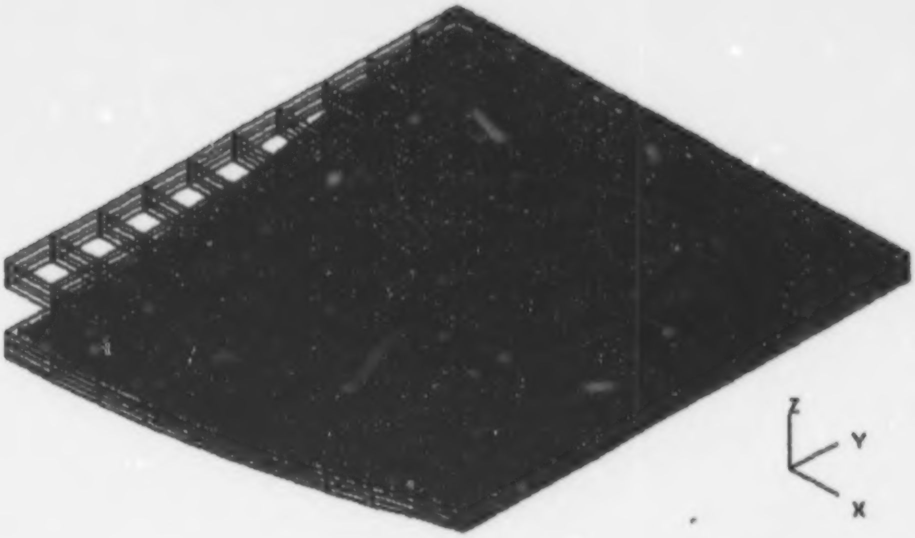

Displacements, Load Case 1:

Figure 2.12(Continued): Original and Deformed Configuration of a Simply Supported Plate Subjected to Uniform Pressure Modeled by 8-Noded Solid Elements.
(b) 10×10×4 Mesh.

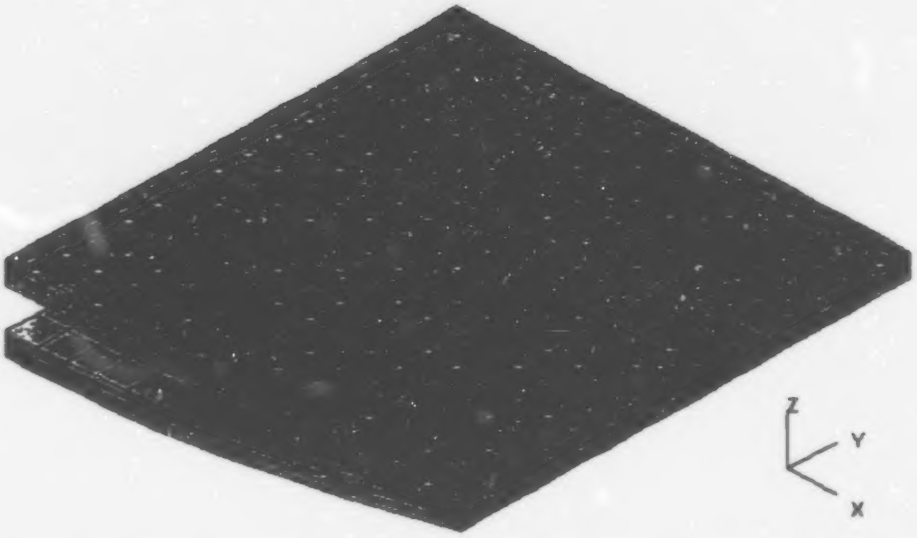

Displacements, Load Case 1

Figure 2.12(Continued): Original and Deformed Configuration of a Simply Supported Plate Subjected to Uniform Pressure Modeled by 8-Noded Solid Elements.
(c) 15×15×6 Mesh.

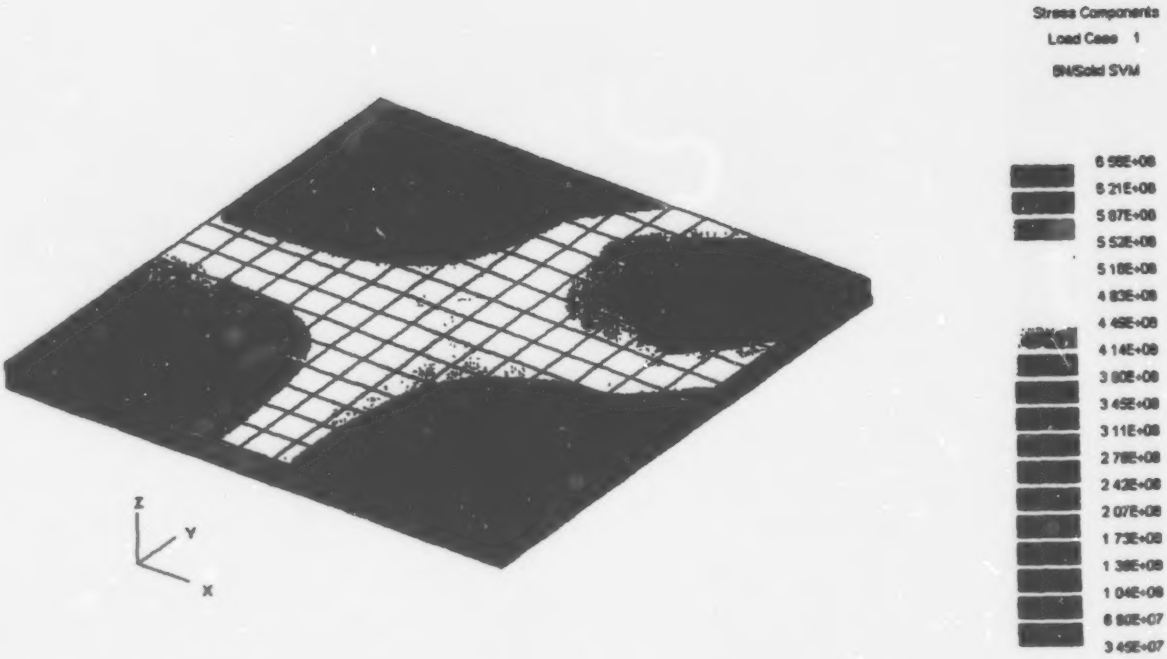

Figure 2.13: Von Mises Stress Distribution in the Simply Supported Plate Predicted by the 15×15×6 Mesh of the 8-Noded Solid Element.

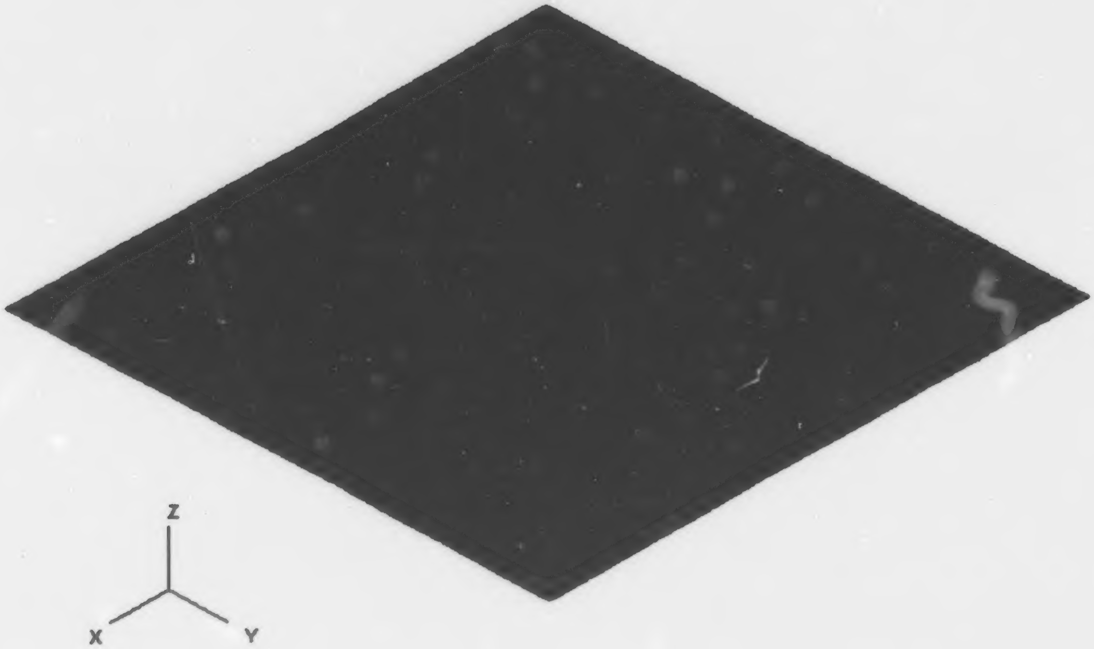

Figure 2.14: 3-Noded Triangular Plate Element Meshes of the Simply Supported Plate. (a) 10×10 Mesh.

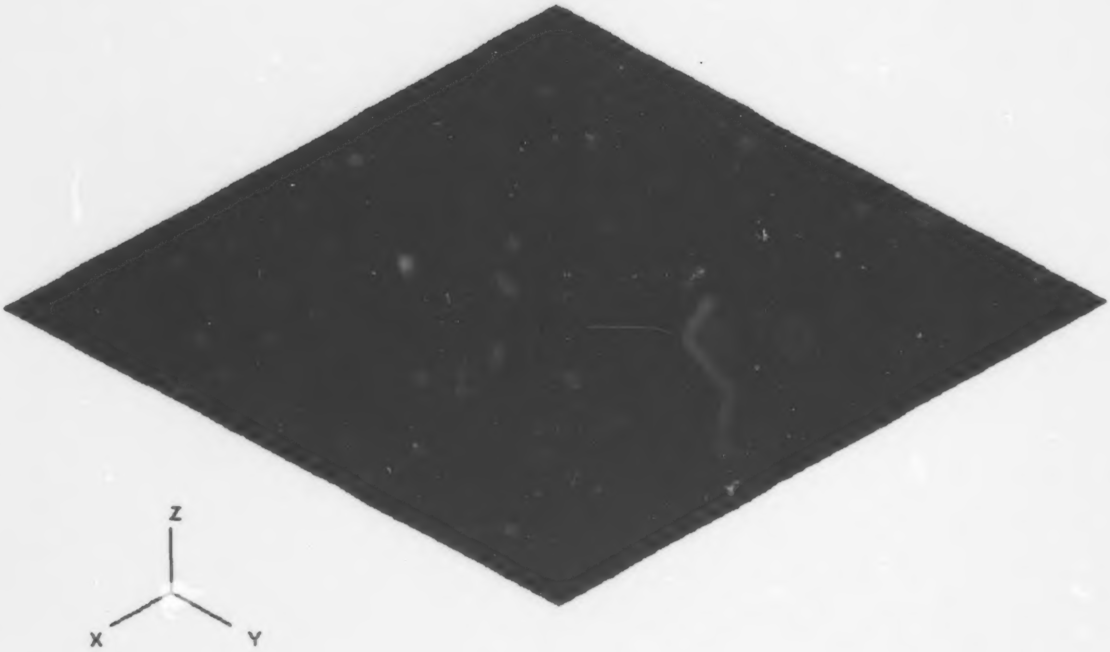

Figure 2.14(Continue): 3-Noded Triangular Plate Element Meshes of the Simply Supported Plate. (b) 20×20 Mesh.

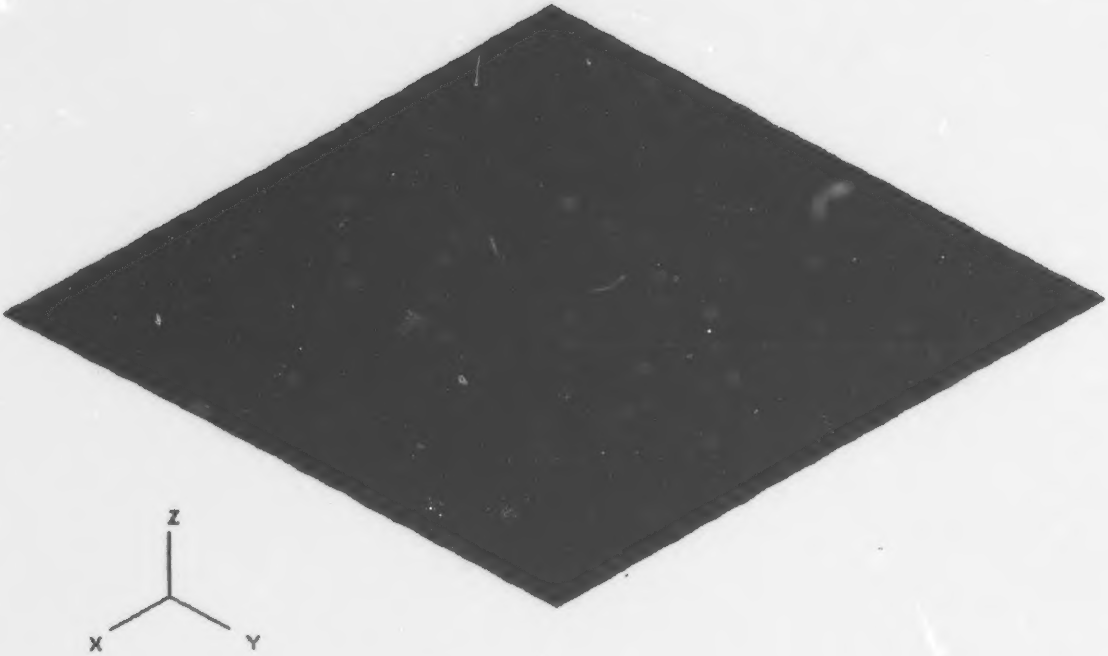

Figure 2.14(Continued): 3-Noded Triangular Plate Element Meshes of the Simply Supported Plate. (c) 40×40 Mesh.

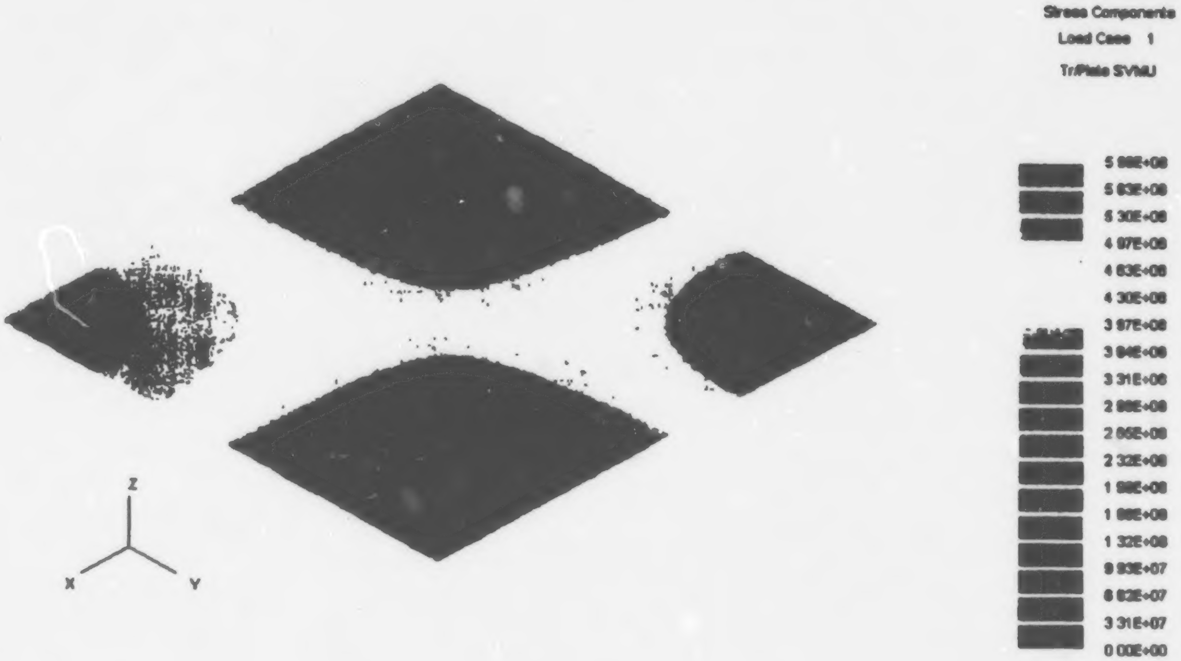

Figure 2.15: Von Mises Stress Distribution in the Simply Supported Plate Predicted by the 40×40 Mesh of the 3-Noded Triangular Plate Element.

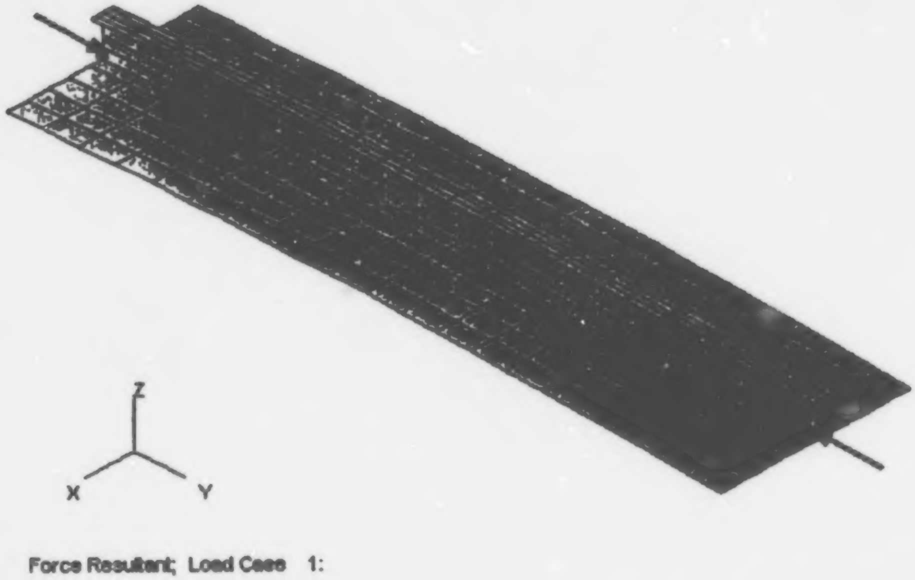
Z
X
Y
Force Resultant; Load Case 1:

Figure 2.16: 4-Noded Quadrilateral Shell Element Meshes of a Typical Stiffened Panel. (a) Coarse Mesh.

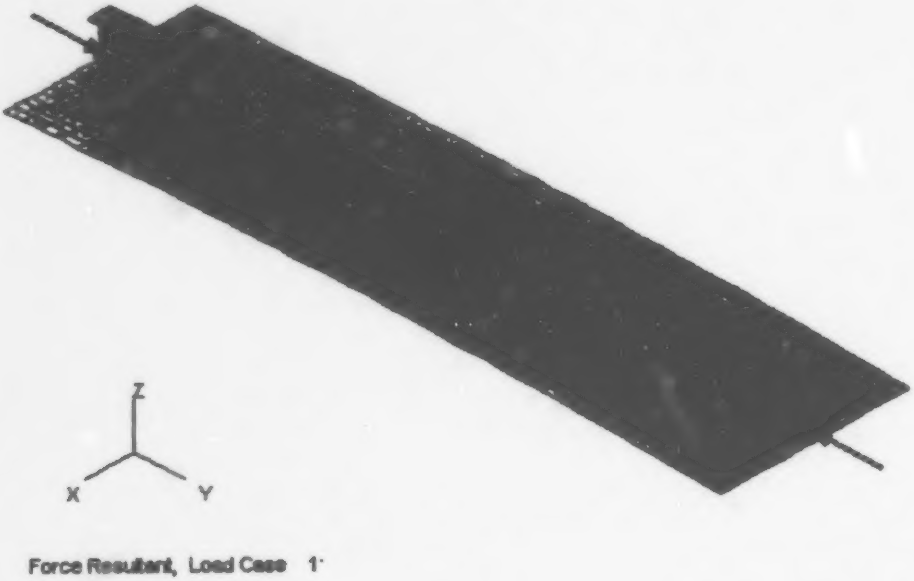
Z
X
Y
Force Resultant, Load Case 1

Figure 2.16(Continued): 4-Noded Quadrilateral Shell Element Meshes of a Typical Stiffened Panel. (b) Intermediate Mesh.

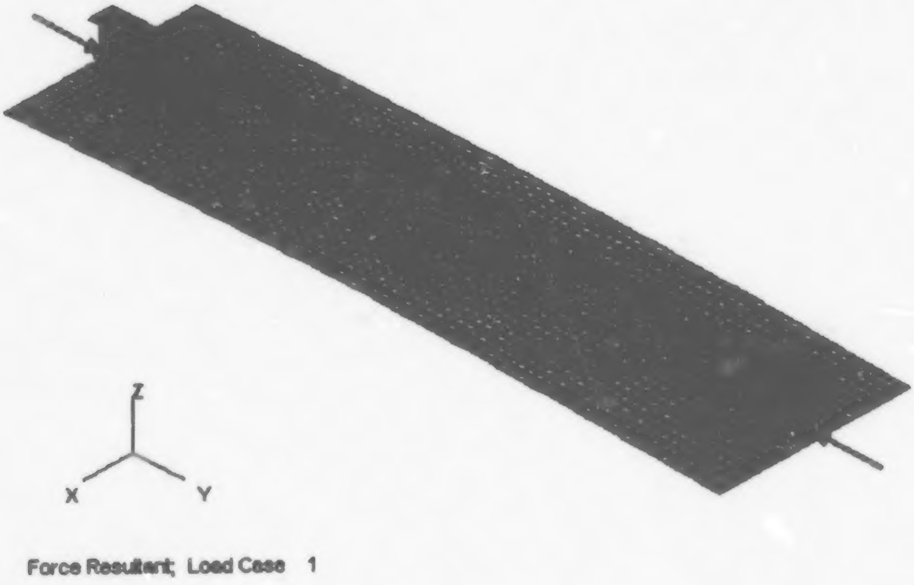
Z
X
Y
Force Resultant; Load Case 1

Figure 2.16(Continued): 4-Noded Quadrilateral Shell Element Meshes of a Typical Stiffened Panel. (c) Fine Mesh.

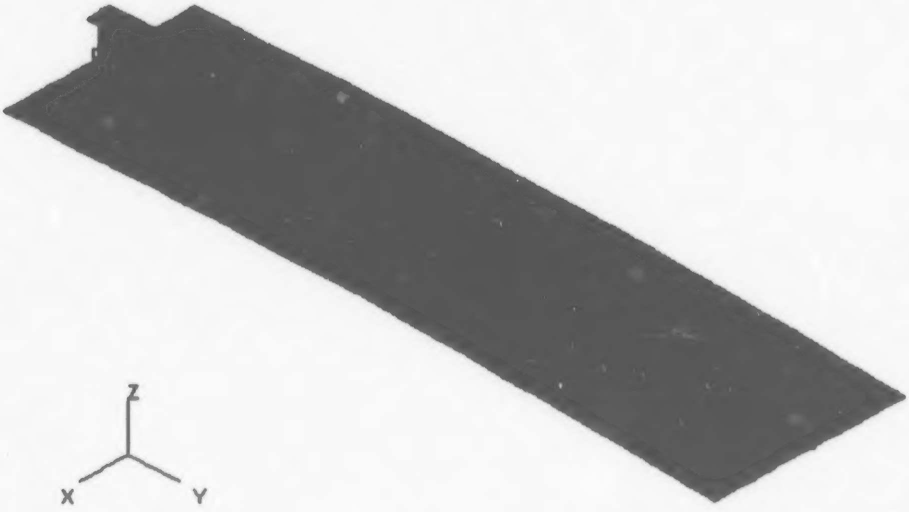

Figure 2.17: 3-Noded Triangular Plate/Shell Element Meshes of a Typical Stiffened Panel. (a) Coarse Mesh.

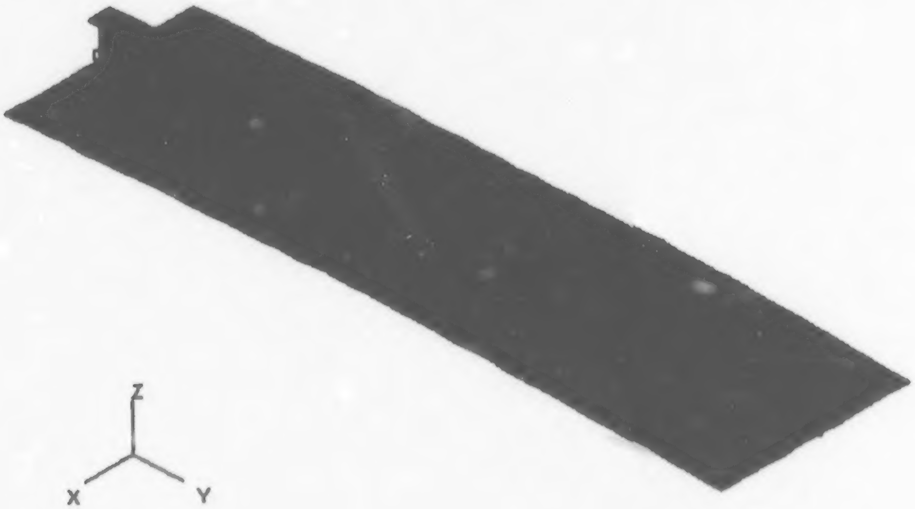

Figure 2.17(Continued): 3-Noded Triangular Plate/Shell Element Meshes of a Typical Stiffened Panel. (b) Intermediate Mesh.

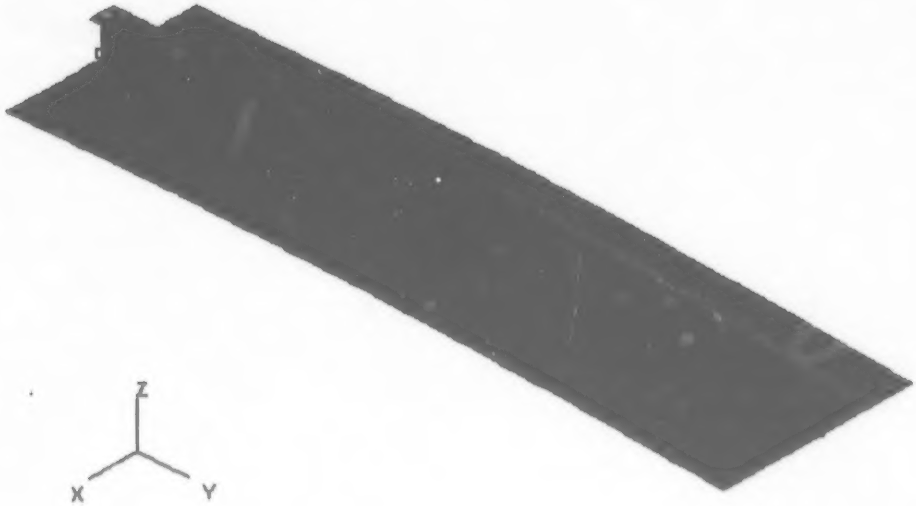

Figure 2.17(Continued): 3-Noded Triangular Plate/Shell Element Meshes of a Typical Stiffened Panel. (c) Fine Mesh.

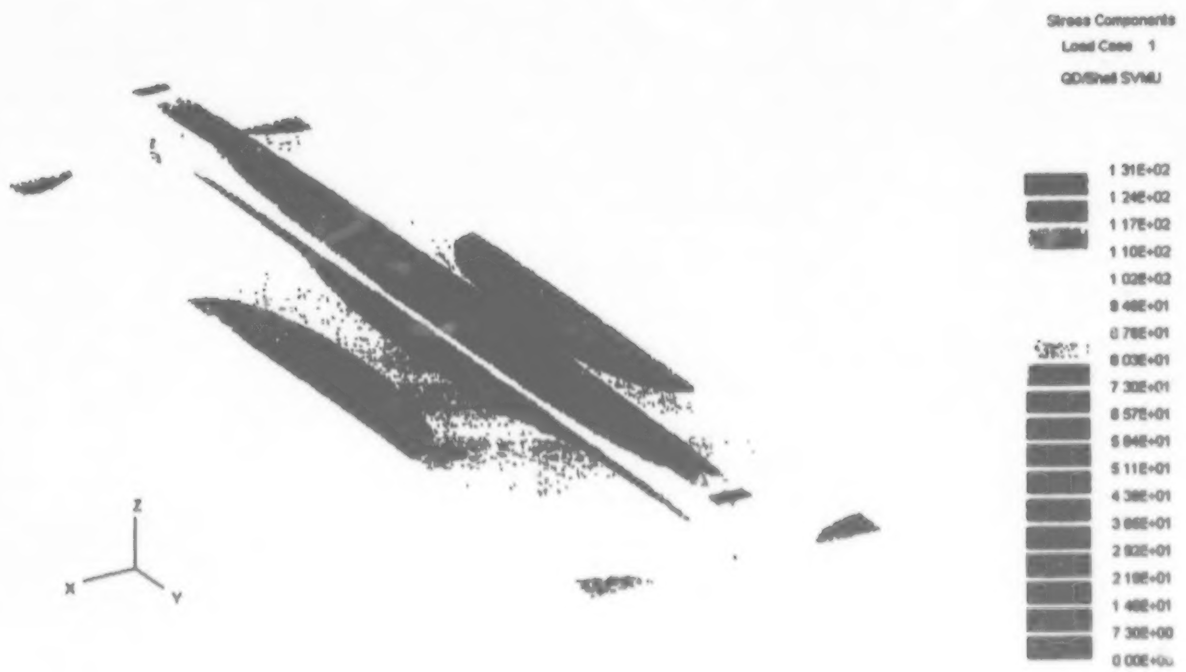

Figure 2.18: Von Mises Stress Distribution in the Stiffened Panel Predicted by the Fine Mesh of the Stiffened Panel.

3. DEVELOPMENT OF A THERMAL STRESS ANALYSIS CAPABILITY IN VAST FOR AUTOMATIC GENERATION OF RESIDUAL STRESSES FOR NON-LINEAR ANALYSIS OF STIFFENED PANELS

3.1 Development of a Thermal Stress Analysis Capability in VAST

One of the purposes of developing a thermal stress analysis capability in the VAST finite element program was to generate self-equilibrium, consistent residual stress distributions for load-shortening calculations of stiffened panels with large geometric imperfections. In load-shortening curve computations for stiffened panels, a block-form distribution of the residual stresses is commonly used to approximate the residual stress field due to welding. In this idealized residual stress distribution, constant uni-axial tensile stresses is assumed in the plate around the plate-web junction, whereas constant compressive stresses is assumed elsewhere in the plate. The web and flange are assumed residual stress free. Due to its simplicity, this idealized residual stress pattern is very easy to use in nonlinear analysis. However, with the increase of the imperfection level, this pattern becomes progressively more non-self-equilibrating and causes significant errors in the predicted load-shortening characteristics [3.1, 3.2]. Consider a stiffened panel with geometric parameters as:

$$\beta=4.0,\ \lambda=0.3,\ A_S/A=0.2 \text{ and } \omega_0=0.3\beta^2 t$$

where β indicates the plate slenderness ratio; λ the column slenderness ratio; ω_0 the maximum initial imperfection at plate center; and A_S, A the cross-sectional areas of the stiffener and the stiffened panel, respectively. As demonstrated in an earlier report [3.2], the non-self-equilibrated residual stress field produced significant initial deformations which resulted in a negative axial load at the beginning of the predicted load-shortening curve. In addition, this initial deformation considerably changed the form of the prescribed initial geometric imperfection. For geometric imperfection sensitive structures, such as axially loaded stiffened panels, small changes in initial imperfections could result in completely different nonlinear failure mechanisms.

It has been discovered that a more realistic residual stress distribution can be generated by simulating the material cool-down process following welding by performing a thermal stress analysis [3.3]. In this analysis, negative temperature variations are prescribed at both the plate-web and flange-web junctions. As a result, tensile stresses are generated in those regions and compressive stresses are generated automatically in the rest of the stiffened panel to achieve equilibrium. In the original procedure described in Reference [3.3], fully nonlinear thermal stress analyses were utilized in which geometric and material nonlinearities caused by the thermal load were taken into account. Because the generated residual stresses were in self-equilibrium with respect to the final deformed configuration, which included both the initial imperfections and the deformations caused by the thermal loads, two thermal stress analyses had to be performed to obtain the self-equilibrated residual stress field while preserving the original geometric imperfections. However, due to the fact that the maximum tensile residual stress should not exceed the yield stress and the additional deformation caused by the thermal load is usually small, we could argue that a fully nonlinear, elastic-plastic thermal stress analysis is unnecessary for the purpose of generating residual stresses. Consequently, a simplified and more efficient method was developed in the present work which requires only one linear thermal stress analysis, and in which the generated residual stress patterns are self-equilibrated with respect to the initial configuration of stiffened panels.

In order to derive the finite element formulation for thermal stress computations, the coupled thermal-mechanical constitutive relations must first be considered. For linear elastic isotropic material, these constitutive equations can be expressed as:

F2

$$
\begin{aligned}
\varepsilon_x &= \frac{1}{E}\left(\sigma_x - \nu\sigma_y - \nu\sigma_z\right) + \alpha T \\
\varepsilon_y &= \frac{1}{E}\left(\sigma_y - \nu\sigma_z - \nu\sigma_x\right) + \alpha T \\
\varepsilon_z &= \frac{1}{E}\left(\sigma_z - \nu\sigma_x - \nu\sigma_y\right) + \alpha T \\
\tau_{xy} &= \frac{1}{G}\gamma_{xy} \\
\tau_{yz} &= \frac{1}{G}\gamma_{yz} \\
\tau_{zx} &= \frac{1}{G}\gamma_{zx}
\end{aligned}
\tag{3.1}
$$

where ε, γ denote normal and shear strains, and σ, τ indicate the normal and shear stresses, respectively. E indicates the Young's modulus; ν, the Poisson's ratio and G, the shear modulus defined by:

$$
G = \frac{E}{2(1+\nu)}. \tag{3.2}
$$

The thermal strains are calculated as the product of the coefficient of thermal expansion, α, and the temperature variation from the reference state, T. The coefficient of thermal expansion is a material property and can be obtained by appropriate experiments for different materials. At this point, it is worthwhile pointing out that the coupling between the mechanical and thermal fields is a one way coupling, since temperature changes in structures often cause significant stresses, while on the other hand, the geometric variation caused by strains is normally small and has a negligible effect on the heat transfer solutions.

In the constitutive equation given in Equation (3.1), the total strains are expressed as summation of mechanical strains and thermal strains. Of those, only the mechanical strains are related to the stress field. However, the constitutive relations shown in Equation (3.1) are not yet in a form that can be readily used in finite element derivations. Following the standard procedure, stresses can be written in terms of strains and in matrix form as:

$$\sigma = D\left(\varepsilon - \varepsilon^{th}\right) \tag{3.3}$$

where D is the regular elasticity matrix and the thermal strain vector can be expressed as:

$$\varepsilon^{th} = \{\alpha T \quad \alpha T \quad \alpha T \quad 0 \quad 0 \quad 0\}^T \tag{3.4a}$$

for general 3-D deformations;

$$\varepsilon^{th} = \{\alpha T \quad \alpha T \quad 0 \quad 0 \quad 0\}^T \tag{3.4b}$$

for plane stress and plate/shell applications; and

$$\varepsilon^{th} = \{(1+\nu)\alpha T \quad (1+\nu)\alpha T \quad 0 \quad 0 \quad 0\}^T \tag{3.4c}$$

for the plane strain situation.

Following the standard finite element procedure, we make use of the principle of virtual work and obtain the weak form of the equilibrium equation between internal force and external load vectors as:

$$\int_V B^T \sigma \, dV = R \tag{3.5}$$

where B denotes the strain-displacement matrix defined by:

$$\varepsilon = BU. \tag{3.6}$$

In Equation (3.6), U indicates the nodal displacement vector, and R, the external load vector. Substituting the stress-strain relations (3.3) into the above equation leads to:

$$\int B^T D\left(\varepsilon - \varepsilon^{th}\right) dV = R. \tag{3.7}$$

Separating the left hand side into two terms and moving the one associated with the thermal strain vector to the right hand side, we have:

$$\left(\int \boldsymbol{B}^T \boldsymbol{D} \boldsymbol{B}\, dV\right)\boldsymbol{U} = \boldsymbol{R} + \int \boldsymbol{B}^T \boldsymbol{D} \varepsilon^{th}\, dV . \qquad (3.8)$$

Defining the element stiffness matrix and the thermal load vector as:

$$\boldsymbol{K} = \int \boldsymbol{B}^T \boldsymbol{D} \boldsymbol{B}\, dV \quad \text{and} \quad \boldsymbol{R}^{th} = \int \boldsymbol{B}^T \boldsymbol{D} \varepsilon^{th}\, dV , \qquad (3.9a,b)$$

Equation (3.8) can be simplified as:

$$\boldsymbol{K}\boldsymbol{U} = \boldsymbol{R} + \boldsymbol{R}^{th} . \qquad (3.10)$$

From this equation, it is readily recognized that the displacement vectors associated with the thermal loads can be computed by simply adding an equivalent thermal load vector, $\boldsymbol{R}^{th}$, to the existing external load vector, $\boldsymbol{R}$. After the displacement vector is obtained, element stresses can then be computed using the constitutive equations given in (3.3). From Equation (3.7), it is evident that these thermal stresses are in self-equilibrium with respect to the initial undeformed configuration if external load vanishes.

Because of the involvement of the strain-displacement matrix in the expression of the equivalent thermal load vector as defined in Equation (3.9b), it was more appropriate to compute the thermal load vector along with the element stiffness matrix, rather than the regular load vectors. In the present work, the thermal load vectors are calculated and assembled in the element subroutines in the ELEMS1 module. The global thermal load vector is stored on an intermediate binary file and used in the DISP1 module to build the total load vector. During the implementation, it was noticed that the procedure for calculating the internal force vector and the equivalent thermal load vector are very similar. As a result, a significant portion of the computer code previously developed for internal force vector had been reused in the present development.

The specification of the thermal load applied to a structure required input of nodal temperature changes. The temperature changes at each numerical integration point could then be evaluated through the appropriate interpolation schemes. In the present implementation, three methods are provided for specifying the nodal temperature variations. The first method is to obtain them from binary temperature files generated by previous heat transfer analyses using the heat transfer program, VASTF, in the VAST program suite. Before reading the temperature information, finite element mesh parameters, such as the total number of geometric and displacement nodes, NGN and NDN, stored in the binary temperature file, are first compared with the corresponding parameters in the current structural analysis model. If they did not agree, an error message would be issued and the execution terminated. The other two methods use a text file, named PREFX.NET, which was supplied by the user. This file either contains temperature changes at each displacement node of the structural model, or temperature changes at all eight corners of solid, shell and beam elements. The later option would be very useful for modeling temperature gradients through the thickness of the structural elements. A parameter, ITHERM, has been added on the first data card under header IELEMA to indicate the existence of thermal loads. The format of the input temperature data is also controlled by ITHERM as:

- ITHERM= 1: temperature variations are supplied at displacement nodes in the .NET file provided by the user;
- ITHERM= 2: temperature variations are supplied at element corners in the .NET file;
- ITHERM=-1: temperature variations are supplied at displacement nodes in a binary file from previous heat transfer analyses.

The coefficient of thermal expansion is defined for each element group along with the other material properties.

Using the procedure outlined in the proceeding paragraphs, the thermal stress analysis capability was incorporated into seven most commonly used elements in the VAST program, including:

- IEC=1: 8-Noded Thick/Thin Shell Element;
- IEC=2: 20-Noded Solid Element;
- IEC=4: 3-Noded Triangular Plate/Shell Element;
- IEC=5: 4-Noded Quadrilateral Shell Element;
- IEC=6: 13-Noded Transition Element;
- IEC=7: 3-Noded Curved Beam Element; and
- IEC=16: 8-Noded Solid Element.

Of these element types, the 3-noded triangular plate/shell element and the 8-noded solid element provided the greatest challenge with respect to the implementation of thermal stress analysis capability. Because the triangular plate element is based on the classical plate theory, the membrane and bending strain components utilized in this element are separated and evaluated using different shape functions. In addition, direct integration was used through the thickness direction in element stiffness and internal force calculations. As a result, implementing a thermal stress capability in this element involved expressing the temperature field as explicit functions of the through-the-thickness coordinate, z. On the other hand, the implementation of the thermal load vector in the 8-noded solid element was complicated by the existence of the internal degrees-of-freedom associated with the incompatible bubble displacement modes.

In order to verify the newly developed thermal stress analysis capability in VAST, three example problems were considered using various meshes of different element types.

Example 1: Thermal-Elastic Analysis of a Cantilever Beam. In this example, a cantilevered beam subjected to a linear temperature variation through the thickness was considered. The problem geometry, material properties and boundary conditions are displayed in Figure 3.1. The coefficient of thermal expansion was assumed constant throughout the beam structure. The prescribed pattern of temperature variation resulted in pure bending deformation. However, since the boundary conditions allowed the cantilever to deform freely in both x- and y-directions, the beam remained stress free in its deformed configuration. The analytical solution to this problem was presented in Reference [3.4] and a finite element solution had been obtained using the 20-noded solid elements of the ADINA program [3.5]. The finite element mesh and deformed configuration obtained by ADINA are reproduced in Figure 3.2. It should be noted that in ADINA analysis, only the upper half of the beam was modeled and anti-symmetric boundary conditions were applied on the neutral surface.

In the present study, seven different meshes with different element types were generated to model the cantilevered beam. These included a three element mesh of 8-noded shell, a three element mesh of 3-noded beam, a six element mesh of 4-noded quadrilateral shell, a twelve element mesh of 3-noded plate, a three element mesh of 20-noded solid and a six element mesh of 8-noded solid element. The final mesh contained one 8-noded shell and one 20-noded solid which were connected by a 13-noded transition element. The VAST solutions are compared with the analytical solution and the ADINA result in Table 3.1 and the deformed configurations predicted by the first six meshes of the VAST elements are presented in Figure 3.3(a-f). All these solutions are in exact agreement with the published results, except the one obtained using the transition element. A close examination indicated that this small discrepancy is due to the inconsistent treatment of 2D and 3D elasticity matrices in the transition element. In order to improve the accuracy of this element, an enhanced finite element formulation must be utilized.

Example 2: Thermal-Elastic Analysis of a Simply-Supported Circular Plate. In this example, a simply-supported circular plate subjected to an uniform temperature gradient through its thickness was considered. The problem geometry and material properties are shown in Figure 3.4. A positive temperature gradient of 20.0 was used in the present analysis, which resulted in temperatures of 50.0 and -50.0 on the top and bottom surfaces, respectively. Due to the application of the simply-supported boundary condition, the circular plate remains stress-free after application of the temperature variation. This problem has also been solved by ADINA, where four collapsed 4-noded quadrilateral shell elements were utilized to model a quarter of the plate [3.5], as reproduced in Figure 3.5. The predicted center deflection is in exact agreement with the analytical solution given in Reference [3.4].

In the present work, three different meshes were considered. The first two meshes were composed of four 3-noded plate/shell and four collapsed 4-noded quadrilateral shell elements, respectively. The third mesh contained eight collapsed 8-noded solid elements. In addition to checking the newly developed thermal stress analysis capability, this example problem was also utilized to verify the collapsed element option of the 4-noded shell and 8-noded solid elements.

The VAST solutions are compared with the published results in Table 3.2. The center deflections predicted by the 3-noded plate and collapsed 4-noded shell were in exact agreement with the analytical solution and the ADINA result obtained using shell elements. However, the solution of the lower-order solid element was considerably stiffer. This was probably because that the mesh of the 8-noded solid element utilized in the present study is too coarse to represent the bending dominated deformation pattern involved in this problem. The original and final deformed shapes obtained using the collapsed 4-noded shell and 8-noded solid elements of VAST are presented in Figure 3.6.

Example 3: Thermal Buckling of a Hinged Rectangular Plate. This example was used to verify the linear buckling analysis capability when initial stresses were induced by thermal loads. The problem geometry and material properties for this example problem are given in Figure 3.7. The temperature distribution was assumed to be uniform over the entire plate and the initial reference temperature was assumed to be zero degree. Because the in-plane motion of the plate is fully constrained through the hinged boundary condition, biaxial compressive membrane stresses were developed during the temperature change, which eventually resulted in the buckling of the plate. Because only symmetric buckling modes were of interest in the present example problem, one-quarter of the plate was included into the finite element mesh. The first thermal buckling mode had been solved by ADINA previously using four 8-noded shell elements [3.5]. The finite element mesh and the buckling mode shape of the ADINA analysis were reproduced in Figure 3.8. The buckling temperature predicted by ADINA was in close agreement with the analytical solution given in Reference [3.4].

In the present investigation, this example problem was solved using five VAST element types, including the 8-noded shell, 20-noded solid, 3-noded plate, 4-noded shell and 8-noded solid elements. As in regular linear buckling analyses, static analyses were first conducted to generate the initial stresses, and eigenvalue analyses was then performed to compute the buckling mode shapes and critical load factors. In VAST solutions, a reference temperature change of 100°F was utilized in the static analyses to generate thermal stresses and the first two buckling modes were calculated in the eigenvalue analyses. The VAST solutions are compared with the analytical and ADINA results in Table 3.3, where good agreement between all solutions are observed. The buckling mode shapes predicted by VAST are presented in Figure 3.9(a-e). The first mode shapes obtained by all the VAST analyses are in excellent agreement with the one predicted by ADINA.

3.2 Automatic Generation of Residual Stresses for Load-Shortening Curve Calculation of Stiffened Panel Structures

As mentioned at the beginning of this chapter, one of the main purposes for developing a thermal stress capability in VAST is to provide a means for generating self-equilibrated and consistent residual stresses for load-shortening curve computations of stiffened panels with large initial geometric imperfections. When a load-shortening curve needs to be generated for a given stiffened panel, a linear thermal stress analysis is first performed, followed by a plastic, post-buckling analysis using the consistent thermal stresses generated in the first run as residual stresses. This analysis procedure resolves the problem associated with the non-equilibrium block residual stress pattern. However, for practical stiffened panel configurations, it is not always an easy task to pre-select appropriate values of the coefficient of thermal expansion and temperature variation to ensure that the maximum thermal stress generated in the structure equals to the initial yield stress.

In order to develop a fully automated procedure for residual stress generation, a stress scaling factor has been utilized in the present work. This stress scaling factor is defined as the minimum yield stress to thermal stress ratio over the entire stiffened panel structure as:

$$f = min\left(\frac{\sigma_{Y_i}}{\sigma_{VM_{ij}}}\right),\ j \in \{1, 2, ...NELM_i\},\ i \in \{1, 2, ...NEG\} \tag{3.11}$$

where *NEG* denotes the total number of element groups and $NELM_i$ the number of elements in the ith group. σ_{Y_i}, indicates the initial yield stress defined in the .GOM file for the current element group and $\sigma_{VM_{ij}}$, is the representative von Mises stress in the current element induced by the prescribed pseudo-thermal loads. It should be noticed that the method for evaluating $\sigma_{VM\,i,j}$ is not unique. In the present study, three different methods were considered, based on effective stresses evaluated at the element corners, the numerical integration points, and the element center, respectively. Based on the numerical results to be presented later, the third method provided the most desirable nonlinear results and has been adopted in the VAST program. In the present implementation, this stress scaling factor is calculated in the STRESS module at the end of the thermal stress analysis and stored on an intermediate binary file for future use. In the present version of VAST, this algorithm for calculating the stress scaling factor is only available in two elements, including the 8-noded shell (IEC=1) and the 4-noded shell (IEC=5) elements.

In nonlinear analysis using the VAST program, initial stresses can be defined either through the use of the .T53 file generated by a previous linear static analysis, or from a user supplied text file, PREFX.IST. These two options are controlled by parameter ISTIF=-1 and 1, respectively. In the present work, a third option, which is activated by ISTIF=-3, has been implemented. In this option, VAST still reads initial stresses from the .T52 file, but automatically scale them using the stress scaling factor calculated earlier in the previous thermal stress analysis.

To test the effectiveness of the present method, the stiffened panel shown in Figure 9.27 of Reference [3.2] was reconsidered. For this particular stiffened panel, the use of the block form residual stress pattern resulted in a totally unreasonable negative axial load at the beginning of the load-shortening curve. The geometric parameters for the panel are:

$$\beta = 4.0,\ \lambda = 0.3,\ A_S/A = 0.2,\ \omega_0 = 0.3\,\beta^2 t$$

where β indicates the plate slenderness ratio; λ, the column slenderness ratio; A_S/A, the ratio of the stiffener cross-section area to the total cross-section area; ω_0 the maximum plate imperfection, and t, the thickness of the plate. Stiffener type Tee #4 (Flange: 76.2mm×14.2mm; Web: 145.3mm×7.2mm) and the end-to-end boundary condition were used in this analysis.

The finite element mesh of this stiffened panel is displayed in Figure 3.10. A nonlinear plastic post-buckling analysis was first performed using the block form residual stress distribution. As reported earlier in Reference [3.2], an unnatural negative axial load was obtained at the beginning of the load-shortening curve as shown in Figure 3.11. In this figures, the averaged axial stress and strain are normalized using the yield stress and strain, respectively. The final deformed configuration is presented in Figure 3.12. In this analysis, very small solution steps were utilized at the early stages of the analysis to ensure the accuracy of the nonlinear solution.

Before making additional nonlinear runs, a linear thermal stress analysis was performed to generate self-equilibrium and consistent residual stresses. In this thermal analysis, a totally artificial thermal expansion coefficient of $1.0/C^0$ was specified over the whole structure, but a negative temperature change of $-1.0C^0$ was only prescribed at the plate-web junction. Because the thermal stresses were scaled using the stress scaling factor prior to the nonlinear analysis, the values of the coefficient of thermal expansion and temperature variation used in the thermal analysis could be defined arbitrarily. The resulting distribution of axial thermal stress component in the mid-surface is displayed in Figure 3.13. As expected, large tensile stresses were generated near the junction of plate and web, whereas compressive stresses developed in the rest of the panel, so equilibrium state was reached respect to the original configuration. Using different methods for calculating the stress scaling factor, three load-shortening curves were obtained, which are also shown in Figure 3.11. Differing from the curve generated using the block form residual stress distribution, these curves did not show the negative load and was in excellent agreement with the load-shortening curve obtained without residual stresses in the pre-buckling range. Among the three curves computed using the residual stresses generated by thermal stress analysis, the curve obtained using the scaling factor based on effective stress at element center showed an evident reduction on the pre-buckling stiffness and peak load level. However, the use of the block form residual stress resulted in an increased post-buckling stiffness. This was probably due to the additional imperfection caused by the initial deformation related to the non-self-equilibrium residual stress pattern. The final deformed configurations predicted using various forms of residual stresses were virtually identical.

To generate residual stresses for the above nonlinear analysis, temperature variation was only prescribed at the plate-web junction. In order to investigate the significance of temperature change at the web-flange junction, one additional nonlinear analysis was conducted, in which a temperature variations of $-1.0C^0$ was at both junctions. The predicted load-shortening curve is presented in Figure 3.14, which, however, is in close agreement with the result obtained using temperature variation at only the plate-web junction.

The same stiffened panel was then analyzed using the 8-noded thick/thin shell element. A coarse 8-noded shell element mesh was first considered as shown in Figure 3.16. This mesh contained roughly the same number of degrees-of-freedom as the 4-noded quadrilateral shell mesh shown in Figure 3.10. The final collapsed configuration of the stiffened panel predicted using the higher-order elements is displayed in Figure 3.16 and the load-shortening curves obtained using different residual stress patterns are compared in Figure 3.17. Similar to the solutions using the 4-noded shells, the use of the block form residual stress distribution again resulted in negative axial load at the beginning of the load-shortening curve. Comparing with the curve obtained without residual stresses, the curve using the thermal residual stresses showed a perfect initial slope and a reduced pre-buckling stiffness. However, the peak load predicted by using the thermal residual stress was slightly higher than those in the other two curves. In addition, it was also interesting to notice that the residual stress pattern obtained using the 8-noded elements, as shown in Figure 3.18, was significantly different from that predicted by the 4-noded shell element.

In order to investigate whether this over estimation of the peak load was caused by the relative coarseness of the finite element mesh, a significantly refined mesh of 8-noded shell element was created as shown in Figure 3.19. The final deformed configuration, load-shortening curves and thermal stress distributions obtained using this finer mesh are displayed in Figures 3.20, 3.21 and 3.22, respectively. However, these results were virtually identical to those obtained by using the coarser mesh, indicating the convergence of the 8-noded shell solutions. The reason why the peak load was over estimated by the 8-node shell elements with the thermally generated residual stresses has not been fully understood at the present time.

To further investigate the accuracy of the 8-noded higher-order shell element for calculating load-shortening curves of stiffened panels, we considered a more typical stiffened panel configuration defined by:

$$\beta = 2.0,\ \lambda = 0.6,\ A_S/A = 0.2,\ \omega_0 = 0.1\,\beta^2 t.$$

The finite element mesh is shown in Figure 3.23. The contour plot of the axial component of the thermal stresses on the shell upper surface is given in Figure 3.24 and the axial stress variation along the plate width at one end is displayed in Figure 3.25, which is in close agreement with the measured residual stress pattern presented in Reference [3.3]. The amplitude of the thermal stresses in these figures was obviously unrealistic. This was due to the arbitrary selection of the coefficient of thermal expansion and temperature variation in the thermal stress analysis. However, after the application of the stress scaling factor, the maximum axial stress at the plate center was reduced to the initial yield stress. The load-shortening curves predicted by VAST with and without residual stresses are compared in Figure 3.26, where the use of residual stresses resulted in a significantly reduced peak load. For the present stiffened panel dimensions and imperfection levels, the load-shortening curves obtained using the block form and thermally generated residual stress patterns were in very close agreement. The final deformed shape predicted in these three analyses were identical and is shown in Figure 3.27.

Table 3.1: Comparison of VAST Results With Analytical and ADINA Solutions for Thermal-Elastic Analysis of a Cantilever Beam

FE Code	Element Type	Tip Deflection (in)
VAST	8-noded thick/thin shell element	-0.00540
VAST	3-noded curved beam element	-0.00540
VAST	4-noded quadrilateral shell element	-0.00540
VAST	3-noded plate/shell element	-0.00540
VAST	20-noded solid element	-0.00540
VAST	8-noded solid element	-0.00540
VAST	8-noded shell, 20-noded solid and 13-noded transition elements	-0.00539
ADINA	20-noded solid element	-0.00540
Analytical	-	-0.00540

Table 3.2: Comparison of VAST Results With Analytical and ADINA Solutions for Thermal-Elastic Analysis of a Simply-Supported Circular Plate

FE Code	Element Type	Center Deflection
VAST	3-noded plate/shell element	0.5000
VAST	4-noded quad shell element (collapsed)	0.5000
VAST	8-noded solid element	0.3827
ADINA	4-noded quad shell element (collapsed)	0.5000
Analytical	-	0.5000

Table 3.3: Comparison of VAST Results With Analytical and ADINA Solutions for Thermal Buckling Analysis of a Hinged Rectangular Plate

FE Code	Element Type	Critical Temperatures	
		Mode 1	Mode 2
VAST	8-noded thick/thin shell element	99.080	279.37
VAST	20-noded solid element	103.91	372.57
VAST	3-noded plate/shell element	100.85	271.72
VAST	4-noded quadrilateral shell element	104.93	320.57
VAST	8-noded solid element	108.93	284.14
ADINA	8-noded thick/thin shell element	101.40	-
Analytical	-	102.80	-

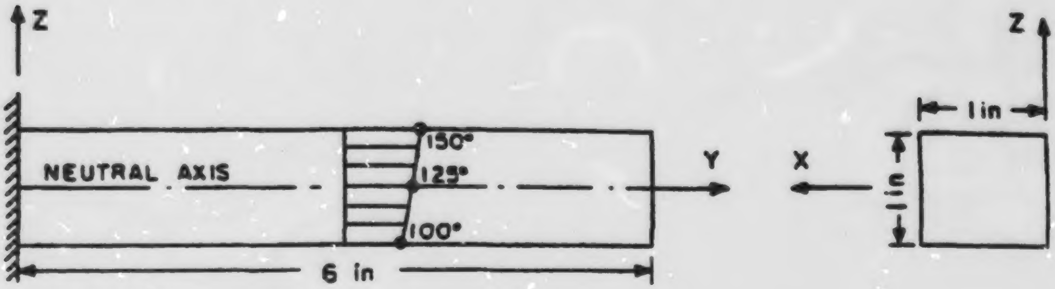
Z
NEUTRAL AXIS
150°
125°
100°
6 in
Y
X
Z
1 in
1 in

SIDE AND END VIEWS

	70°F	200°F	
E	$3.0 \cdot 10^7$	$3.0 \cdot 10^7$	lb/in²
ν	0.3	0.3	
α	$6.0 \cdot 10^{-6}$	$6.0 \cdot 10^{-6}$	in/in/°F

REFERENCE TEMPERATURE = 125°F

Figure 3.1: Problem Geometry, Material Properties and Boundary Conditions for Thermal-Elastic Analysis of a Cantilevered Beam.

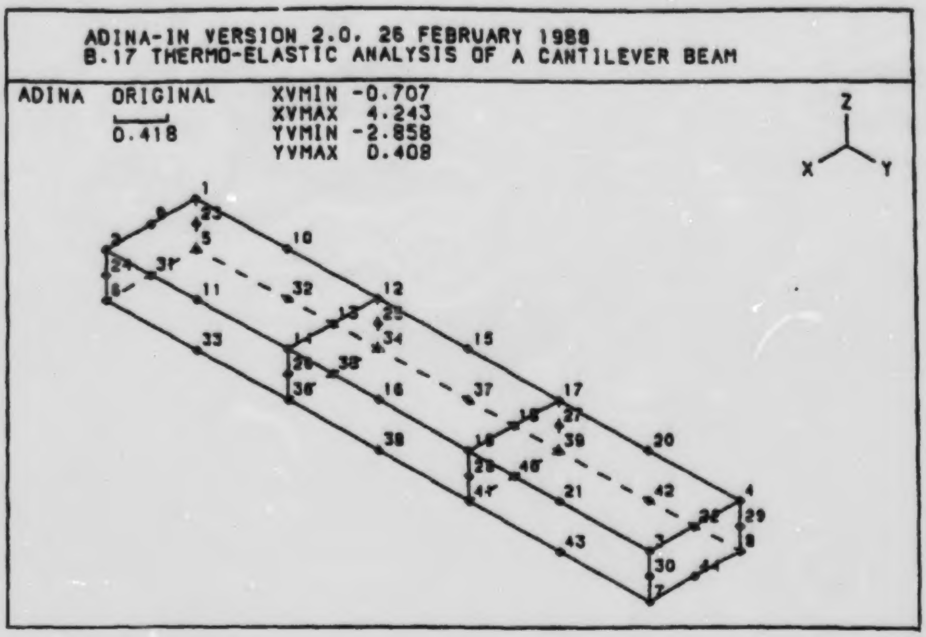

```
ADINA-IN VERSION 2.0, 26 FEBRUARY 1988
B.17 THERMO-ELASTIC ANALYSIS OF A CANTILEVER BEAM

ADINA  ORIGINAL      XVMIN -0.707
                     XVMAX  4.243
       0.418         YVMIN -2.858
                     YVMAX  0.408
```

Z
X
Y
1
9
23
5
2
24
31
6
10
11
32
12
13
25
34
14
33
26
35
36
16
15
37
17
18
27
19
39
38
20
28
40
41
21
42
4
29
8
43
3
30
44
7

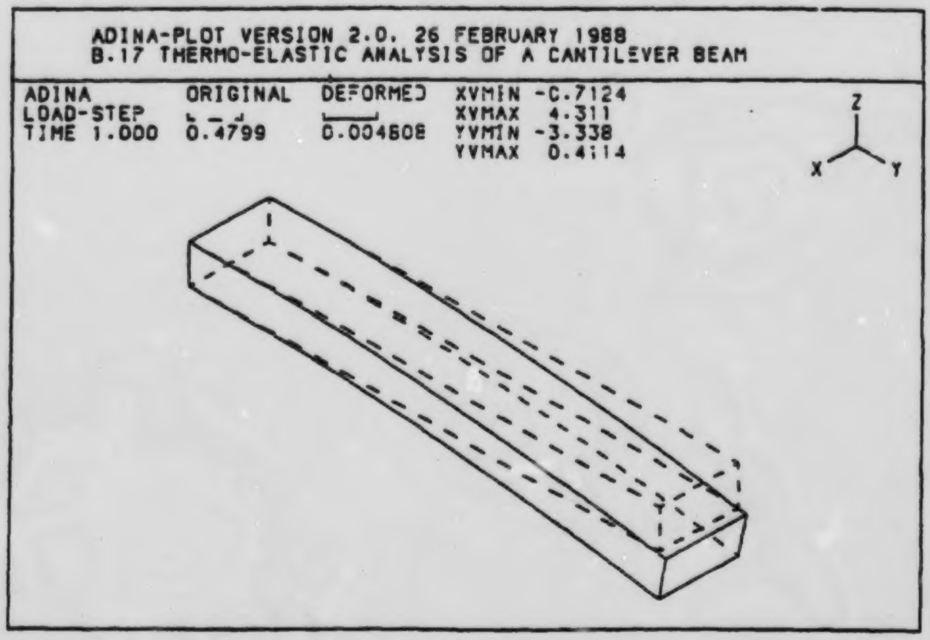

```
ADINA-PLOT VERSION 2.0, 26 FEBRUARY 1988
B.17 THERMO-ELASTIC ANALYSIS OF A CANTILEVER BEAM

ADINA          ORIGINAL    DEFORMED     XVMIN -0.7124
LOAD-STEP                               XVMAX  4.311
TIME 1.000     0.4799      0.004608     YVMIN -3.338
                                        YVMAX  0.4114
```

Figure 3.2: Initial Finite Element Mesh and Final Deformed Configuration of the Cantilevered Beam Obtained by the ADINA Program.

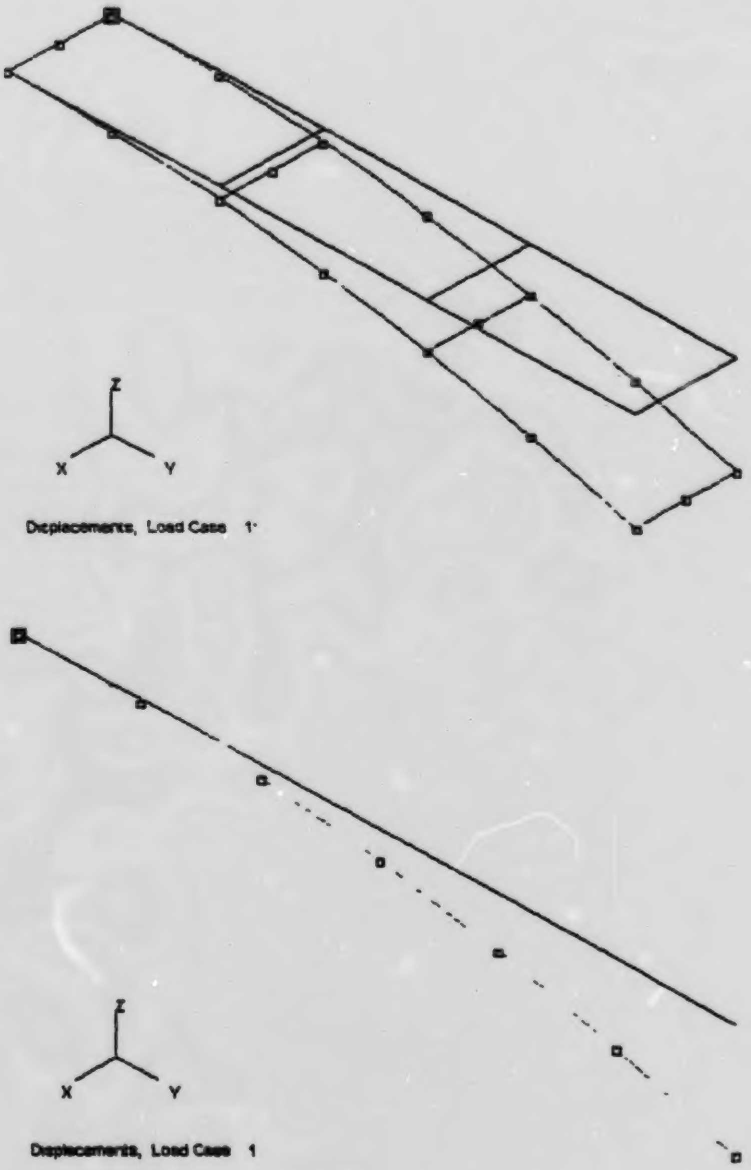
Z
X
Y
Displacements, Load Case 1
Z
X
Y
Displacements, Load Case 1

Figure 3.3: Initial Finite Element Mesh and Final Deformed Configuration of the Cantilevered Beam Obtained by the VAST Program.
(a) 8-Noded Shell Element, (b) 3-Noded Beam Element.

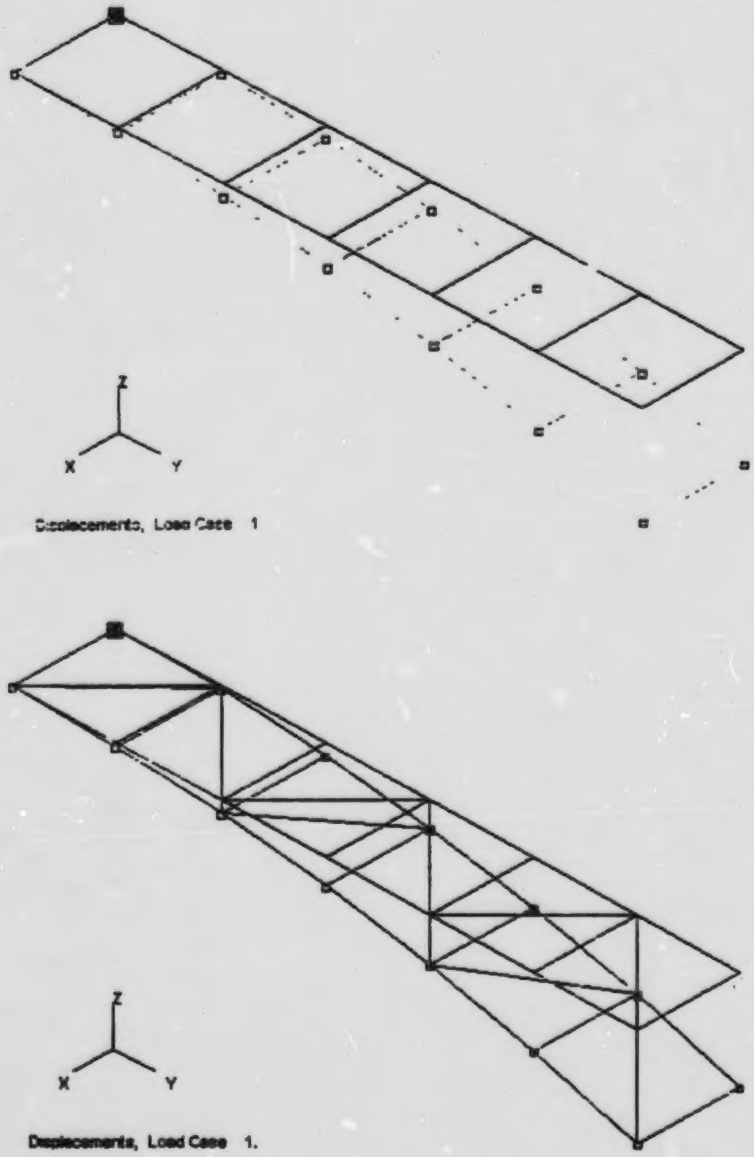
Z
X
Y
Displacements, Load Case 1
Z
X
Y
Displacements, Load Case 1.

Figure 3.3: (Continued) Initial Finite Element Mesh and Final Deformed Configuration of the Cantilevered Beam Obtained by the VAST Program.
(c) 4-Noded Quadrilateral Shell Element, (d) 3-Noded Plate/Shell Element.

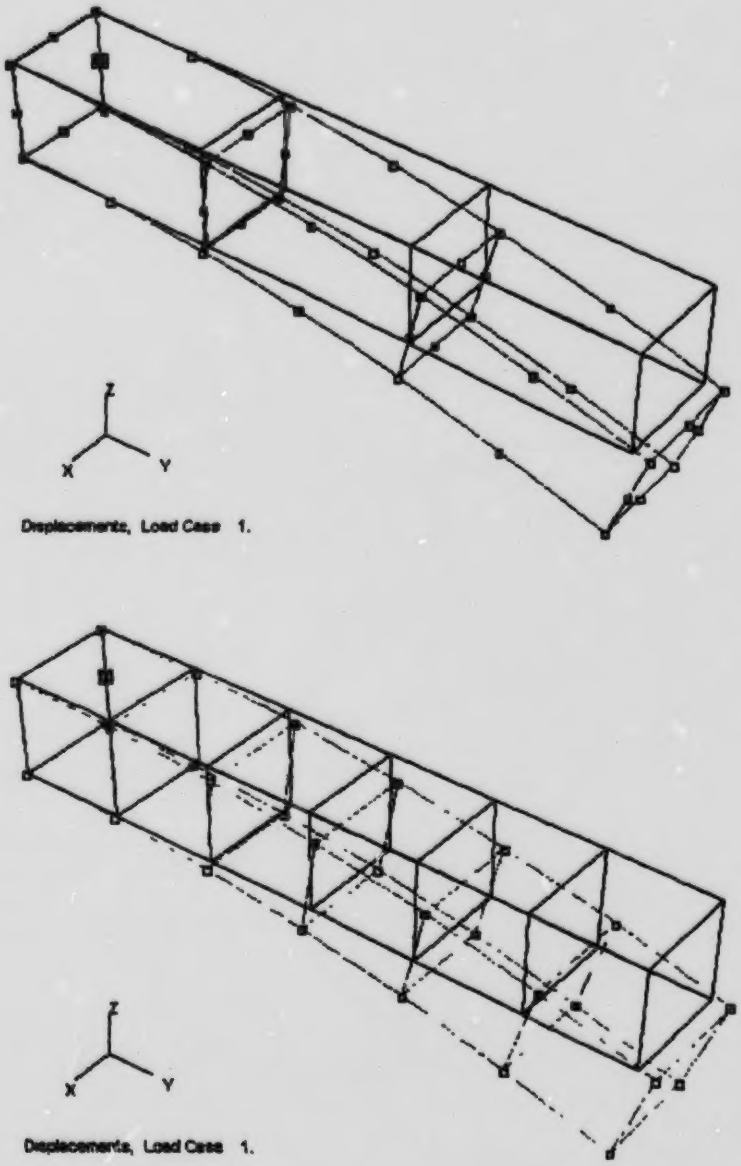
Z
X
Y
Displacements, Load Case 1.
Z
X
Y
Displacements, Load Case 1.

Figure 3.3: (Continued) Initial Finite Element Mesh and Final Deformed Configuration of the Cantilevered Beam Obtained by the VAST Program.
(e) 20-Noded Solid Element, (f) 8-Noded Solid Element.

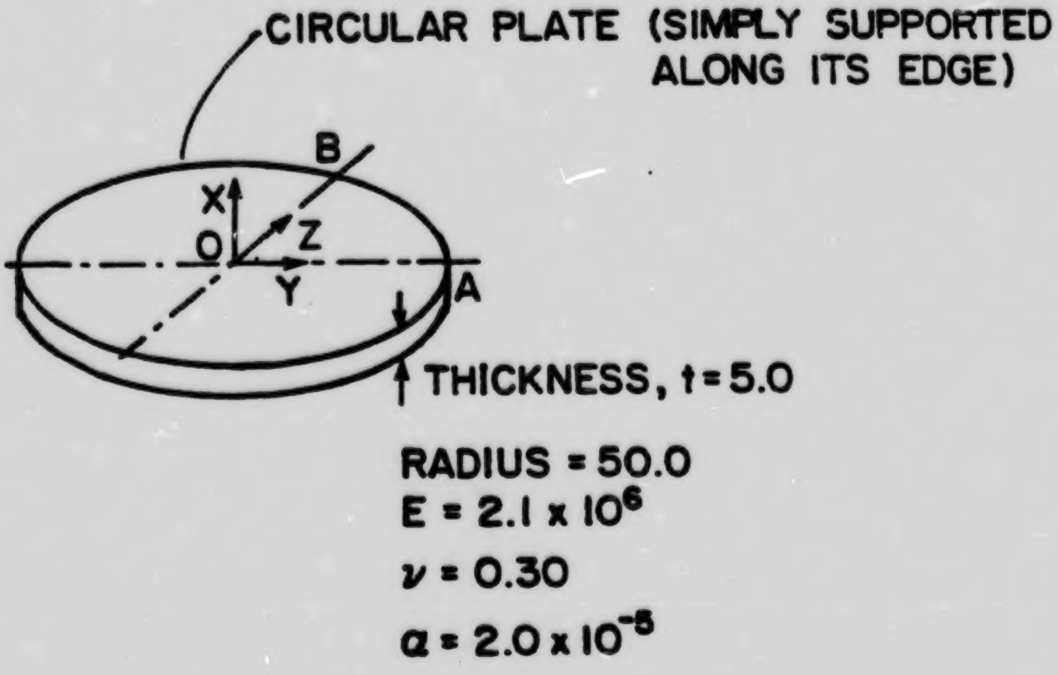
CIRCULAR PLATE (SIMPLY SUPPORTED ALONG ITS EDGE)
B
X
O
Z
Y
A
THICKNESS, t = 5.0
RADIUS = 50.0
E = 2.1 x 10^6
ν = 0.30
α = 2.0 x 10^-5

Figure 3.4: Problem Geometry and Material Properties for Thermal-Elastic Analysis of a Simply-Supported Circular Plate.

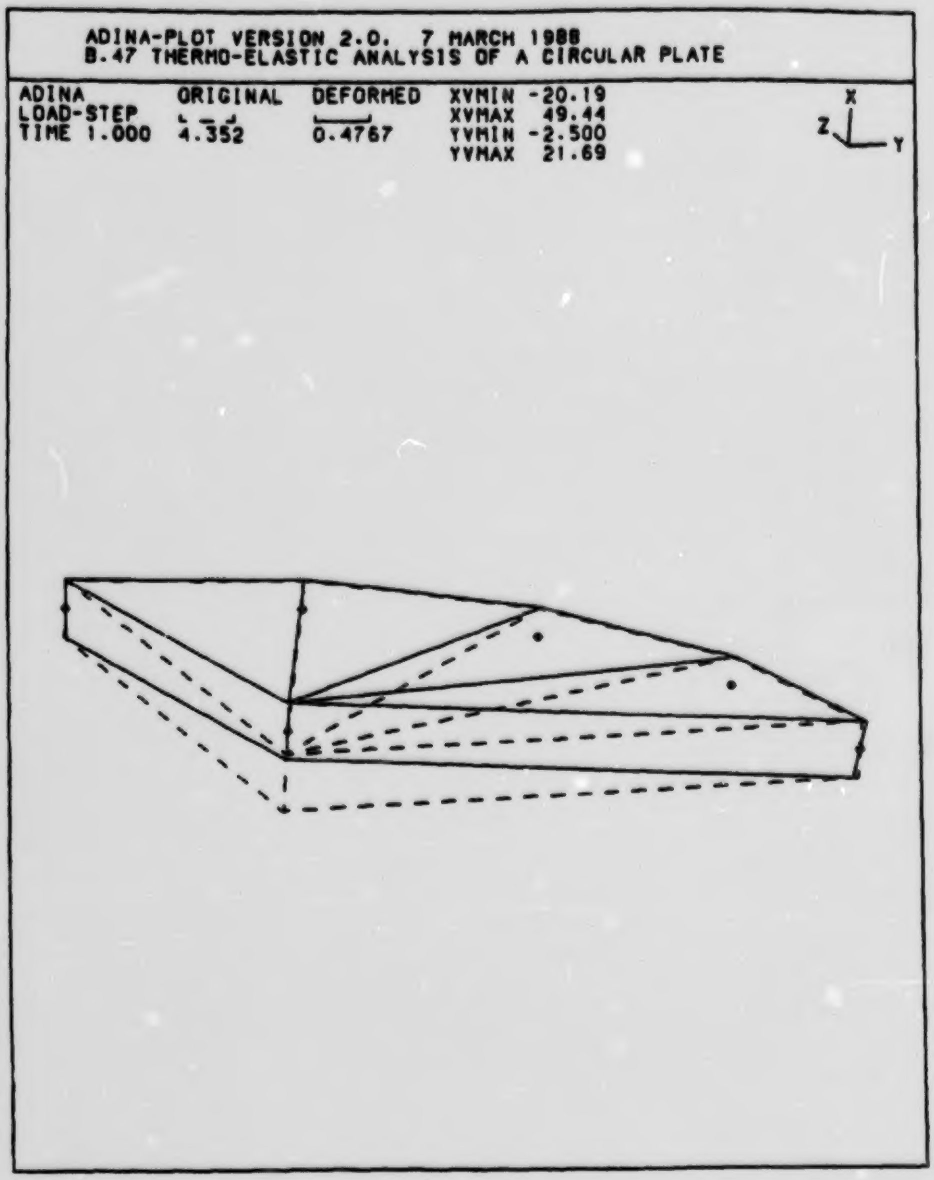
ADINA-PLOT VERSION 2.0, 7 MARCH 1988
B.47 THERMO-ELASTIC ANALYSIS OF A CIRCULAR PLATE
ADINA
LOAD-STEP
TIME 1.000
ORIGINAL
4.352
DEFORMED
0.4767
XVMIN -20.19
XVMAX 49.44
YVMIN -2.500
YVMAX 21.69
X
Z
Y

Figure 3.5: Initial Finite Element Mesh and Final Deformed Configuration of the Circular Plate Obtained by the ADINA Program.

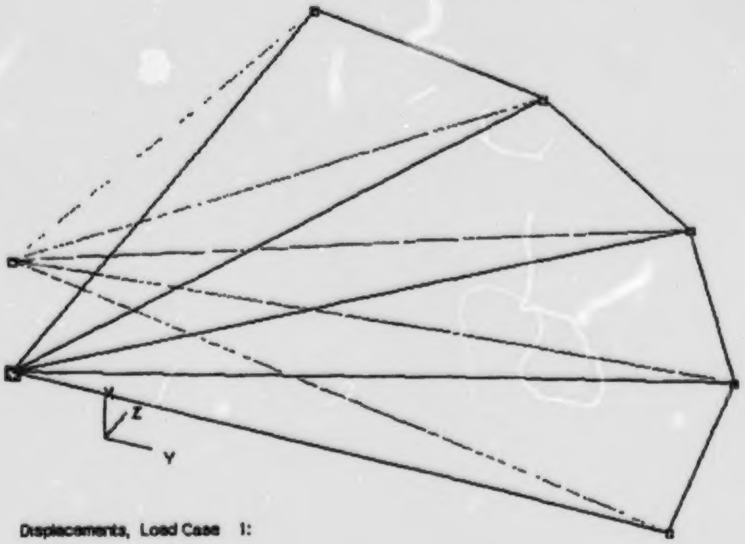
Y
Z
Y
Displacements, Load Case 1:

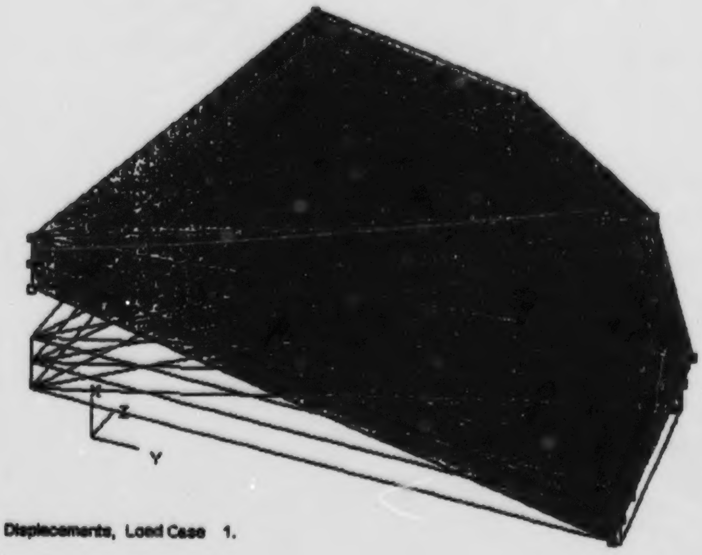
Y
Z
Y
Displacements, Load Case 1.

Figure 3.6: Initial Finite Element Mesh and Final Deformed Configuration of the Circular Plate Obtained by the VAST Program.
(a) Collapsed 4-Noded Shell Element, (b) Collapsed 8-Noded Solid Element.

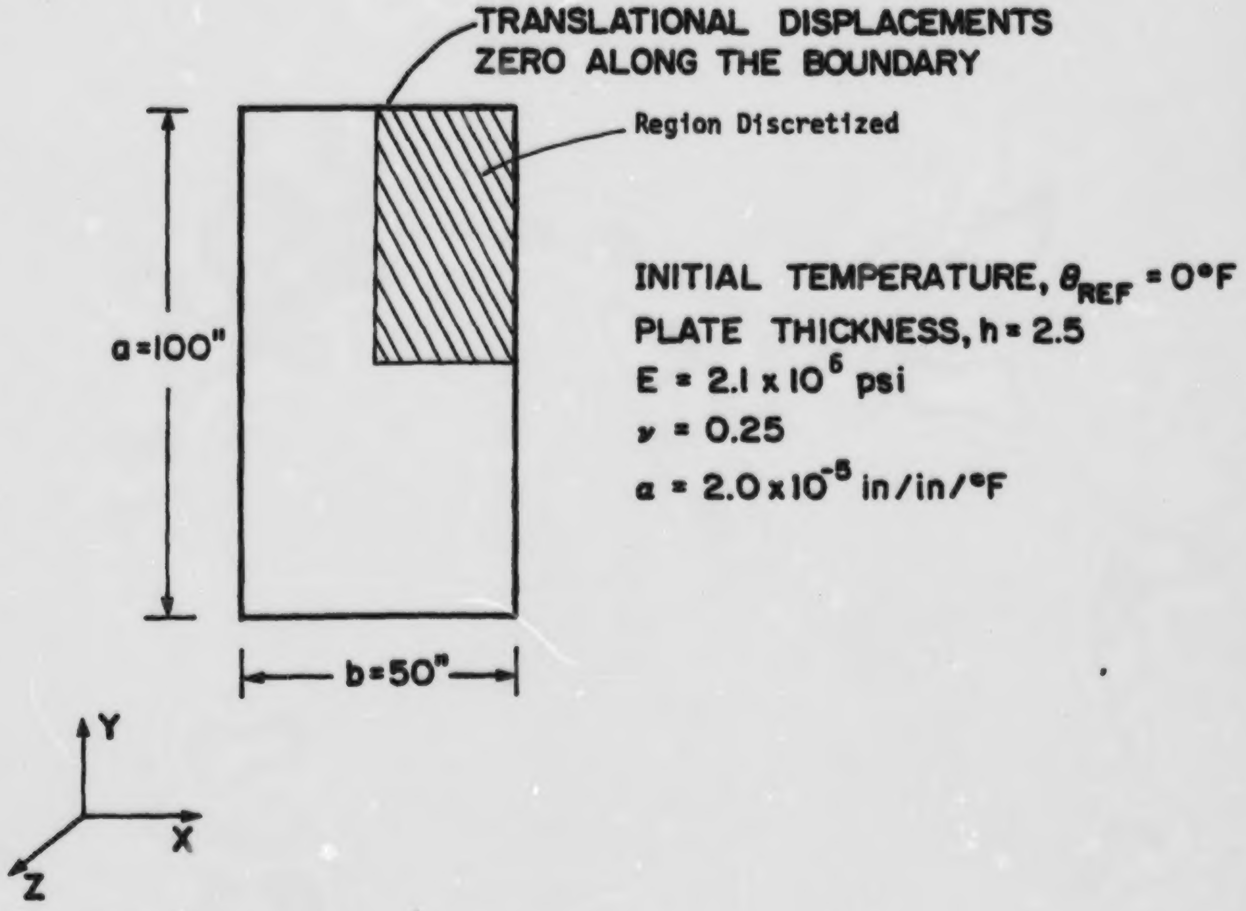
TRANSLATIONAL DISPLACEMENTS ZERO ALONG THE BOUNDARY
Region Discretized
a=100"
b=50"
INITIAL TEMPERATURE, θ_{REF} = 0°F
PLATE THICKNESS, h = 2.5
E = 2.1 x 10^6 psi
ν = 0.25
α = 2.0 x 10^{-5} in/in/°F
Y
X
Z

Figure 3.7: Problem Geometry, Material Properties and Boundary Conditions for Thermal Buckling Analysis of a Hinged Rectangular Plate.

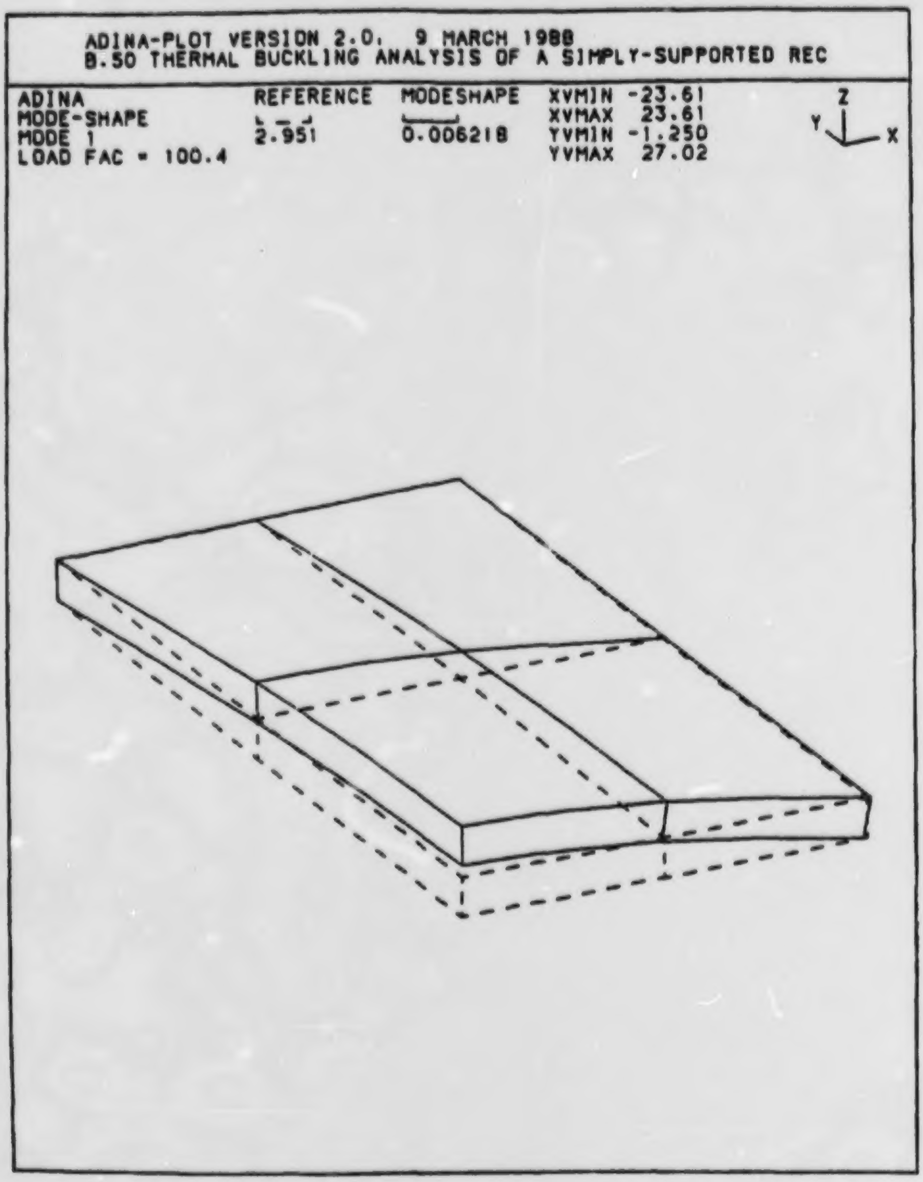
ADINA-PLOT VERSION 2.0, 9 MARCH 1988
B.50 THERMAL BUCKLING ANALYSIS OF A SIMPLY-SUPPORTED REC
ADINA
MODE-SHAPE
MODE 1
LOAD FAC = 100.4
REFERENCE
2.951
MODESHAPE
0.006218
XVMIN -23.61
XVMAX 23.61
YVMIN -1.250
YVMAX 27.02
Z
Y
X

Figure 3.8: Finite Element Mesh and the First Thermal Buckling Mode Shape of the Hinged Rectangular Plate Obtained by the ADINA Program.

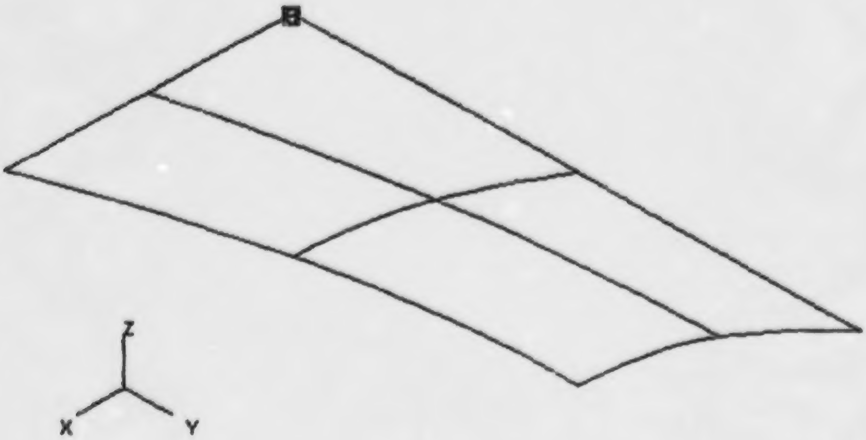

Buckling Mode Shape 1 Critical Load Factor 0.9908E+00

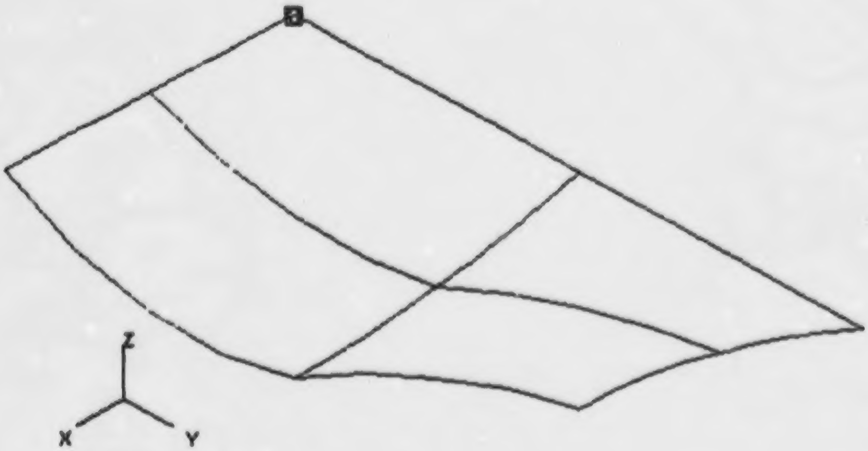

Buckling Mode Shape 2 Critical Load Factor 0.2794E+01

Figure 3.9: The First and Second Thermal Buckling Mode Shapes of the Hinged Rectangular Plate Predicted by the VAST Program.
(a) 8-Noded Thick/Thin Shell Element.

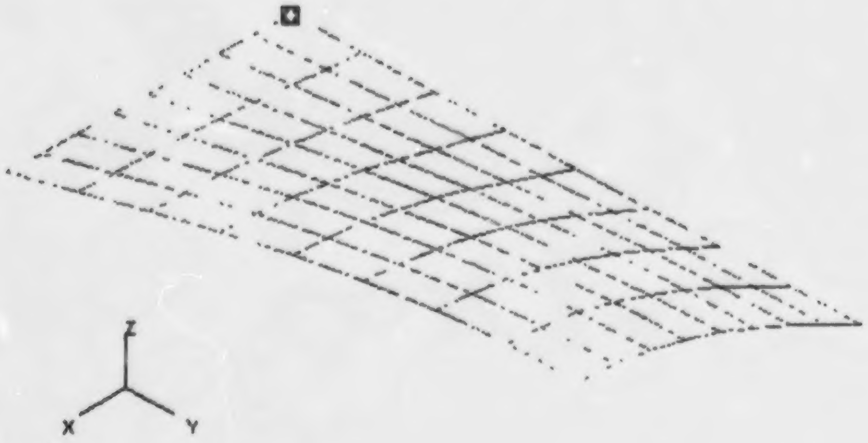

Buckling Mode Shape 1 Critical Load Factor 0.1016E+01

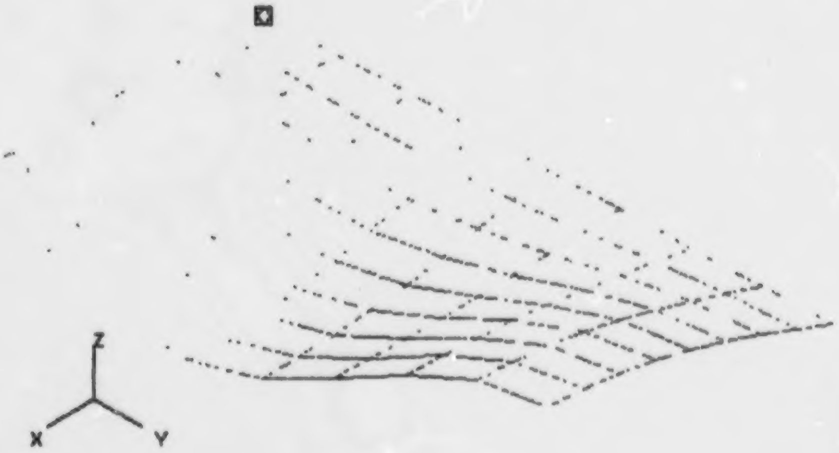

Buckling Mode Shape 2 Critical Load Factor 0.2703E+01

Figure 3.9: (Continued) The First and Second Thermal Buckling Mode Shapes of the Hinged Rectangular Plate Predicted by the VAST Program.
(b) 4-Noded Quadrilateral Shell Element.

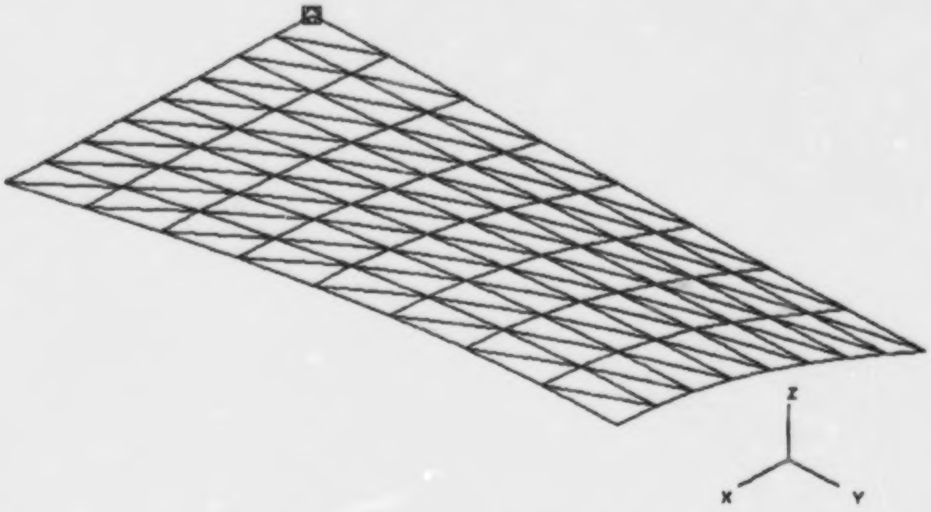

Buckling Mode Shape 1 Critical Load Factor 0.1007E+01

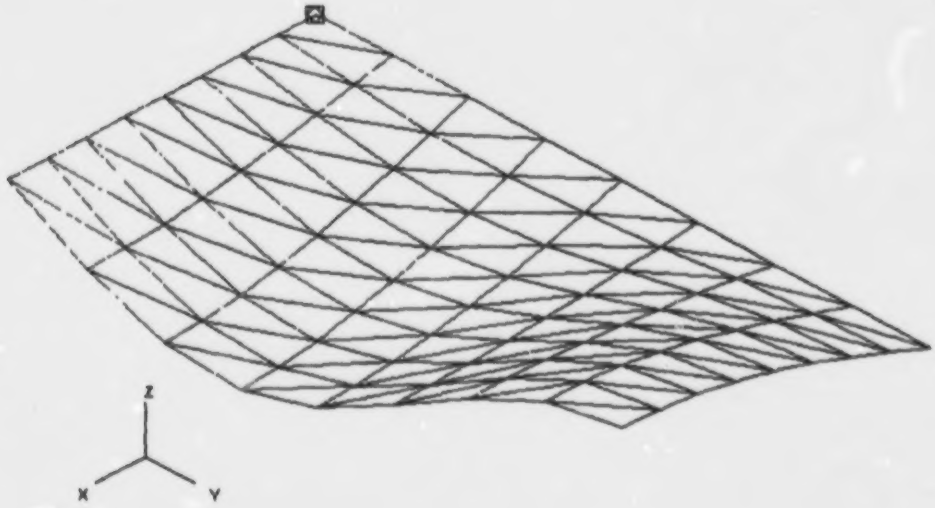

Buckling Mode Shape 2 Critical Load Factor 0.2706E+01

Figure 3.9: (Continued) The First and Second Thermal Buckling Mode Shapes of the Hinged Rectangular Plate Predicted by the VAST Program.
(c) 3-Noded Plate/Shell Element.

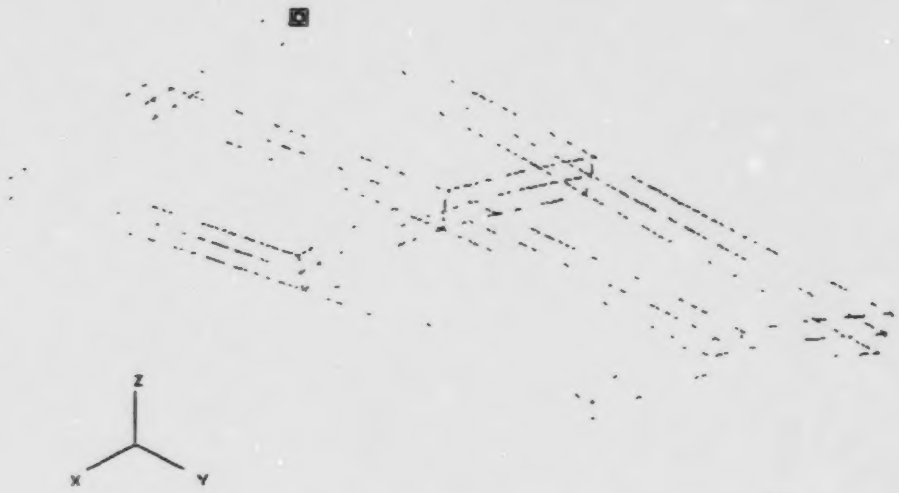

Bucking Mode Shape 1 Critical Load Factor 0 1106E+01

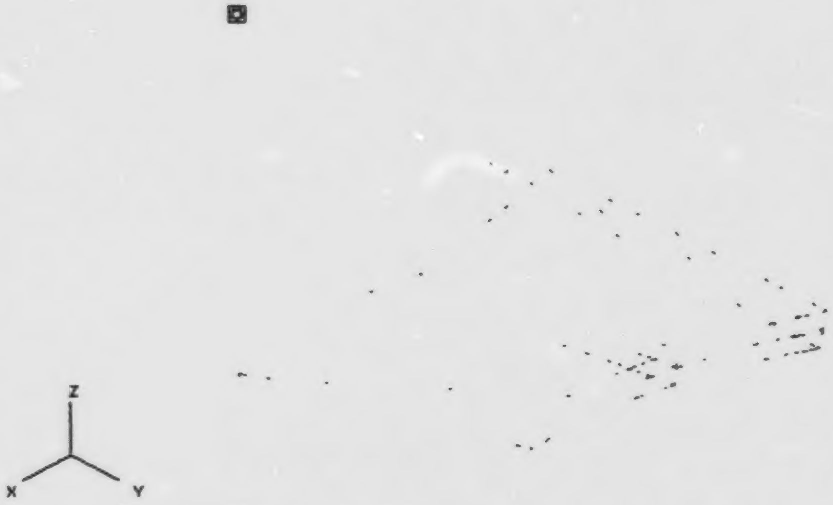

Bucking Mode Shape 2 Critical Load Factor 0 3007E+01

Figure 3.9: (Continued) The First and Second Thermal Buckling Mode Shapes of the Hinged Rectangular Plate Predicted by the VAST Program. (d) 20-Noded Solid Element.

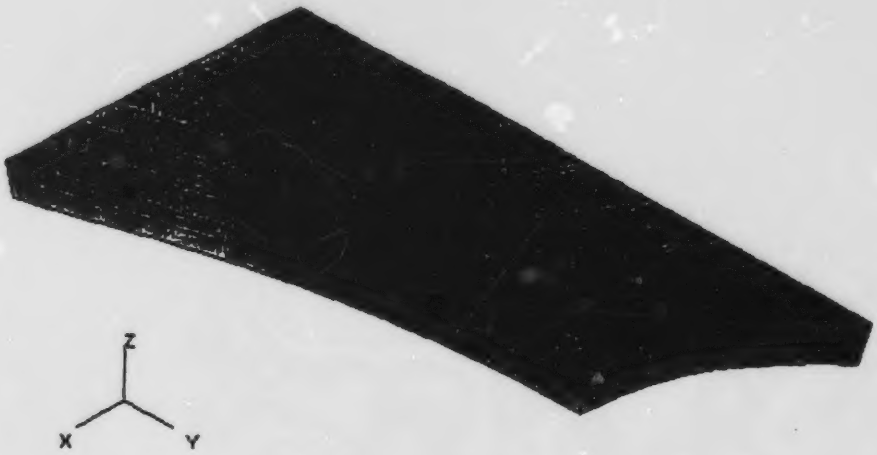

Buckling Mode Shape 1 Critical Load Factor 0.1089E+01

Buckling Mode Shape 2 Critical Load Factor 0.2841E+01

Figure 3.9: (Continued) The First and Second Thermal Buckling Mode Shapes of the Hinged Rectangular Plate Predicted by the VAST Program.
(e) 8-Noded Solid Element.

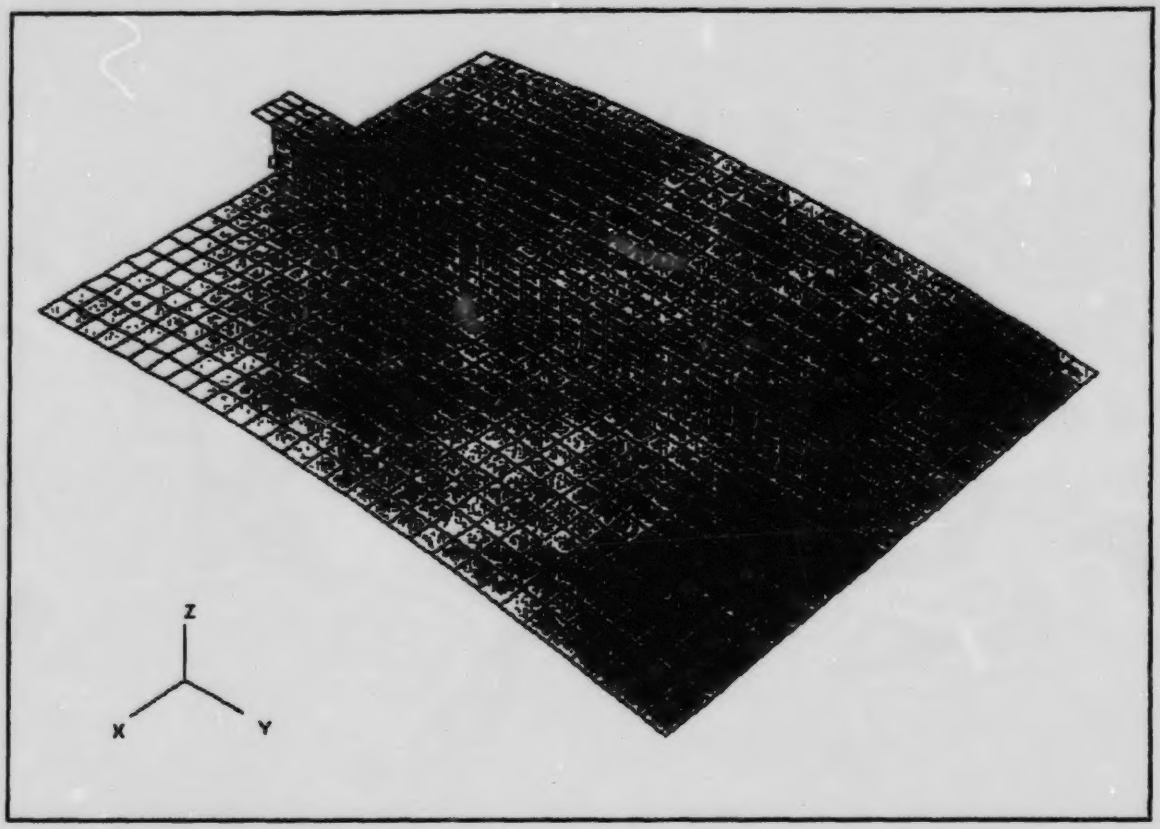

Figure 3.10: Four-Noded Quadrilateral Shell Element Mesh for Stiffened Panel with β=4.0, λ=0.3, A_r=0.2, ω_0=0.3 β^2 t.

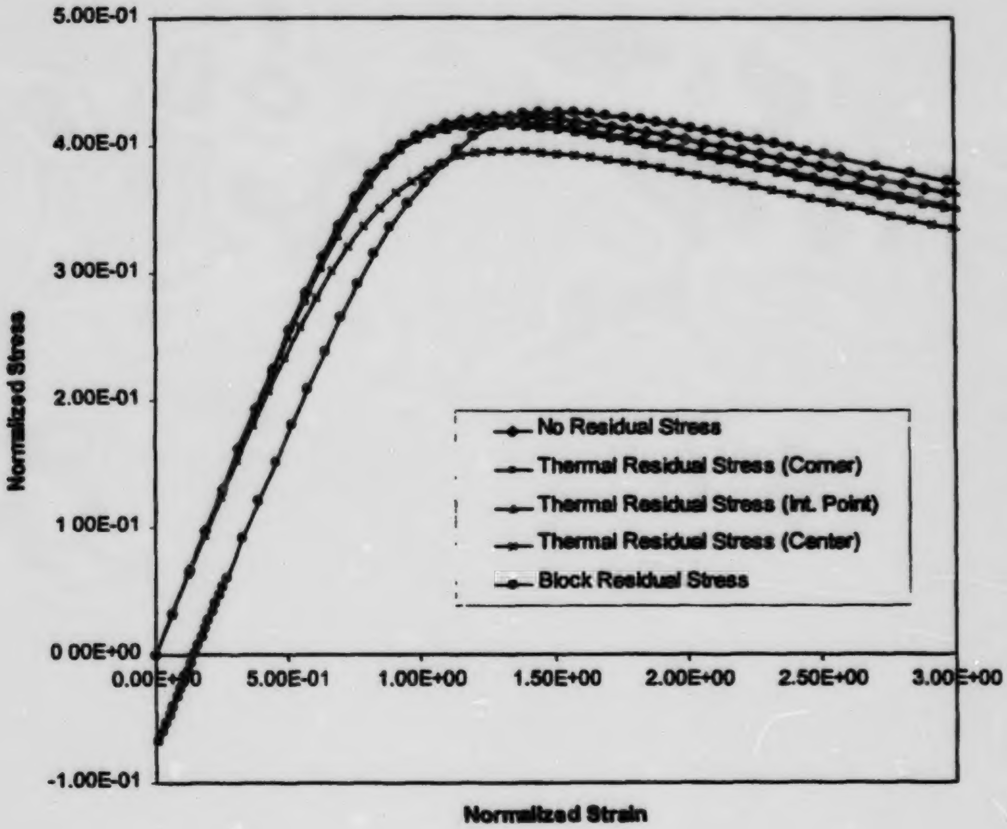

Figure 3.11: Comparison of Load-Shortening Curves Obtained by Using the Four-Noded Element and Various Residual Stress Distributions.

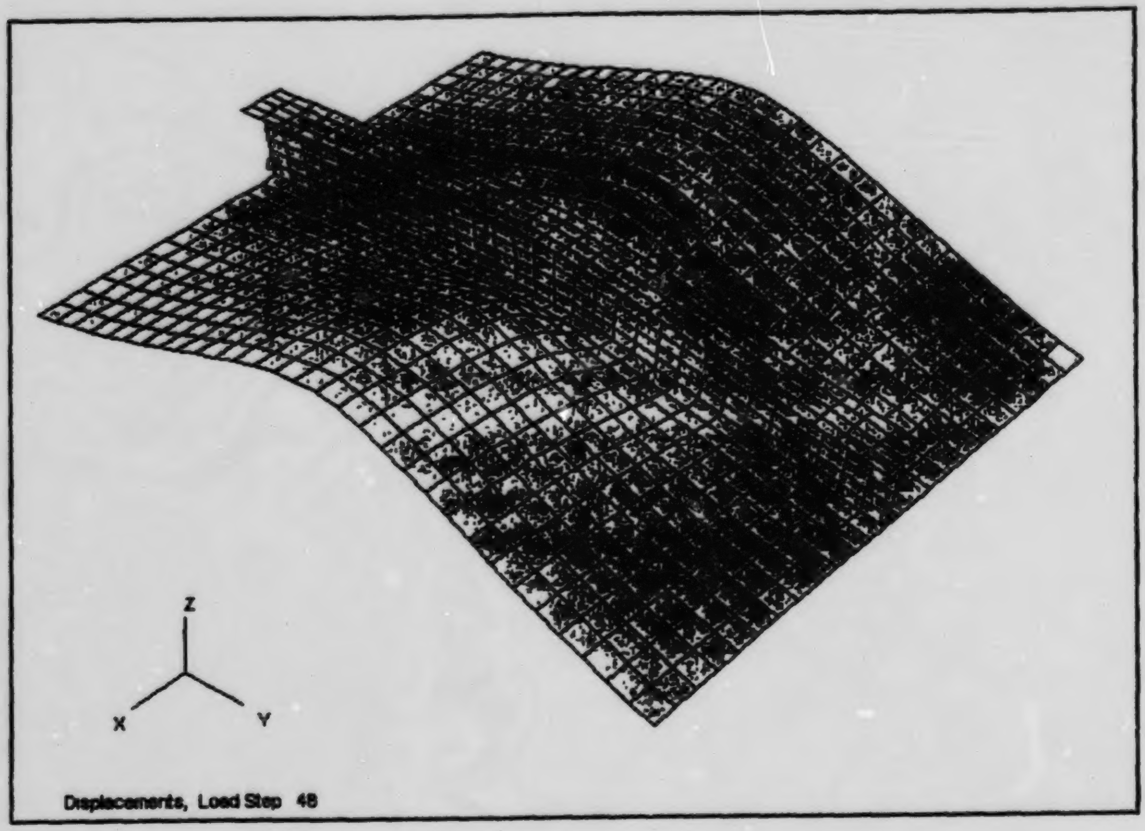
Z
X
Y
Displacements, Load Step 48

Figure 3.12: Final Deformed Configuration of the Stiffened Panel Predicted by the Four-Noded Shell Element.

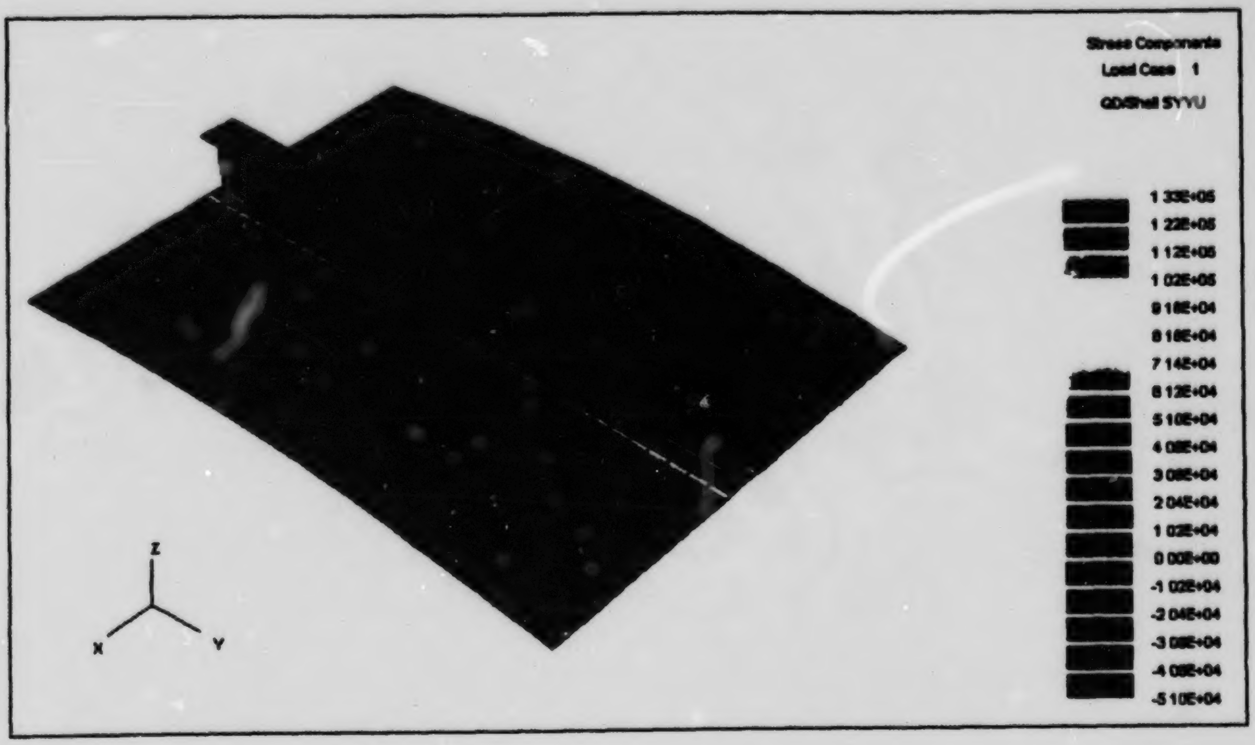
Stress Components
Load Case 1
QD/Shell SYYU
1.33E+05
1.22E+05
1.12E+05
1.02E+05
9.18E+04
8.16E+04
7.14E+04
6.12E+04
5.10E+04
4.08E+04
3.06E+04
2.04E+04
1.02E+04
0.00E+00
-1.02E+04
-2.04E+04
-3.06E+04
-4.08E+04
-5.10E+04
Z
X
Y

Figure 3.13: Axial Stress Distribution in the Stiffened Panel Predicted by Thermal Stress Analysis.

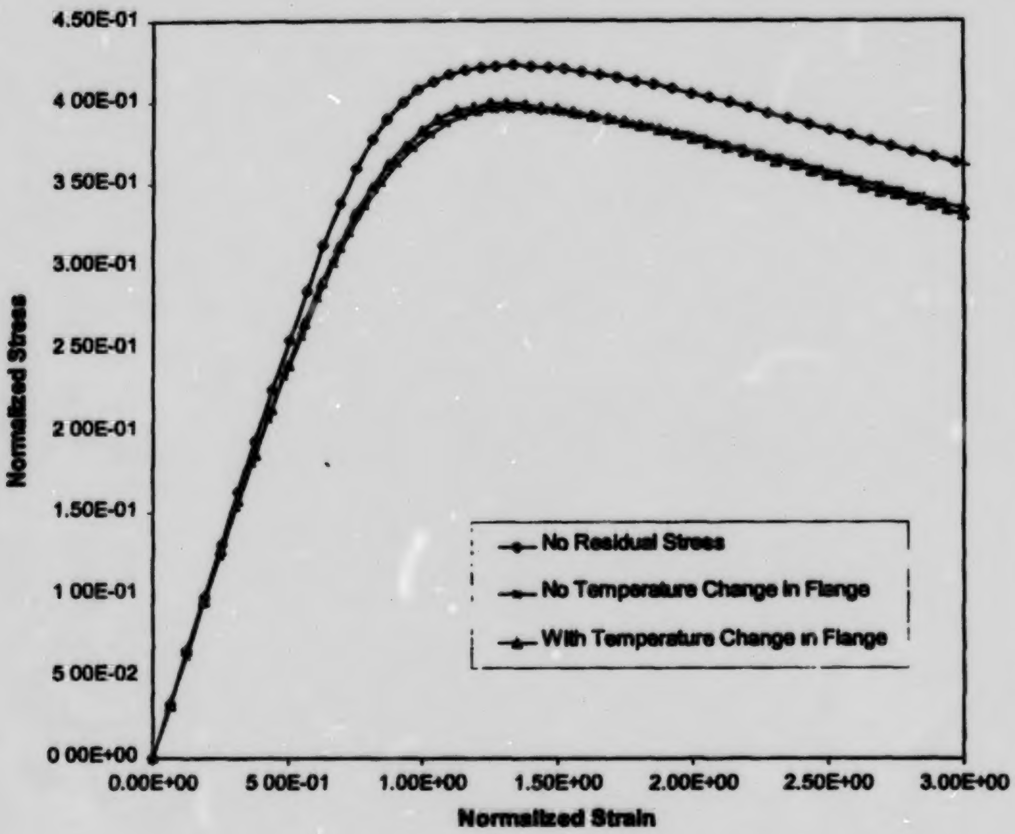

Figure 3.14: Comparison of Load-Shortening Curves Obtained by Using Thermal Residual Stresses Generated With and Without Temperature Variation at the Web-Flange Junction.

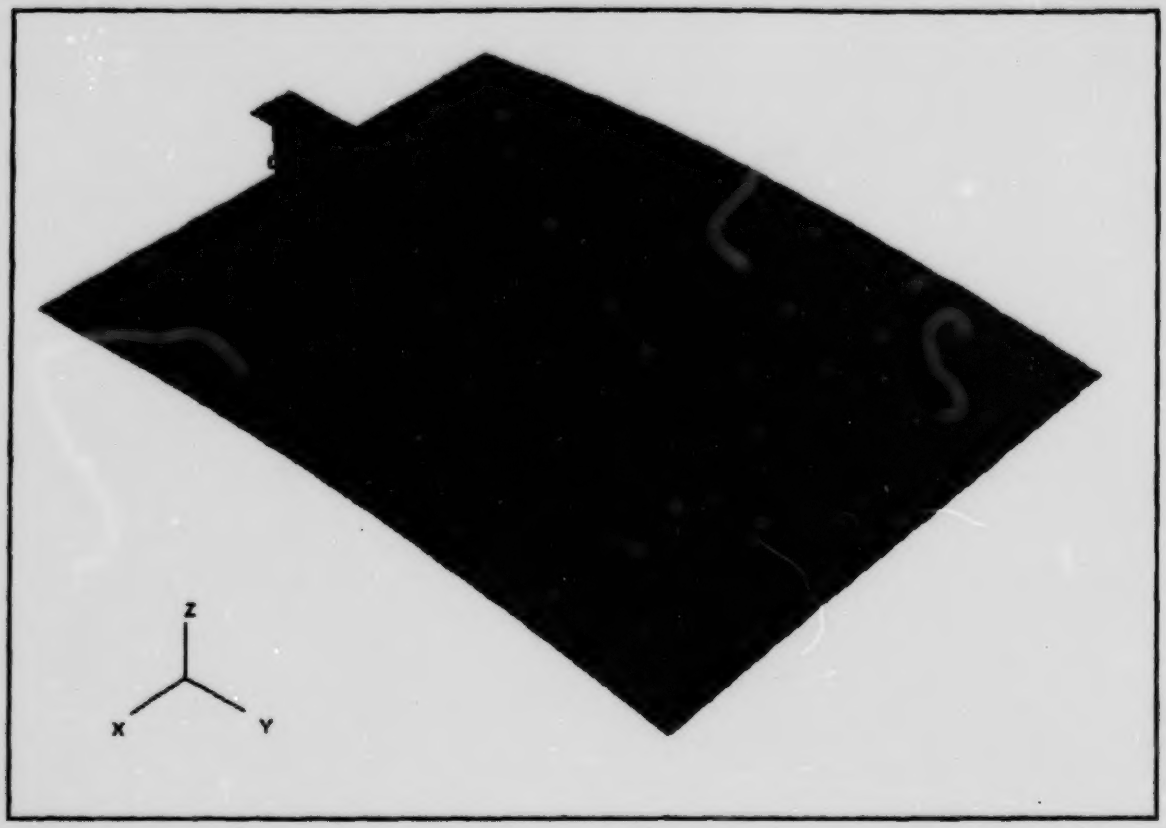

Figure 3.15: Eight-Noded Thick/Thin Shell Element Mesh for Stiffened Panel with $\beta=4.0$, $\lambda=0.3$, $A_r=0.2$, $\omega_0=0.3\ \beta^2 t$.

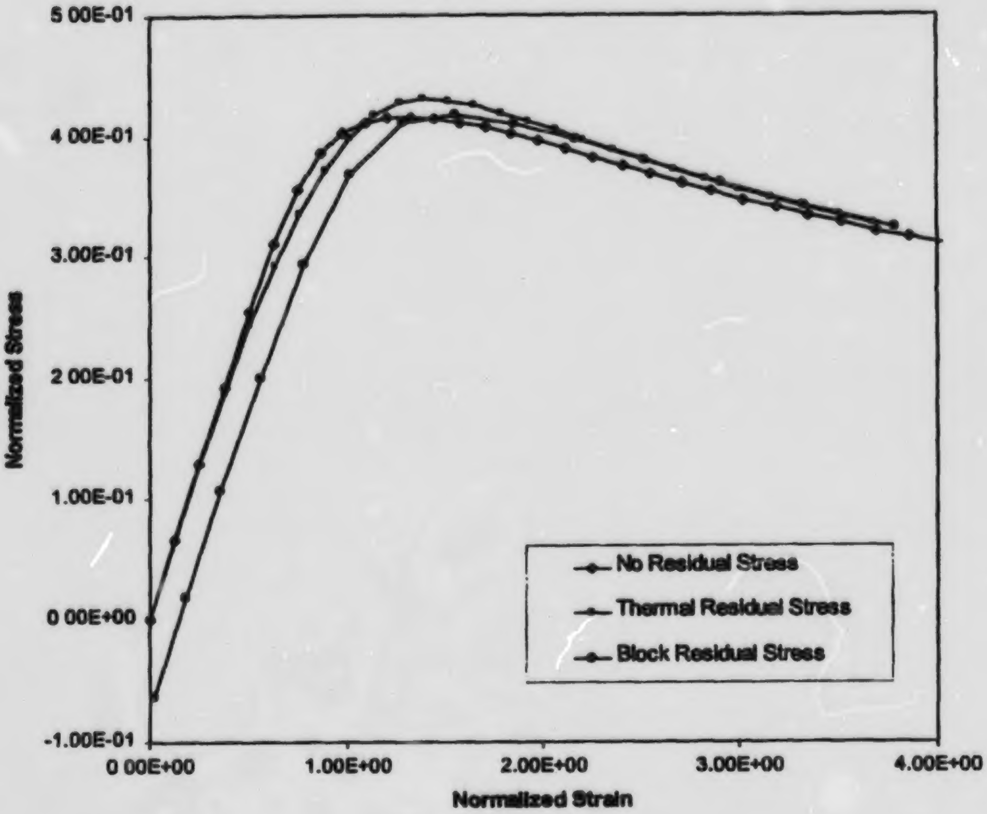

Figure 3.16: Comparison of Load-Shortening Curves Obtained by Using the Eight-Noded Element and Various Residual Stress Distributions.

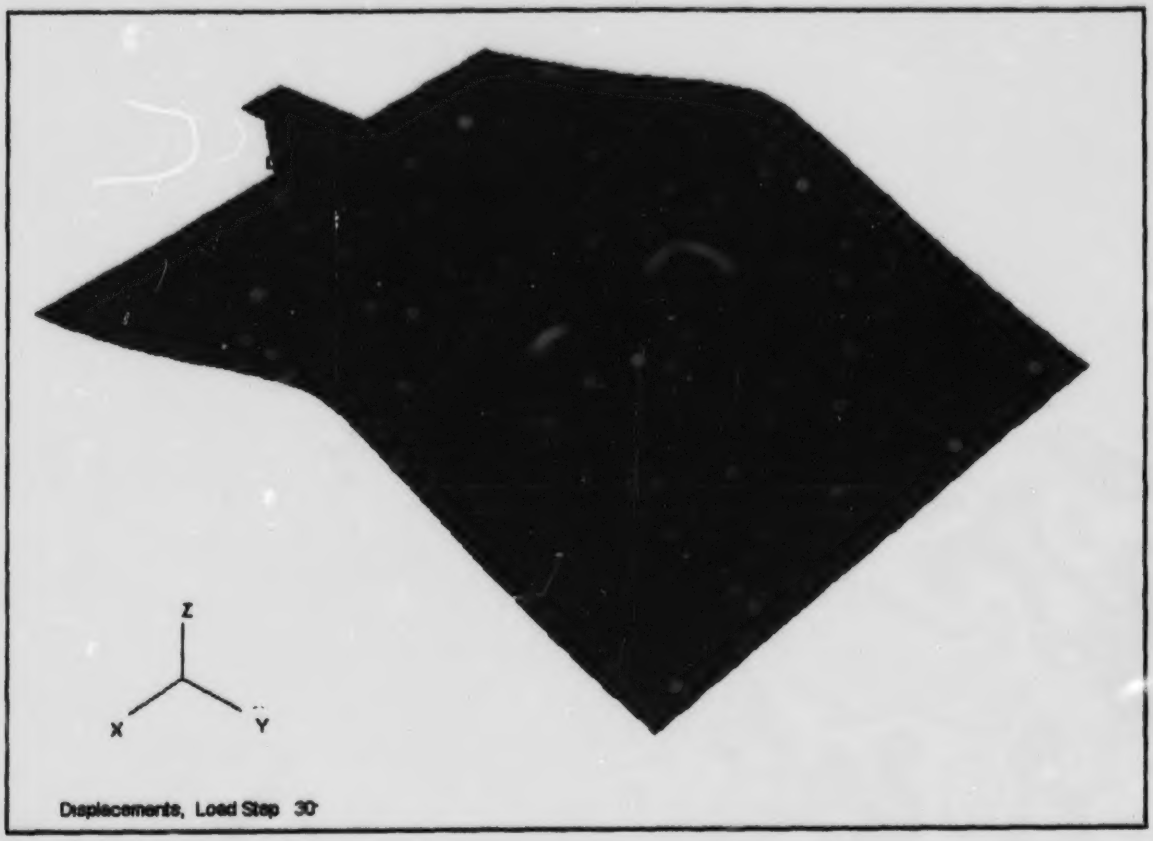
Z
X
Y
Displacements, Load Step 30

Figure 3.17: Final Deformed Configuration of the Stiffened Panel Predicted by the Eight-Noded Shell Element.

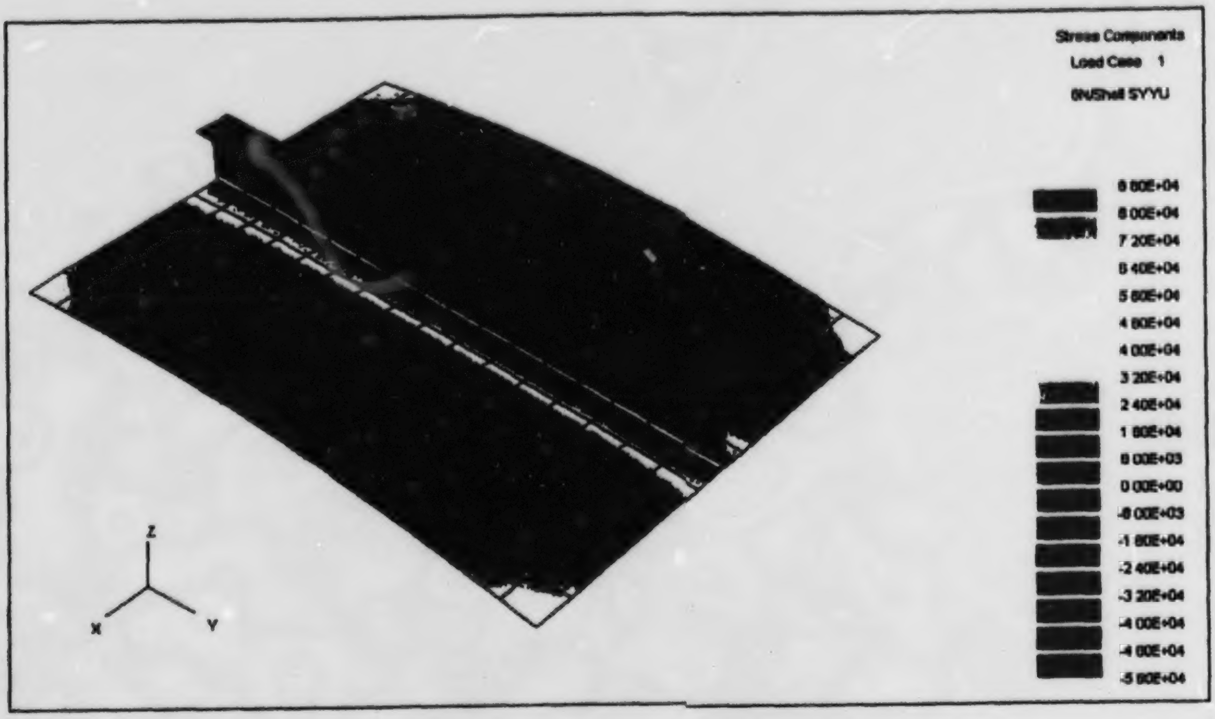

Figure 3.18: Axial Stress Distribution in the Stiffened Panel Predicted by Thermal Stress Analysis Using the Eight-Noded Shell Element.

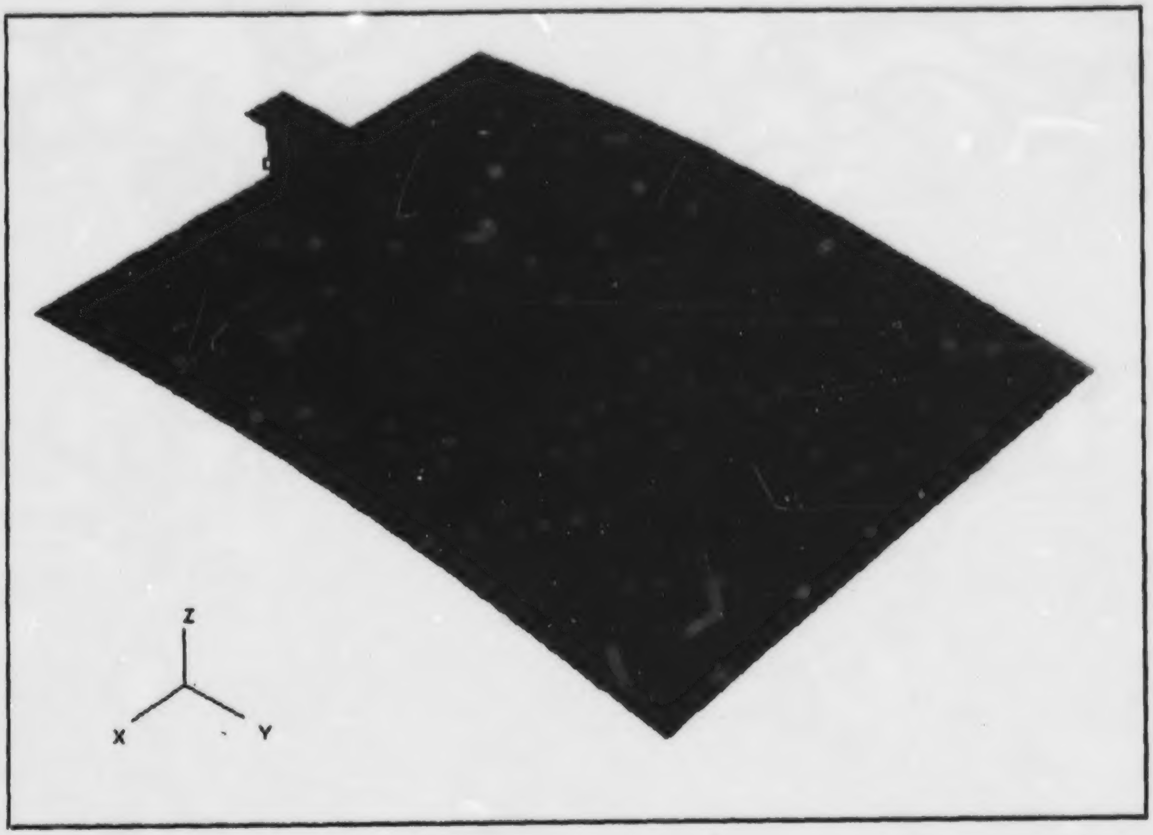

Figure 3.19: Refined Eight-Noded Thick/Thin Shell Element Mesh for Stiffened Panel with β=4.0, λ=0.3, A_r=0.2, ω_0=0.3 β^2 t.

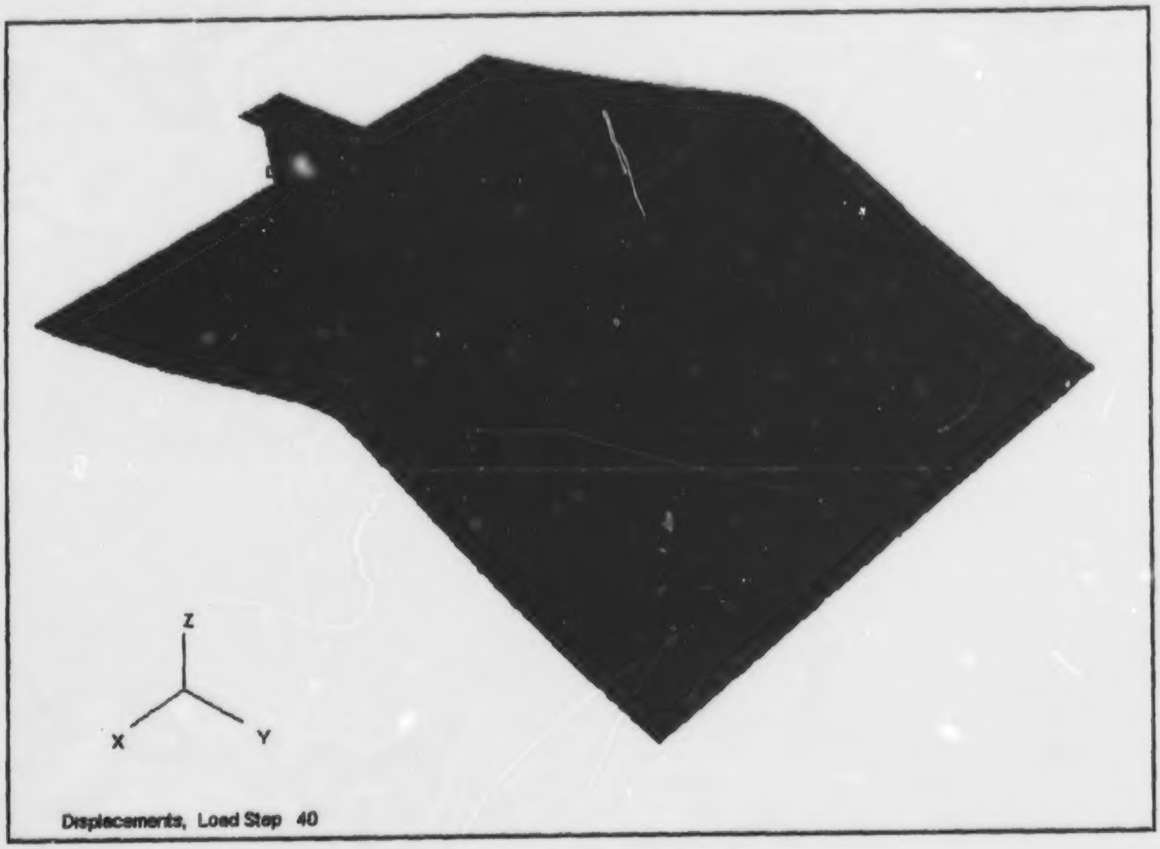
Z
X
Y
Displacements, Load Step 40

Figure 3.20: Final Deformed Configuration of the Stiffened Panel Predicted by the Refined Eight-Noded Shell Element Mesh.

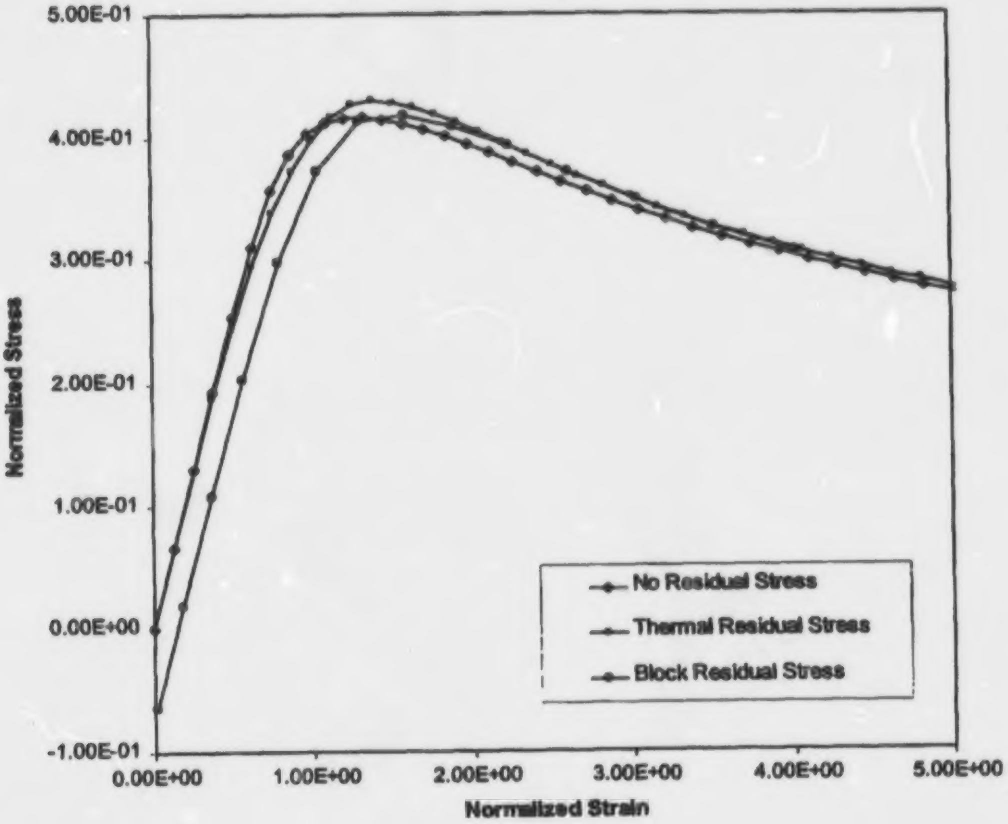

Figure 3.21: Comparison of Load-Shortening Curves Obtained by Using the Refined Eight-Noded Element and Various Residual Stress Distributions.

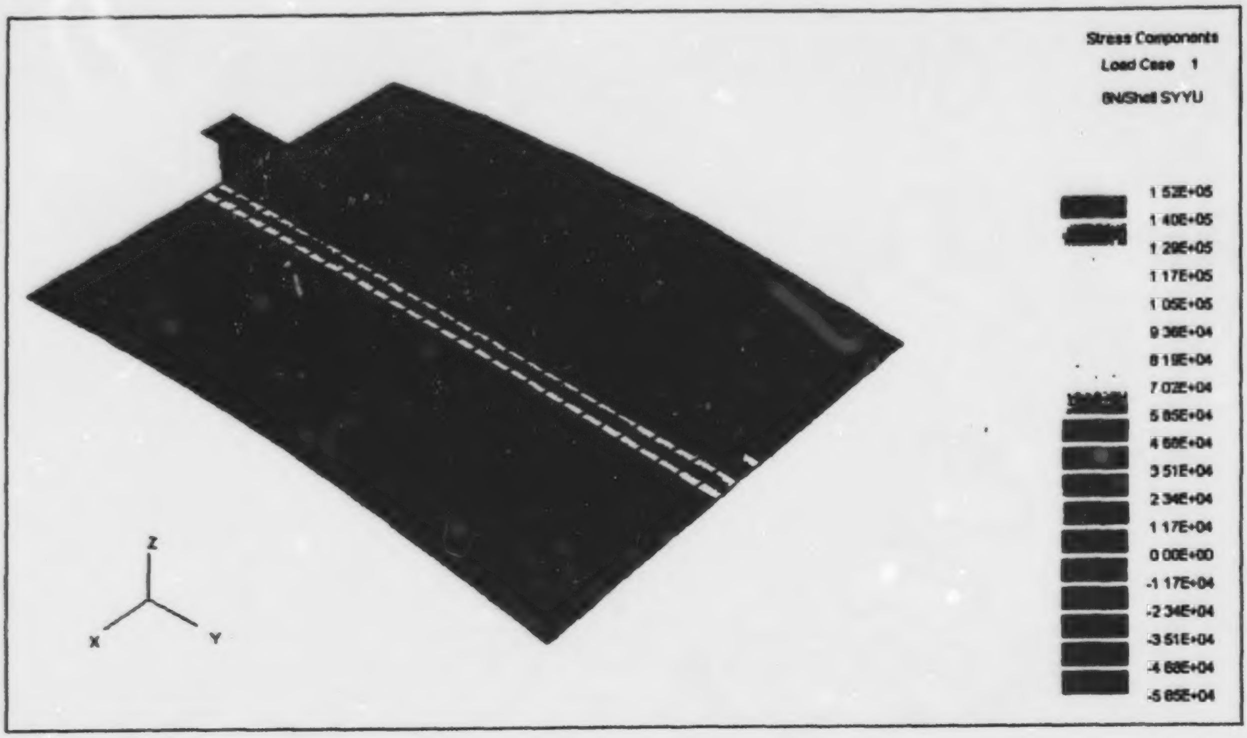

Figure 3.22: Axial Stress Distribution in the Stiffened Panel Predicted by Thermal Stress Analysis Using the Refined Eight-Noded Element Mesh.

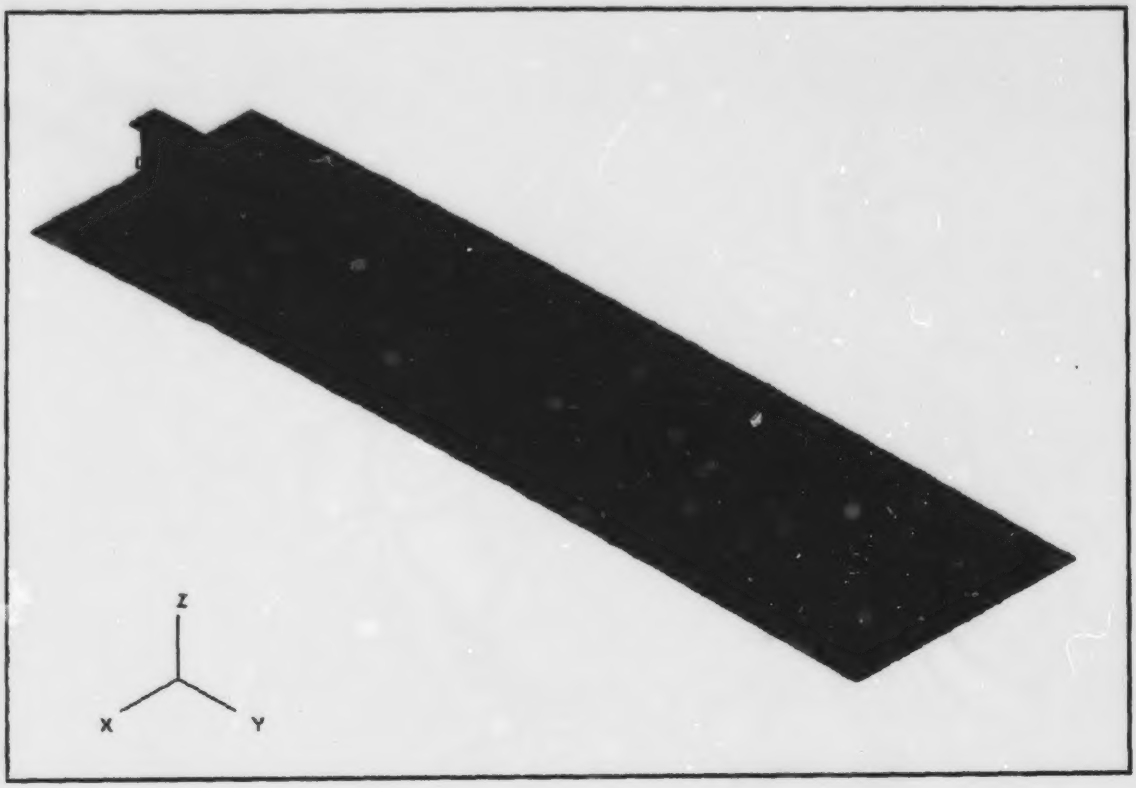

Figure 3.23: Eight-Noded Thick/Thin Shell Element Mesh for Stiffened Panel with β=2.0, λ=0.6, A_r=0.2, ω_0=0.1 β^2 t.

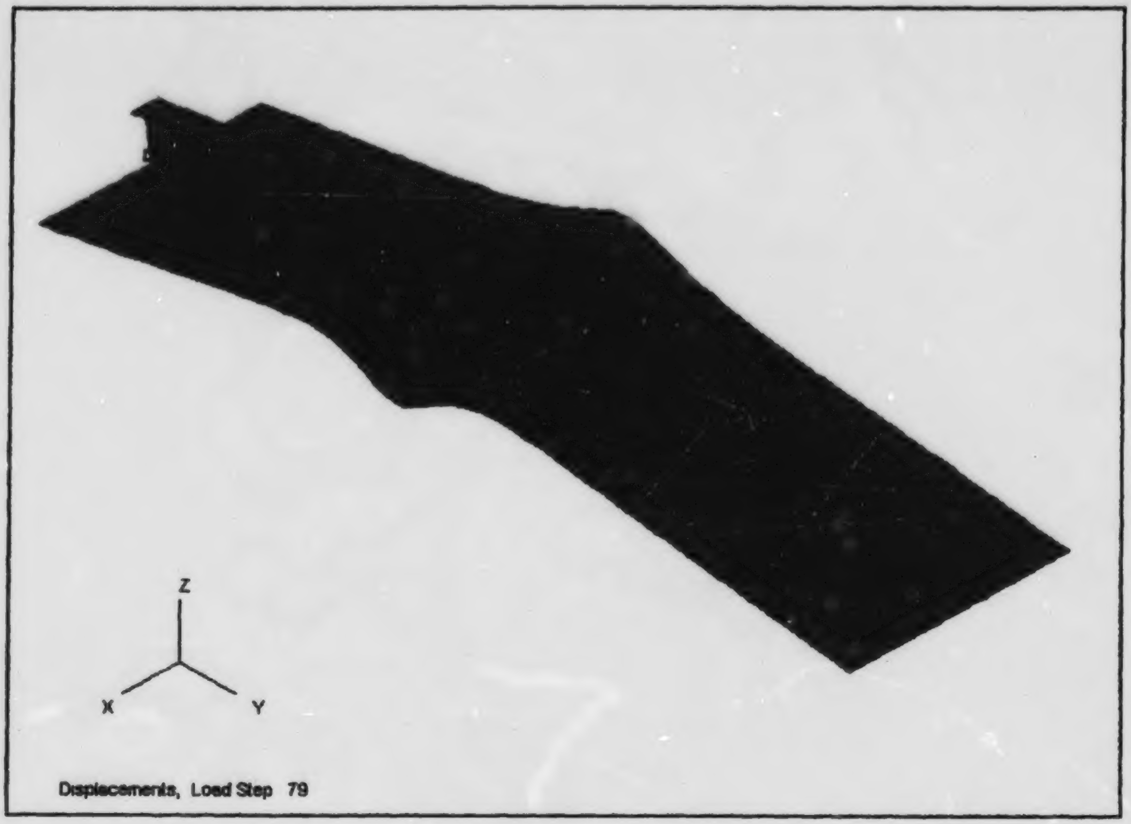
Z
X
Y
Displacements, Load Step 79

Figure 3.24: Final Deformed Configuration of the Stiffened Panel Predicted by Eight-Noded Shell Element.

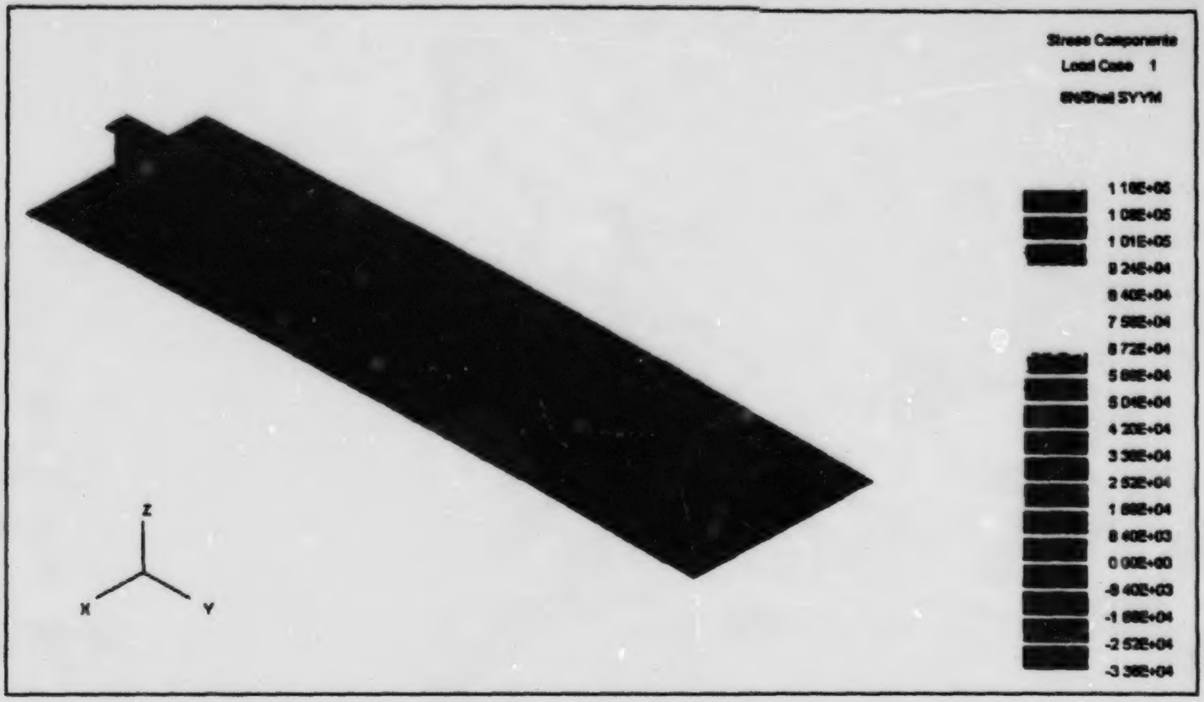

Figure 3.25: Axial Thermal Stress Distribution in the Stiffened Panel Predicted by Using the Eight-Noded Shell Element.

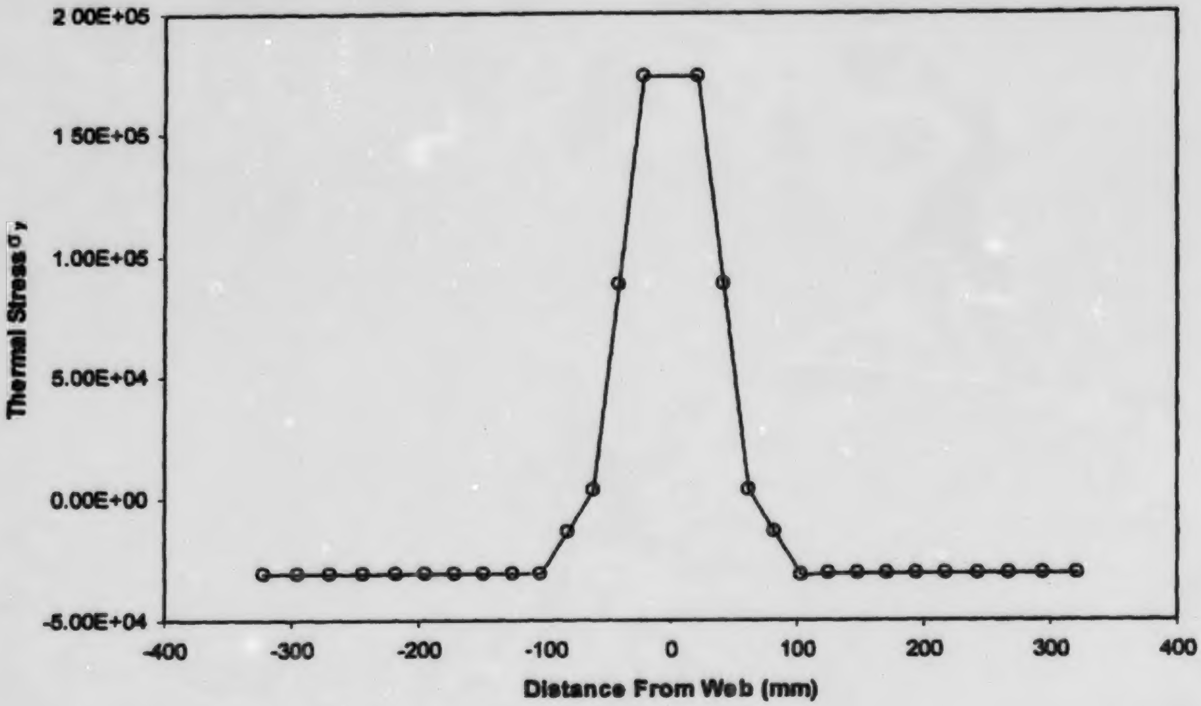

Figure 3.26: Axial Thermal Stress Distribution Along the Plate Width at the End of the Stiffened Panel.

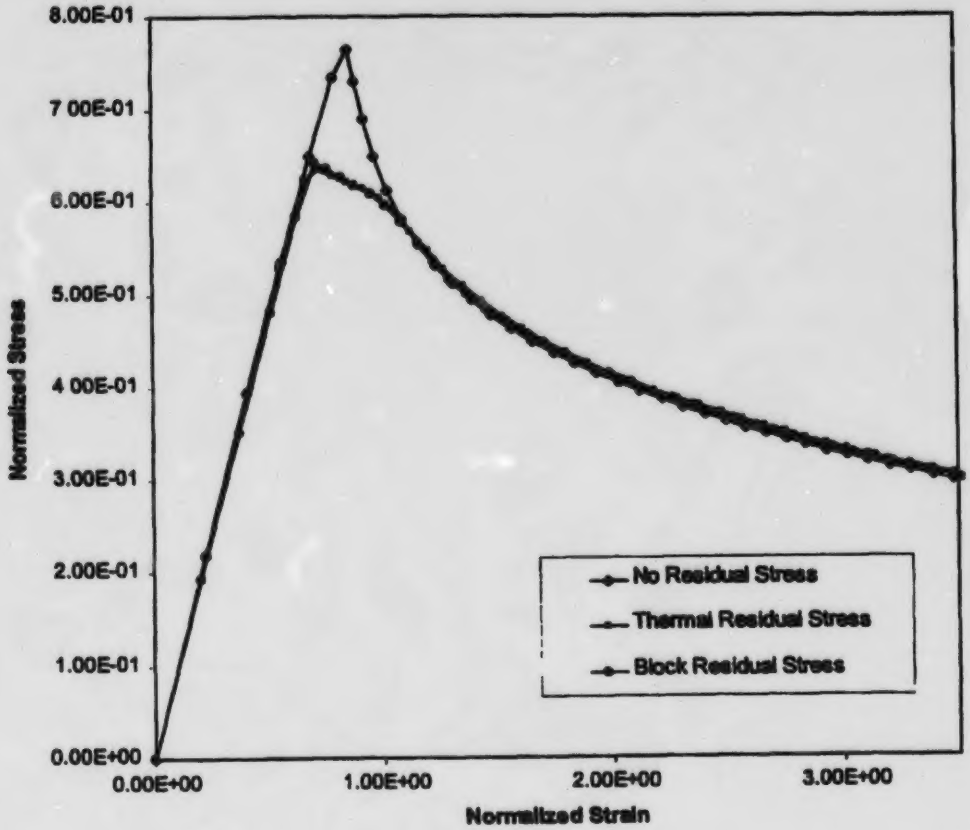

Figure 3.27: Comparison of Load-Shortening Curves Obtained by Using the Eight-Noded Shell Element and Various Residual Stress Distributions.

4. IMPROVEMENT OF THE EFFICIENCY OF STRESS MODULE FOR MULTIPLE DISPLACEMENT VECTORS

In the original STRESS module of the VAST program, the calculation of element stresses for multiple solution vectors included two nested levels of do-loops. The outer loops were for element groups and elements in each group, which involved I/O operations on the element stress matrix file, .T43, whereas the inner loop was over multiple displacement vectors, involving I/O operations of the displacement file. These displacement vectors could result from linear static analyses with multiple load cases, linear dynamic analyses with multiple time steps, or frequency response analyses with multiple excitation frequencies.

In order to permit element ranges for stress calculations to be specified in an arbitrary order, the stress matrix file, .T43, was rewound each time a new data card for an element range was read in. However, it should be noted that if all elements were selected, only one data card needed to be supplied, so the .T43 file was rewound once during the stress computation. For linear static analyses resulting in a single displacement vector, this vector was kept in core during the stress computations, so the I/O operation associated with the displacement file was very small. However, when multiple displacement vectors needed to be processed, they were first copied to a standard sequential scratch file at the beginning of the STRESS module. In this file, each displacement vector was stored on a separate record. This scratch file was then passed into element subroutines and rewound over and over again inside the element loop, so that only one displacement vector was kept in core at a time.

For analyses involving a very large number of displacement vectors, this do-loop structure and file handling procedure could make the STRESS module extremely inefficient, especially when only stresses in a few elements are to be calculated. This was due to the fact that the elapsed time required by repeated I/O operations on the element stress matrix file, .T43, and the displacement file significantly outweighed the time required for arithmetic operations.

In order to improve the efficiency for stress calculation for multiple solution vectors, the STRESS module has been completely restructured under the present contract. This restructuring involved three major modifications to the program:

i. Before calculating stresses, read in all the input data cards defining element ranges required for stress computation and store this information in a global array. Generate an intermediate scratch file which only contains the stress matrices of the specified elements;

ii. Change the order of the do-loops in the STRESS module, so that the outside loop is over the displacement vectors and the inside loop is over the elements which have been selected for stress calculation; and

iii. Keep as many displacement vectors in the core memory as possible, so that the displacement file is processed only once during the execution of the STRESS module and the I/O operations on the scratch file containing element stress matrices are also minimized.

However, it should be realized that in nonlinear analyses, the stress and strain matrices need to be reformulated in the stress module due to the difference in the linearization algorithms for the large rotation field required in the element stiffness and stress calculation modules. As a result, in the improved STRESS module, the element subroutines for linear and nonlinear analyses are treated differently. This, however, will not degrade the performance of VAST, because in nonlinear analyses, a single load case is always considered.

In order to compare the performance of the original and improved STRESS modules in analyses involving single and multiple solution vectors, a ship detail model has been considered. This model is displayed in Figure 4.1, which contained 5340 nodes and 5331 4-noded quadrilateral shell elements. Three groups of VAST runs, which included 1, 50 and 500 solution vectors, respectively, were performed and the elapsed times spent by the original and improved STRESS modules in each case are compared in Table 4.1. Based on these results, it is readily recognized that the modified STRESS module greatly reduces the computation time, especially when large number of displacement vectors exist and stresses are only required in selected elements. The elapsed times spent on I/O operations of the displacement file in the original STRESS module are also shown in bracket. It is evident that this figure grows rapidly with the increase of the number of displacement vectors. As a result, reduction on these I/O operations is extremely effective for improving the overall efficiency of the STRESS module. The only case in which the original STRESS module is more efficient than the improved one is where there is only one displacement vector and stresses in all elements are calculated.

During the above modification of the STRESS module, it was also discovered that on a PC, recalculating element stress matrices in the STRESS module would be far more efficient than writing them to the stress matrix file .T43 in the element stiffness routines and then reading them back to memory in the STRESS module. This is especially true when stresses in only a few elements are calculated. Table 4.2 compared elapsed times taken by each module in an iteration of materially-nonlinear-only and combined geometrically and materially nonlinear analyses of a typical stiffened panel shown in Figure 4.2. In a materially-nonlinear-only analysis with VAST, element strain matrices are stored on .T43 in the element stiffness module and retrieved when element strains and stresses are to be calculated. This implementation method was adopted because the strain matrices in a materially-nonlinear-only analysis are identical to those in regular linear elastic analyses. However, for analysis involving geometric nonlinearity, stress matrices must be reformulated in the STRESS module. Based on the timing results highlighted in Table 4.2, the VAST program is more efficient in a combined nonlinear analysis in the ELEMS1 and STRESS modules, which both involve I/O operations on the .T43 file. These results indicate a potential for further improvement of the ELEMS1 and STRESS modules for both linear and nonlinear analyses.

Table 4.1: Comparison of Elapsed Times Required by the Original and Modified STRESS Modules for Different Numbers of Elements and Load Cases.

Number of Elements for Stress Computation	Elapsed Time (Min.)		Saving (%)
	Original STRESS Module	Modified STRESS Module	
(a) 1 Load Case			
2 Elements	0.059 (0.001)*	0.017	71.19
60 Elements	1.682 (0.001)	0.017	98.99
5331 Elements	0.491 (0.030)	0.549	-11.81
(b) 50 Load Cases			
2 Elements	0.131 (0.043)	0.035	73.28
60 Elements	1.586 (0.235)	0.042	97.35
5331 Elements	20.98 (19.43)	2.332	88.88
(c) 500 Load Cases			
2 Elements	3.242 (2.419)	0.996	69.27
60 Elements	55.71 (32.63)	1.120	97.99
5331 Elements	1622.99 (1607.90)	13.02	99.20

* Times in bracket were associated with I/O operations on the displacement (T52) file.

Table 4.2: Comparison of Elapsed Times Taken by Each Module of Material-Nonlinear-Only and Combined Geometrically and Materially Nonlinear Analyses of a Typical Stiffened Panel Model.

(a) Load Step 1

VAST Module	Materially-Nonlinear-Only		Combined Nonlinear	
	Iteration 1	Iteration 2	Iteration 1	Iteration 2
ELEMS	0.594	0.220	0.254	0.188
DECOM	0.520	0.486	0.478	0.490
LOADS	0.004	-	0.009	-
DISPS	0.155	0.147	0.158	0.169
INTERF	0.058	0.060	0.051	0.050
STRESS	0.477	0.568	0.074	0.102

(b) Load Step 2

VAST Module	Materially-Nonlinear-Only		Combined Nonlinear	
	Iteration 1	Iteration 2	Iteration 1	Iteration 2
ELEMS	0.278	0.211	0.250	0.193
DECOM	0.488	0.472	0.497	0.480
DISPS	0.148	0.145	0.170	0.165
INTERF	0.050	0.057	0.056	0.057
STRESS	0.473	0.572	0.072	0.106

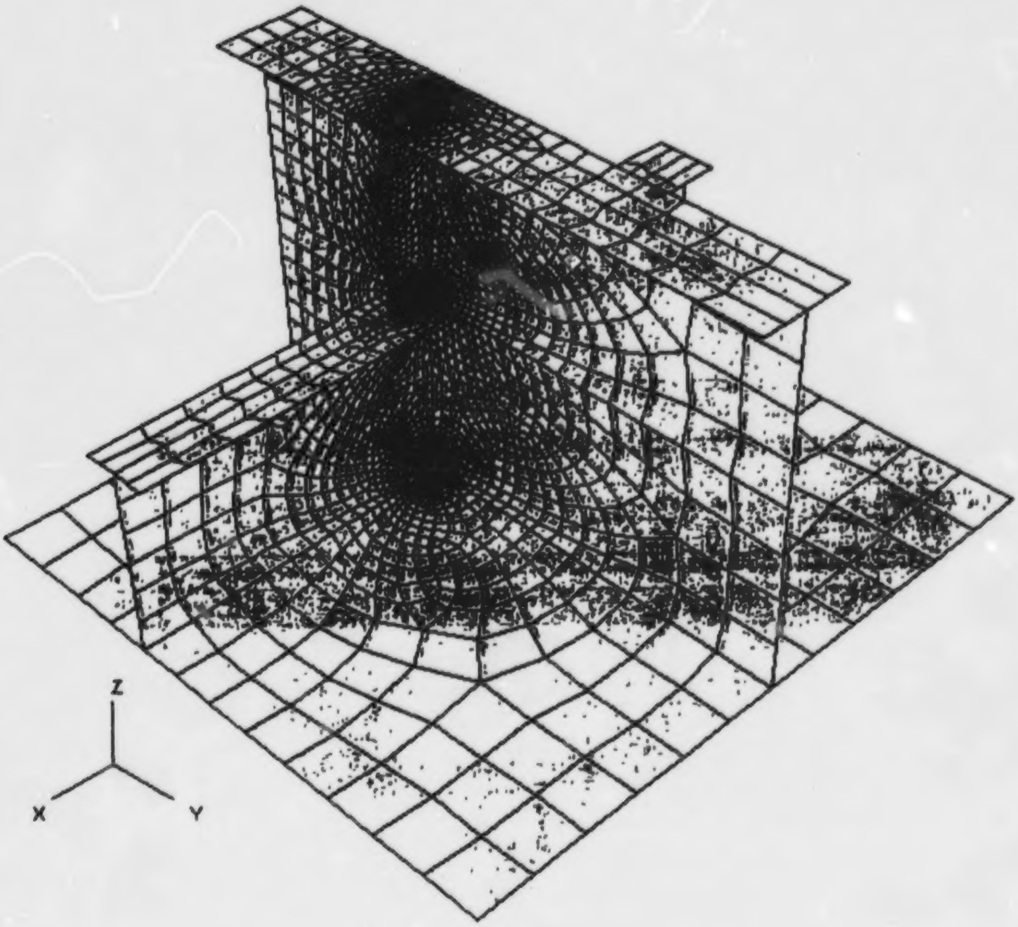

Figure 4.1: A Ship Detail Model Used for Benchmarking the STRESS Module.

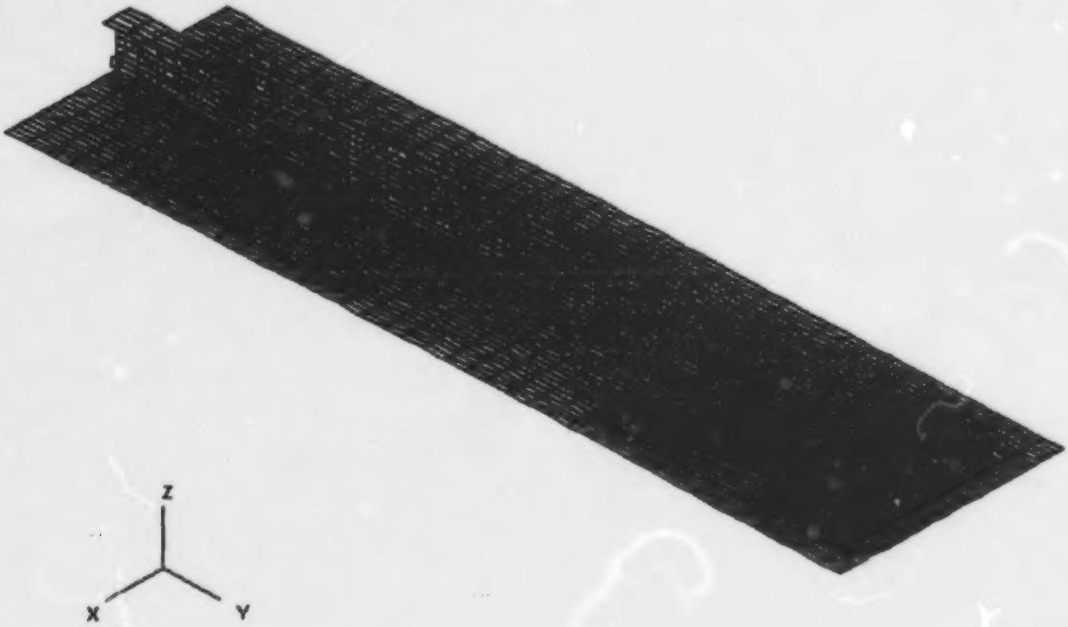

Figure 4.2: A Typical Stiffened Panel Model Used for Benchmarking Nonlinear Analysis Capabilities.

5. IMPLEMENTATION OF MULTIPLE SOLUTION STEP SIZES FOR NON-LINEAR AND DYNAMIC ANALYSES

One of the requirements of the current contract is to provide a capability for nonlinear analysis with variable solution step sizes. This requires the definition of multiple solution blocks with different solution parameters in a single VAST run. As mentioned in previous reports [5.1], there is also a need to fully automate the nonlinear analysis procedure for generating load-shortening curves of stiffened panels which includes a linear static analysis, a linear buckling analysis, a linear thermal stress analysis and finally a nonlinear plastic post-buckling analysis. This analysis procedure could be automated by developing a capability allowing multiple VAST analyses in a single execution. Such a capability has been developed in this work.

In VAST analysis, although several different data files must be provided to describe problem geometry, boundary conditions, external loads and so on, the analysis type and solution parameters are only defined in the .USE file. As a result, the most convenient and effective way of implementing this multiple-analysis capability is to combine the individual .USE files into an extended one, in which each individual .USE file is led by an arbitrary keyword of six characters, unique for each analysis, and ended by the character string "END". The header searching routine in the main module of VAST has been modified so that for a particular analysis, it only searches through the appropriate section of the .USE file corresponding to the present analysis. As a result, the input data for different modules can still be placed in an arbitrary order as before. The VAST execution stops when the end of the .USE file is reached.

To verify this newly developed multiple-analysis capability in the VAST program, three example problems were considered.

Example 1: Geometrically Nonlinear Analysis of A Shallow Spherical Shell. In the first example problem, we solved for the geometrically nonlinear response of a shallow spherical shell, as shown in Figure 5.1. This test problem had been solved previously to verify the nonlinear formulation in the VAST program [5.2]. In the present study, this problem was used to verify the newly developed multiple solution option in VAST. For this purpose, the entire snap-through behavior was traced using four solution blocks with different displacement increments. The load-center deflection curve is presented in Figure 5.2 where data points in different solution steps are distinguished by symbols. This load-shortening curve is in excellent agreement with the one predicted using a constant step size. The .USE file utilized in this analysis is listed in Table 5.1. For the convenience of defining solution increments, the classic displacement control method had been used in all solution blocks in the present analysis. However, it should be noted that a mixture of solution techniques in a single nonlinear analysis is certainly permissible.

Example 2: Linear Dynamic Analysis of a Solid Block. Although the development of the multiple-analysis capability had been motivated by nonlinear static analysis, this technique can obviously utilized in linear and nonlinear dynamic analyses where different time step sizes need to be defined. In the second test example, we considered linear dynamic response of a solid block subjected to a concentrated sinusoidal load at the center of the upper surface, as shown in Figure 5.3. Boundary conditions were applied on the bottom surface of the block, where the z-translation was constrained over the entire surface and minimum restraints were applied in the x-y plane. The dynamic responses of the solid block in the first two periods were obtained using two different VAST analyses. The first run used 160 constant time steps of $0.25\text{x}10^{-3}$ sec., whereas in the second run, three different time steps, $0.25\text{x}10^{-3}$ sec., $0.5\text{x}10^{-3}$ sec. and $1.0\text{x}10^{-3}$ sec., were utilized. The expanded .USE file is given in Table 5.2. Because element stiffness and mass matrices do not change during linear dynamic analysis, they only need to be formulated and assembled once in the first solution block. However, the effective stiffness matrix used in the direct integration algorithm is a function of the time step size, and must be re-formulated and re-decomposed in the second and third solution blocks. The vertical displacement time histories predicted by VAST using the constant and variable time steps are compared in Figures 5.4 and 5.5, for the center and corner nodes, respectively. These two solutions are in very good agreement. The discrepancies between them indicate the different solution accuracy achieved by using different time step sizes.

It is worth pointing out that although the original version of the DISP3 module in VAST possessed a restart capability, it was implied in the program that the time step size was not altered in the restart run. In order to perform dynamic analysis with variable time steps, DISP3 had to be modified. Since in analyses with variable time steps, the time corresponding to a solution vector on the results file, .T52, can no longer be calculated by the product of the time step size and time step number, the time has now been stored on the same record as the solution vector. This format is similar to the load parameter in nonlinear analyses.

Example 3: Automated Load-Shortening Curve Computation of a Typical Stiffened Panel. In the third problem, we conducted a fully automated calculation of the load-shortening curve of a typical stiffened panel as shown in Figure 5.6. To ensure numerical stability, a small amount of a pre-selected linear buckling mode needs to be added to the finite element mesh as additional geometric imperfection. As mentioned in Chapter 2 of this report, for stiffened panels with large geometric imperfections, a linear thermal stress analysis is also required to generate self-equilibrium consistent residual stress pattern. If the original version of VAST is utilized for this analysis, four separate runs, namely a linear static run, a linear buckling run, a linear thermal stress analysis run, and finally a nonlinear run, would have to be performed to obtain a single load-shortening curve. Using the multiple-analysis capability in the present version of VAST, this analysis procedure can be fully automated by using the .USE file given in Table 5.3. The final deformed configuration and the normalized load-shortening curve are displayed in Figures 5.7 and 5.8, respectively.

It should be mentioned at this point that in order to automate the load-shortening analysis problem, VAST had been modified to overcome a difficulty observed with regard to the specification of the amplitude of the selected buckling mode shape to be added to the finite element model. In VAST, a node number, a degree-of-freedom and the amplitude of mode shape at the specified DOF must be supplied. However, this node number and degree-of-freedom can not be determined prior to the buckling analysis. In order to resolve this problem, the VAST program was modified to allow the user to provide either the node number or the degree-of-freedom, and let VAST to determine the appropriate degree-of-freedom or the appropriate node number according to the maximum displacement in the specified eigenmode.

Table 5.1: USE File for Geometrically Nonlinear Analysis of a Hinged Shallow Spherical Shell Subjected to a Center Point Load Using Variable Displacement Increments

```
BLK1
SHALLOW SPHERICAL SHELL, MITC4 (IEC=5), 3X3 MESH
    1    1    1    0
    1   10 1.000E+05    1    3 300.00000   -1
    0 0.000E+00
    2
    1    3-1.000E+01
    1    0    0    0    0    3    0    1    1    1
IELEMA
    1    0    0    1    0
IASSEM
    2    1
ISTIFM
    1    0
IDECOM
    1    0
ILOAD1
    0    1    0    0
IDISP1
    0    0    0    0    0
INTERF
    0    0
ISTRES
    0    0
    0
END
BLK2
SHALLOW SPHERICAL SHELL, MITC4 (IEC=5), 3X3 MESH
    1    1    1    0
   11   30 1.000E+05    1    3 300.00000   -1
    0 0.000E+00
    2
    1    3-0.500E+01
    1    0    0    0    0    3    0    1    1    1
IELEMA
    1    0    0    1    0
IASSEM
    2    1
ISTIFM
    1    0
IDECOM
    1    0
ILOAD1
    0    1    0    0
IDISP1
    0    0    0    0    0
INTERF
    0    0
ISTRES
    0    0
    0
END
BLK3
SHALLOW SPHERICAL SHELL, MITC4 (IEC=5), 3X3 MESH
    1    1    1    0
   31   50 1.000E+05    1    3 300.00000   -1
    0 0.000E+00
    2
    1    3-0.250E+01
    1    0    0    0    0    3    0    1    1    1
IELEMA
    1    0    0    1    0
IASSEM
    2    1
ISTIFM
    1    0
IDECOM
    1    0
ILOAD1
    0    1    0    0
IDISP1
    0    0    0    0    0
INTERF
    0    0
ISTRES
    0    0
    0
END
BLK4
SHALLOW SPHERICAL SHELL, MITC4 (IEC=5), 3X3 MESH
    1    1    1    0
   51   60 1.000E+05    1    3 300.00000   -1
    0 0.000E+00
    2
    1    3-1.000E+01
    1    0    0    0    0    3    0    1    1    1
IELEMA
    1    0    0    1    0
IASSEM
    2    1
ISTIFM
    1    0
IDECOM
    1    0
ILOAD1
    0    1    0    0
IDISP1
    0    0    0    0    0
INTERF
    0    0
ISTRES
    0    0
    0
END
```

Table 5.2: USE File for Linear Dynamic Analysis of a Solid Block Using Variable Time Steps

```
TBLCK1
8-NODE SOLID, LINEAR DYNAMICS, TIME BLOCK 1
     0     0     0
     1     0     1     1     1     1     0     1     3     0     0
IELEMA
     1     0     1     1     0
IASSEM
     0     1
ISTIFM
     1     1
IMASSM
     0     0     0
     0
IDECOM
     3     0
 0.0002500
ILOAD1
     0     1     0     0
IDISP3
    40     0     0     0     0     0     0     0     0     0
END
TBLCK2
8-NODE SOLID, LINEAR DYNAMICS, TIME BLOCK 2
     0     0     0
     0     0     0     0     0     1     0     0     3     0     0
IDECOM
     3     0
 0.0005000
IDISP3
    20    40     0     0     0     0     0     0     0     0
END
TBLCK3
8-NODE SOLID, LINEAR DYNAMICS, TIME BLOCK 3
     0     0     0
     0     0     0     0     0     1     0     0     3     0     0
IDECOM
     3     0
 0.0010000
IDISP3
    20    60     0     0     0     0     0     0     0     0
END
```

Table 5.3: USE File for Automated Load-Shortening Curve Calculation of a Typical Stiffened Panel.

```
LINEAR
load shortening stiffened panel model (lsp30)
    0    0    1    0
    1    0    0    0    0    3    0    1    1    1

IELEMA
    1    0    0    1    0
IASSEM
    0    1
ISTIFM
    1    0
IDECOM
    1    0
ILOAD1
    0    1    0    0
IDISP1
    0    0    0    0    1
ISTRES
    0    0
    0
END
BUCKLING
load shortening stiffened panel model (lsp30)
    0    0    0    0
    1    0    1    1    0    1    1    0    0    0

IELEMA
    1   -2    0    1    0
IASSEM
    0    1
ISTIFM
    1    0
IDECOM
    1    0
IEIGN1
    1    0    1    1
    1    2  500 0.000E+00
END
THERMAL
load shortening stiffened panel model (lsp30)
    0    0    1    0
    1    0    0    0    0    3    0    1    1    1

IELEMA
    5    0    0    1    0    1
    2    0    3 0.611E+00
IASSEM
    0    1
ISTIFM
    1    0
IDECOM
    1    0
ILOAD1
    0    1    0    0
IDISP1
    0    0    0    0    1
ISTRES
    0    0
    0
END
```

```
NONLINEAR
load shortening stiffened panel model (lsp30)
    1    1    1    0
    1   80 0.350E+21 1091    2 14.735563   10
   10 0.000E+00
    4
 1091    2 0.515324    5    0.2000    1.0000
    1    0    0    0    0    3    0    1    1    1

IELEMA
    5   -3    0    1    0
    2    0    3 0.611E+00
IASSEM
    0    1
ISTIFM
    1    0
IDECOM
    1    0
ILOAD1
    0    1    0    0
IDISP1
    0    0    0    0    1   33
    1    2    3    4    5    6    7    8    9   10   11   12   13   14   15   16
   17   18   19   20   21   22   23   24   25   26   27   28   29   30   31   32
   33
INTERF
    0    0
ISTRES
    0    0
    0
END
```

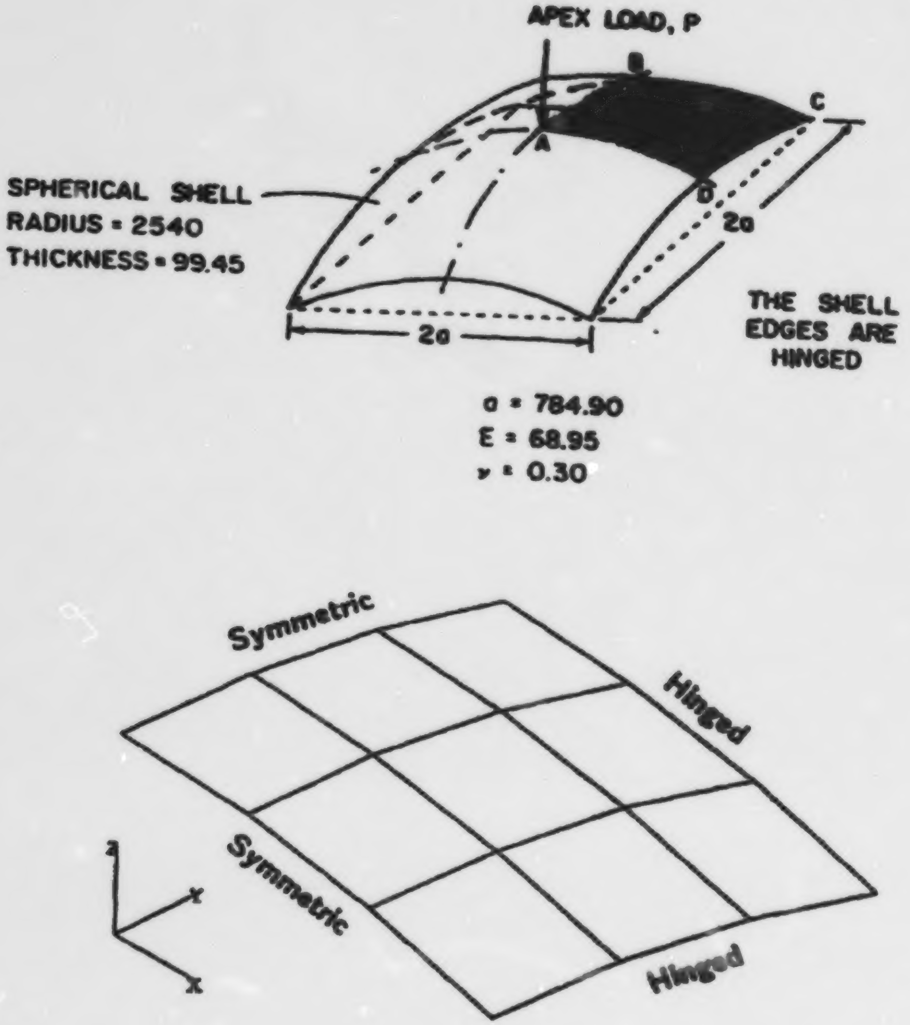
APEX LOAD, P
B
C
A
D
SPHERICAL SHELL
RADIUS = 2540
THICKNESS = 99.45
2a
2a
THE SHELL EDGES ARE HINGED
a = 784.90
E = 68.95
ν = 0.30
Symmetric
Hinged
Symmetric
Hinged
z
y
x

Figure 5.1: Problem Geometry, Material Property and Finite Element Mesh for Geometrically Nonlinear Analysis of a Shallow Spherical Shell.

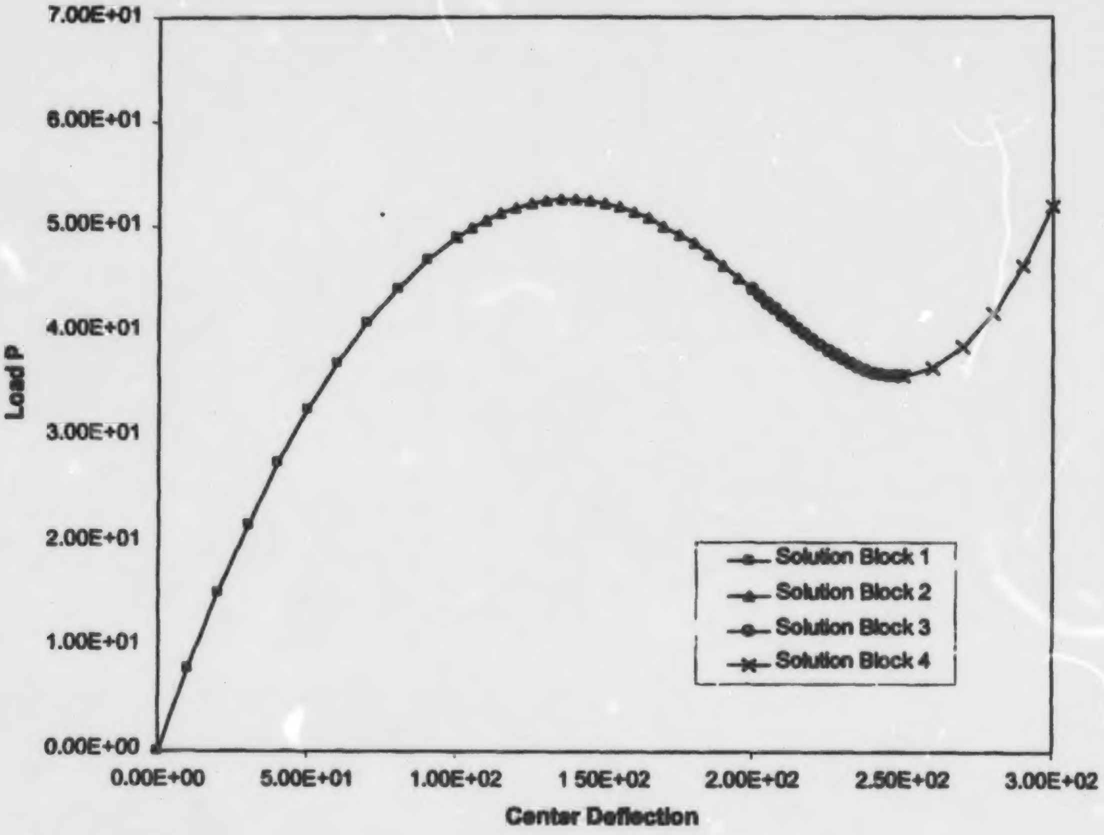

Figure 5.2: Load-Center Deflection Curve of the Spherical Shell Predicted Using Four Different Displacement Increments.

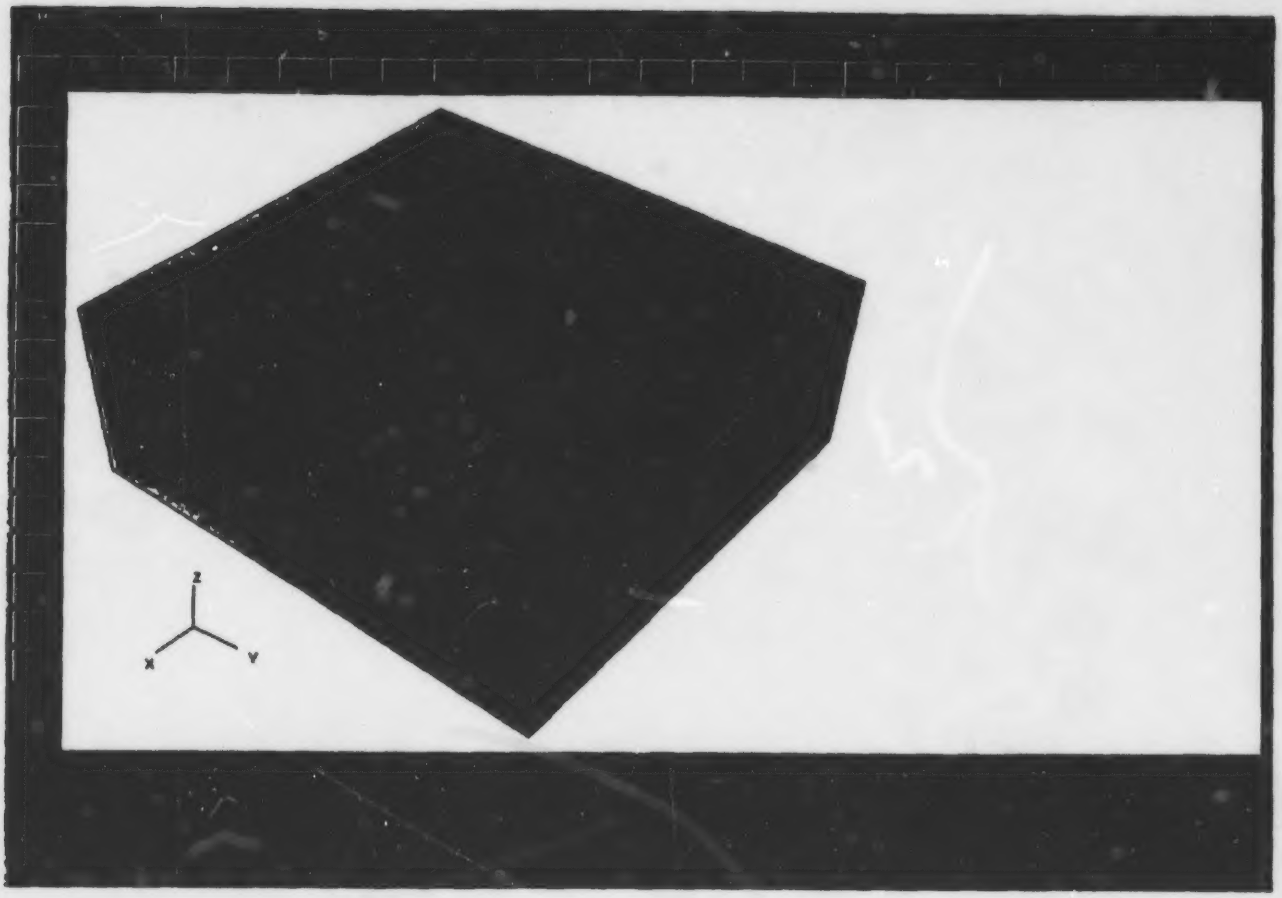

Figure 5.3: Finite Element Mesh of a Solid Block Employed for Linear Dynamic Analysis.

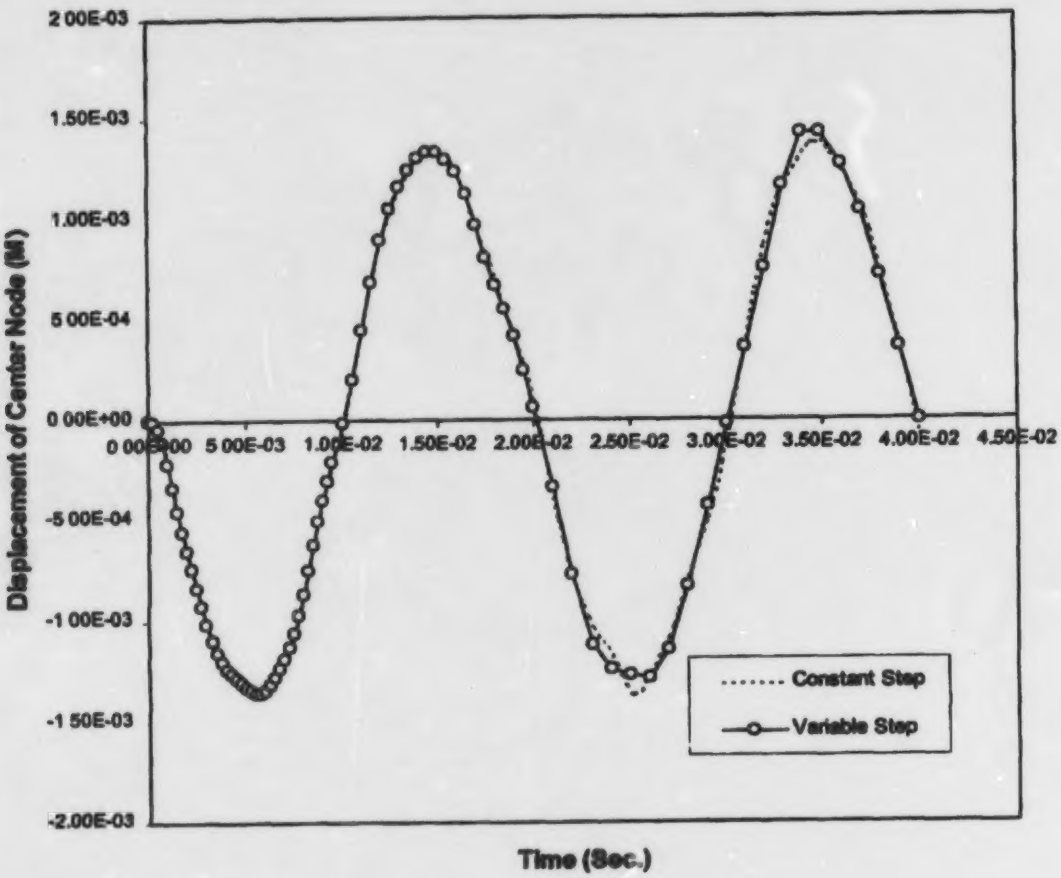

Figure 5.4: Comparison of Time Histories of Center Vertical Displacement Obtained Using Constant and Variable Time Steps.

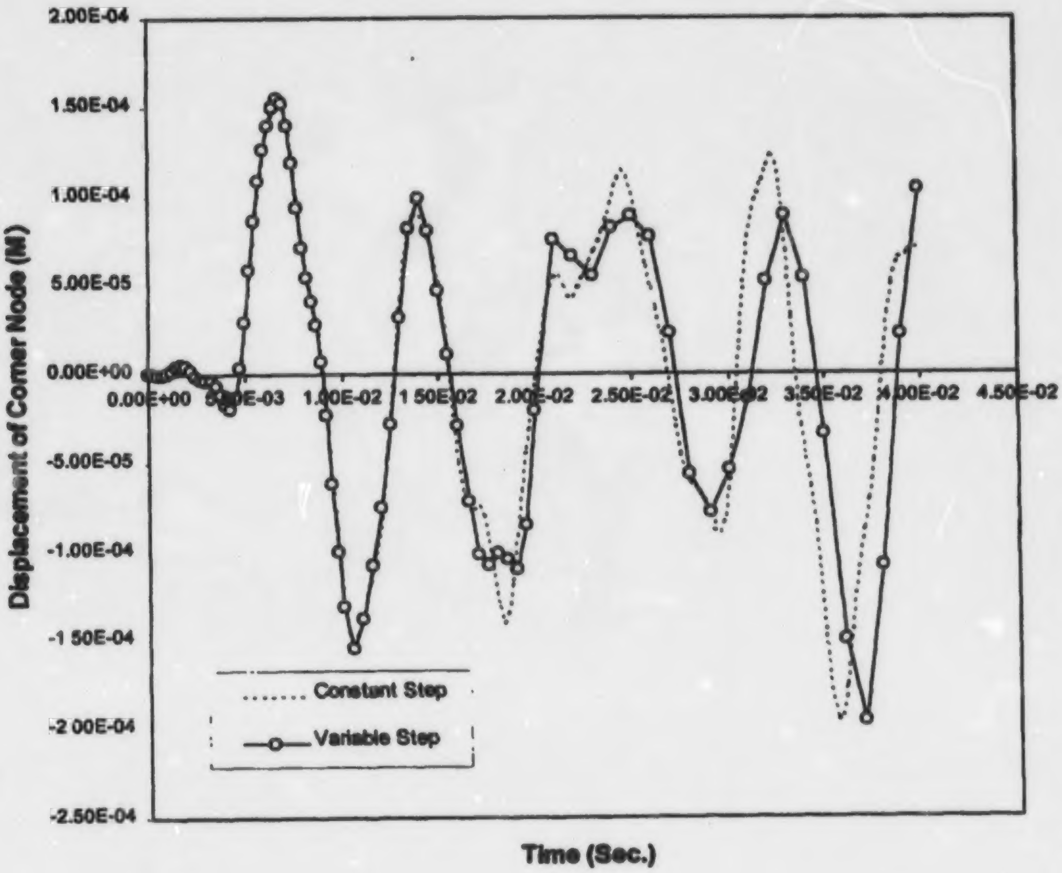

Figure 5.5: Comparison of Time Histories of Corner Vertical Displacement Obtained Using Constant and Variable Time Steps.

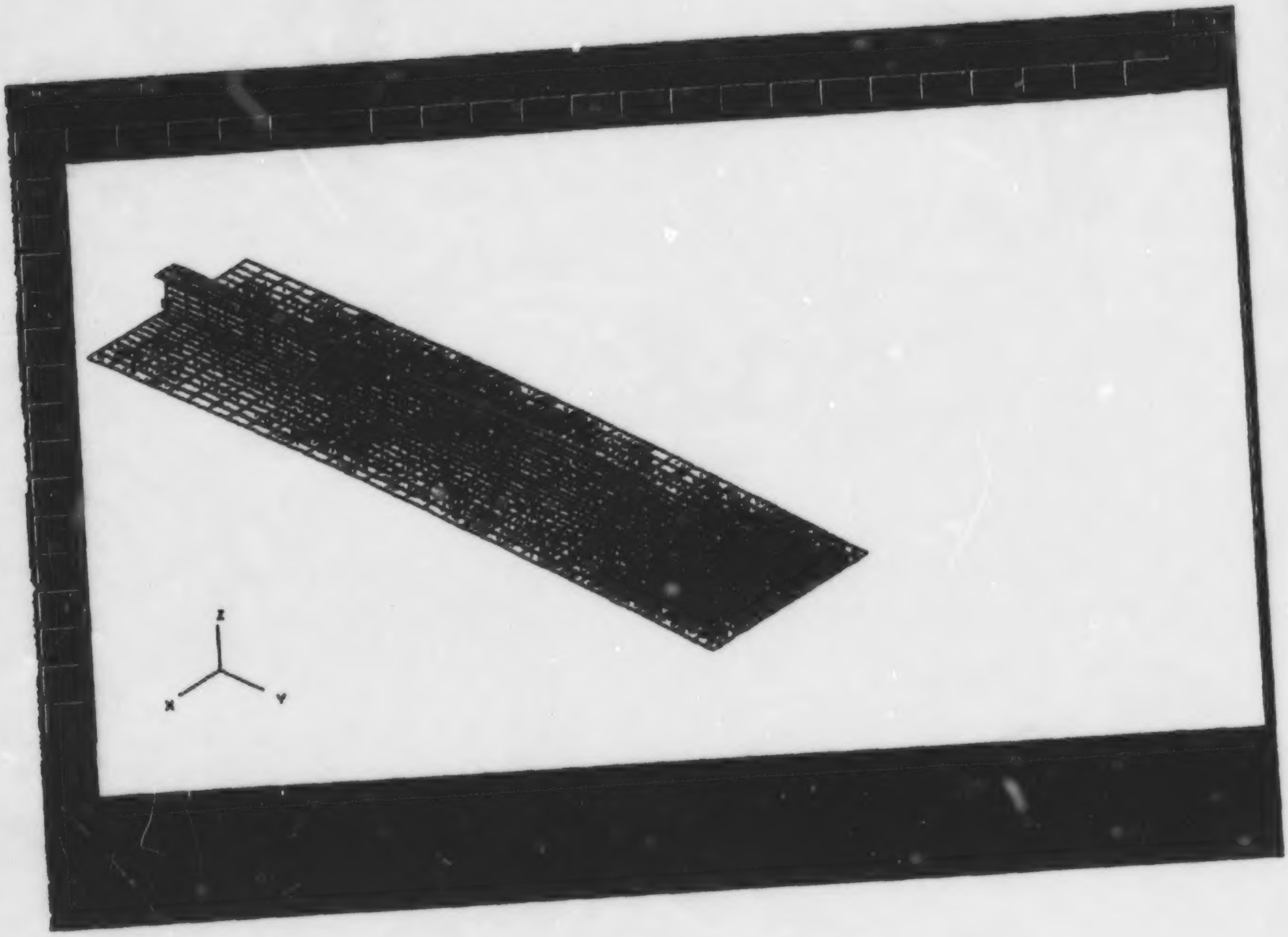

Figure 5.6: Finite Element Mesh of A Typical Stiffened Panel for Load-Shortening Curve Calculation.

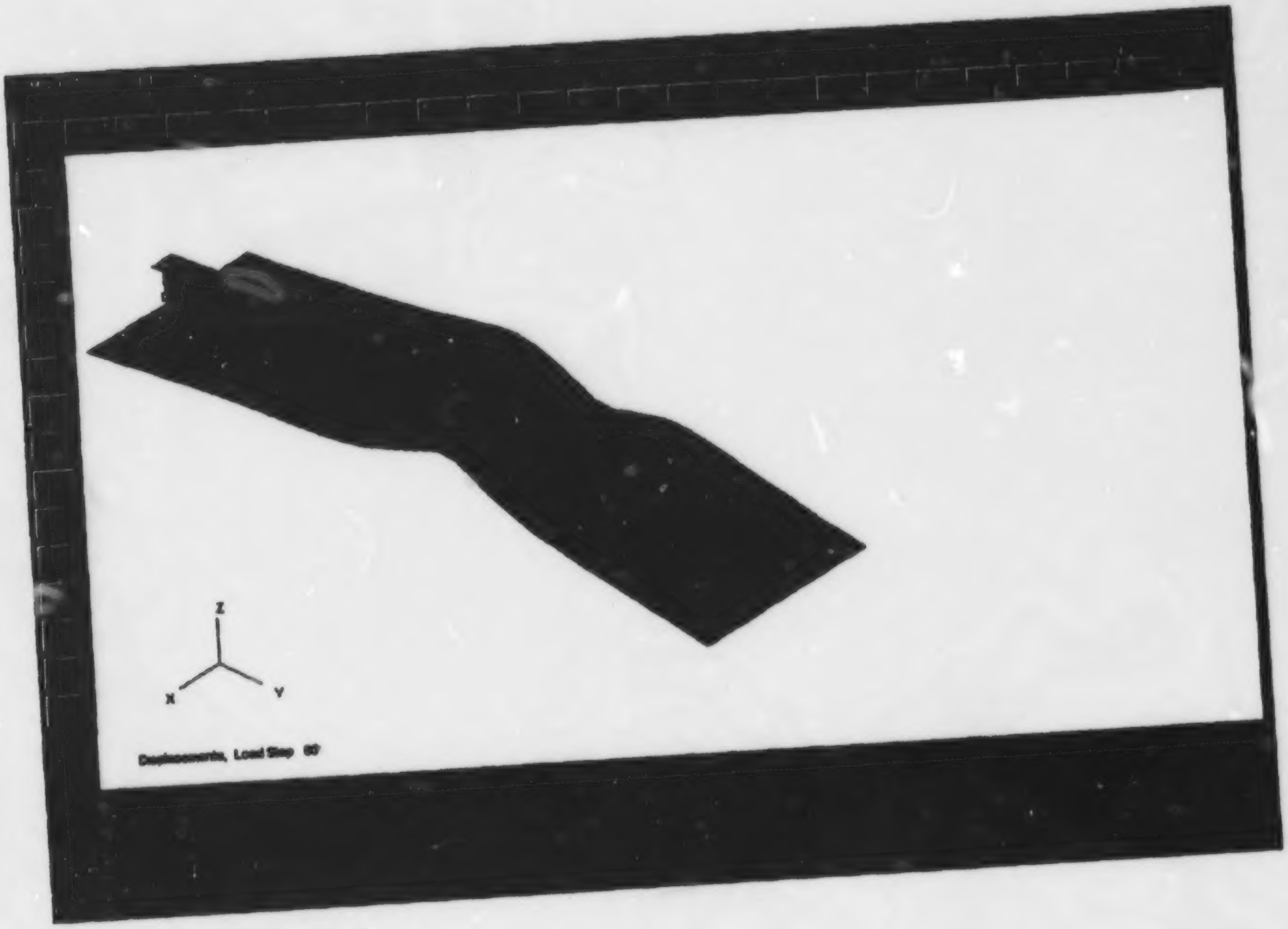
Z
X
Y
Displacements, Load Step

Figure 5.7: Final Deformed Configuration of the Stiffened Panel Predicted Fully Automatically by VAST.

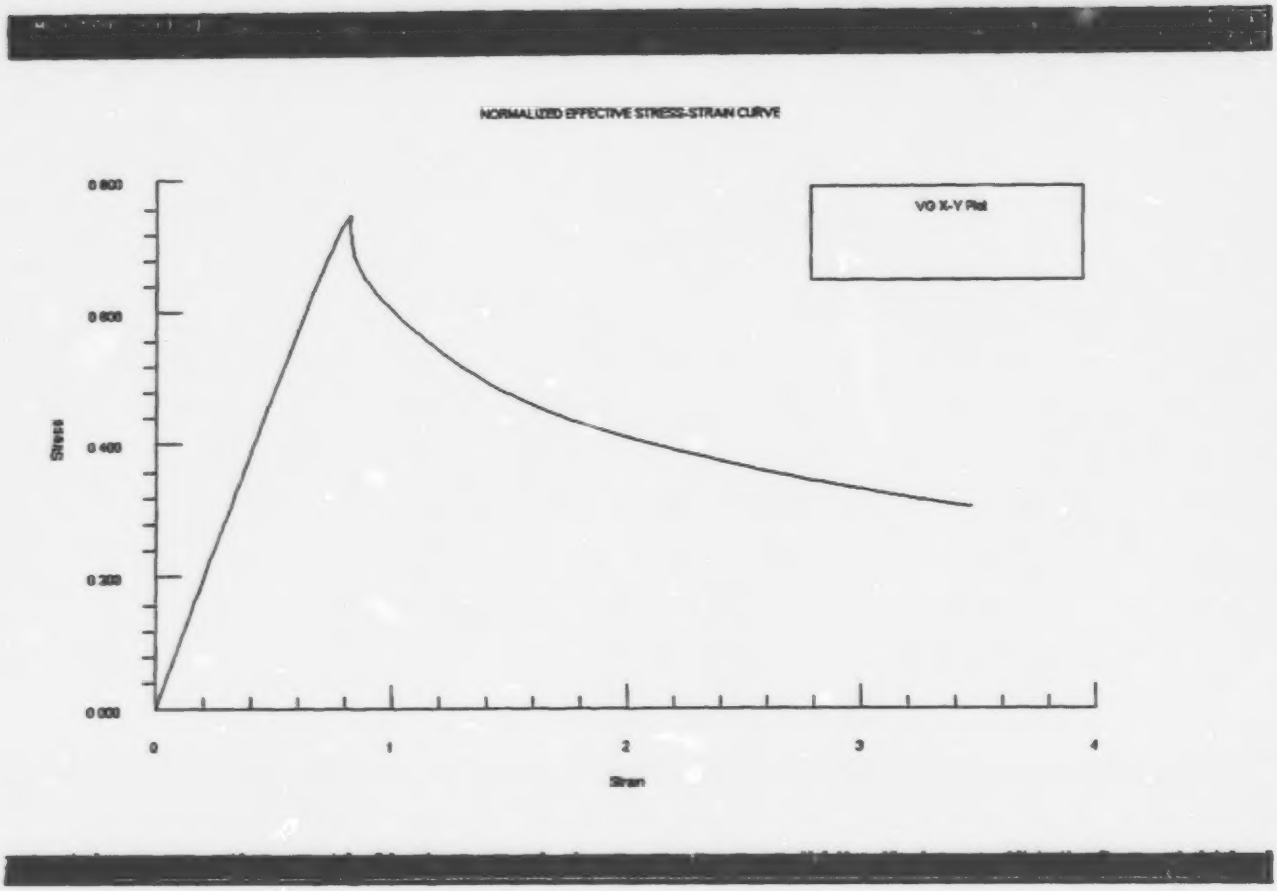

Figure 5.8: The Normalized Load-Shortening Curve of the Stiffened Panel Predicted Fully Automatically by VAST.

6. USE OF FOURIER SERIES TO DEFINE ADDITIONAL GEOMETRIC IMPERFECTIONS FOR STIFFENED PANELS

In plastic, post-buckling finite element analyses for generating load-shortening curves of stiffened panels, including stiffener imperfection and plate imperfection are normally used to describe the degree of initial distortions in the stiffened panel [6.1]. Because these initial distortions are usually measured at the centers of stiffener and plates on real ship structures, half sine wave distributions have been utilized to express the axial variation of these imperfections.

However, for some stiffened panels, especially those with large column slenderness ratio, λ, these geometric imperfections are insufficient for ensuring numerical stability in highly nonlinear finite element analyses. An analysis procedure for improving the stability and reliability of nonlinear analyses was developed and presented in References [6.1] and [6.2]. In this procedure, a small magnitude of a selected linear buckling mode shape was added to the finite element mesh of the stiffened panel as an additional geometric imperfection. Although this method had been proved to be very effective, it required a linear elastic analysis and a linearized buckling analysis before the nonlinear run could take place. As a result, additional computational effort was required for this procedure. Under the present contract, it was intended to develop a simplified procedure in which the additional imperfections were represented using Fourier series, and consequently, eliminate the need for the linear elastic and buckling analyses.

In order to study the sensitivity of the nonlinear finite element solutions to the form and magnitude of the added imperfection, a stiffened panel which had been studied extensively in Reference [6.1] was reconsidered. This panel was defined by the following parameters:

$$\beta = 3.0,\ \lambda = 0.9,\ A_S/A = 0.35,\ \omega_0 = 0.1\,\beta^2 t.$$

Stiffener type Tee #4 and the end-to-end boundary condition were still utilized as in earlier studies [6.1]. The finite element mesh of this panel is shown in Figure 6.1.

As has been experienced before, when only the original half-sine geometric imperfections were included, numerical difficulties were encountered in the nonlinear analysis. As shown in Figure 6.2, the peak load was significantly over estimated. Furthermore, serious convergence difficulty appeared in the post-buckling range right behind the peak load, so the automatic solution step adjustment algorithm in VAST reduced the solution step size considerably, making the nonlinear analysis impractical. The final deformed configuration is shown in Figure 6.3, which shows higher order sine components which did not exist in the original initial geometric imperfection.

After superimposing a very small magnitude of the first buckling mode shape onto the stiffened panel as an additional imperfection, the VAST nonlinear analysis finished without any numerical difficulty and the predicted peak load was significantly lower than the one obtained with only the original stiffened and plate imperfections, as also indicated in Figure 6.2. The buckling mode added to the finite element model is shown in Figure 6.4 and the maximum additional distortion was only 1/32 of the original imperfection at the plate center. The final deformed configuration of the stiffened panel predicted using the additional imperfection is displayed in Figure 6.5, where large plastic deformations are localized at the mid-span of the stiffened panel, as typically seen in collapsed stiffened panels [6.3].

In order to introduce higher order sine components of initial distortions onto the finite element model of stiffened panels, the automatic finite element model generator, LSPANEL, which was initially developed in a previous contract [6.1], was modified to include up to four higher-order imperfection terms in addition to the existing half-sine stiffener and plate imperfections. These higher-order terms corresponded to three, five, seven and nine half sine waves in the axial direction. The amplitudes of these sine terms were scaled along the length so that maximum imperfections always appeared at the mid-span. Based on the earlier observations to the buckling mode shapes, an anti-symmetric variation of the higher-order imperfection terms was assumed in the lateral direction of the stiffened panel. The patterns of the higher-order imperfections corresponding to three, five, seven and nine half sine waves are presented in Figures 6.6-6.9, respectively. The magnitudes of the imperfections added to the finite element model are controlled by four coefficients, a_3, a_5, a_7, a_9, which are defined as ratios of the magnitudes of the higher-order sine imperfections to the maximum original imperfection at the plate center.

Comparing these higher-order sine wave imperfections with the buckling mode shape, it was readily recognized that the shape of the nine half sine wave imperfection shown in Figure 6.9 was in close correlation with the buckling mode shape presented in Figure 6.4. For this reason, numerical results were first obtained by adding different amounts of the nine half-sine wave imperfection into the finite element model. The predicted load-shortening curves are compared with the earlier solutions in Figure 6.10. For all three nonlinear analyses, complete plastic, post-buckling behavior of the stiffened panel was obtained without any numerical difficulties. However, to reach the same peak load level, a much larger amplitude of the higher-order sine imperfection had to be used than that of the buckling mode. Due to the large amplitude, the use of higher-order sine wave imperfections resulted in an underestimation of the pre-buckling of the stiffened panel. The final deformed shapes predicted by using different amounts of higher-order sine imperfection were virtually identical, so only one of them is shown in Figure 6.11. This deformed shape is in excellent agreement with the one shown in Figure 6.5 predicted by using the first buckling mode as additional imperfection.

In order to investigate the effect of other sine waves on the predicted nonlinear behavior of stiffened panel, two additional runs were conducted, one with only the nine half sine wave term, and the other with all four higher-order imperfection terms added. The load-shortening curves obtained in these two analyses are almost identical as shown in Figure 6.12. This finding suggested that adding the higher-order sine wave components, which are not contained in the lowest buckling mode shape, onto the finite element model had virtually no impact on the nonlinear solution. This observation was very important to the present procedure as it indicated that nonlinear analyses using a uniform distribution of the higher-order sine wave functions as additional imperfections would work just as well as those using exact Fourier series representations of linear buckling mode shapes. Furthermore, as shown in Figure 6.13, the amplitudes of these higher-order imperfection components could be selected quite arbitrarily as long as they remained small comparing with the original imperfection.

In order to ensure that the procedure for using higher-order sine functions to replace buckling mode shape in load-shortening curve computations was applicable to all stiffened panels required in the data base, we calculated the buckling mode suitable for being used in nonlinear analyses for 16 representative stiffened panel configurations. The results are presented in Figures 6.14 to 6.29. A review of these buckling modes indicated that all of them could be sufficiently represented by the four half-sine functions shown in Figures 6.4-6.9.

Although the above results did confirm the possibility of using of higher-order Fourier terms to define additional geometric imperfection required by nonlinear analyses, the use of buckling mode shapes still appeared to be more favorable, due to its generality, robustness and accuracy. As had been demonstrated in Chapter 5, using the newly developed multiple-analysis capability of VAST, the nonlinear analysis procedure based on buckling mode shape could be fully automated and performed in a single execution of the VAST program. For this reason, the use of buckling mode in load-shortening curve computation is highly recommended.

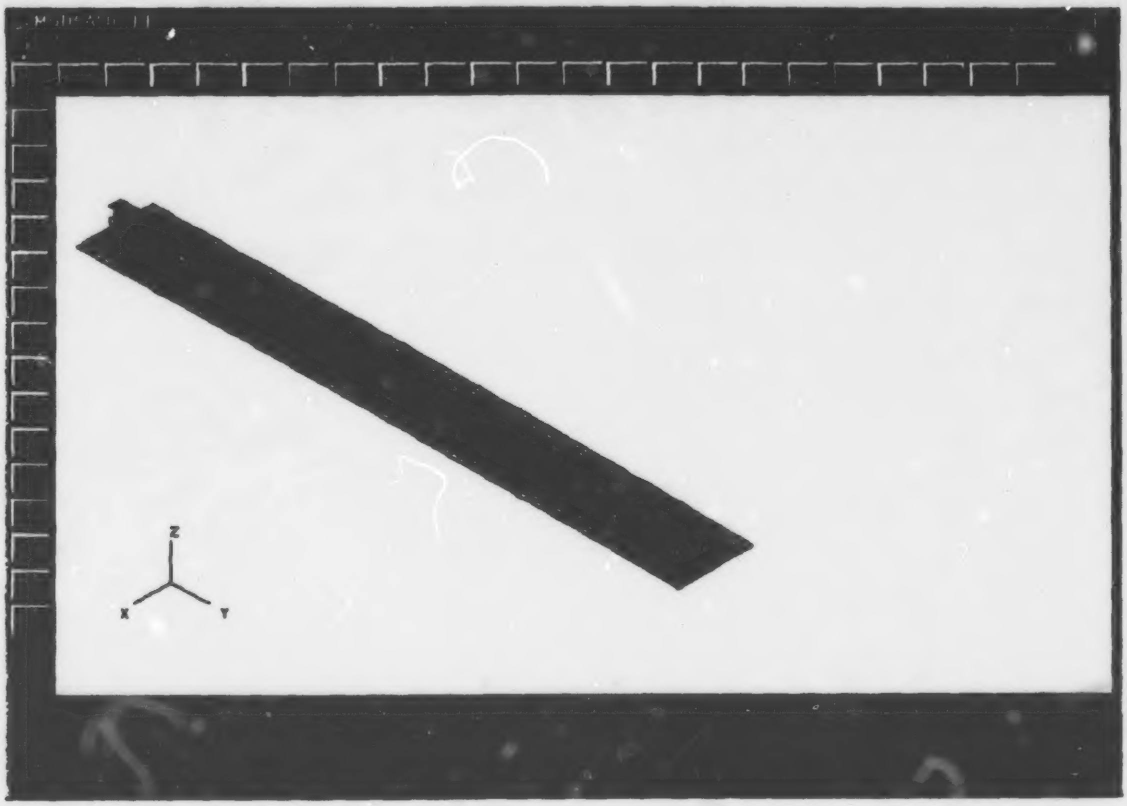

Figure 6.1: Finite Element Mesh for Stiffened Panel with Geometric Parameters: β=3.0, λ=0.9, A_r=0.35, ω_0=0.1 β^2t.

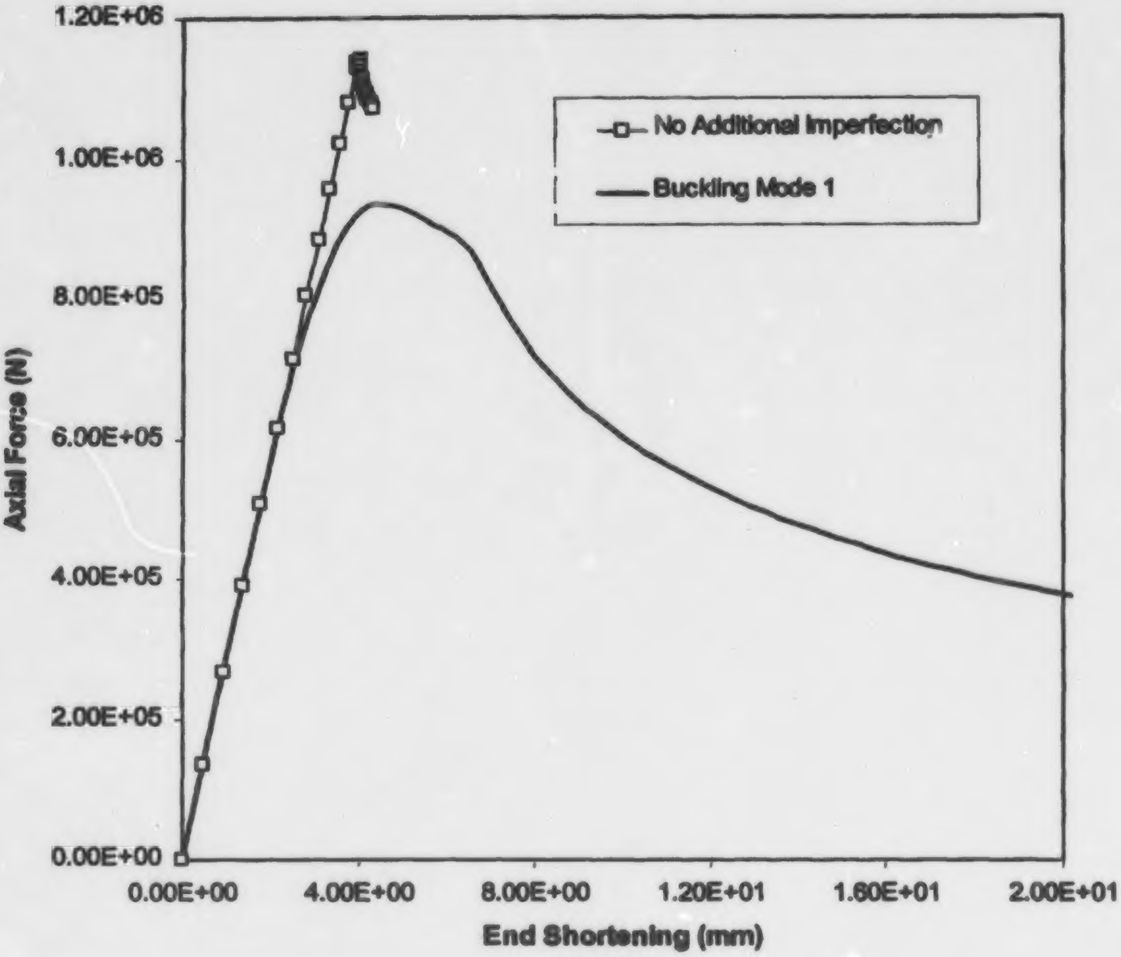

Figure 6.2: Load-Shortening Curves of the Stiffened Panel Obtained by Using the Original and Additional Geometric Imperfection Based on Buckling Mode.

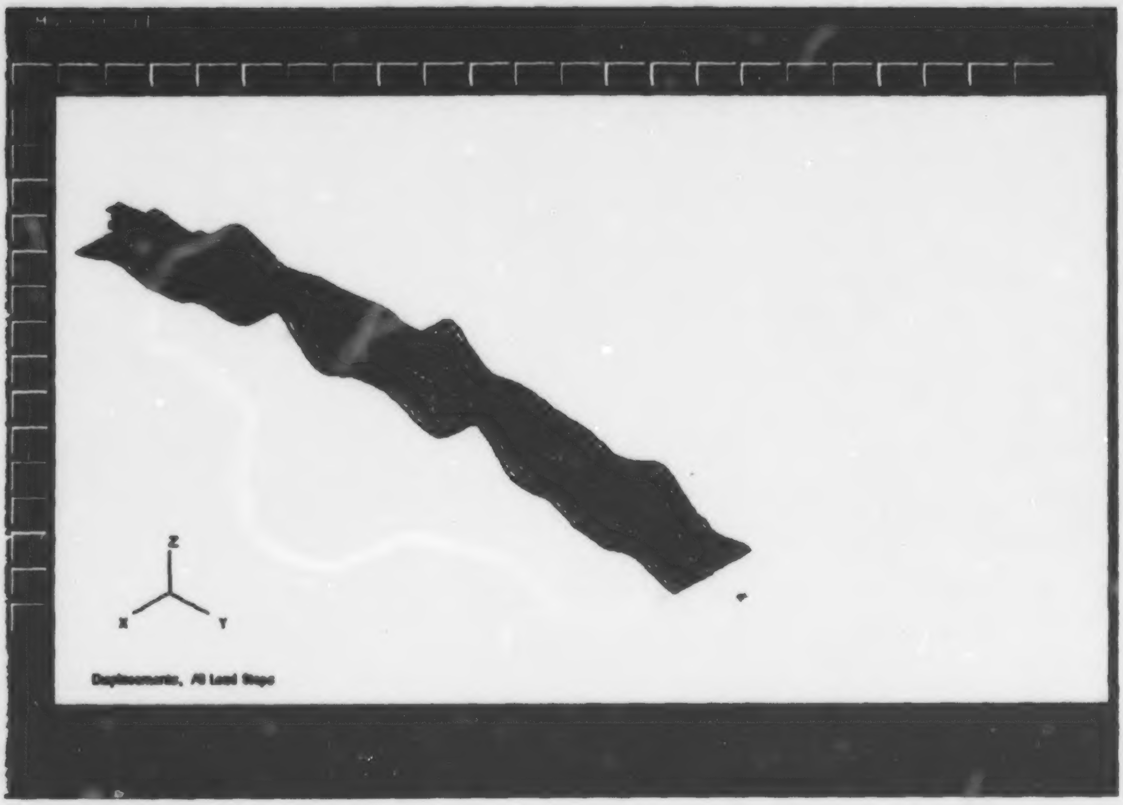
Z
X
Y
Displacements, All Load Steps

Figure 6.3: Final Deformed Configuration of the Stiffened Panel Obtained by Using Only the Original Stiffener and Plate Imperfections.

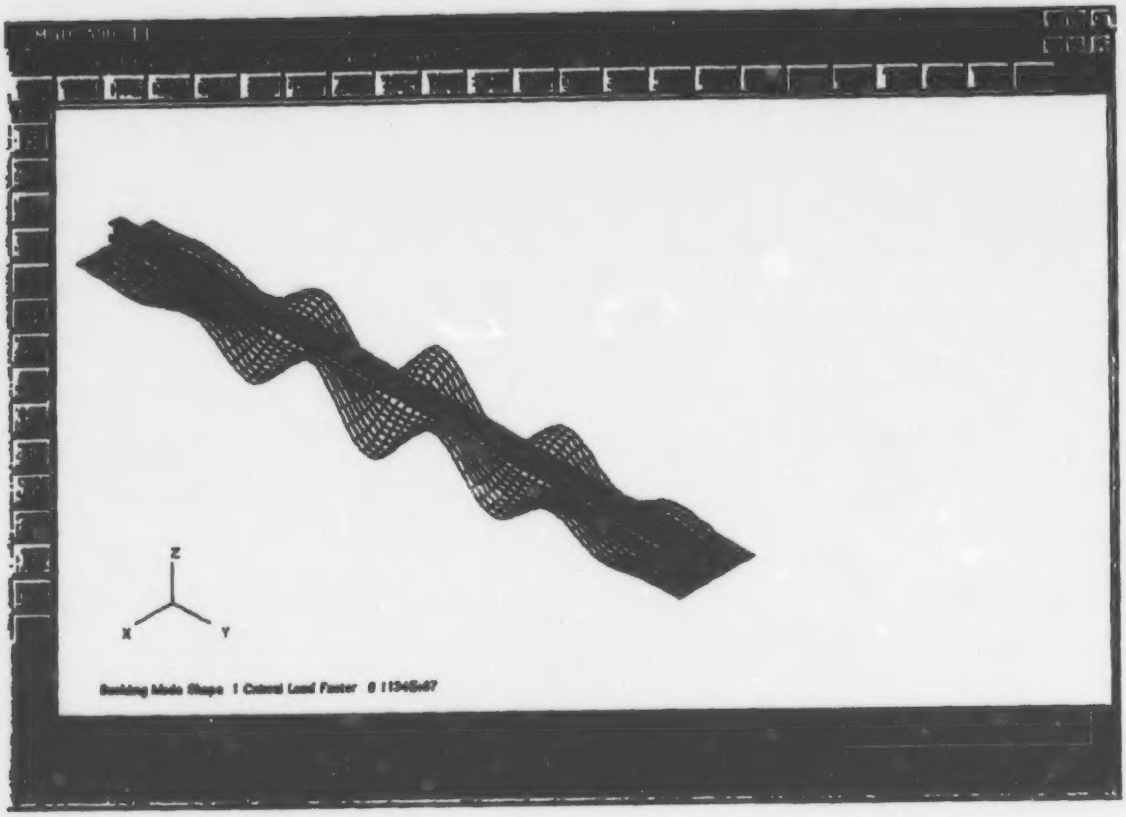
Z
X
Y
Buckling Mode Shape 1 Critical Load Factor 0.1134E+07

Figure 6.4: The Linear Buckling Mode Shape Superimposed Onto the Finite Element Model as Additional Imperfection.

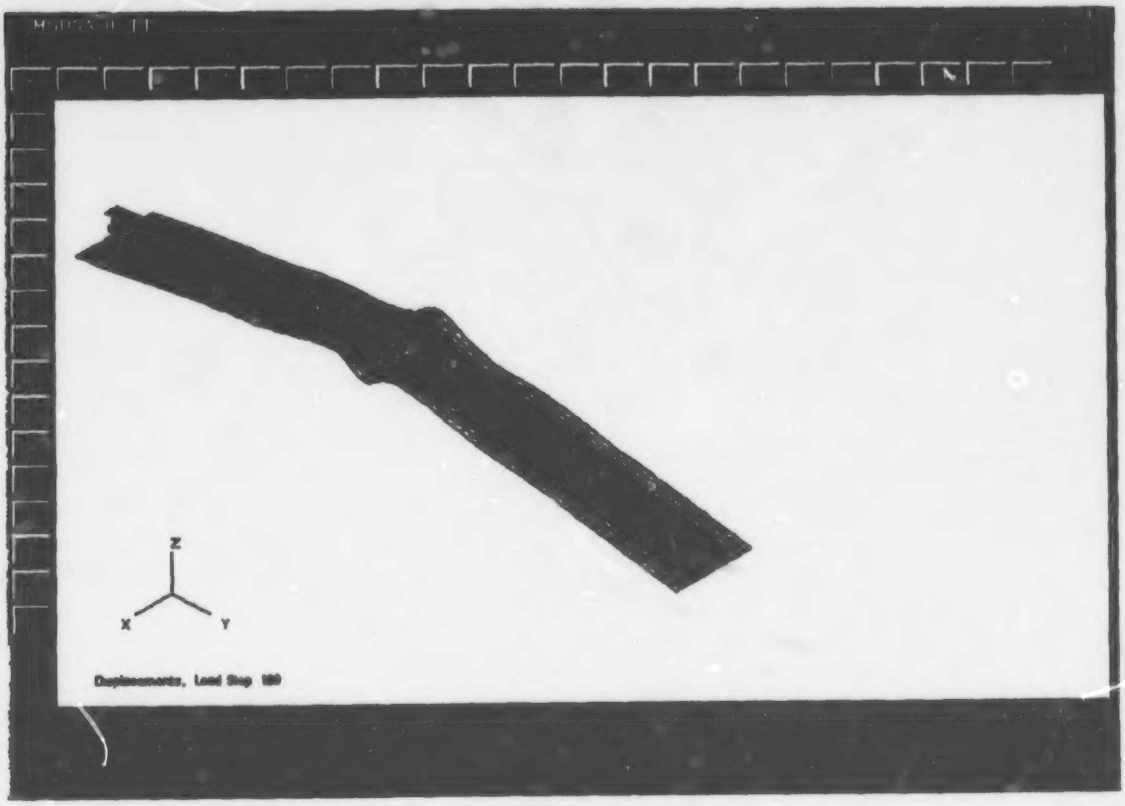
Z
X
Y
Displacements, Load Step 100

Figure 6.5: Final Deformed Configuration of the Stiffened Panel Obtained by Using the Buckling Mode Shape as Additional Imperfection.

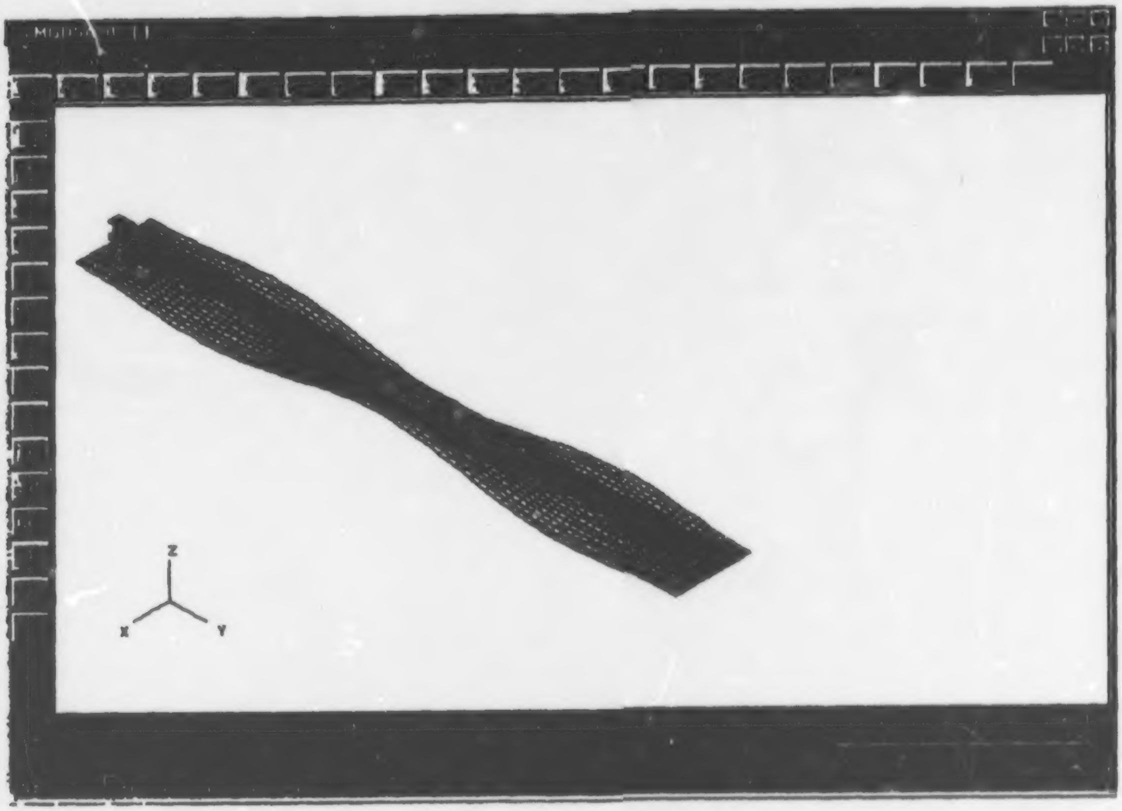

Figure 6.6: Higher-Order Imperfection Pattern with Three Half Sine Waves.

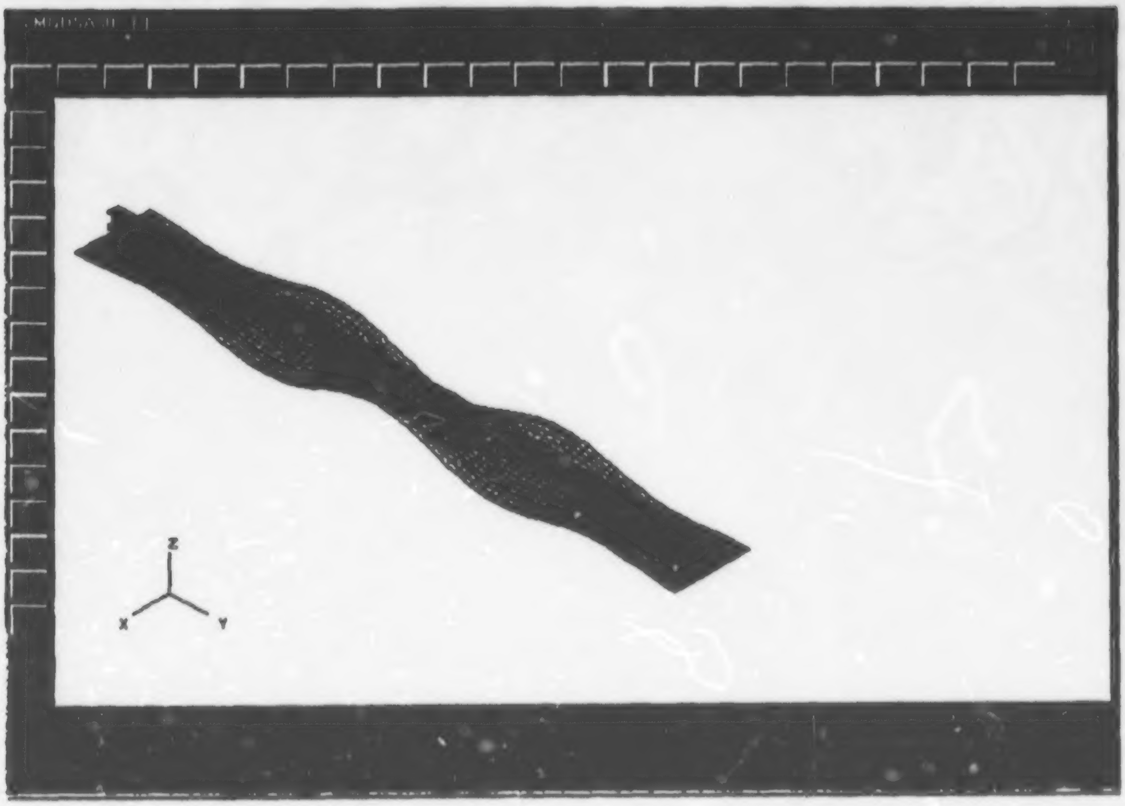

Figure 6.7: Higher-Order Imperfection Pattern with Five Half Sine Waves.

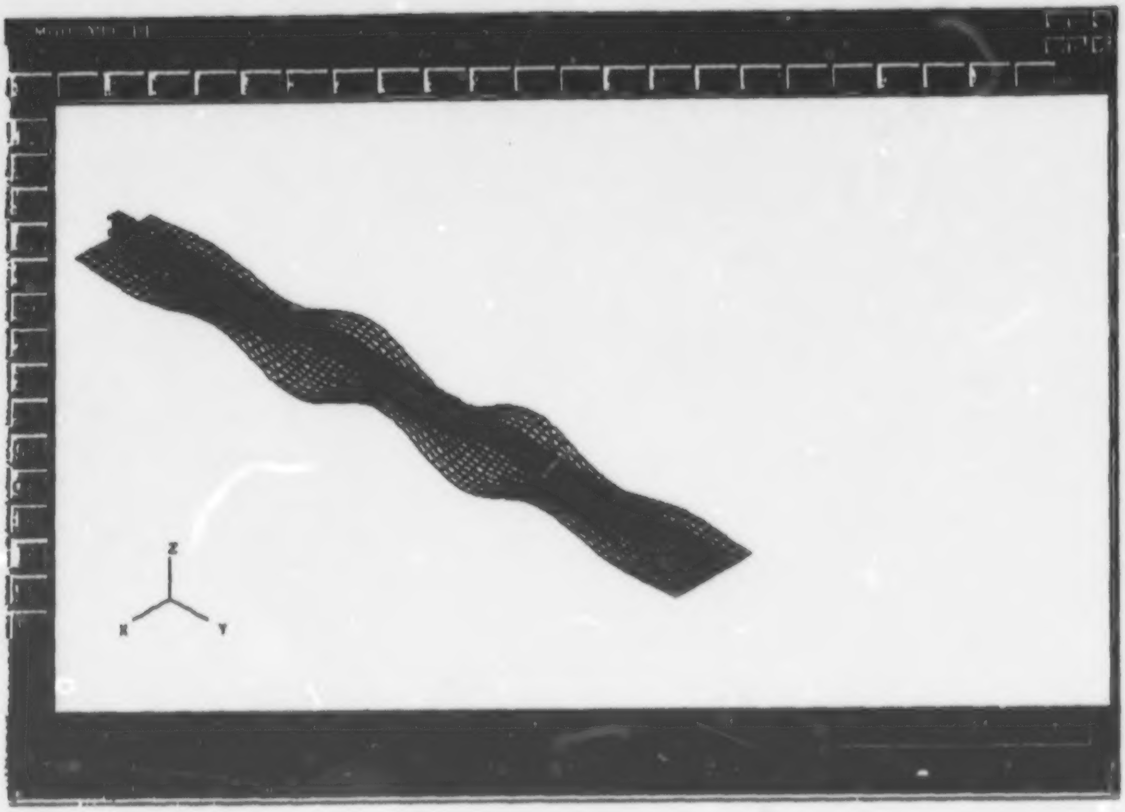

Figure 6.8: Higher-Order Imperfection Pattern with Seven Half Sine Waves.

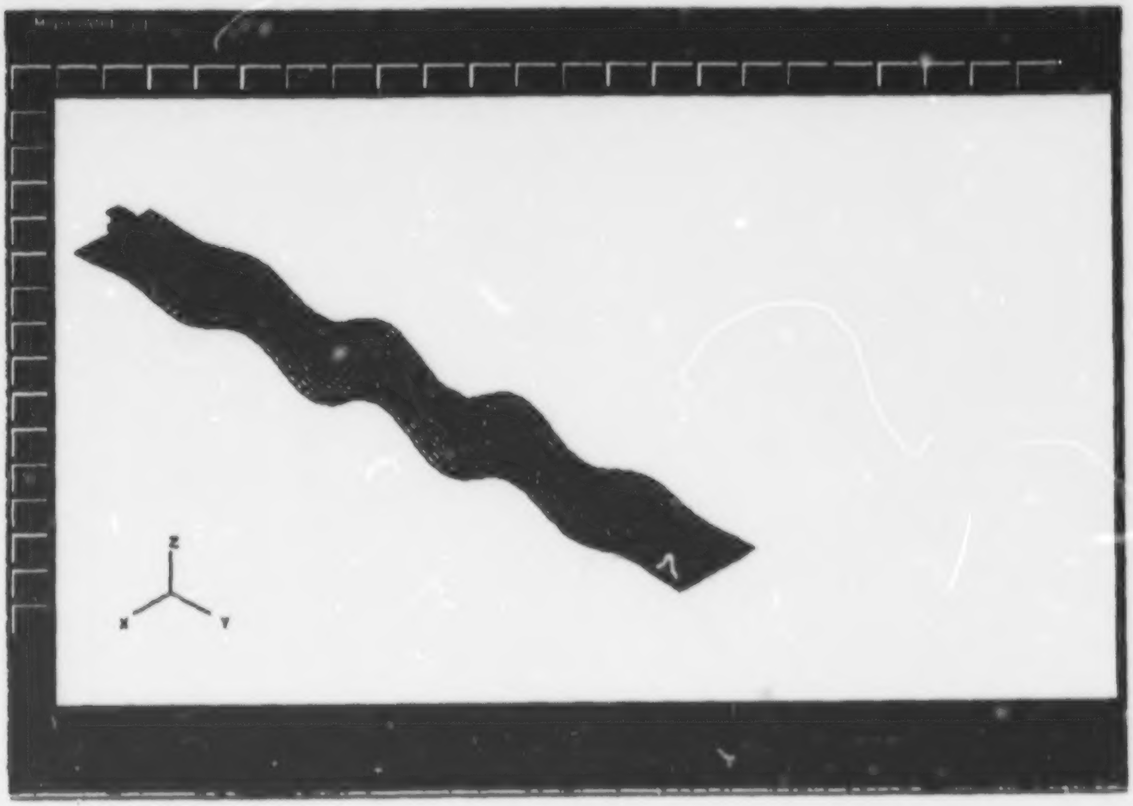

Figure 6.9: Higher-Order Imperfection Pattern with Nine Half Sine Waves.

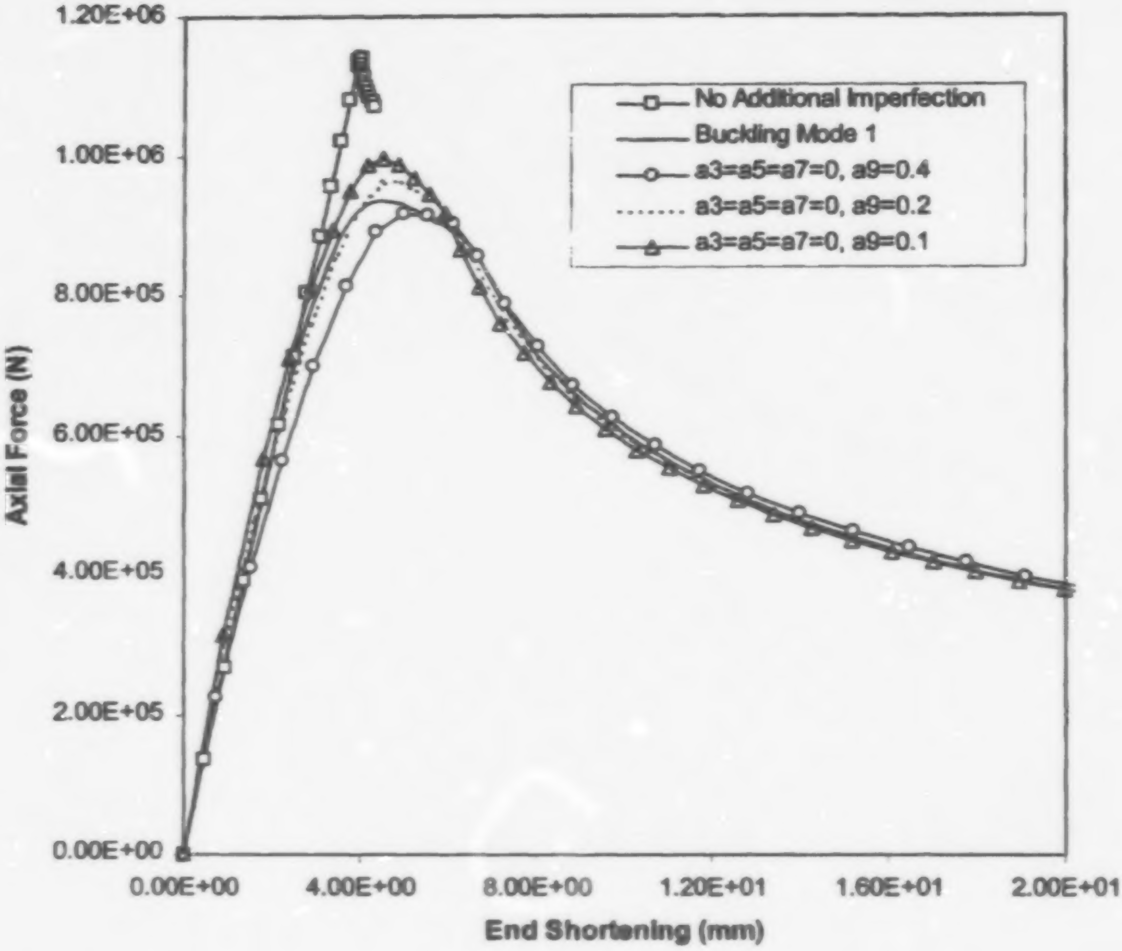

Figure 6.10: Load-Shortening Curves of the Stiffened Panel Obtained by Using Different Amounts of the Nine Half-Since Wave Imperfection.

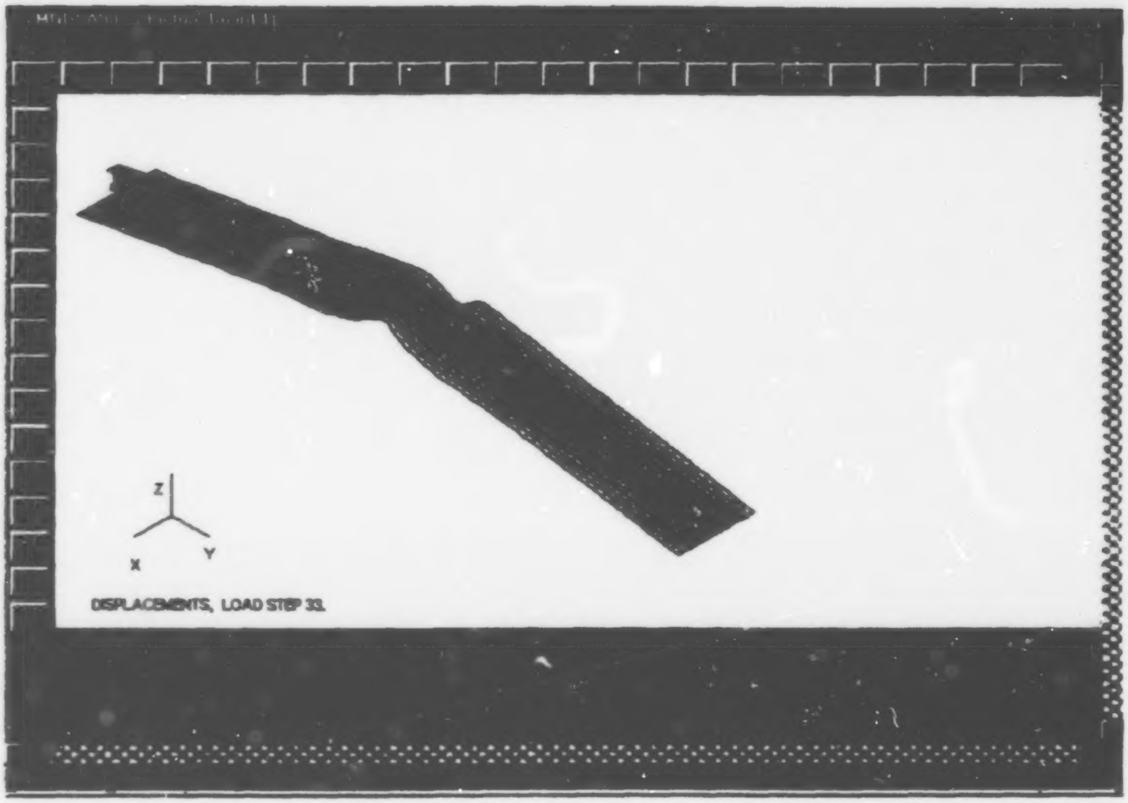
Z
X
Y
DISPLACEMENTS, LOAD STEP 33.

Figure 6.11: Final Deformed Configuration of the Stiffened Panel Obtained Using the Nine Half Sine Wave Imperfection.

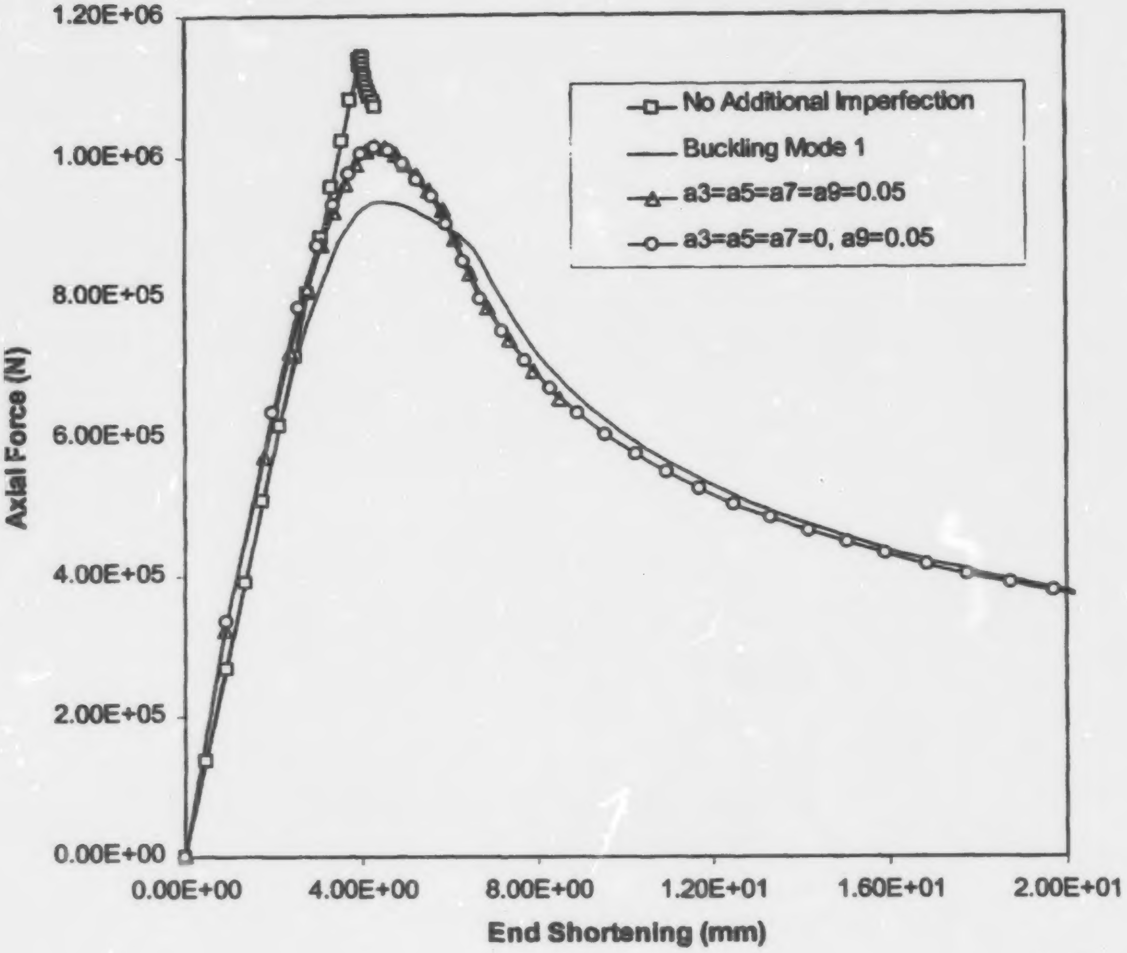

Figure 6.12: Load-Shortening Curves of the Stiffened Panel Obtained by Using One and Four Higher-Order Sine Wave Imperfections.

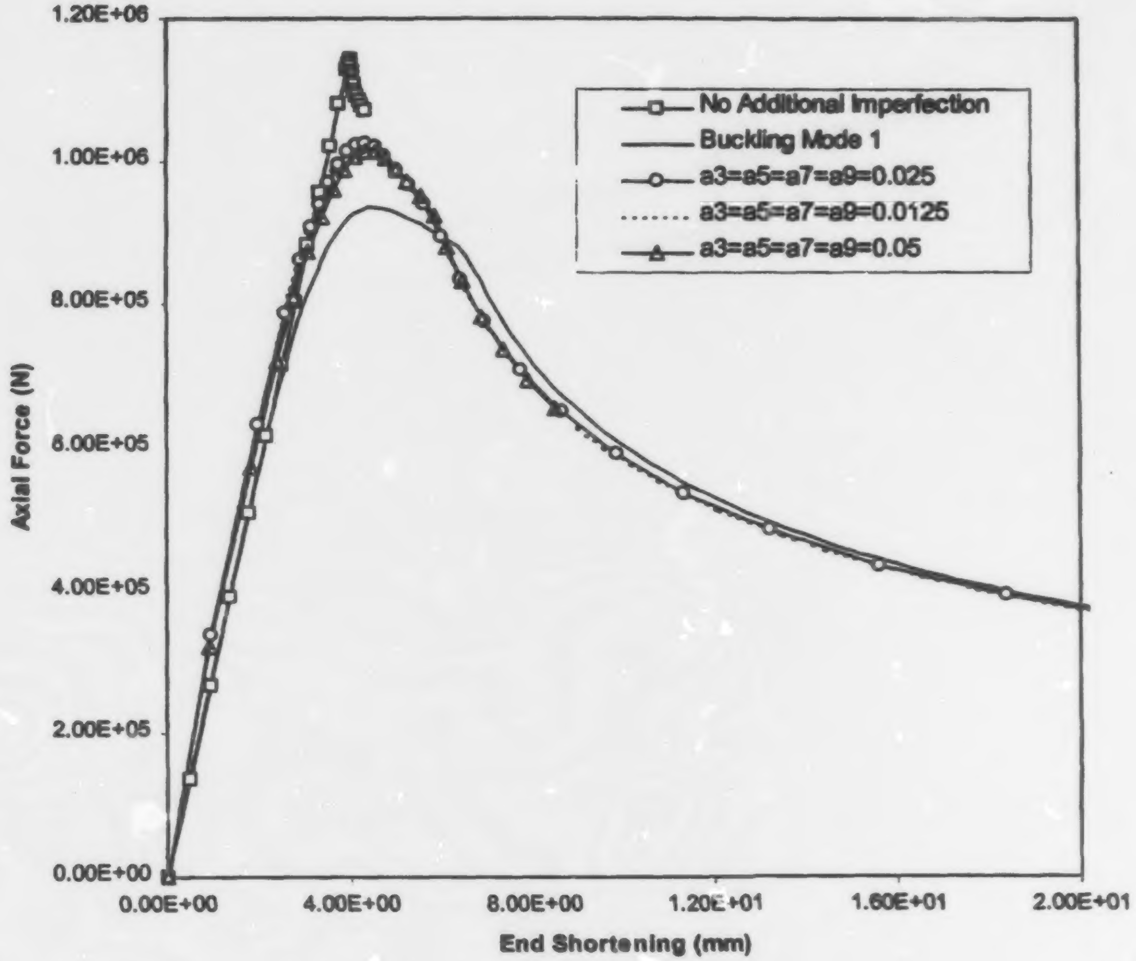

Figure 6.13: Load-Shortening Curves of the Stiffened Panel Obtained by Using Different Amounts of All Four Higher-Order Imperfections.

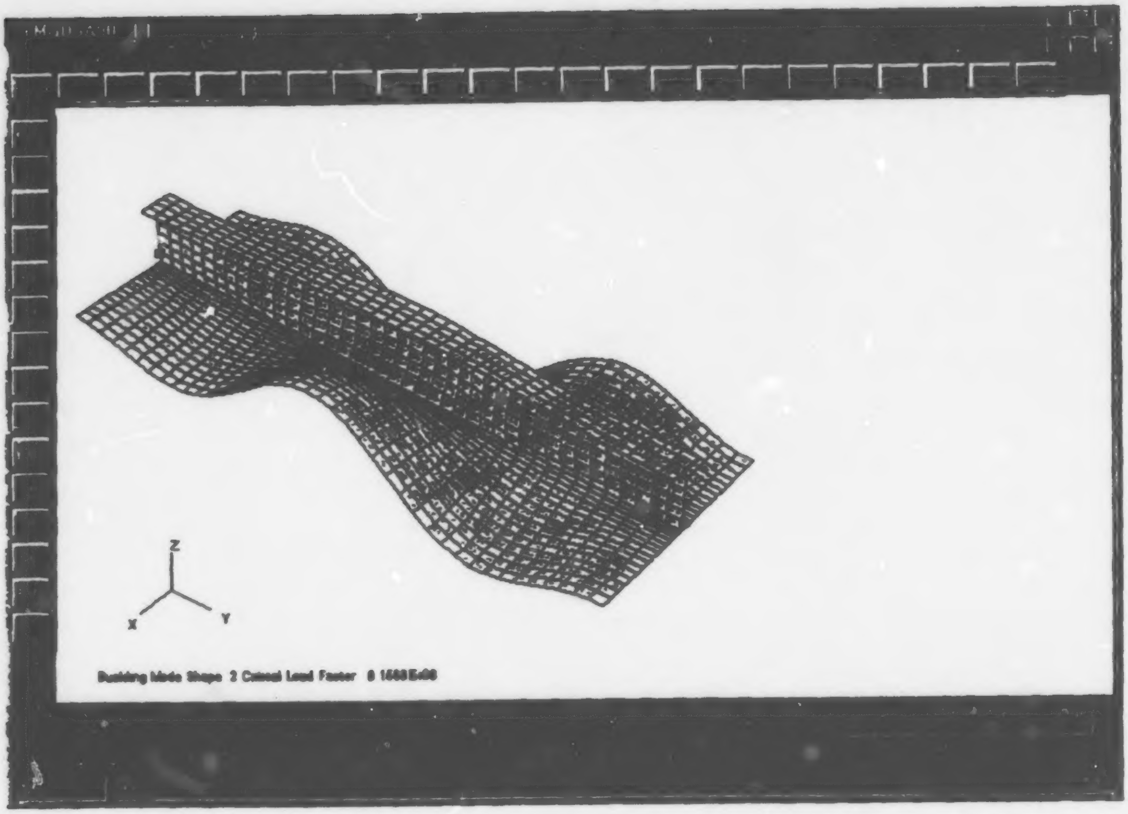
Z
X
Y
Buckling Mode Shape 2 Critical Load Factor

Figure 6.14: Linear Buckling Mode Suitable for being Used in Load-Shortening Curve Calculation for Stiffened Panel With β=1.0, λ=0.3.

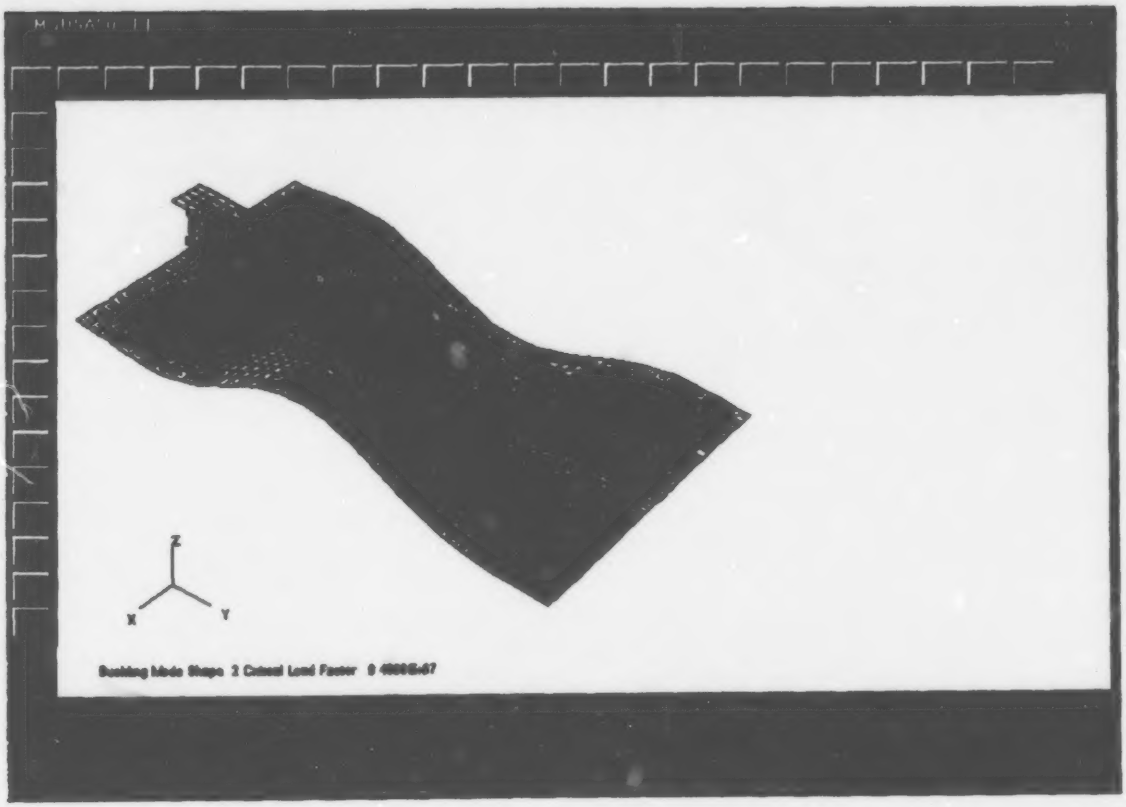
Z
X
Y
Buckling Mode Shape 2 Critical Load Factor

Figure 6.15: Linear Buckling Mode Suitable for being Used in Load-Shortening Curve Calculation for Stiffened Panel With β=2.0, λ=0.3.

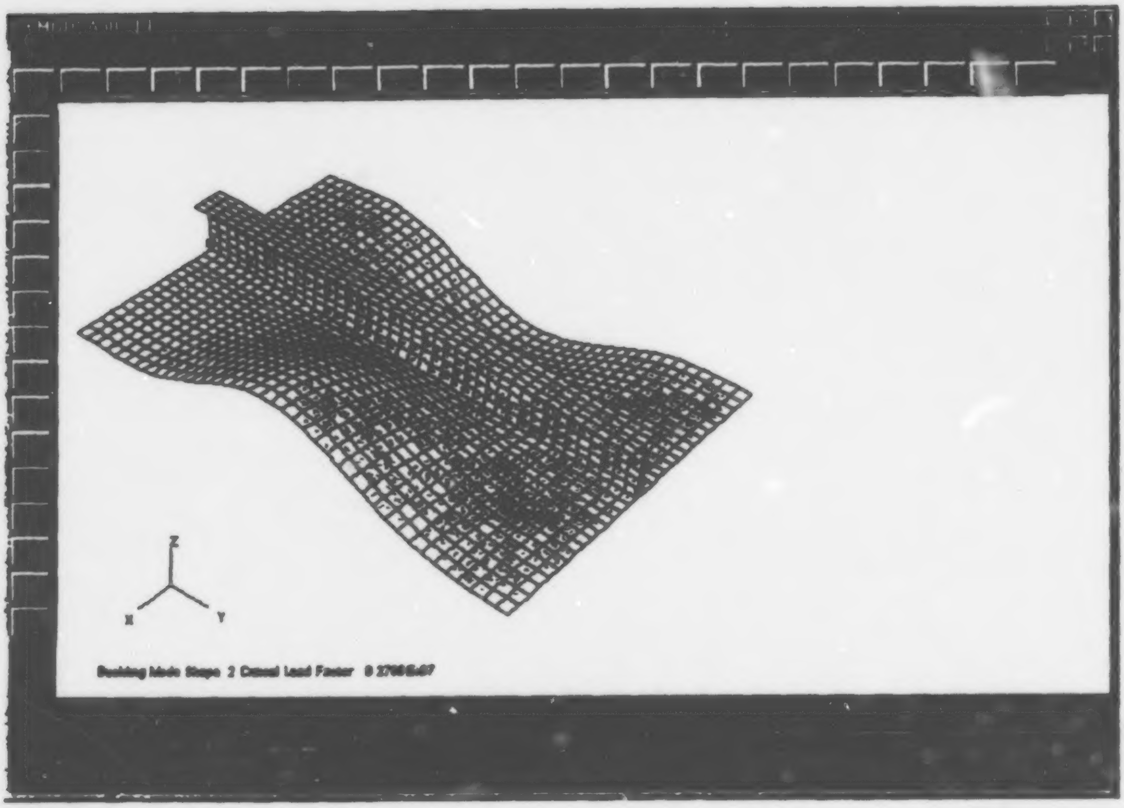
Z
X
Y
Buckling Mode Shape 2 Critical Load Factor

Figure 6.16: Linear Buckling Mode Suitable for being Used in Load-Shortening Curve Calculation for Stiffened Panel With β=3.0, λ=0.3.

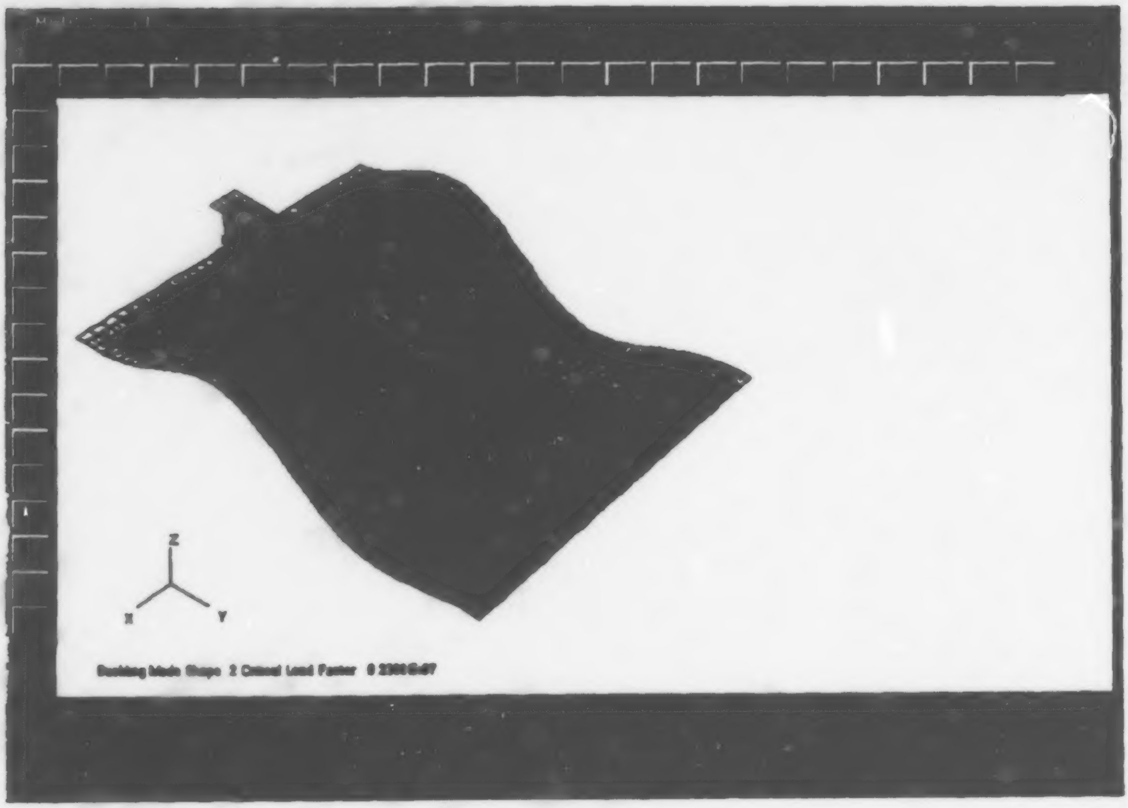

Buckling Mode Shape 2 Critical Load Factor

Figure 6.17: Linear Buckling Mode Suitable for being Used in Load-Shortening Curve Calculation for Stiffened Panel With β=4.0, λ=0.3.

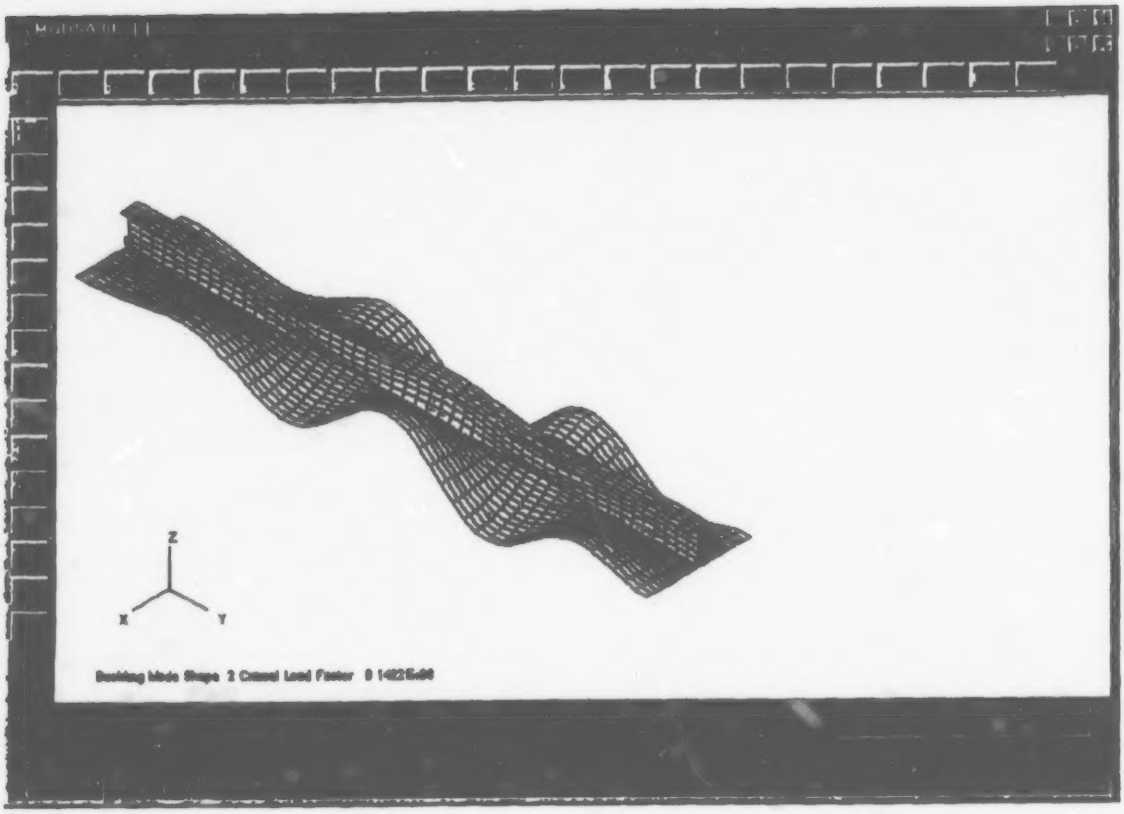
Z
X
Y
Buckling Mode Shape 2 Critical Load Factor

Figure 6.18: Linear Buckling Mode Suitable for being Used in Load-Shortening Curve Calculation for Stiffened Panel With β=1.0, λ=0.6.

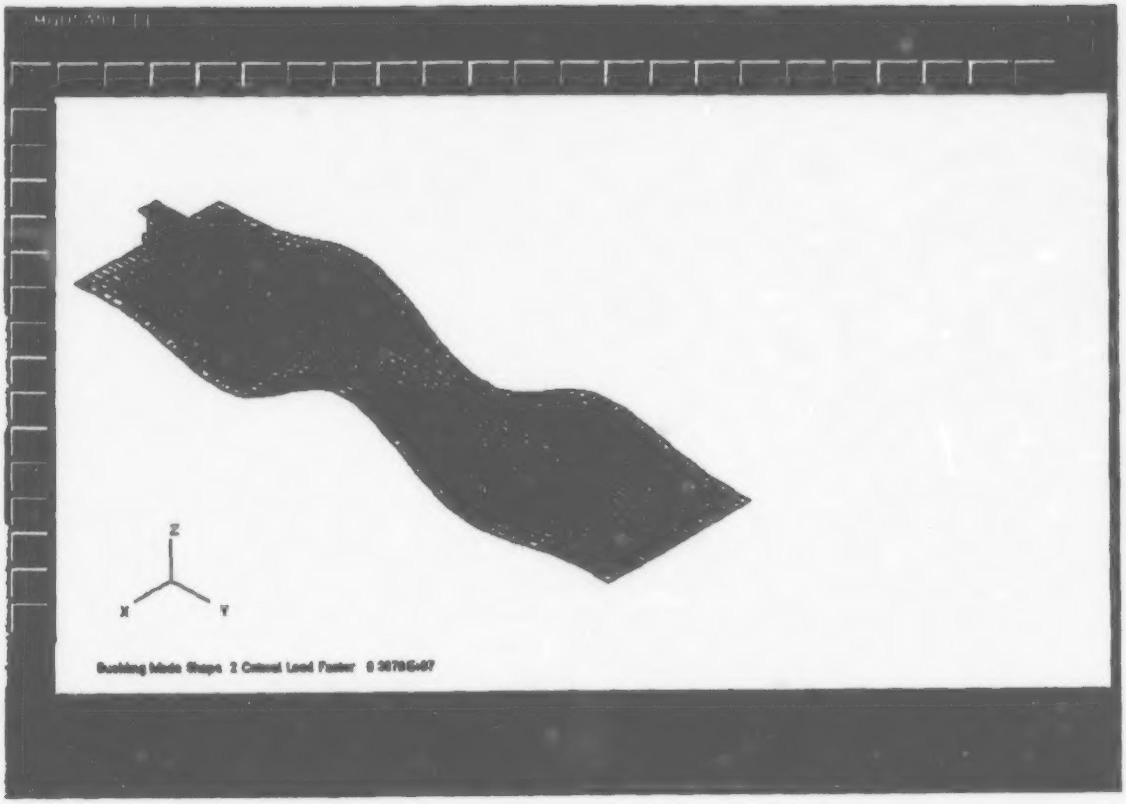

Buckling Mode Shape 2 Critical Load Factor [illegible]

Figure 6.19: Linear Buckling Mode Suitable for being Used in Load-Shortening Curve Calculation for Stiffened Panel With β=2.0, λ=0.6.

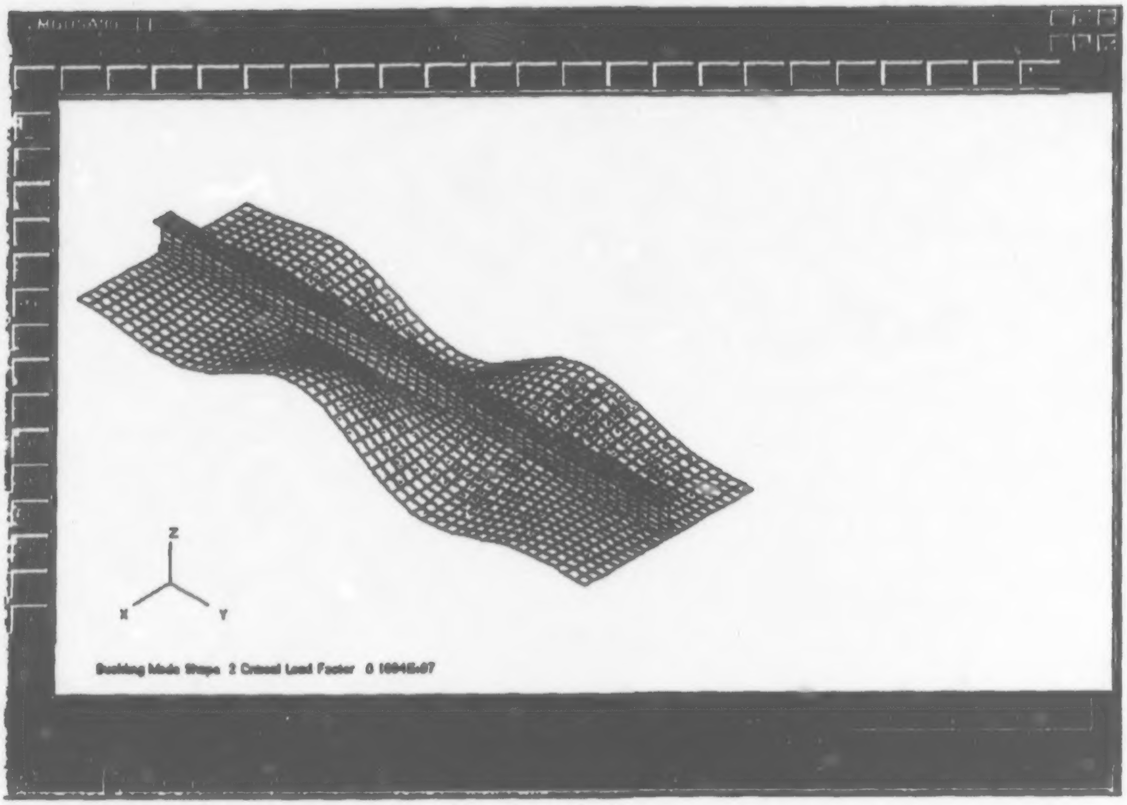
Z
X
Y
Buckling Mode Shape 2 Critical Load Factor 0.1694E+07

Figure 6.20: Linear Buckling Mode Suitable for being Used in Load-Shortening Curve Calculation for Stiffened Panel With β=3.0, λ=0.6.

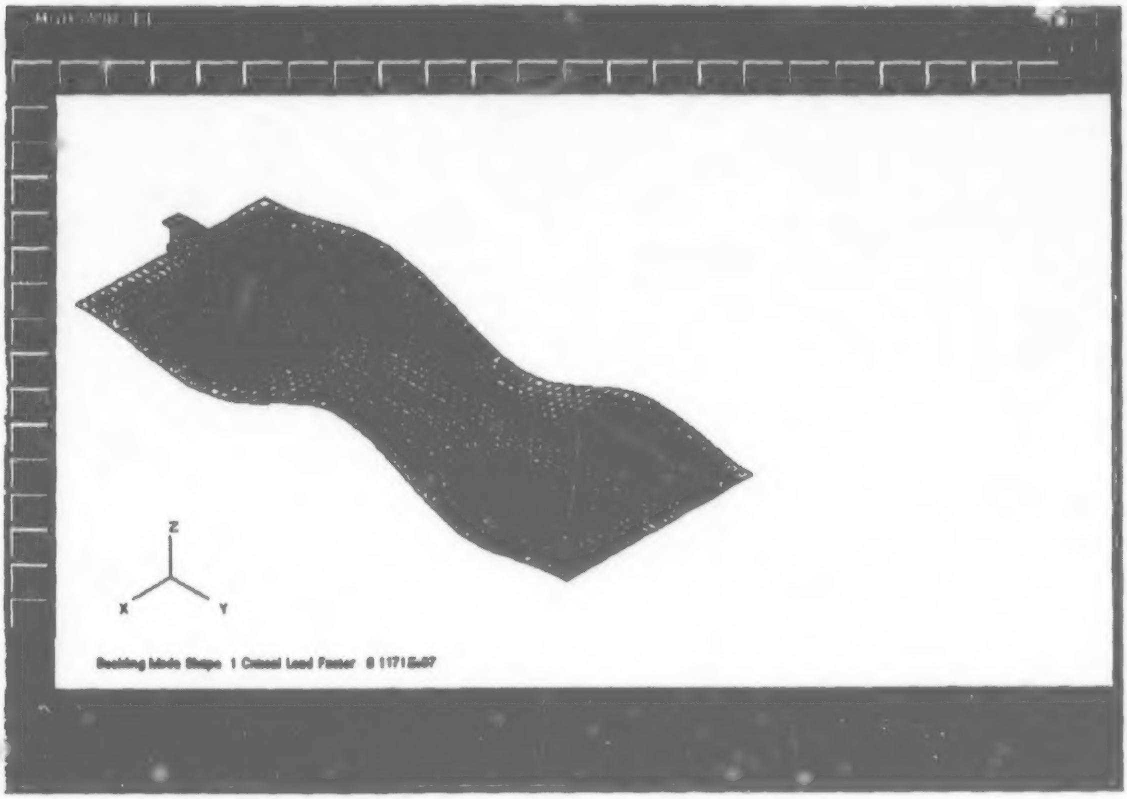

Buckling Mode Shape 1 Critical Load Factor 8.1171E+07

Figure 6.21: Linear Buckling Mode Suitable for being Used in Load-Shortening Curve Calculation for Stiffened Panel With β=4.0, λ=0.6.

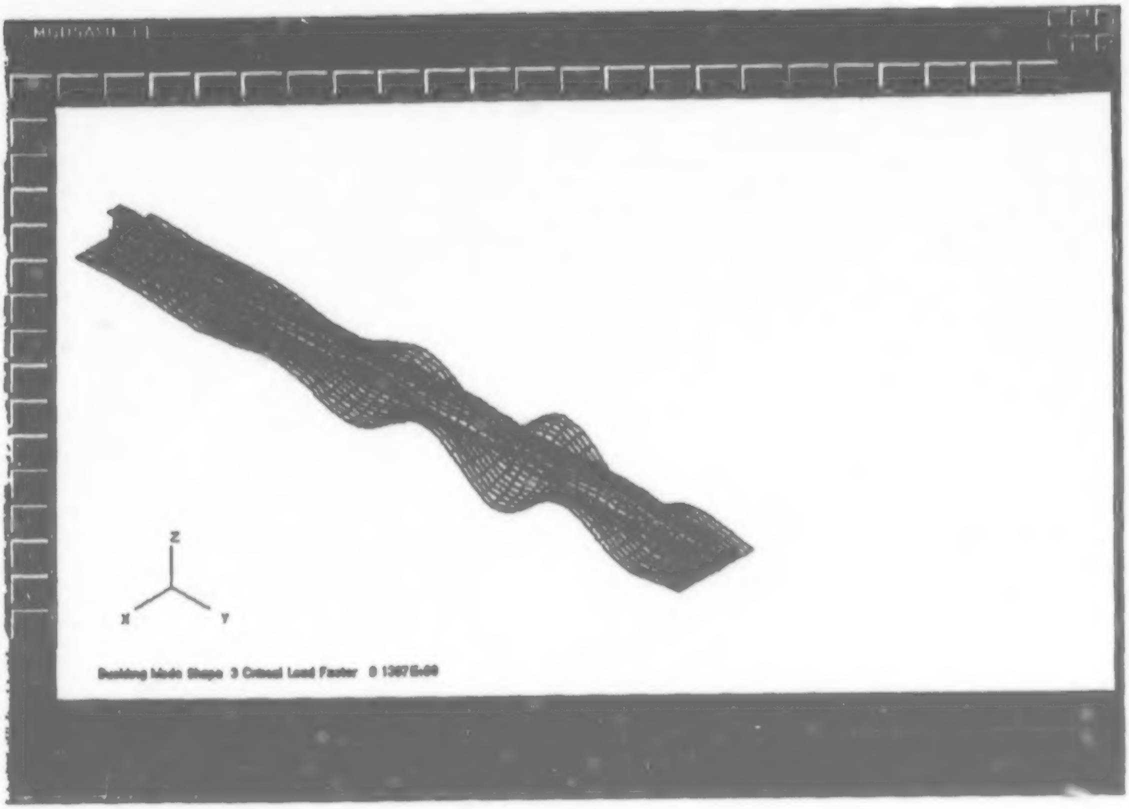
Z
X
Y
Buckling Mode Shape 3 Critical Load Factor 0.1367E+00

Figure 6.22: Linear Buckling Mode Suitable for being Used in Load-Shortening Curve Calculation for Stiffened Panel With β=1.0, λ=0.9.

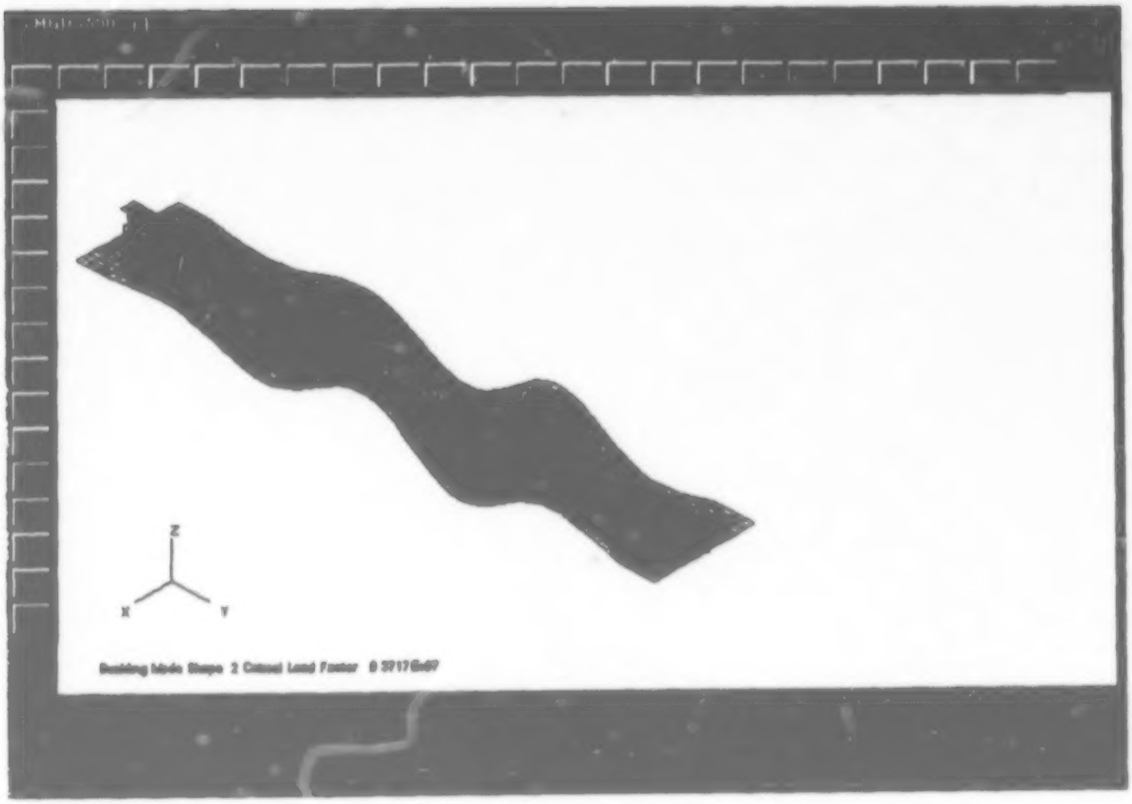
Z
X
Y
Buckling Mode Shape 2 Critical Load Factor 0.3717E+07

Figure 6.23: Linear Buckling Mode Suitable for being Used in Load-Shortening Curve Calculation for Stiffened Panel With β=2.0, λ=0.9.

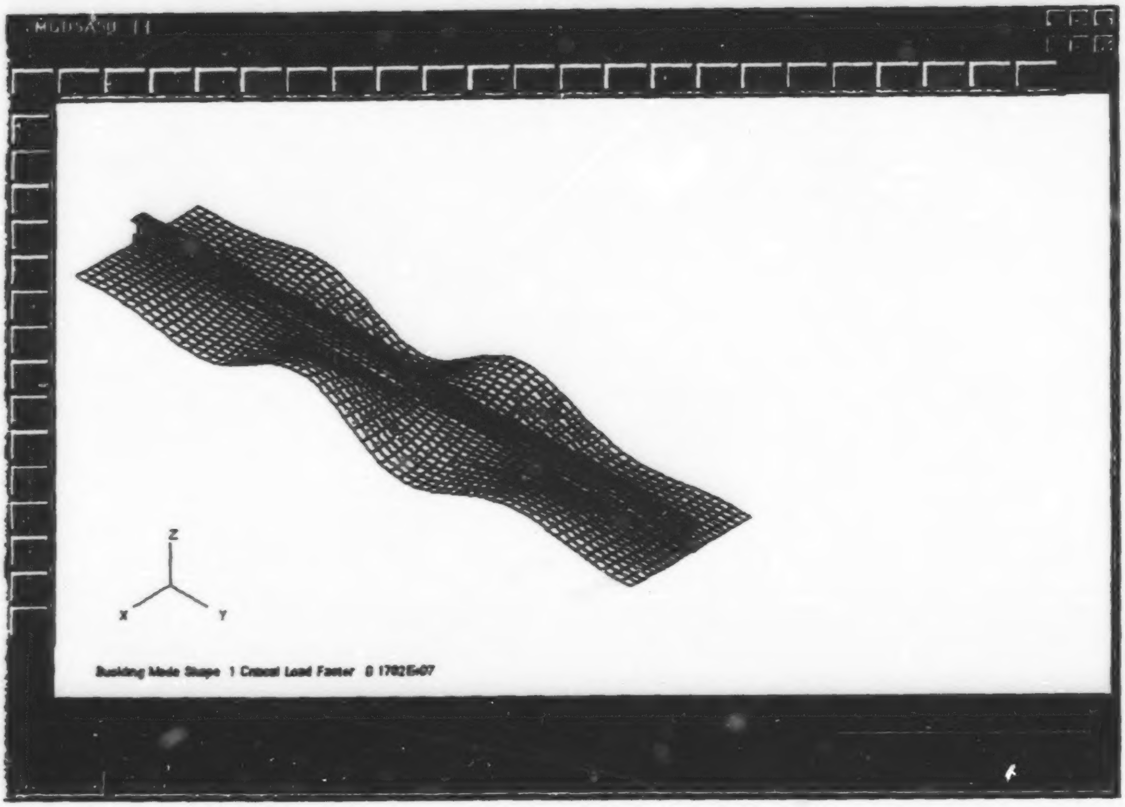

Buckling Mode Shape 1 Critical Load Factor 0.1782E+07

Figure 6.24: Linear Buckling Mode Suitable for being Used in Load-Shortening Curve Calculation for Stiffened Panel With β=3.0, λ=0.9.

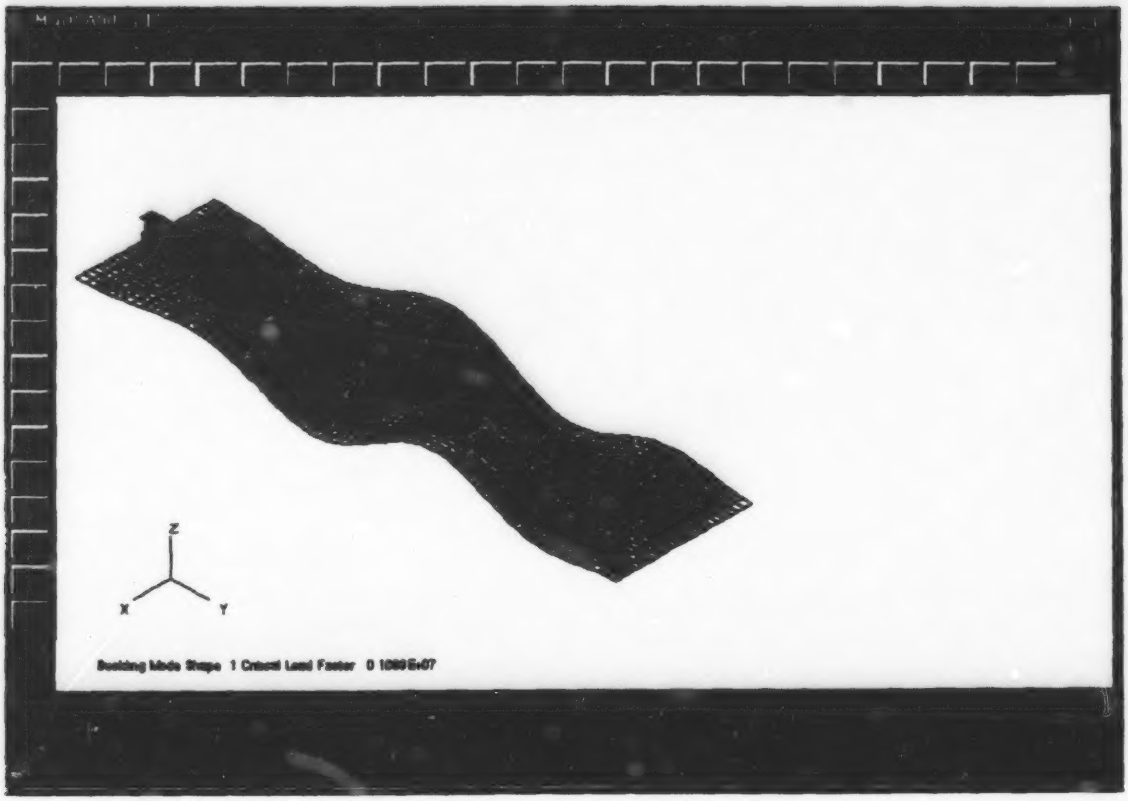
Z
X
Y
Buckling Mode Shape 1 Critical Load Factor 0.1069E+07

Figure 6.25: Linear Buckling Mode Suitable for being Used in Load-Shortening Curve Calculation for Stiffened Panel With β=4.0, λ=0.9.

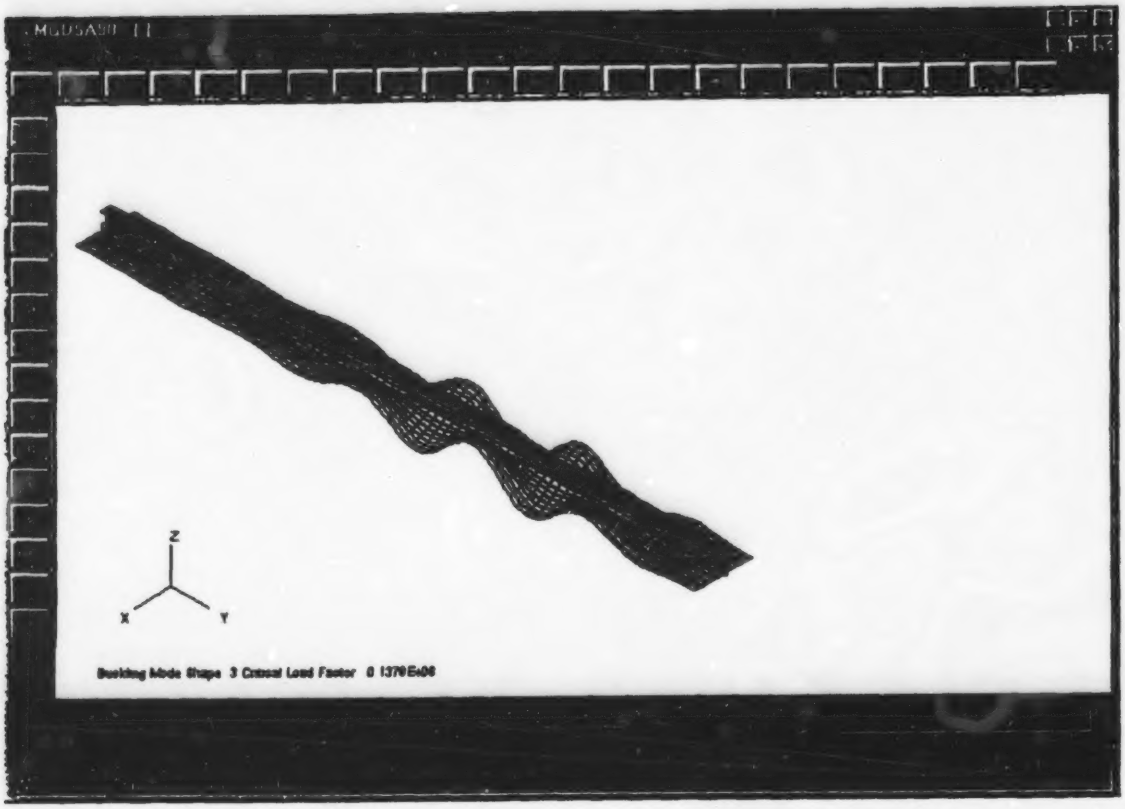
MODSA90 [1]
Z
X
Y
Buckling Mode Shape 3 Critical Load Factor 0.1379E+06

Figure 6.26: Linear Buckling Mode Suitable for being Used in Load-Shortening Curve Calculation for Stiffened Panel With β=1.0, λ=1.2.

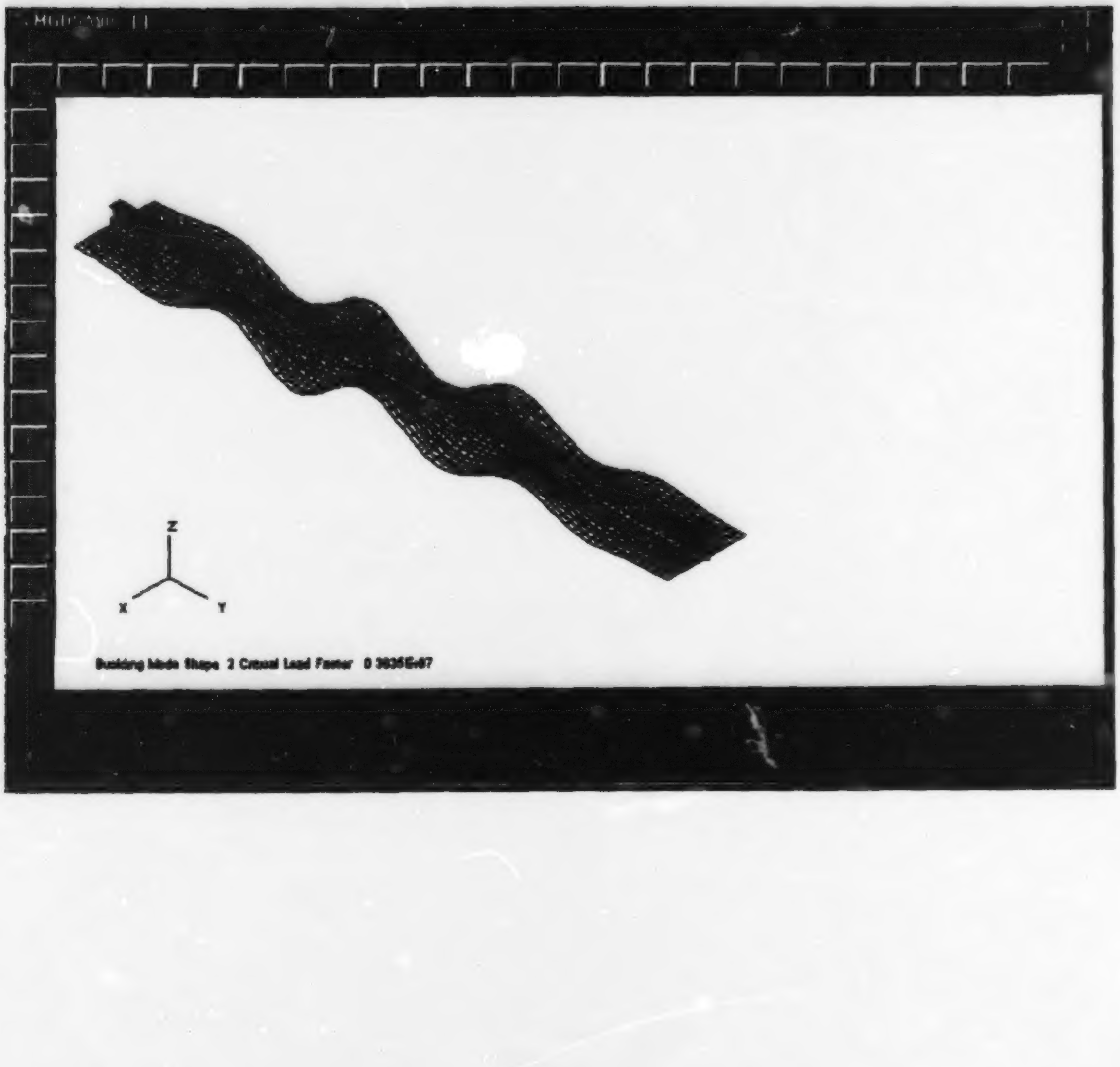
Z
X
Y
Buckling Mode Shape 2 Critical Load Factor 0.3836E+07

Figure 6.27: Linear Buckling Mode Suitable for being Used in Load-Shortening Curve Calculation for Stiffened Panel With β=2.0, λ=1.2.

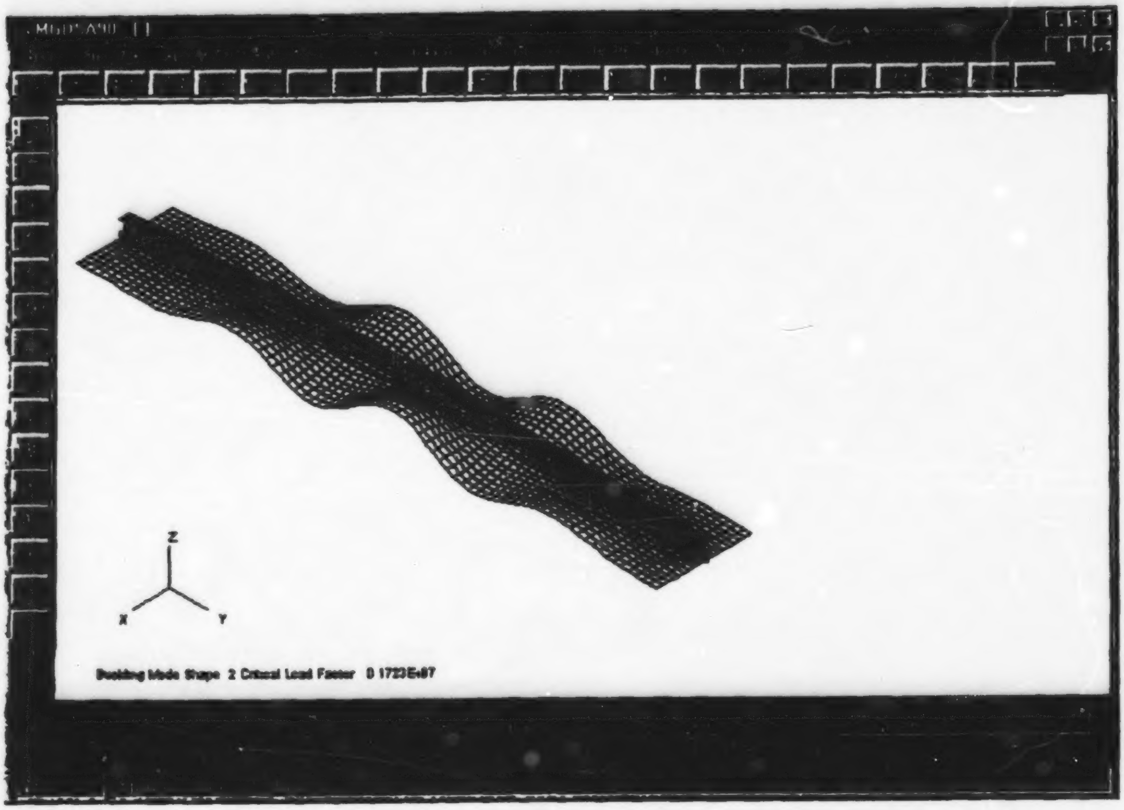

Buckling Mode Shape 2 Critical Load Factor 0.1723E+07

Figure 6.28: Linear Buckling Mode Suitable for being Used in Load-Shortening Curve Calculation for Stiffened Panel With β=3.0, λ=1.2.

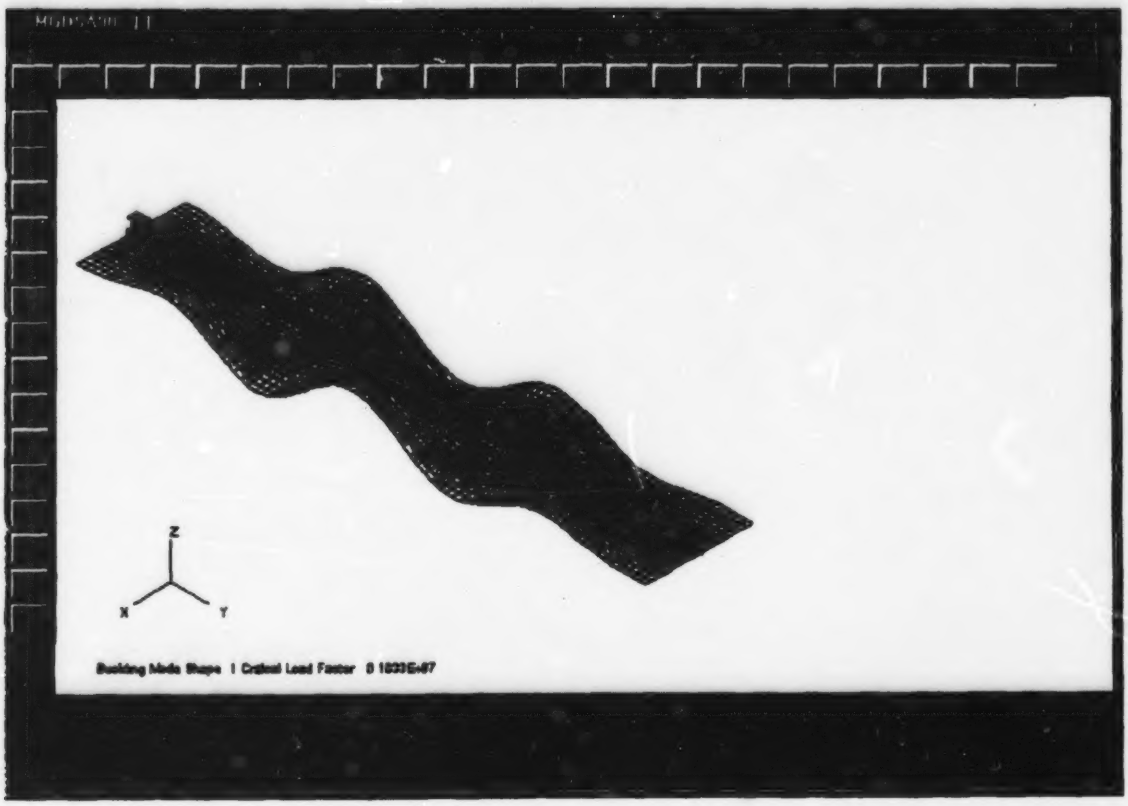
Z
X
Y
Buckling Mode Shape 1 Critical Load Factor 8.1033E+07

Figure 6.29: Linear Buckling Mode Suitable for being Used in Load-Shortening Curve Calculation for Stiffened Panel With β=4.0, λ=1.2.

7. ADEQUACY ASSESSMENT OF THE NORMALIZED EFFECTIVE STRESS-STRAIN CURVE DATABASE FOR ULTIMATE STRENGTH ANALYSES OF THE CPF MODEL

In the previously generated normalized effective stress-strain curve database of ultimate strength evaluation of the CPF, a group of 16 curves were calculated for each given stiffener type, plate imperfection level and boundary condition [7.1]. These curves correspond to four values of the plate slenderness ratio given by $\beta=1,2,3,4$, and four values of the column slenderness ratio given by $\lambda=0.3,0.6,0.9,1.2$, where the plate and column slenderness ratios are functions of the geometric and material properties of the stiffened panel and defined as:

$$\beta = \frac{b}{t}\sqrt{\frac{\sigma_Y}{E}} \quad \text{and} \quad \lambda = \frac{a}{\pi r}\sqrt{\frac{\sigma_Y}{E}}$$

where a denotes the length of the panel; b the width of the plate; t the thickness of the plate; r the radius of gyration of the stiffened panel cross-section; E the Young's modulus; and σ_Y the yield stress.

For longitudinally stiffened panels with intermediate values of β and λ, a linear interpolation scheme is utilized to calculate their load-shortening curves from the generic curves available in the database. However, for stiffened panels with β and λ outside the ranges $\beta \in [1,4]$ and $\lambda \in [0.3,1.2]$, extrapolation must be used. When the β and λ values are considerably far from the above ranges, significant errors could be introduced in the extrapolated load-shortening curve. As a result, the assessment of the adequacy of the previously developed load-shortening curve database was accomplished in three steps. In the first step, the ranges of the β and λ parameters of a CPF stiffened panels were computed. These results confirmed the existence of longitudinally stiffened panels with the β and λ parameters outside the range of pre-generated load-shortening curves. In the second step, parametric studies were conducted to determine the variations of the load-shortening curves beyond the previously considered ranges of the β and λ values. These studies demonstrated the potential errors associated with the extrapolation. Finally, in the third step, the effects of other factors, such as the stiffener/total area ratio, the level of stiffener imperfection and the level of maximum residual stresses, on the overall nonlinear behavior of stiffened panels were investigated.

7.1 Determination of Ranges of the β and λ Parameters for a Typical CPF Model

As mention earlier, the first step for assessing the adequacy of the previously developed normalized effective stress-strain curve database for ultimate strength analyses of the CPF was to calculate the ranges of the plate and column slenderness ratios, β and λ, on cross-sections of a typical CPF model. However, it is essential that this calculation be performed using an accurate CPF model.

The first attempt we made was to use a set of DIGFEM files provided by DREA. A special purpose computer program was developed to process the DIGFEM data and compute β and λ values for each stiffened panel on each available cross-section. From these β and λ values, the maximum and minimum values were obtained for each cross-section throughout the entire ship. It was found that the ranges of the β and λ parameters on CPF were $0.007 < \beta < 9.006$ and $0.047 < \lambda < 1.461$, which were clearly exceed the ranges of the available load-shortening curves. However, close examination of the four cross-sections on which the maximum and minimum β and λ values were identified revealed that at least some of these sections contained questionable geometric and/or material properties. For example, the maximum β value of 9.006 appeared in the central portion of deck 2 at station 30.5 shown in Figure 7.1. Details of the stiffened panel (at node 101) and the surrounding structures are displayed in Figure 7.2. The width of the plating associated with this panel was over 11.0 meters, but the thickness was only 5.0 mm. The minimum β value of 0.007 appeared at station 50.75, which are shown in Figures 7.3 and 7.4. Although the plate width and stiffener properties were reasonable, the plate thickness of plate segments 8-20, 20-9 and 9-10 was as thick as 1950.0 mm! Based on the above study, it was concluded that the DIGFEM files provided by DREA were not suitable for calculating the ranges of β and λ. A telephone conversation with Terry MacFarlane confirmed some of the errors in the DIGFEM files, however, he was not able to conduct a complete verification due to the lack of proper graphics tools available to him.

An alternative method for obtaining the ranges of the β and λ parameters on a CPF was to use the newly developed ultimate strength analysis program. This program was able to take both the DIGFEM files and the cross-section files generated by MGDSA. A special application interface, named ultimate strength analysis, has been developed in MGDSA to allow users to select cross-sections to be analyzed from a global finite element model. In the present study, we started with a VAST finite element model of the CPF and removed all the superstructures. The resulting finite element mesh of the ship without the superstructure is shown in Figure 7.5. Twenty one cross-sections were considered. The locations of these cross-sections are presented in Table 7.1 and three typical sections are displayed in Figures 7.6-7.8. For each of these cross-sections, the ultimate strength program provided a summary of cross-section information as shown in Figure 7.9 which included the ranges of the geometric parameters.

The ranges of the geometric parameters predicted by the ultimate strength program for all the selected cross-sections are presented in Table 7.1. These results indicated that almost all cross-sections contained stiffened panels which are outside the range of the generic load-shortening curve database. However, a close examination of the cross-sections shown in Figures 7.6-7.8, it is readily recognized that in cross-sections generated by MGDSA, the stiffener locations are only approximate. This is due to the unavailability of the precise stiffener locations in the global finite element mesh of the CPF. In order to investigate how significant these errors were, cross-section defined by the DIGFEM file format, in which the precise location of each stiffener was digitized, should be considered for verification purposes. One DIGFEM section that did not contain questionable geometric and material properties was considered. This section is shown in Figure 7.10, and it was at the same location as the MGDSA section shown in Figure 7.6. For the section defined in DIGFEM file, the ultimate strength program produced the following ranges of the geometric parameters:

$$0.11461 < \lambda < 0.74462, 1.70431 < \beta < 3.71266, \ 0.09215 < A_s / A < 0.53875 .$$

These results are in reasonable agreement with those in the third row of Table 7.1, indicating that the errors in the stiffener locations do not greatly affect the ranges of the geometric parameters in Table 7.1.

7.2 Parametric Study on Nonlinear Behavior of Stiffened Panels with Extreme Values of Geometric Parameters β and λ

The investigation presented in the previous section confirmed the existence of longitudinally stiffened panels which were not covered by the generic load-shortening curve database. For these stiffened panels, extrapolation must be performed to obtain an approximation of their nonlinear behavior. In order to check the validity of the extrapolation scheme, geometrically and materially nonlinear finite element analyses must be performed on selected stiffened panels with extreme values of geometric parameters.

The effect of the column slenderness ratio, λ, was first studied. As mentioned earlier, in the generic load-shortening curve database, four λ values were considered, namely $\lambda=0.3$, 0.6, 0.9 and 1.2. In the present analysis, five additional values, $\lambda=0.1$, 0.2, 1.5, 1.8 and 2.0, were considered. The other geometric parameters included $\beta=2.0$, $A_S/A=0.2$, maximum compressive residual stress $\sigma_r=0.15\sigma_Y$, plate imperfection $\omega_0=0.2\beta^2t$ and stiffener imperfection $\Delta=0.0015a$, where σ_Y indicates the yield stress and a denotes the length of the stiffened panel in the axial direction. The load-shortening curves resulting from nonlinear analyses of these nine panels are compared in Figure 7.11 and the peak loads are presented in Figure 7.12. From these figures, it is readily recognized that the extrapolation scheme might generate significant errors in the resulting load-shortening curves. For panels with extremely small λ value, plate imperfection became more significant, which led to a reduced load carrying capability. In this region, the extrapolation scheme resulted in an overestimation of the strength of the panel. On the other hand, the stiffened panels with extremely large λ value behaved like slender beams. Although they were very flexible, they could still carry some load, and based on Figure 7.12, the peak load reduces with increasing λ value. However, this trend was not predicted in the extrapolation scheme, which resulted in a zero load carrying capacity at $\lambda\cong1.75$ and completely unreasonable negative peak load beyond that point.

The effect of the β parameter was then considered. Besides the four β values considered earlier, load-shortening curves were also obtained for five additional stiffened panels with more extreme

β values, as β=0.25, 0.5, 5.0, 6.0 and 8.0, through full nonlinear finite element analyses. The column slenderness ratio λ was set to 0.6 in these analyses. All other parameters were identical to those described in the preceding paragraph. The load-shortening curves obtained for these nine panels are presented in Figure 7.13 and the variation of the peak load with β is shown in Figure 7.14. Once again, the possibility, that the extrapolation scheme might result in significant over or underestimation of the load carrying capacities of stiffened panels with very small or very large β values, was clearly revealed. Based on these results, it becomes evident that the load-shortening curve database should be expanded to include additional curves.

7.3 Parametric Study on Effects of Other Parameters on the Nonlinear Behavior of Stiffened Panels

In addition to the column and plate slenderness ratios, λ and β, several other parameters, including the stiffener/total area ratio, the levels of plate and stiffener imperfections and the magnitude of the residual stresses, also have significant effects on the nonlinear plastic, post-buckling behavior of stiffened panels. The stiffener/plate area ratio has a significant effect on the geometric configuration of the panels, whereas changing the levels of imperfection and residual stress alters the deformation patterns and internal stress distributions, which may cause significant variations of mechanical behavior of the structure.

In the previous work toward generating the normalized generic load-shortening curve database, three values were considered for the stiffener/plate area ratio as A_S/A=0.2, 0.275 and 0.35, and for each of them, a group of 16 curves were obtained corresponding to four β values and four λ values, as mentioned earlier in this chapter. However, based on the results in Table 7.1, the maximum and minimum values of the stiffener/plate area ratio of stiffened panels on CPF were considerably beyond this range. In order to investigate the significance of the parameter A_S/A on the nonlinear behavior of stiffened panels, a parametric study was carried out, in which eight values of the area ratio were considered, including A_S/A=0.07, 0.1, 0.12, 0.16, 0.2, 0.3, 0.5 and 0.8. The load-shortening curves obtained for these panels using nonlinear finite element analyses are presented in Figure 7.15 and the peak loads are shown in Figure 7.16 as a function of A_S/A.

These results indicated that the stiffener/plate area ratio A_S/A does have a very significant effect on the load-carrying capacity of stiffened panels, and the relationship between the peak load and parameter A_S/A is nonlinear. The peak load drops very rapidly when A_S/A approaches zero and increases slowly when A_S/A approaches to unity. There might be a sudden change of failure mode between $A_S/A=0.3$ and 0.5, as suggested by a sudden change of the shape of load-shortening curves shown in Figure 7.15. Although the present study indicated that A_S/A is a very important factor, it was not properly accounted for in the NS94 and ULTMAT ultimate strength analysis programs. In these programs, only interpolation (or extrapolation) on β and λ were implemented. As a result, for each ultimate strength analysis, one value of A_S/A must be assumed for the entire cross-section. This would obviously lead to unreasonable predictions of the moment-curvature curves of ship cross-sections due to the wide variation of the A_S/A values as indicated in Table 7.1.

Although three levels of plate imperfections were considered in previous studies, the magnitude of the stiffener imperfection was always fixed to 1/1000 of the panel length and its effect on the nonlinear behavior of stiffened panels was never addressed. In the present contract, four additional magnitudes of stiffener imperfections were considered and the results are presented in Figures 7.17 and 7.18. These results indicated that the level of stiffener imperfection had a significant impact on the peak load, but had little effect on the post-buckling behavior of the stiffened panel. The peak load reduced almost linearly with the increase of the level of stiffener imperfection.

The effect of the magnitude of residual stress was then investigated. Load-shortening curves were obtained for stiffened panels with various levels of residual stress and the results are shown in Figures 7.19 and 7.20. In these analyses, the thermal stress capability has been utilized to generate self-equilibrium residual stress patterns. All load-shortening curves have identical initial slope, but the peak load varies considerably with the level of the residual stress. The relation between the peak load and the maximum compressive residual stress is also close to linear. However, because no data are available on the level of residual stress in the CPF, it is impossible to estimate the significance of the residual stress variations on the predicted moment-curvature curves.

Based on the results of the above parametric study, the stiffener/plate area ratio, plate and stiffener imperfection and residual stress all have a significant effect on the load-shortening behaviour of stiffened panels and must be properly considered in ultimate strength analyses. This can be accomplished by adding more curves to the generic load-shortening curve database and enhancing the interpolation algorithms in the ultimate strength programs to take into account more parameters.

Table 7.1: Ranges of the Column Slenderness Ratio (λ), the Plate Slenderness Ratio (β) and the Stiffener/Total Area Ratio (A_s/A) Computed by the Ultimate Strength Program for Various Cross-sections of a Typical CPF Model.

Section No.	Axial Co-ordinate	λ		β		A_s/A	
		Min.	Max.	Min.	Max.	Min.	Max.
1	-3000	0.1511	0.6230	1.0640	3.9505	0.1344	0.7480
2	0	0.0909	0.6572	1.5081	4.5819	0.1230	0.6413
3	6000	0.0879	0.6351	1.7526	4.1697	0.1130	0.5669
4	12000	0.1574	0.7493	0.7910	5.8880	0.0951	0.7190
5	18000	0.1209	0.7986	0.9634	5.8047	0.0930	0.7071
6	24000	0.1315	0.8869	0.7515	8.4966	0.0748	0.6345
7	30000	0.1182	0.8430	0.9134	8.5562	0.0838	0.7508
8	36000	0.1186	0.8655	1.4049	9.1182	0.0790	0.6850
9	42000	0.1201	0.7631	1.0298	6.7361	0.1041	0.6728
10	48000	0.1187	0.6537	1.0335	4.5148	0.1080	0.6081
11	54000	0.1844	0.7083	0.9325	4.7344	0.1068	0.4630
12	66000	0.1169	0.7732	1.1746	6.7361	0.1041	0.9197
13	72000	0.1129	0.6462	1.1247	5.2925	0.1101	0.8898
14	78000	0.1118	0.7732	1.1252	6.7361	0.1041	0.8897
15	84000	0.1289	0.7502	1.1032	6.1918	0.1100	0.6002
16	90000	0.1195	0.8119	0.7675	7.3485	0.0912	0.6110
17	96000	0.1135	0.9034	1.0619	7.5046	0.0720	0.6387
18	102000	0.1268	0.8403	1.3797	8.2129	0.0831	0.6322
19	108000	0.1053	0.7732	1.0616	6.7361	0.1041	0.8897
20	114000	0.1297	0.9836	1.5017	5.7395	0.0586	0.7426
21	120000	0.3141	1.0991	1.6244	4.4907	0.0417	0.2228

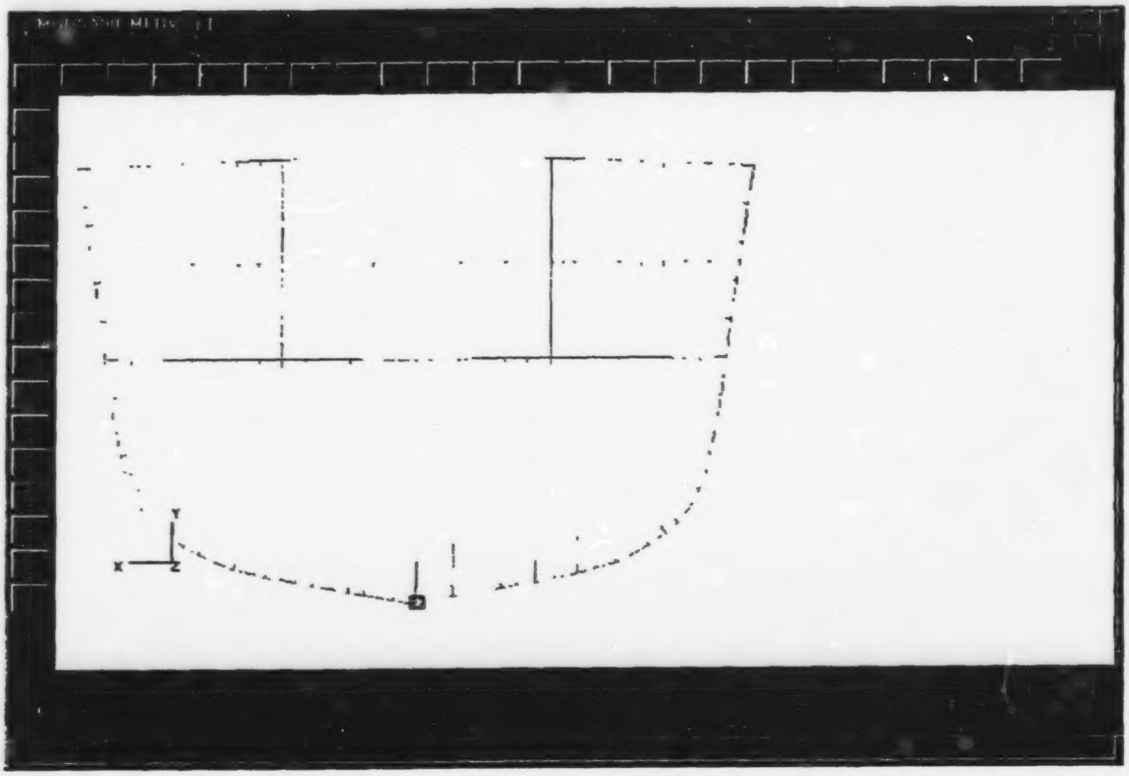

Figure 7.1: CPF Cross-section at Station 30.5 Which Contains Stiffened Panels with the Maximum Plate Slenderness Ratio β.

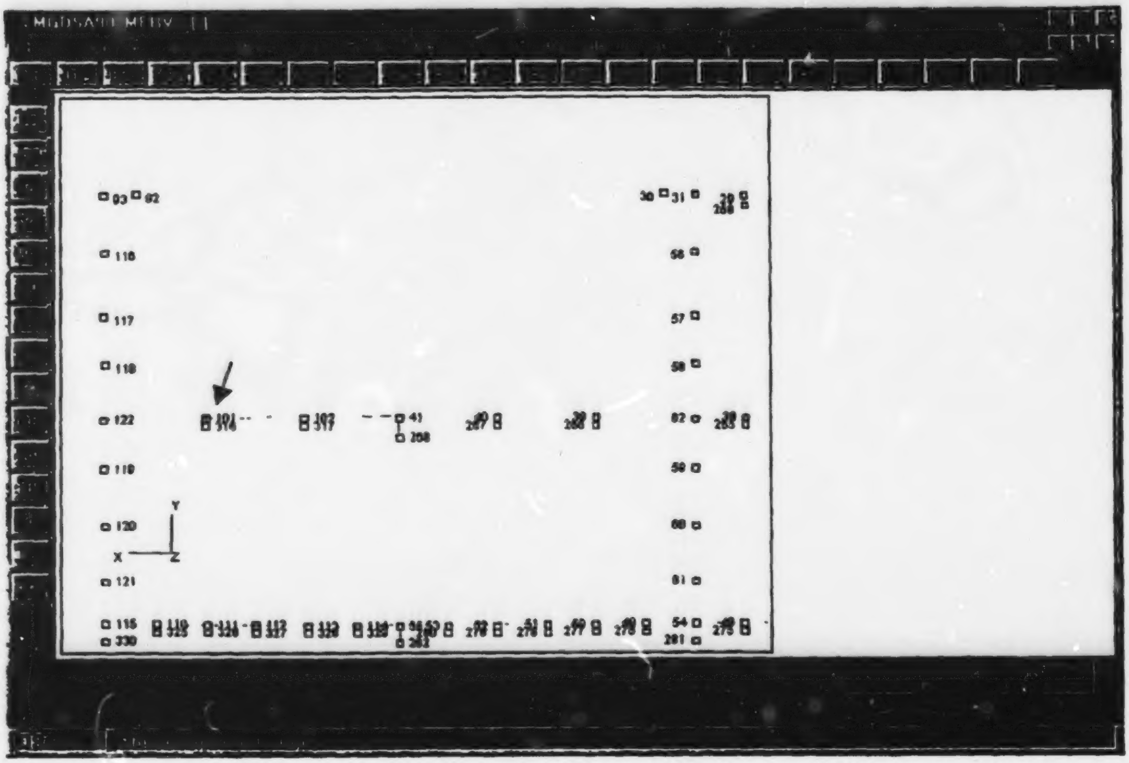
93
92
116
117
118
122
119
120
121
115
330
41
208
30
31
56
57
58
82
59
60
61
54
281
X
Y
Z

Figure 7.2: Details of CPF Cross-section at Station 30.5 Which Contains Stiffened Panels with the Maximum Plate Slenderness Ratio β.

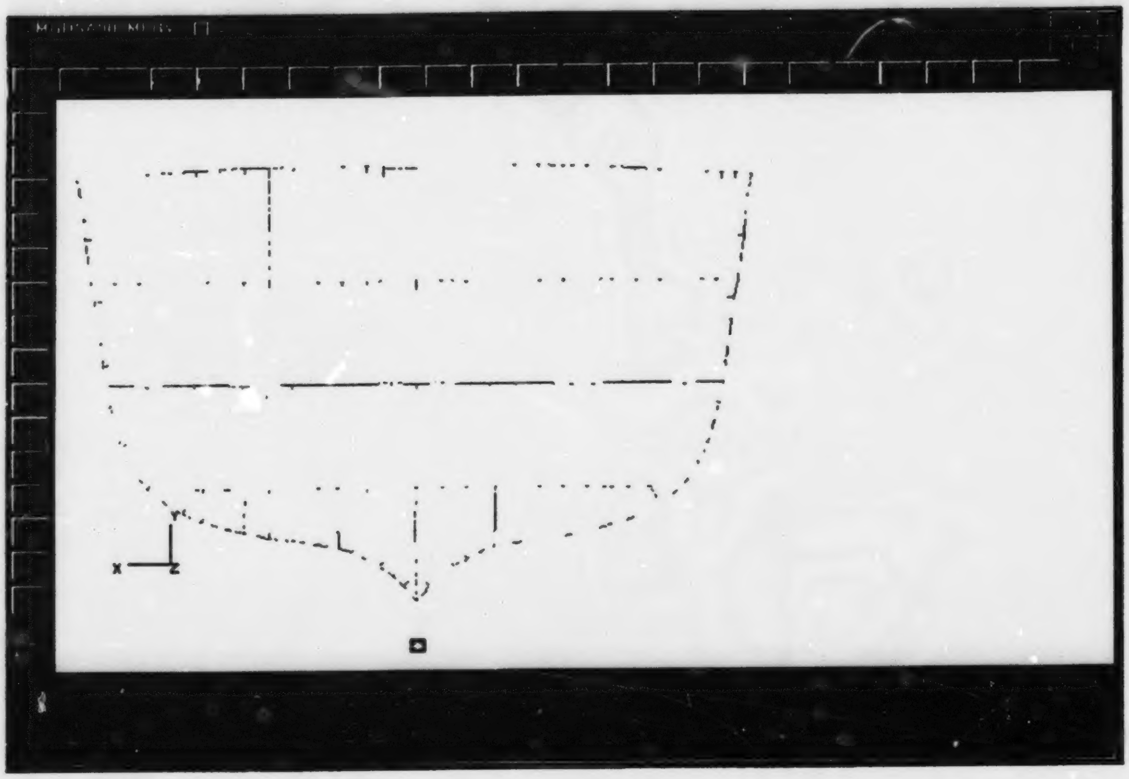

Figure 7.3: CPF Cross-section at Station 50.75 Which Contains Stiffened Panels with the Minimum Plate Slenderness Ratio β.

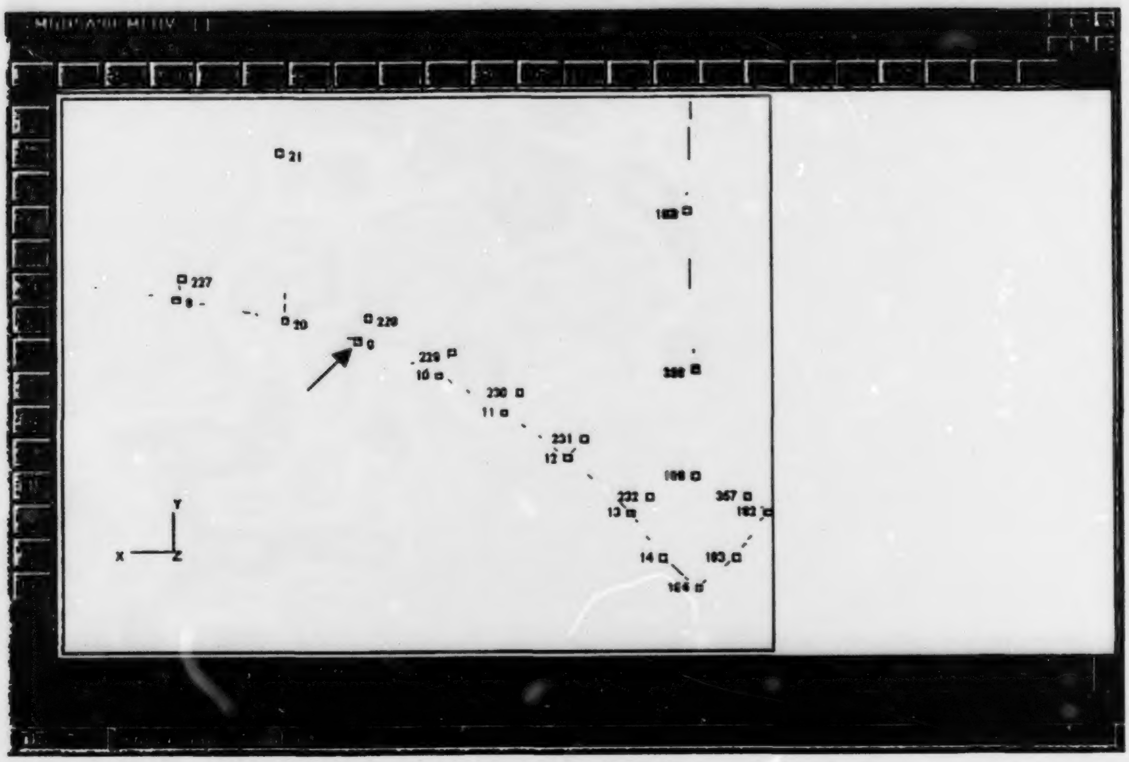
21
227
8
20
228
9
229
10
230
11
231
12
232
13
14
184
183
182
357
186
Y
X
Z

Figure 7.4: Details of CPF Cross-section at Station 50.75 Which Contains Stiffened Panels with the Minimum Plate Slenderness Ratio β.

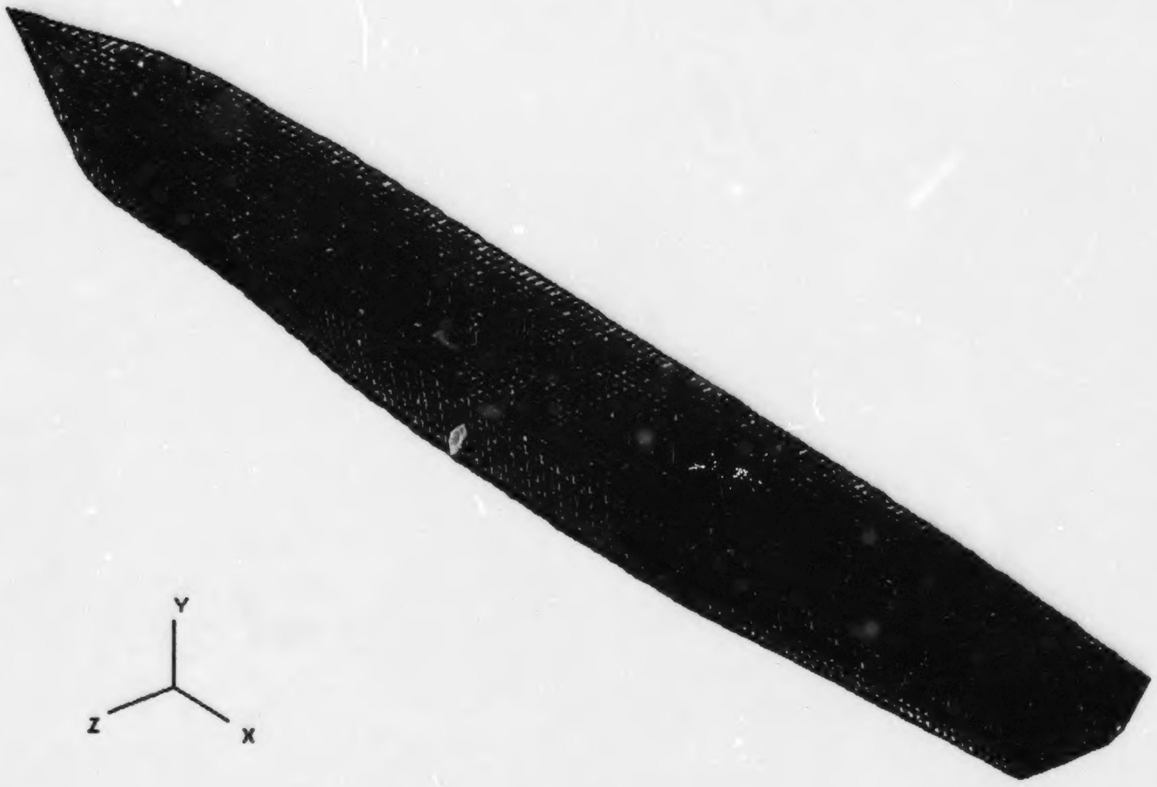

Figure 7.5: Global Finite Element Mesh of a CPF Model After Removal of Superstructures.

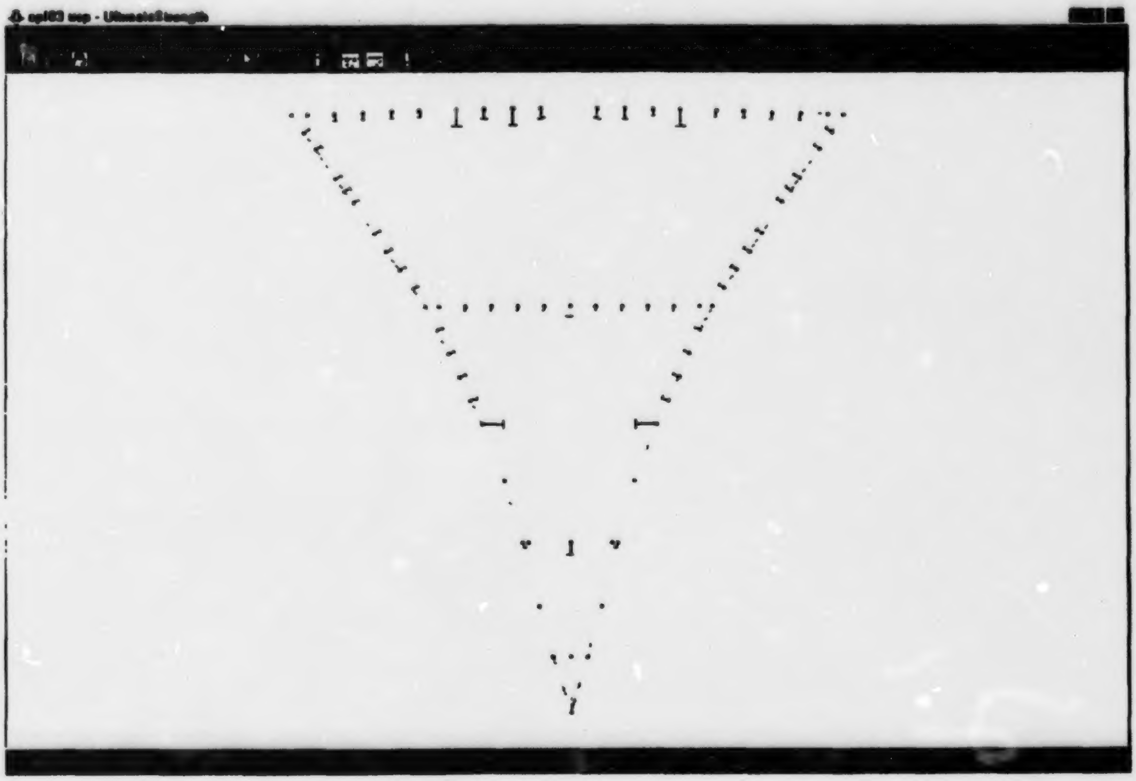

Figure 7.6: CPF Cross-section at Station 3.0 Generated by MGDSA.

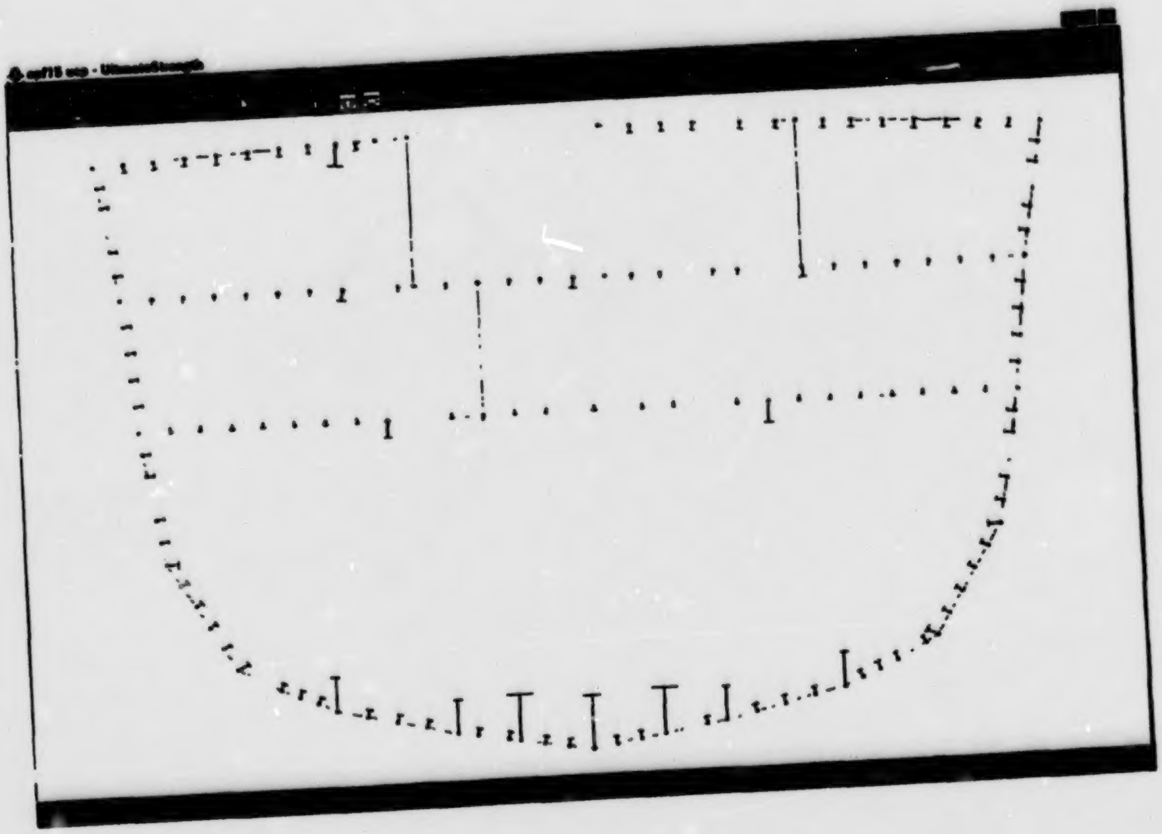

Figure 7.7: CPF Cross-section at Station 39.0 Generated by MGDSA.

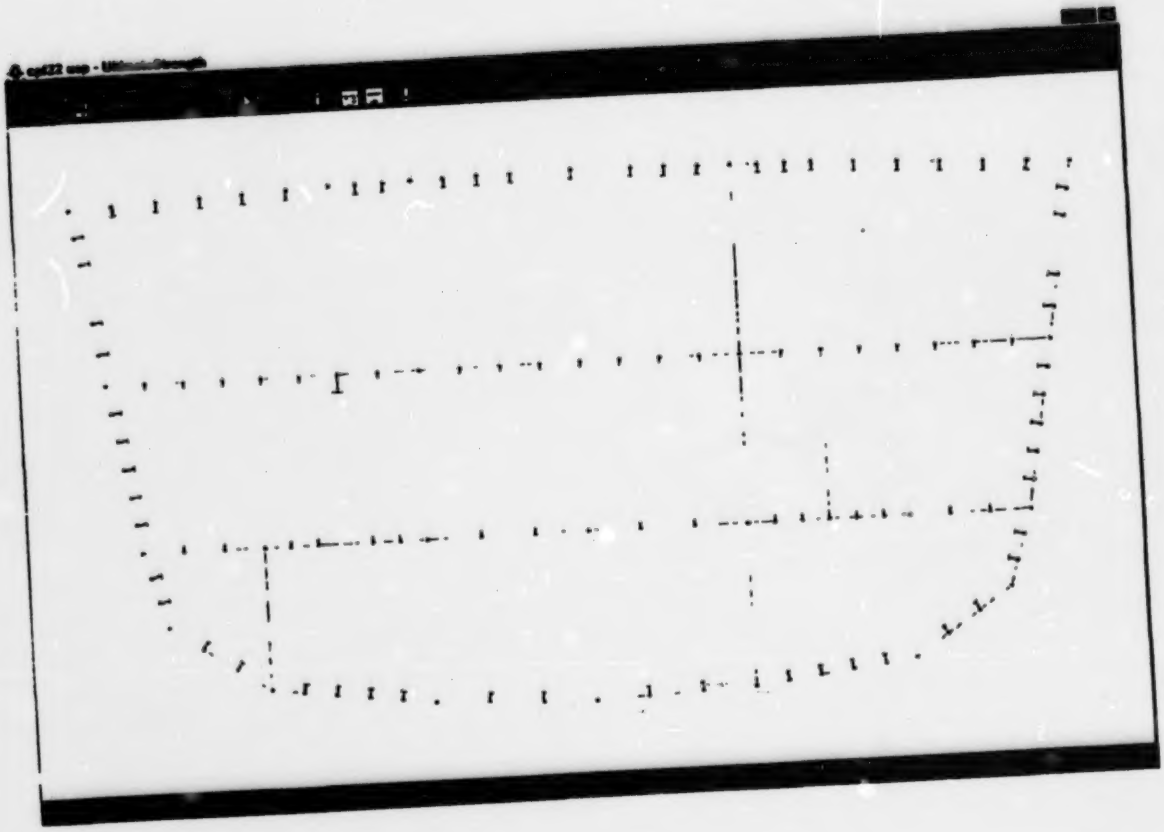

Figure 7.8: CPF Cross-section at Station 60.0 Generated by MGDSA.

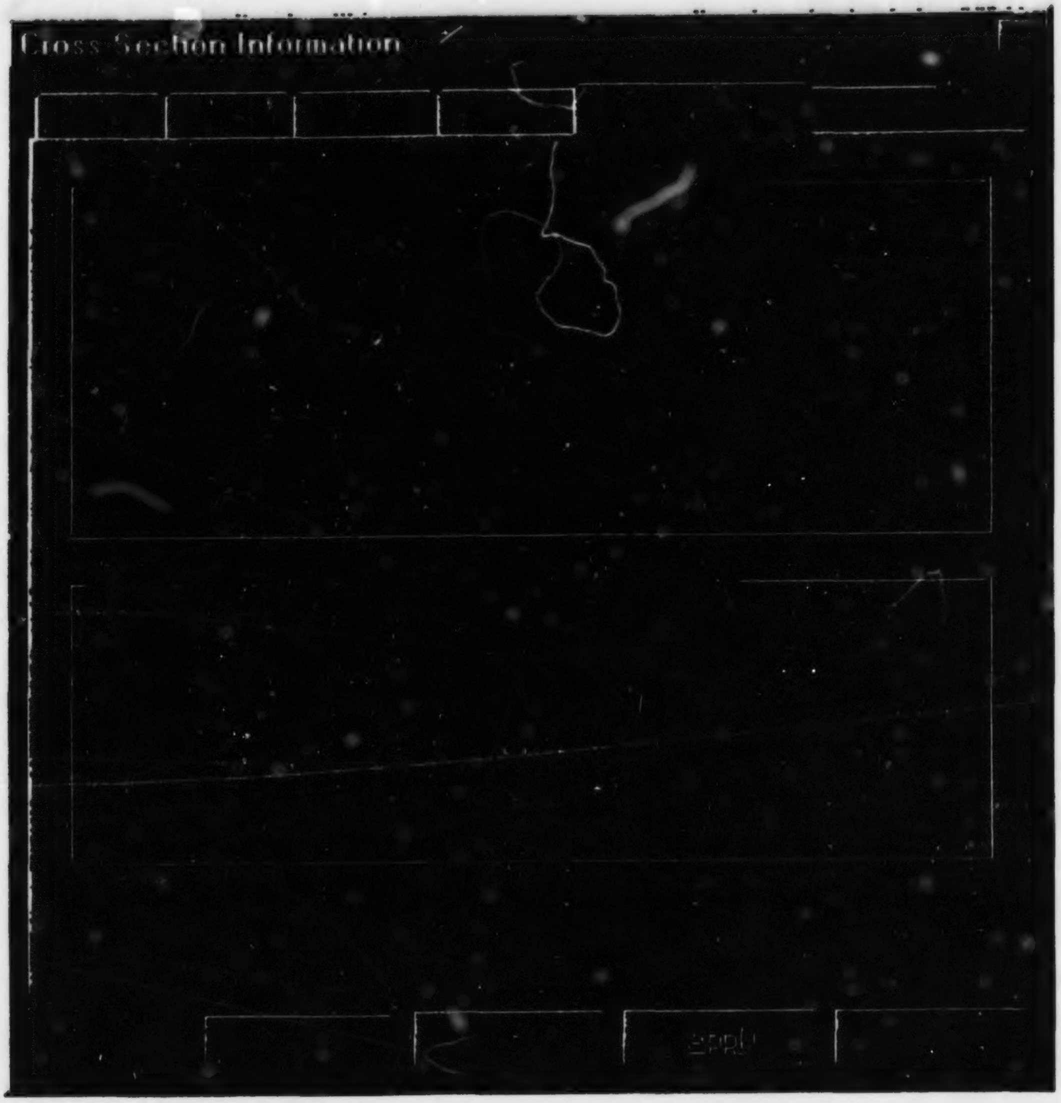

Cross Section Information

Figure 7.9: Cross-section Information Dialog Box of the Ultimate Strength Analysis Program.

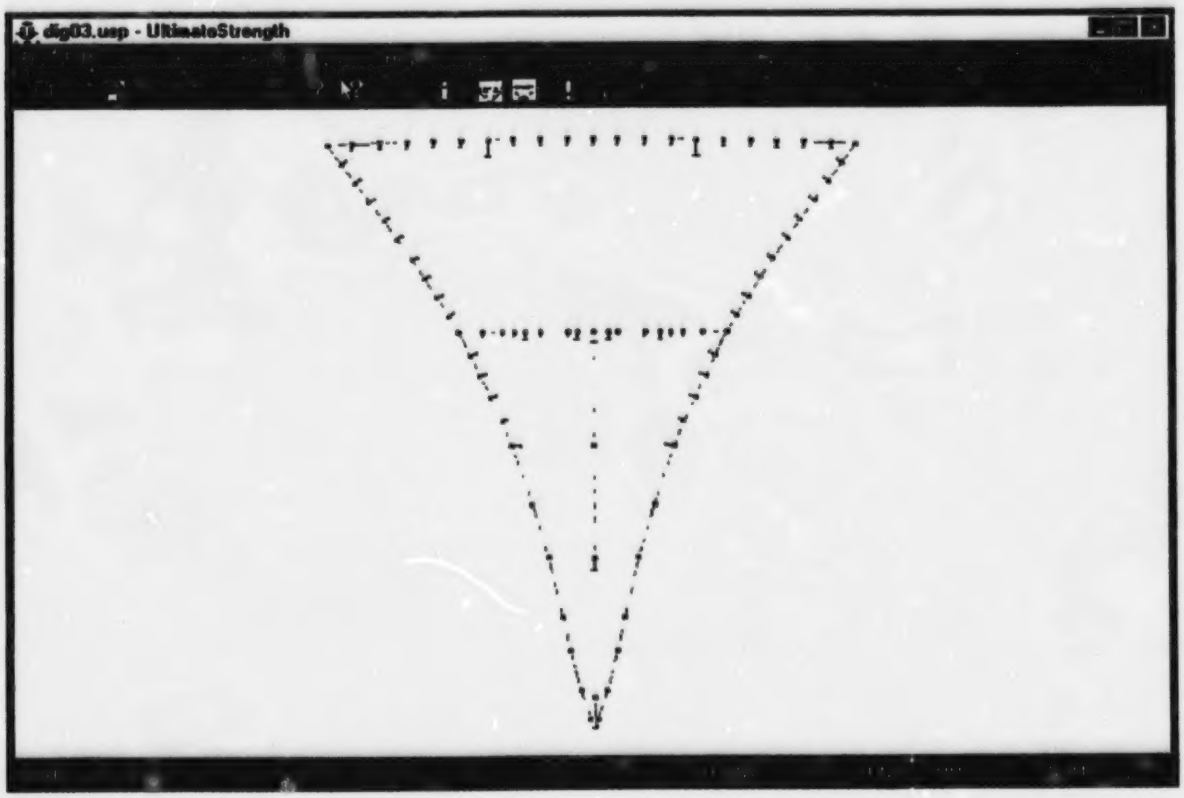
dig03.usp - UltimateStrength

Figure 7.10: CPF Cross-section at Station 3.0 Generated Using the DIGFEM File.

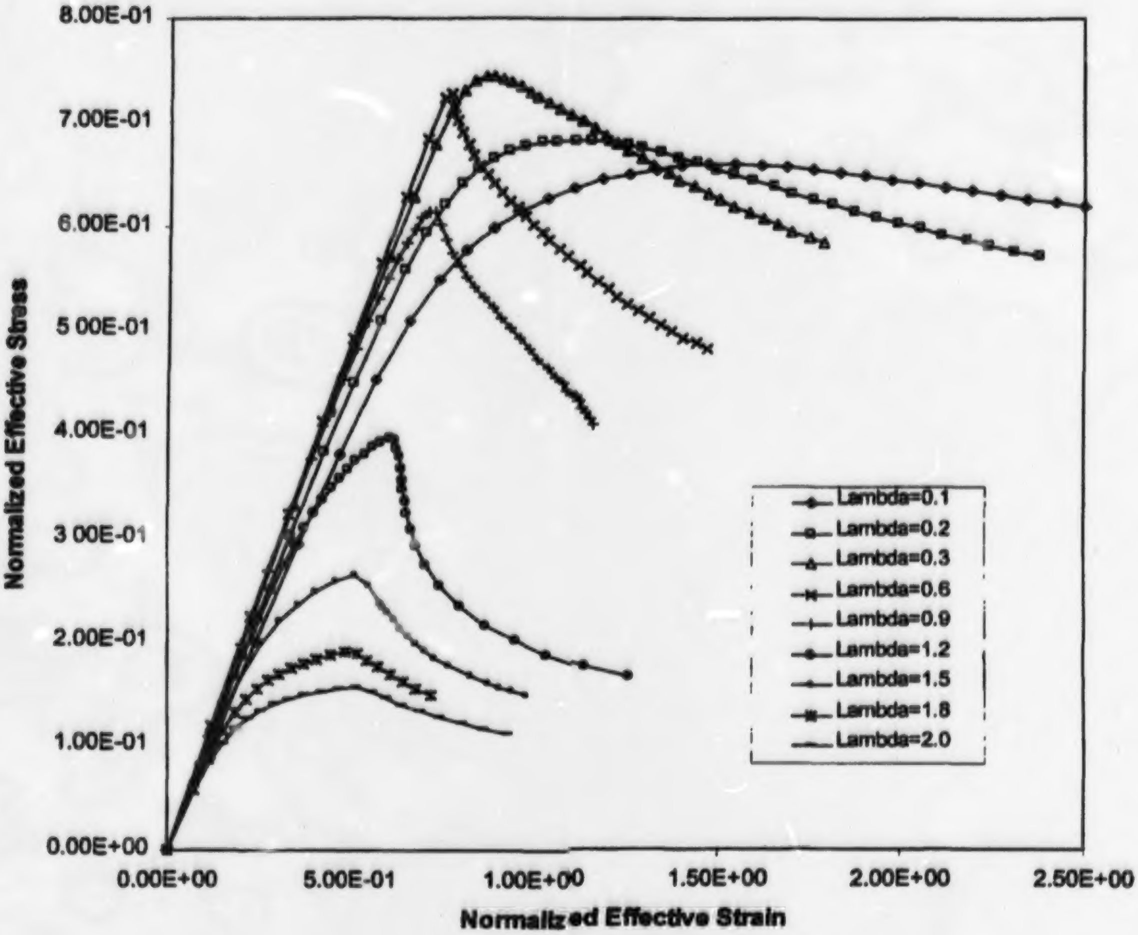

Figure 7.11: Comparison of Load-Shortening Curves for Stiffened Panels with Different Column Slenderness Ratio λ.

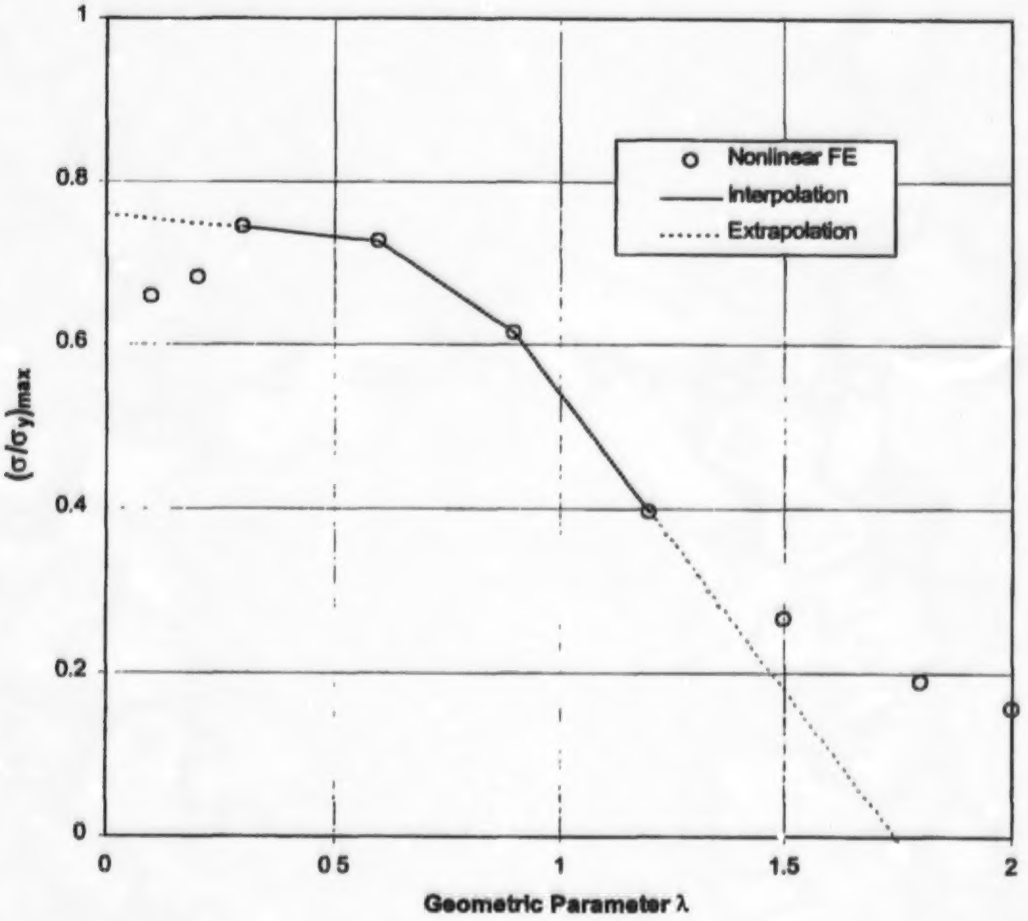

Figure 7.12: Comparison of Peak Loads Predicted by the Nonlinear Finite Element Method and the Interpolation (Extrapolation) Scheme for Different λ Values.

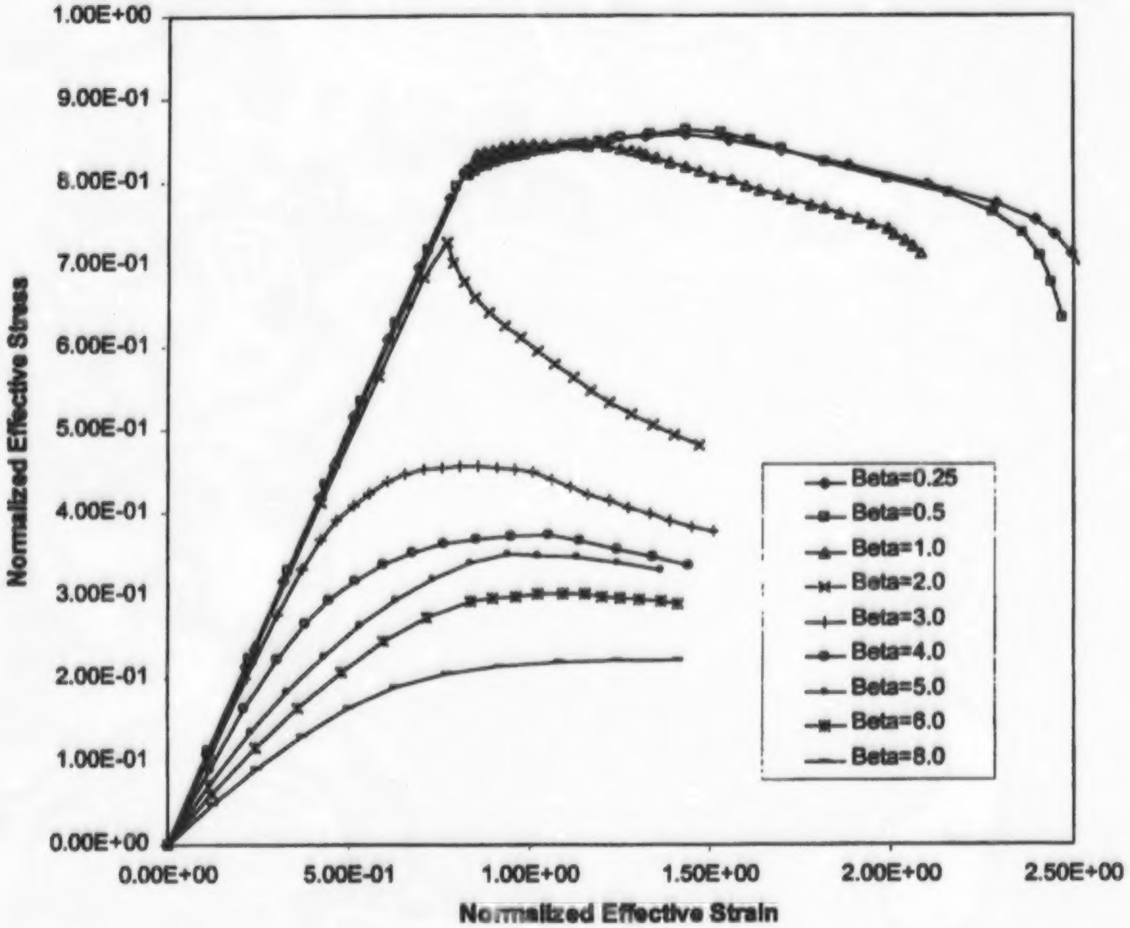

Figure 7.13: Comparison of Load-Shortening Curves for Stiffened Panels with Different Plate Slenderness Ratio β.

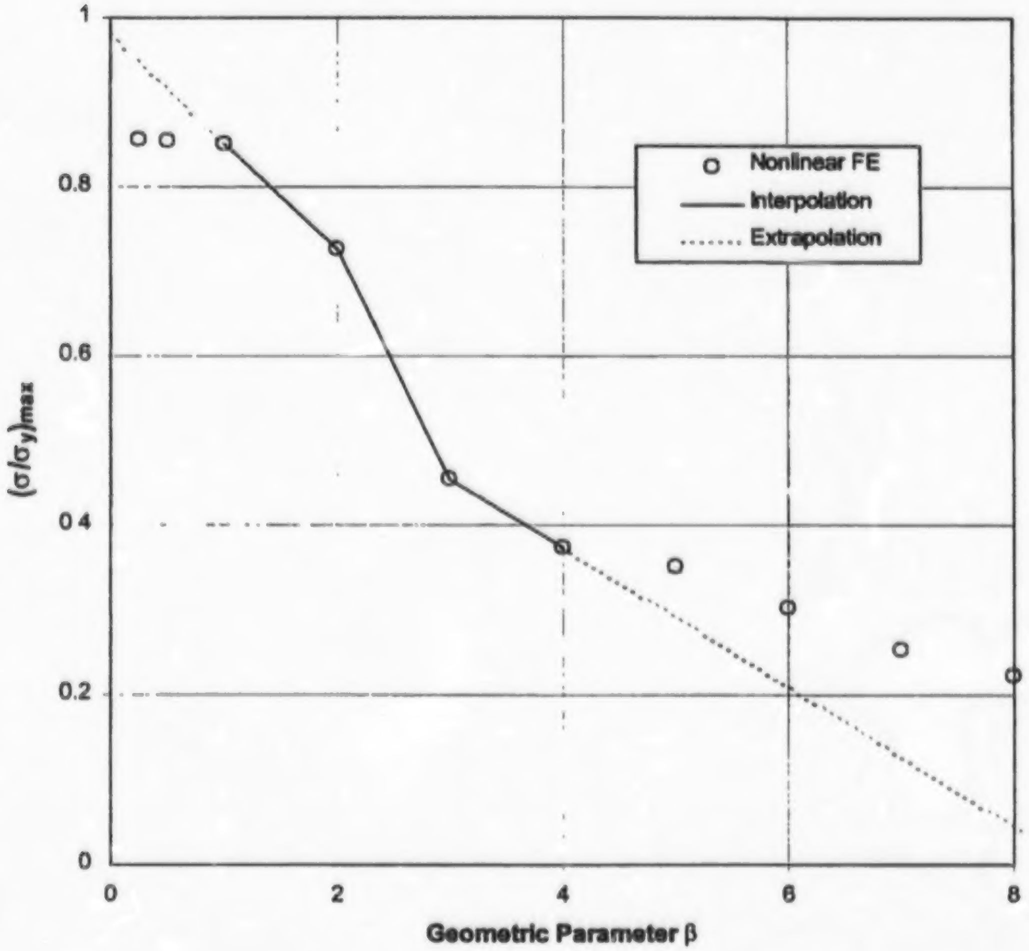

Figure 7.14: Comparison of Peak Loads Predicted by the Nonlinear Finite Element Method and the Interpolation (Extrapolation) Scheme for Different β Values.

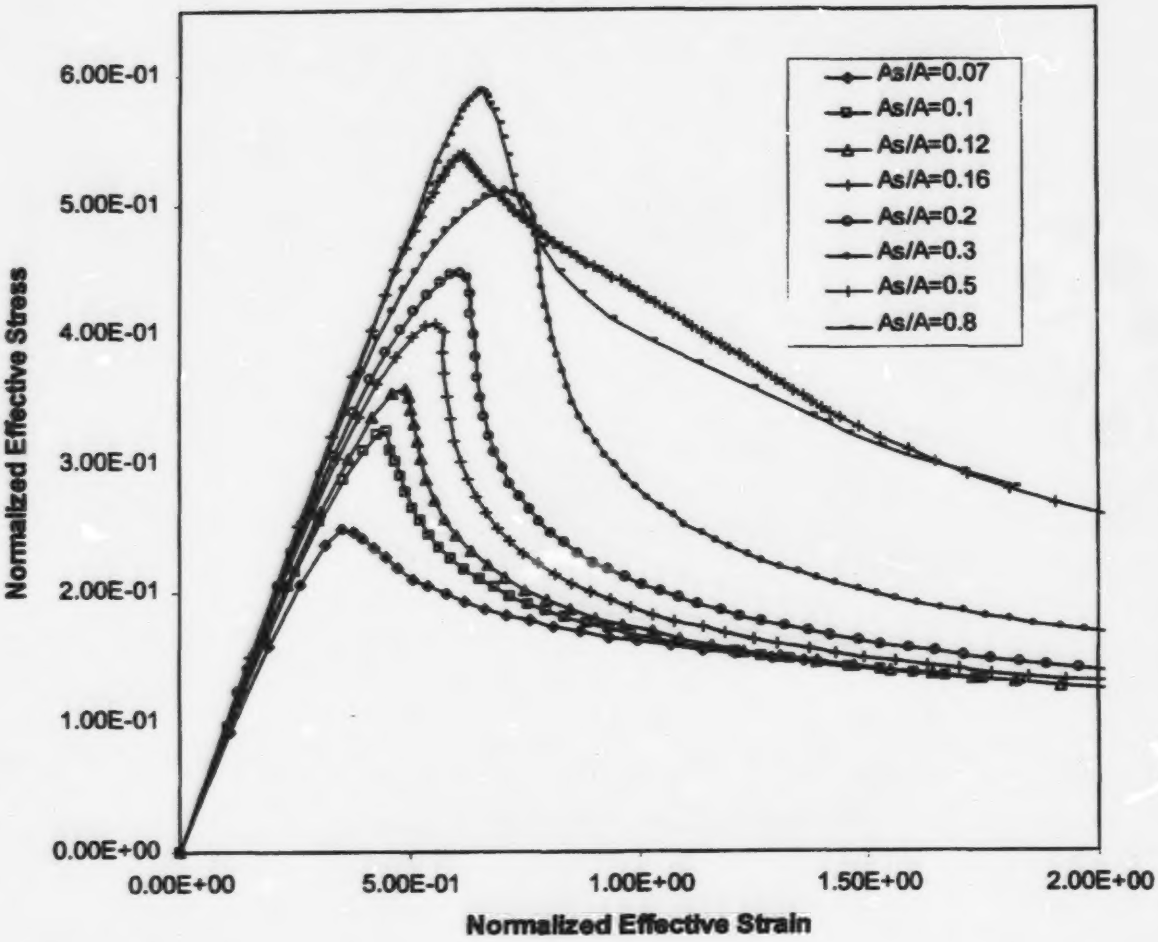

Figure 7.15: Comparison of Load-Shortening Curves for Stiffened Panels with Different Stiffener/Plate Area Ratio A_s/A.

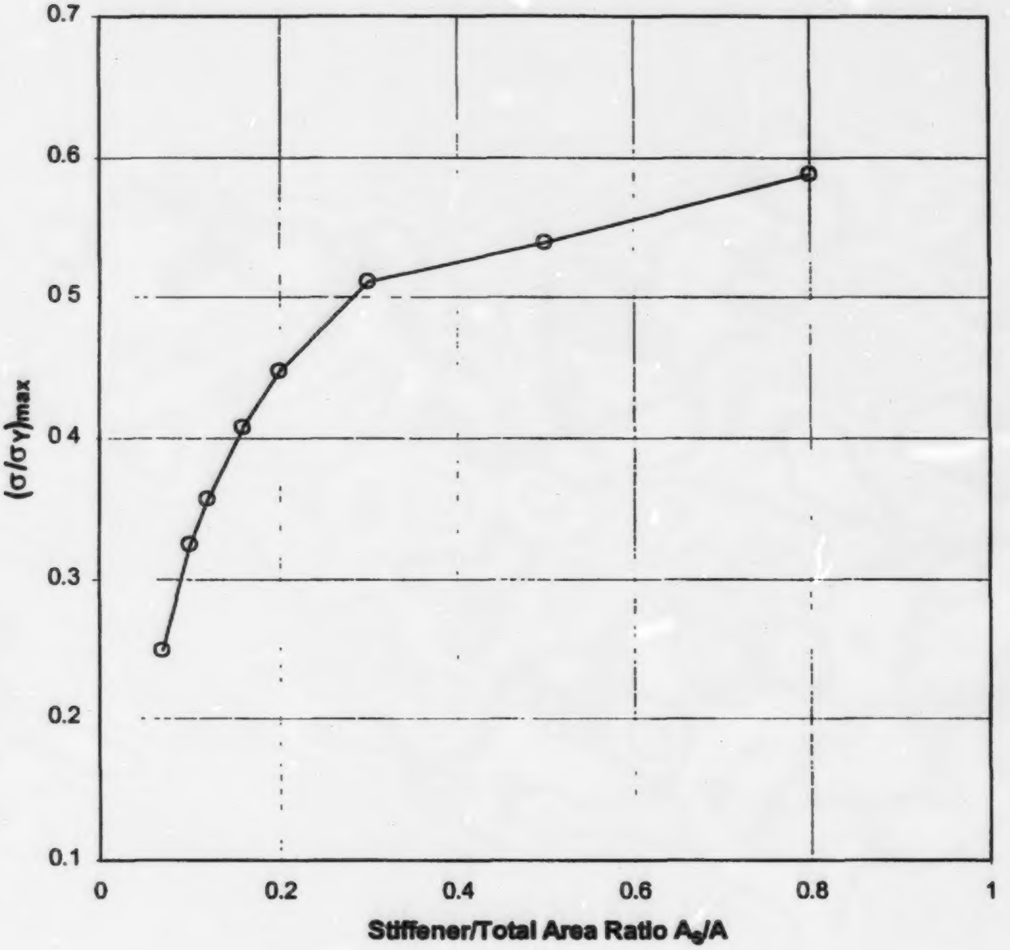

Figure 7.16: Peak Loads Predicted by the Nonlinear Finite Element Method for Stiffened Panels with Different A_S/A Values.

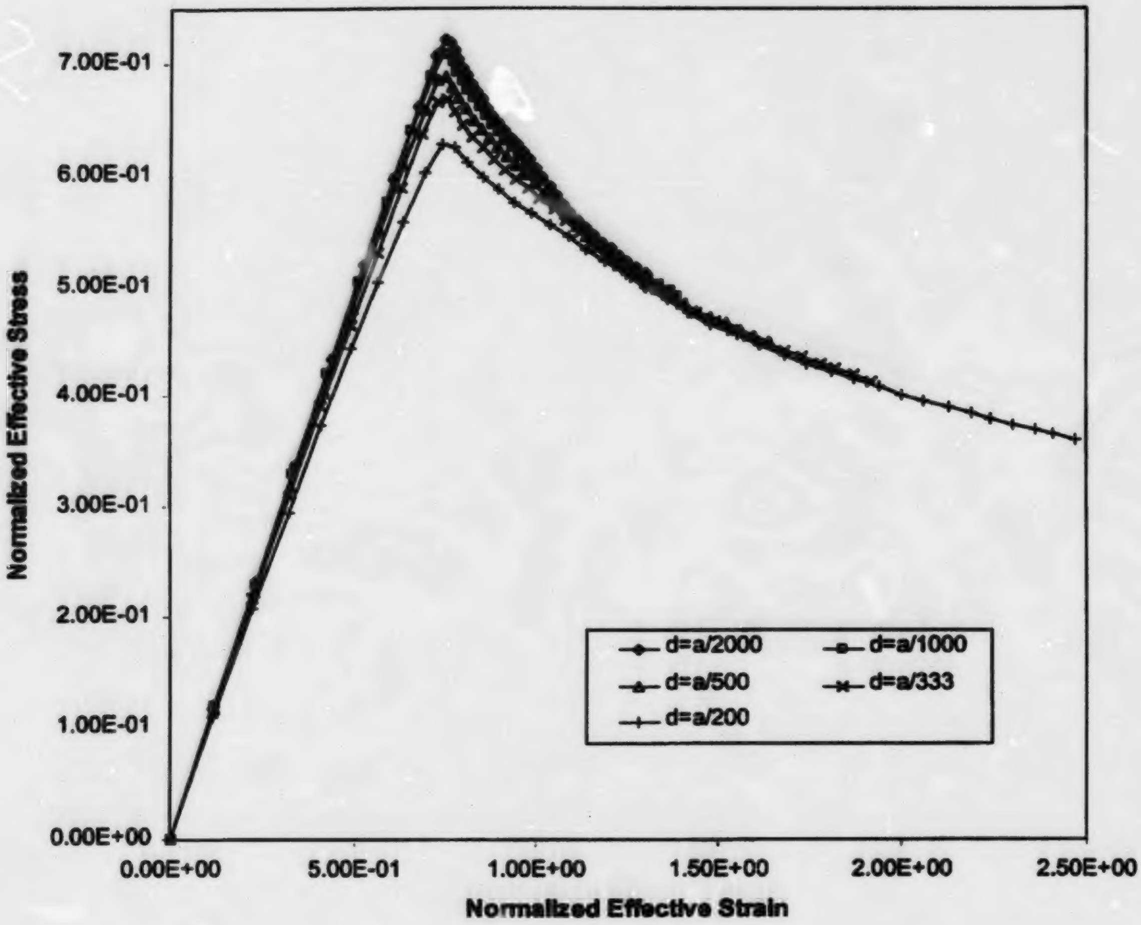

Figure 7.17: Comparison of Load-Shortening Curves for Stiffened Panels with Different Magnitudes of Stiffener Imperfection.

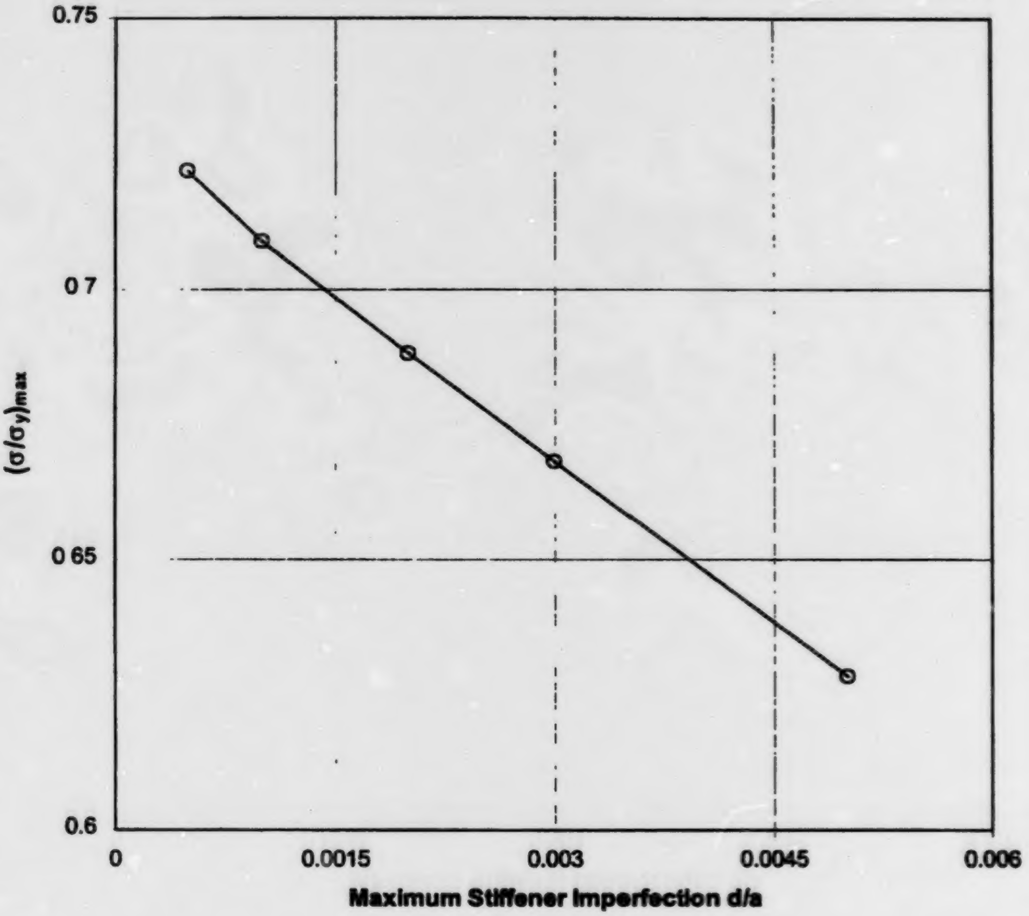

Figure 7.18: Peak Loads Predicted by the Nonlinear Finite Element Method for Stiffened Panels with Different Magnitudes of Stiffener Imperfection.

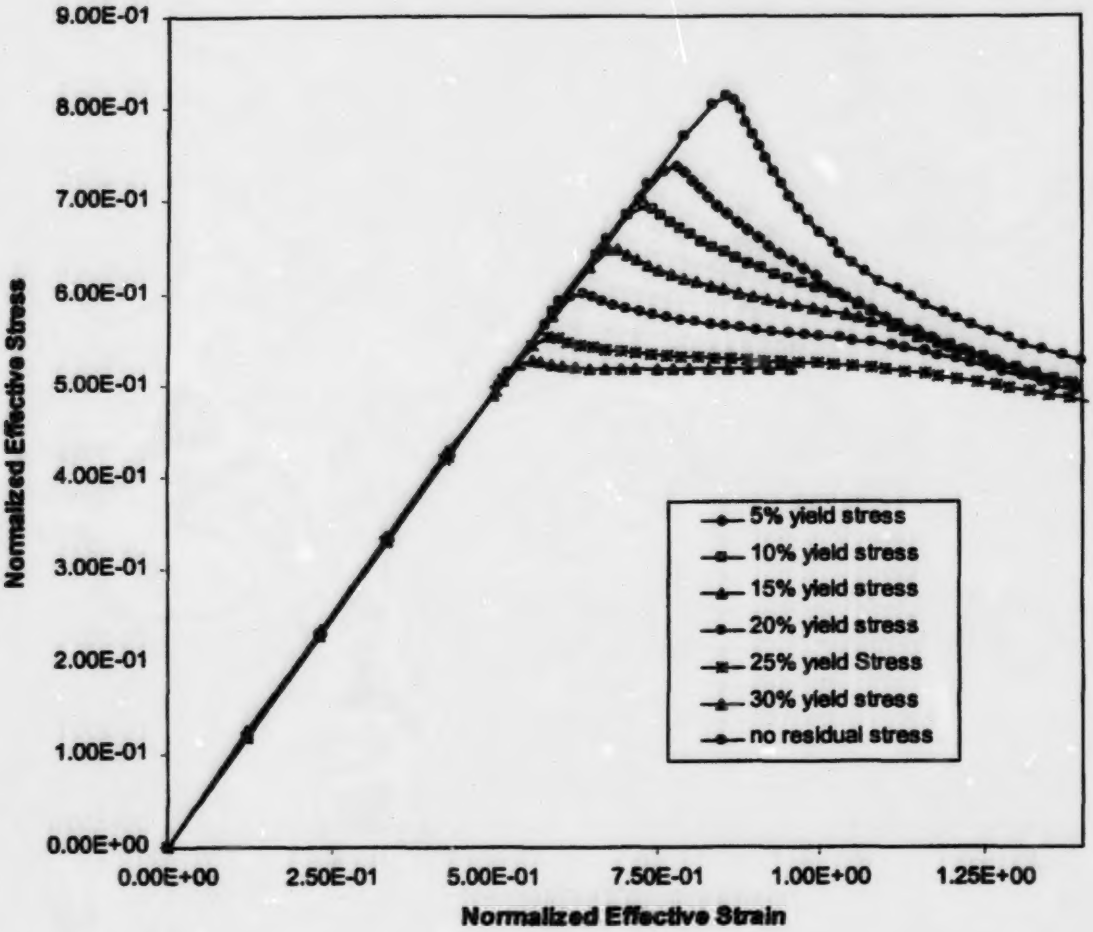

Figure 7.19: Comparison of Load-Shortening Curves for Stiffened Panels with Different Magnitudes of Residual Stress.

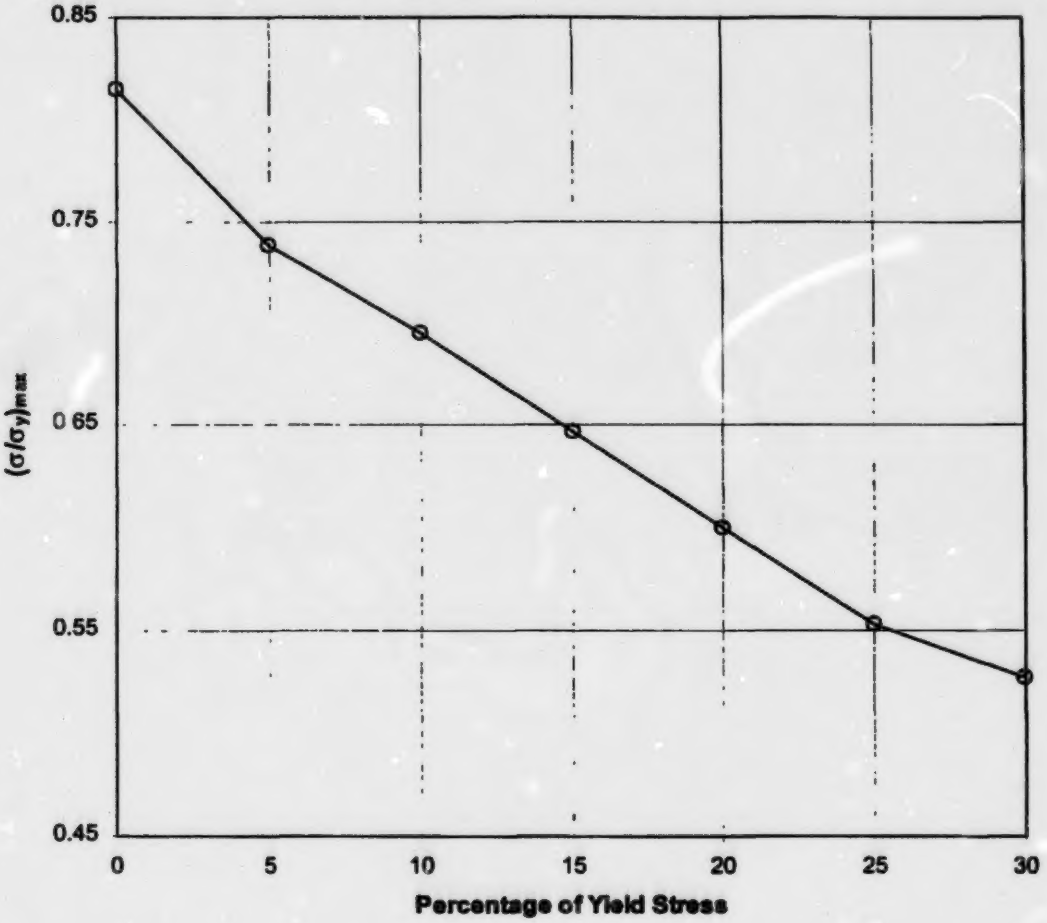

Figure 7.20: Peak Loads Predicted by the Nonlinear Finite Element Method for Stiffened Panels with Different Magnitudes of Residual Stress.

8. CONCLUSIONS AND RECOMMENDATIONS FOR FURTHER WORK

In the present contract, the efficiency of the VAST finite element program for linear and nonlinear analyses has been improved. First of all, an iterative linear algebraic equation solver based on the preconditioned conjugate gradient method has been implemented, and seven preconditioners, which were derived based on the stationary iterative methods and the original and modified incomplete factorization algorithms have been provided. Secondly, in order to create accurate residual stress fields for load-shortening curve calculations for stiffened panels with severe geometric imperfections, a linear elastic thermal stress analysis capability has been developed in seven structural and solid elements in VAST. Thirdly, the STRESS module has been completely restructured to achieve a significantly improved performance for multiple load cases. Fourthly, a capability of conducting multiple analyses with single execution has been developed in VAST. With this feature, different solution steps could be used in different sections of nonlinear and dynamic analyses, and the process of calculating load-shortening curves of stiffened panels was fully automated. All the newly developed capabilities were verified using extensive numerical studies.

In an attempt to simplify the procedure of load-shortening curve computation, the possibility of using higher-order harmonic functions to define additional geometric imperfection has been investigated. The numerical results indicated that stable nonlinear solutions could be obtained by using a uniform distribution of the higher order harmonic terms, however, to achieve the same peak load, a greater amplitude of the harmonic mode imperfection was normally required than that of the buckling mode imperfection, resulting in a underestimation of the pre-buckling stiffness of the stiffened panel. The adequacy of the previously developed load-shortening curve data for ultimate strength analysis of the CPF has also been assessed. This assessment included a calculation of the ranges of geometric parameters, λ and β, for representative ship cross-sections and an investigation of the effects of other parameters on the nonlinear behavior of stiffened panels. The numerical results suggested expansion of the load-shortening curve database and modification of the interpolation algorithm in the ultimate strength programs.

During the present work, it has been realized that the efficiency of the VAST program can be further improved by carrying out the following modifications.

i. An in-core solution algorithm should be developed for nonlinear analyses. Since the present structure of the VAST program is designed to allow restart from an arbitrary module involved in an analysis, all disk files are closed at the end of every module and reopened at the beginning of the subsequent module. This obviously requires a significant number of I/O operations. However, for nonlinear analyses, restart can only be performed at the beginning of a selected load step and restart from an intermediate module is not permissible. On the other hand, the model size for nonlinear analysis is normally relatively small and can be easily kept completely in-core on a modern personal computer. It is expected that a significant improvement in efficiency should be achieved by eliminating all the unnecessary file handling operations.

ii. A data pre-processor module should be developed in VAST. This pre-processor will calculate the in-core space requirement for a given finite element analysis and determine whether this analysis can be performed completely in-core. If the model is found to be too big to fit in core, the regular solution procedure will be activated. The band width reduction algorithm will be executed in this module to find the optimum order of the nodes and the skyline structure will also be formed so that the element stiffness matrices will be assembled into the global stiffness matrix directly when they are generated. For out-of-core solver, this pre-processor module will also provide useful information, such as the appropriate record length of the direct-access file containing element stiffness matrices.

iii. As has been presented in the final section of Chapter 2, the pre-conditioner derived using the multi-level or multi-grid concept is highly efficient for structural analyses with very poorly-conditioned stiffness matrices, such as those resulted from thin shell structures. This pre-conditioner should be implemented into the VAST program.

iv. Because the convergence of the conjugate gradient method is only guaranteed for positive definite problems and its performance is heavily dependent on the condition number of the coefficient matrix, the direct solution algorithm is obviously still attractive for plastic, post-buckling analyses of thin shell structure. The efficiency of the direct solver is closely related to the number of fill-in terms below the skyline in the assembled stiffness matrix, which can be minimized by using high quality minimum degree ordering algorithms. As a result, an investigation should be conducted to survey the most recently developed minimum degree ordering algorithms, and the difference between these algorithms and the existing bandwidth reduction algorithm in VAST should be studied. From the reviewed minimum degree ordering algorithms, some of the promising algorithms should be implemented and benchmarked.

v. It has been clearly demonstrated in Chapter 4 that recalculation of the stress matrices in the STRESS module is more efficient than carrying them on the .T43 file. This should be implemented in VAST in the next phase of the work.

vi. The efficiency of the DISP1 module should be improved for multiple load cases. This can be achieved by keeping multiple load vectors in-core during the forward reduction and backward substitution. Similar approaches can also be used to speed up the modules for subspace iterative method, added mass matrix calculation, and random vibration.

vii. In EIGEN1, the efficiency of the matrix-vector production should be improved by using the sparse storage of the global mass or geometric stiffness matrix.

9. REFERENCES

Chapter 2:

[2.1] O. AXELSSON and V.A. BARKER, *Finite Element Solution of Boundary Value Problems, Theory and Computation*, Academic Press, Inc., Orlando, 1984.

[2.2] A. JENNINGS and J.J. McKEOWN, *Matrix Computation* (Second Edition), Wiley, Chichester, 1992.

[2.3] A. M. BRUASET, *A Survey of Preconditioned Iterative Methods*, Longman Scientific & Technical, New York, 1994.

[2.4] O. AXELSSON, *Iterative Solution Methods*, Cambridge University Press, 1994.

[2.5] C. T. KELLEY, *Iterative Methods for Linear and Nonlinear Equations*, Society for Industrial and Applied Mathematics, Philadelphia, 1995.

[2.6] G.H. GOLUB and C.F. VAN LOAN, *Matrix Computations* (Third Edition), The John Hopkins University Press, 1996.

[2.7] A. GREENBAUM, *Iterative Methods for Solving Linear Systems*, Society for Industrial and Applied Mathematics, Philadelphia, 1997.

[2.8] J.A. MEIJERINK and H.A. VAN DER VORST, "An Iterative Solution Method for Linear Systems of Which the Coefficient Matrix is a Symmetric *M*-Matrix", *Mathematics of Computation*, Vol.31, No.137, pp.148-162, (1977).

[2.9] M.A. AJIZ and A. JENNINGS, "A Robust Incomplete Cholesky-Conjugate Gradient Algorithm", *International Journal for Numerical Methods in Engineering*, Vol.20, pp.949-966, (1984).

[2.10] M.T. JONES and P.E. PLASSMANN, "An Improved Incomplete Cholesky Factorization", *ACM Transactions on Mathematical Software*, Vol.21, No.1, pp.5-17, (1995).

[2.11] M.T. JONES and P.E. PLASSMANN, "Algorithm 740: Fortran Subroutines to Compute Improved Incomplete Cholesky Factorizations", *ACM Transactions on Mathematical Software*, Vol.21, No.1, pp.18-19, (1995).

[2.12] D.S. KERSHAW, "The Incomplete Cholesky-Conjugate Gradient Method for the Iterative Solution of Systems of Linear Equations", *Journal of Computational Physics*, Vol.26, pp.43-65, (1978).

[2.13] T.A. MANTEUFFEL, "An Incomplete Factorization Technique for Positive Definite Linear Systems", Mathematics of Computation, Vol.34, No.150, pp.473-497, (1980).

[2.14] E.L. POOLE, N.F. KNIGHT, JR. and D.D. DAVIS, JR., "High-Performance Equation Solvers and Their Impact on Finite Element Analysis", *International Journal for Numerical Methods in Engineering*, Vol.33, pp.855-868, (1992).

[2.15] M. BERCOVIER and A. ROSENTHAL, "Using the Conjugate Gradient Method with Preconditioning for Solving FEM Approximations of Elasticity Problems", *Engineering Computations*, Vol.3, pp.77-80, (1986).

[2.16] N. MUNKSGAARD, "Solving Sparse Symmetric Sets of Linear Equations by Preconditioned Conjugate Gradients", *ACM Transactions on Mathematical Software*, Vol.6, No.2, pp.206-219, (1980).

[2.17] G. BRUSSINO and V. SONNAD, "A Comparison of Direct and Preconditioned Iterative Techniques for Sparse, Unsymmetric System of Linear Equations", *International Journal for Numerical Methods in Engineering*, Vol.28, pp.801-815, (1989).

[2.18] N.G. PEGG, *The Preconditioned Conjugate Gradient Method for Solving Finite Element Matrix Equations*, Defence Research Establishment Atlantic, DREA Note No. H/88/4, 1988.

[2.19] M. PAPADRAKAKIS, "Accelerating Vector Iteration Methods", *ASME Journal of Applied Mechanics*, Vol.53, pp.291-297, (1986).

[2.20] C.E. JOUGLARD and A.L.G.A. COUTINHO, "A Comparison of Iterative Multi-Level Finite Element Solvers", *Computers & Structures*, Vol.69, pp.655-670 (1998).

[2.21] A.L.G.A. COUTINHO, J.L.D. ALVES, N.F.F. EBECKEN and P.R. DEVLOO, "Two-Level Hierarchical Pre-conditioners for Finite Element Equations", presented at the Winter Annual Meeting of the ASME, Atlanta, Dec 1-6, 1991. Also in ASME publication CED-Vol.4: *Iterative Equation Solvers for Structural Mechanics Problems*, pp.47-55, 1991.

[2.22] I. GUSTAFSSON, "A Class of Preconditioned Conjugate Gradient Methods Applied to Finite Element Equations", in *Preconditioned Conjugate Gradient Methods* (edited by O. Axelsson and L. Yu), Lecture Notes in Mathematics, 1457, pp.44-57, Springer-Verlag, 1990.

[2.23] J.K. DICKINSON and P.A. FORSYTH, "Preconditioned Conjugate Gradient Methods for Three-Dimensional Linear Elasticity", *International Journal for Numerical Methods in Engineering*, Vol.37, pp.2211-2234, (1994).

[2.24] E. GRAHAM and P.A. FORSYTH, "Preconditioning Methods for Very Ill-Conditioned Three-Dimensional Linear Elasticity Problems", *International Journal for Numerical Methods in Engineering*, Vol.44, pp.77-99, (1999).

[2.25] M.C. DRACOPOULOS and M.A. CRISFIELD, "Coarse/Fine Mesh Pre-conditioners for the Iterative Solution of Finite Element Problems", *International Journal for Numerical Methods in Engineering*, Vol.38, pp.3297-3313, (1995).

[2.26] V.E. BULGAKOV and G. KUHN, "High-Performance Multilevel Iterative Aggregation Solver for Large Finite-Element Structural Analysis Problems", *International Journal for Numerical Methods in Engineering*, Vol.38, pp.3529-3544, (1995).

[2.27] J. FISH and V. BELSKY, "Generalized Aggregation Multi-Level Solver", *International Journal for Numerical Methods in Engineering*, Vol.40, pp.4341-4361, (1997).

[2.28] J. MANDEL, "Iterative Methods for p-Version Finite Elements: Preconditioning Thin Solids", Computer Methods in Applied Mechanics and Engineering, Vol.133, pp.247-257, (1996).

[2.29] J.A. MITCHELL and J.N. REDDY, "A Multi-Level Hierarchical Pre-conditioner for Thin Elastic Solids", *International Journal for Numerical Methods in Engineering*, Vol.43, pp.1383-1400, (1998).

Chapter 3:

[3.1] J.C. WALLACE, L. JIANG and M.W. CHERNUKA, "Generation of a Normalized Effective Stress-Strain Curve Database of Stiffened Plates for the Halifax Class Frigate", Martec Technical Report TR-97-39, December, 1997.

[3.2] L. JIANG and M.W. CHERNUKA, "Continued Development of a Normalized Effective Stress-Strain Curve Database of Stiffened Plates for the Halifax Class Frigate", Martec Technical Report TR-98-08, March 1998.

[3.3] T.S.Z. HU, "Nonlinear Finite Element Simulation of the Test Procedure for Stiffened Panels Under Combined Lateral and In-plane Loads", Technical Memorandum 97/219, DREA, March 1997.

[3.4] B.A. BOLEY and J.H. WIENER, *Theory of Thermal Stresses*, John Wiley, 1960.

[3.5] *ADINA Verification Manual – Nonlinear Problems*, ADINA R&D, Inc., 1987.

Chapter 5:

[5.1] L. JIANG, J.C. WALLACE and M.W. CHERNUKA, "An Automatic Mesh Generator and Convergence Study for Calculating Load-Shortening Curves of Stiffened Plates for the Halifax Class Frigate", Martec Technical Report TR-97-33, October, 1997.

[5.2] L. JIANG and M.W. CHERNUKA, "Implementation of a Large Displacement Capability for VAST – Phase II", Martec Technical Report TR-93-14, April, 1993.

Chapter 6:

[6.1] L. JIANG, J.C. WALLACE and M.W. CHERNUKA, "An Automatic Mesh Generator and Convergence Study for Calculating Load-Shortening Curves of Stiffened Plates for the Halifax Class Frigate", Martec Technical Report TR-97-33, October, 1997.

[6.2] L. JIANG and M.W. CHERNUKA, "Continued Development of a Normalized Stress-Strain Curve Database of Stiffened Plates for the Halifax Class Frigate", Martec Technical Report TR-98-08, March, 1998.

[6.3] T.S.Z. HU, "Nonlinear Finite Element Simulation of the Test Procedure for Stiffened Panels Under Combined Lateral and In-plane Loads", Technical Memorandum 97/219, DREA, March 1997.

Chapter 7:

[7.1] L. JIANG and M.W. CHERNUKA, "Continued Development of a Normalized Stress-Strain Curve Database of Stiffened Plates for the Halifax Class Frigate", Martec Technical Report TR-98-08, March, 1998.

UNCLASSIFIED
SECURITY CLASSIFICATION OF FORM
(highest classification of Title, Abstract, Keywords)

DOCUMENT CONTROL DATA

(Security classification of title, body of abstract and indexing annotation must be entered when the overall document is classified)

1 **ORIGINATOR** (the name and address of the organization preparing the document. Organizations for whom the document was prepared, e.g. Establishment sponsoring a contractor's report, or tasking agency, are entered in section 8.)

Martec Ltd.
Suite 400, 1888 Brunswick St.,
Halifax, Nova Scotia B3J 3J8

2 **SECURITY CLASSIFICATION** (overall security classification of the document including special warning terms if applicable)

Unclassified

3 **TITLE** (the complete document title as indicated on the title page. Its classification should be indicated by the appropriate abbreviation (S,C,R or U) in parentheses after the title).
A Procedure

Improved Nonlinear Solution Techniques in the VAST Finite Element Program

4 **AUTHORS** (Last name, first name, middle initial. If military, show rank, e.g. Doe, Maj. John E.)

L. Jiang, M.W. Chernuka

5 **DATE OF PUBLICATION** (month and year of publication of document)

February 2000

6a **NO OF PAGES** (total containing information. Include Annexes, Appendices, etc)

215 (approx.)

6b **NO OF REFS** (total cited in document)

40

7 **DESCRIPTIVE NOTES** (the category of the document, e.g. technical report, technical note or memorandum. If appropriate, enter the type of report, e.g. interim, progress, summary, annual or final. Give the inclusive dates when a specific reporting period is covered)

Contractor Report

8 **SPONSORING ACTIVITY** (the name of the department project office or laboratory sponsoring the research and development. Include address)

Defence Research Establishment Atlantic
P.O. Box 1012
Dartmouth, N.S. B2Y 3Z7

9a **PROJECT OR GRANT NO** (if appropriate, the applicable research and development project or grant number under which the document was written. Please specify whether project or grant)

1gc-14

9b **CONTRACT NO** (if appropriate, the applicable number under which the document was written)

W7707-8-5876

10a **ORIGINATOR'S DOCUMENT NUMBER** (the official document number by which the document is identified by the originating activity. This number must be unique to this document.)

DREA CR 2000-101

10b **OTHER DOCUMENT NOs** (Any other numbers which may be assigned this document either by the originator or by the sponsor.)

11 **DOCUMENT AVAILABILITY** (any limitations on further dissemination of the document, other than those imposed by security classification)

(X) Unlimited distribution
(   ) Defence departments and defence contractors; further distribution only as approved
(   ) Defence departments and Canadian defence contractors; further distribution only as approved
(   ) Government departments and agencies; further distribution only as approved
(   ) Defence departments; further distribution only as approved
(   ) Other (please specify):

12 **DOCUMENT ANNOUNCEMENT** (any limitation to the bibliographic announcement of this document. This will normally correspond to the Document Availability (11). However, where further distribution (beyond the audience specified in (11) is possible, a wider announcement audience may be selected)

Full, unlimited

UNCLASSIFIED
SECURITY CLASSIFICATION OF FORM

UNCLASSIFIED
SECURITY CLASSIFICATION OF FORM
(highest classification of Title, Abstract, Keywords)

13 ABSTRACT (a brief and factual summary of the document. It may also appear elsewhere in the body of the document itself It is highly desirable that the abstract of classified documents be unclassified. Each paragraph of the abstract shall begin with an indication of the security classification of the information in the paragraph (unless the document itself is unclassified) represented as (S), (C), (R), or (U). It is not necessary to include here abstracts in both official languages unless the text is bilingual).

See p. ii for full text

14 KEYWORDS, DESCRIPTORS or IDENTIFIERS (technically meaningful terms or short phrases that characterize a document and could be helpful in cataloguing the document. They should be selected so that no security classification is required Identifiers, such as equipment model designation, trade name, military project code name, geographic location may also be included If possible keywords should be selected from a published thesaurus e g Thesaurus of Engineering and Scientific Terms (TEST) and that thesaurus-identified If it not possible to select indexing terms which are Unclassified, the classification of each should be indicated as with the title)

Ships
Structures
Finite element analysis
FEA graphics

UNCLASSIFIED
SECURITY CLASSIFICATION OF FORM